Valorization of wood and plastic waste by pyro-gasification and syngas cleaning

Augustina Ephraim

Université Fédérale

Toulouse Midi-Pyrénées

THÈSE

en vue de l'obtention du

DOCTORAT DE L'UNIVERSITÉ DE TOULOUSE

délivré par

L'École Nationale Supérieure des Mines d'Albi-Carmaux

---

présentée et soutenue par

Augustina EPHRAIM

le 30 novembre 2016

Valorization of wood and plastic waste by pyro-gasification and syngas cleaning

---

École doctorale et discipline ou spécialité :
MEGEP : Génie des procédés et de l'Environnement

Unité de recherche :
Centre RAPSODEE, CNRS - UMR 5302, Mines Albi

Directeur(s) de Thèse :
M. Ange NZIHOU, Professeur, Mines Albi

Autres membres du jury :
M. Jean-Michel LAVOIE, Professeur, Université de Sherbrooke, *Président*
M. Fabrice PATISSON, Professeur, École des Mines de Nancy, *Rapporteur*
M. Carlo VANDECASTEELE, Professeur, KU Leuven, *Rapporteur*
Mme Chantal BLOCK, Professeur, KU Leuven, *Examinateur*
M. Yong CHI, Professeur, Université de Zhejiang, *Examinateur*
M. Damien LEBONNOIS, Ingénieur, Suez, *Examinateur*
M. Doan PHAM MINH, Maître de Conférences HDR, Mines Albi, *Examinateur, Encadrant*
M. Patrick SHARROCK, Professeur Émérite, Université de Toulouse III, *Invité, Encadrant*
M. Jean-Marc AUDIC, Docteur-Ingénieur, Suez, *Invité*

Valorization of wood and plastic waste by pyro-gasification and syngas cleaning

Augustina EPHRAIM

Under the supervision of

Ange NZIHOU

Under the co-supervision of

Doan PHAM MINH and Patrick SHARROCK

PhD thesis defended on the 30th of November 2016

This work was funded by Suez.

École Nationale Supérieure des Mines d'Albi-Carmaux

To my parents,
who taught me that
"If at first you don't succeed,
Try, try, try again !".

A mes parents,
qui m'ont transmis ce proverbe
"Si tu ne réussis pas la première fois,
Essaie, essaie, essaie encore !"

Abstract / Résumé

Valorization of wood and plastic waste by pyro-gasification and syngas cleaning

Wood and plastic waste are interesting feedstock for the production of syngas via pyro-gasification, mainly due to their abundant supply and good fuel properties. However, syngas derived from waste may contain significant amounts of hydrogen chloride (HCl), which is corrosive and toxic and must therefore be removed.

In this work, co-pyrolysis experiments were first conducted in order to study the influence of mixing different plastics with wood samples on the pyrolysis products. It was found that HDPE and PS significantly increase the heating value and HCl content of the gas product respectively, while PVC increases the yield of char and HCl. Next, pilot-scale experiments were performed, which revealed that adding 1 wt% PVC to wood waste raises the content of tar and HCl in syngas by factors of 2 and 5,5 respectively, and also elevates the chlorine concentration in the char residue 16 time over the value obtained in the absence of PVC.

In parallel, a CFD model was developed to simulate the pyro-gasification of wood waste by coupling fluid flow, heat and mass transfer, and chemical reactions. This model consists of drying, pyrolysis, oxidation and char gasification sub-models. The simulation results were in good agreement with experimental data obtained from the pilot-scale experiments. Furthermore, sensibility analyses on the char gasification sub-model were performed.

Finally, an experimental study was conducted on the removal of HCl from syngas. The study focused on valorizing two industrial solid wastes generated from the process of sodium carbonate and sodium bicarbonate manufacture. Their HCl adsorption performance were compared to those of the commercial sorbents, $NaHCO_3$ et $Ca(OH)_2$. Moreover, the effect of gas matrix on their performance was studied. The industrial wastes showed potential for treating acid gas as compared to the commercial sorbents used. This opens up new approaches to the purification of syngas generated by the pyro-gasification of wood and plastic waste.

Keywords: Waste, Pyrolysis, Gasification, Modelling, Hydrogen chloride, Syngas cleaning.

Valorisation de déchets de bois et matières plastiques par pyrogazéification et épuration des gaz

Les déchets de bois et de plastiques sont des ressources prometteuses pour la production du gaz de synthèse (syngaz) par la pyro-gazéification grâce à leurs disponibilités et leurs caractéristiques énergétiques. Cependant, le syngaz issu de ces déchets peut contenir des teneurs élevées en chlorure d'hydrogène (HCl) qui est corrosif et toxique et qui doit donc être éliminé.

Premièrement, les expériences de pyrolyse des mélanges de bois de peuplier et de plastiques ont mis en évidence l'influence des plastiques sur les produits obtenus. En effet, le HDPE et PS augmente respectivement le pouvoir calorifique du syngaz et le rendement en huiles, tandis que le PVC augmente le rendement en char et le HCl dans le syngaz. Ensuite, les expériences de pyro-gazéification à l'échelle pilote ont montré que l'ajout de 1 % en masse de PVC dans un déchet de bois augmente la teneur en goudrons et HCl dans le syngaz par un facteur respectivement de 2 et 5,5, tandis que la concentration de chlore dans le char résiduel est 16 fois plus élevée.

En parallèle, un model CFD a été développé pour simuler la pyro-gazéification du déchet de bois en couplant les phénomènes d'écoulement de fluides, transfert de masse et de chaleur, et les réactions chimiques. Ce modèle se compose des sous-modèles de séchage, pyrolyse, oxydation et gazéification du char. Les résultats de simulation sont en bon accord avec les données expérimentales obtenues par des expériences dans un gazéifieur à l'échelle pilote. En outre, les analyses de sensibilités du sous-modèle de la gazéification de char ont été réalisées.

Finalement, une étude expérimentale a été conduite sur le traitement de HCl dans le syngaz. L'étude se concentre sur la valorisation de deux résidus solides industriels issus de la production de bicarbonate et carbonate de sodium. Leurs réactivités sont comparés avec celles de deux adsorbants commerciaux, $NaHCO_3$ et $Ca(OH)_2$. L'effet de la matrice gazeuse sur la performance des adsorbants est également examiné. Les résidus industriels ont un potentiel intéressant par rapport aux adsorbants commerciaux. Les résultats obtenus montrent des nouvelles approches pour la purification du syngaz généré par la gazéification des déchets de bois et de plastiques.

Mots-clés: Déchet, Pyrolyse, Gazéification, Modélisation, Chlorure d'hydrogène, Purification du syngaz.

Table of contents

Introduction

Introduction

Waste management is a major issue in most developed and developing countries. According to a recent World Bank report, 1.3 billion tonnes per year of municipal solid waste (MSW) is currently generated worldwide and is expected to double by the year 2025 [1]. As this high level of waste production results in significant economic and environmental costs, many countries particularly in Europe, have set goals to become "Recycling Societies" - one that does not only avoid producing waste but also uses it as a resource [2]. The reality however is that no waste material can be infinitely recycled and certain materials are non-recyclable as they contain harmful impurities. Instead of landfilling such waste, a viable alternative is to recover much of the inherent energy bound in the waste by transforming its combustible fraction into fuel.

Pyro-gasification is a promising thermochemical process for recovering energy from combustible solid waste, which requires temperatures above 800 °C and an oxidant, such as air or steam, to convert the waste into syngas. Syngas is rich in hydrogen (H_2) and carbon monoxide (CO) and has been influential in the development of human society since its first commercial use by the London Gas, Light and Coke Company in 1812, from coal gasification [3]. It has illuminated cities, provided heat and power, and fuelled vehicles through both direct use and conversion to liquid fuels (Figure 1). As global energy demand is projected to rise by nearly 56 % from the year 2010 to a projected 865 EJ in 2040, syngas will become increasingly important for energy production and chemical synthesis [4]. However, for waste-derived syngas, a major technical challenge must be overcome in order to achieve a wider market penetration, which is linked to the development of improved and cheaper syngas cleaning methods in order to meet the increasingly strict specifications of various end-uses devices and environmental emissions regulations [5].

Several types of waste feedstock exist on the market that can be valorized energetically. Amongst them are wood and plastic wastes, which are well-suited for syngas production because of their abundant supply coupled with their currently low recycling rates and good fuel properties [6–8]. Furthermore, standards exist to control the quality of wood and plastic wastes, as well as policy incentives and waste

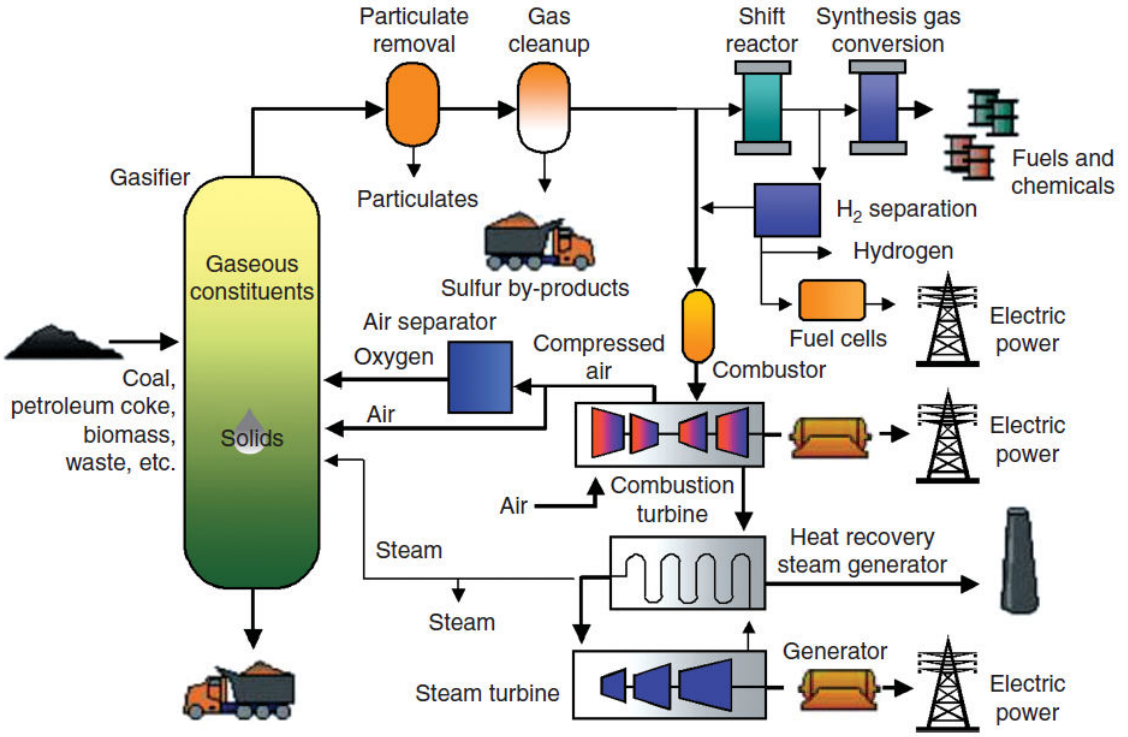

FIGURE 1: Schematic representation of a pyro-gasification system for syngas production, cleaning and use [11]

legislations that encourage energy recovery from these wastes in the European Union (i.e. Renewables directive (2009/28/EC), and Packaging and Packing directive (1994/62/EC). Nonetheless, wood and plastic wastes are heterogeneous and may have significant impurity levels. An important impurity is chlorine, which although naturally present in wood, may be found in significant quantities in wood and plastic waste due to the presence of the plastic, polyvinyl chloride (PVC). When such waste are gasified, hydrogen chloride gas (HCl) forms in the syngas, which may cause several problems including corrosion of metal equipments, health problems and environmental issues [9, 10]. Since it is difficult to avoid the contamination of such waste by PVC, methods for removing HCl from syngas before use are absolutely necessary.

Dry adsorption of HCl in syngas onto metal-based solid particles, such as alkali metal carbonates, is a promising technique for syngas cleaning [12–16]. This process has been sucessfully employed for cleaning flue gas from waste incinerators. A potential benefit of using this technique is that the sorbents can be regenerated using methods such as heating, which can be economically and environmentally interesting when compared to other methods such as wet scrubbing that produce wastewater which are costly to treat. Another advantage to the dry adsorption method is that it opens up opportunities to valorize metal-based solid wastes from industrial processes. This point was of particular interest in this PhD work and thus experiments were performed to compare the performance of two solid waste

sorbents with two commercial ones for HCl adsorption. More research work is however required to improve the performance of such solid waste sorbents, in terms of their capacity for HCl adsorption, and their thermal stability.

In order to control and optimize the quantity and quality of waste-derived syngas, it is important to understand the behaviour of the waste feedstock during pyro-gasification under different operating conditions. Such operating parameters may include temperature, heating rate and residence time for pyrolysis experiments, or oxidant concentration in the case of gasification experiments. Experimental studies in literature on the co-pyrolysis of wood and plastic wastes remain few, especially for mixtures of wood and PVC [17–19]. Current studies sometimes reveal conflicting results concerning the interactions between these two waste types mainly due to the different operating conditions under which the experiments were performed. As part of this thesis work, an attempt at providing greater clarity in this area was ventured by performing co-pyrolysis experiments at the laboratory scale with different wood/plastic mixtures, in order to study the influence of the type and ratio of plastics on the product yields and composition. In addition, pilot-scale pyro-gasification experiments were conducted to study the effect of adding PVC to wood waste on product composition. Furthermore, a kinetic model that predicts the pyrolysis rate of wood/PVC pellets was developed and mechanistic studies were conducted on the interactions between wood and PVC pseudo-components.

Performing pyro-gasification experiments at a large scale can be expensive, and in some cases, pose serious safety risks. Thus, it is desirable to develop a mathematical model that gives a good representation of the chemical and physical phenomena that occur in a gasifier. Such a model can be used to study the gasifier behaviour in order to optimize the gasifier design and operation with minimal temporal and financial costs [20, 21]. It is for these reasons that a one-dimensional (1D) computational fluid dynamics (CFD) model was developed in this work, to simulate the pyro-gasification of waste wood contaminated with chlorine in a downdraft fixed bed reactor. This model consists of wood drying, pyrolysis, oxidation and gasification submodels. Furthermore, the model couples fluid flow, heat and mass transfer and chemical kinetics, to describe the complex chemical and physical phenomena taking place in a gasifier.

Manuscript structure

This manuscript is divided into seven chapters which, with the exception of Chapter 1, have been written in the form of articles with the aim of publishing them in peer-reviewed journals the near future.

Chapter 1 presents a literature review concerning waste pyro-gasification and syngas cleaning. Firstly, different categories of waste-derived fuels are presented, analysed and evaluated for their adequacy as fuels for syngas production. The next part of this chapter discusses the steps involved in waste pyro-gasification as well as the reactors used for this process. Furthermore, existing pyro-gasification models are

examined. Lastly, light is shed on the end-uses of syngas, their corresponding syngas quality requirements as well as the syngas cleaning methods available.

Chapter 2 deals with the characterisation of the physico-chemical and thermal properties of industrial (class B) wood waste and model waste, consisting of virgin poplar wood, high density polyethylene (HDPE), polystyrene (PS) and polyvinyl chloride (PVC).

Chapter 3 is dedicated to an experimental study of the co-pyrolysis of poplar wood and the model plastic mixtures. The influence of plastic type and content on the product yield and composition is investigated and the observed interactions are highlighted.

Chapter 4 presents two pilot-scale pyro-gasification tests in a downdraft gasifier. The first part of the chapter discusses the first experiment involving wood waste as feedstock. Analytical results of the syngas composition including tars, HCl and permanent gas species are presented. The second part concerns the tests with wood waste feedstock containing 1 wt% PVC. In this part, the syngas composition is discussed and mass, chlorine and energy balances on the gasifier are also presented.

Chapter 5 focuses on the kinetic modelling of wood-PVC pellet pyrolysis using thermogravimetric data. Firstly, a reaction scheme is proposed which accounts for interactions between the pseudo-components of wood and PVC during co-pyrolysis. Then, Arrhenius kinetic parameters are obtained using a model-free method and the reaction mechanisms are identified using master plots.

Chapter 6 concerns the computational fluid dynamics (CFD) model developed to simulate the pyro-gasfication of wood waste in a downdraft fixed bed reactor. The first part of this chapter discusses the modelling of the char gasification zone in the downdraft reactor. This submodel is validated using experimental data found in literature. The second part of the chapter discusses the development of a complete pyro-gasificaton model consisting of drying, pyrolysis, char gasification and combustion submodels, and which is validated with the pilot-scale experimental data presented in Chapter 5.

Chapter 7 presents the experimental work performed to investigate and compare the HCl adsorption performance of two solid wastes and two commercialised sorbents under two different atmospheres. Several characterisation of these sorbents are performed before and after the tests, in an effort to link their performance to their physico-chemical properties.

CHAPTER 1

State of the art

Introduction

This chapter gives the relevant background information required to understand the work conducted in this PhD thesis. Hence, the literature review presented here is not exhaustive as the fields of waste pyro-gasification and syngas cleaning are extremely vast.

Section 1.1 presents the waste-derived fuels available on the market. Criteria for selecting the most suitable waste-derived fuels for syngas production are proposed and an evaluation of these fuels are made based on technical, economical, environmental and legal considerations.

Section 1.2 discusses the different processes involved in waste pyro-gasification (drying, pyrolysis, gasification and combustion) as well as their key operating parameters. Different pyro-gasification reactors for syngas production are also presented and compared.

Section 1.3 deals with various models of waste pyro-gasification. The advantages and inconveniences of each model type are discussed. Next, modelling procedures based on thermal analysis data are discussed, with a focus on pyrolysis (thermal decomposition) modelling.

Section 1.4 presents the various applications of syngas produced from waste pyro-gasification. The contaminants usually found in syngas are identified as well as the state-of-the-art methods for cleaning the syngas.

1.1 Waste-derived fuels

1.1.1 Waste classification

The main categories of solid waste generated in Europe are Municipal Solid Waste (MSW), Industrial and Commercial Waste (C&I), Construction and Demolition Waste (C&D), Mining and Quarrying Waste (M&Q) and Agricultural Waste [22]. Figure 1.1 shows the typical composition these waste streams [23].

Several reviews on the production of energy and fuels from components of the above waste streams can be found in literature [6, 24, 25]. From these analyses, the following waste-derived fuels have been identified to be currently available on the market:

- Refuse derived fuel (RDF) is fuel produced from MSW or C&I via a series of processes. These processes generally involve shredding, screening, sorting, drying and pelletization in order to improve the handling characteristics and homogeneity of the fuel [26].

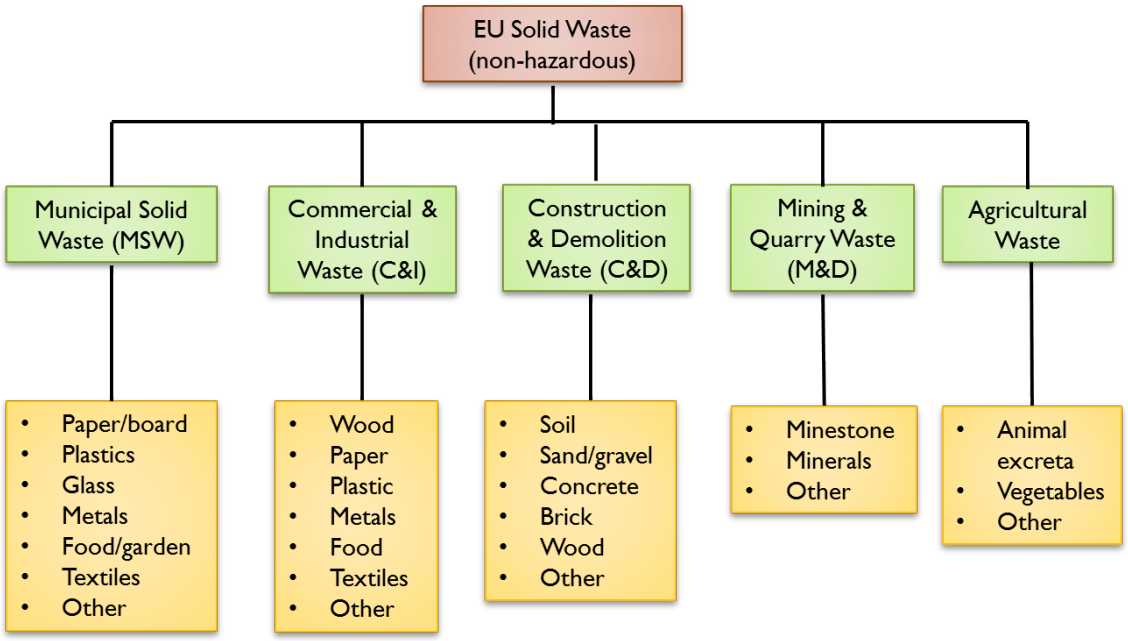

FIGURE 1.1: Classification and composition of solid waste generated in European countries [23]

- Solid recovered fuel (SRF) is comparable to RDF as it is also produced by mechanical, biological or thermal treatment of the input waste. However SRF is more homogeneous and less contaminated than RDF and it complies with tight quality specifications in order to promote its acceptability on the fuel market [27].

- Graded wood waste (GWW) is divided into different classes based on the level of contamination: A, B, C etc. Regulations regarding wood waste classification differ in various European countries. In France, GWW is divided into two categories: Class A is virgin wood and class B consists of industrial wood waste that does not contain halogenated compounds and preservatives (i.e. Creosote and Copper-chromium-arsenic (CCA))[28]

- Dried sewage sludge (DSS) is a by-product of urban and wastewater treatment whose water content has been significantly reduced by mechanical de-watering and thermal drying processes. For energy recovery of sewage sludge via thermochemical routes, the water content of DSS must be below 10 wt% [29].

- Non-recycled plastic waste (NRP) is produced from various sources, the largest source of which is food packaging in MSW due to concerns about food safety and hygiene standards [30]. The six main plastics found in NRP are high density polyethylene (HDPE), low density polyethylene (LDPE), polyethylene terepthalate (PET), polypropylene (PP), polyvinyl chloride (PVC) and polystyrene (PS) [31].

- Tyre derived fuel (TDF) is a fuel composed of shredded scrap tyres. These waste tyres are mainly consumed in the cement industry where they can be mixed with coal or other fuels such as wood to be burned in cement kilns. It is extremely difficult to recycle TDF due to its complex structure and composition which makes energy recovery a viable treatment option for TDF [32].

1.1.2 Waste selection for syngas production

Preparing the criteria for choosing suitable waste for syngas production requires a detailed analysis concerning the environmental, legal, technical and economic issues associated with the generation and use of the different waste streams. The selection criteria and their indicators are presented below and their relation to the governing issues is illustrated in Figure 1.2:

1. Supply of the waste for recovery is significant and reliable.
    - Quantity generated (tonnes/year)
    - Energy recovery rate (tonnes/year)
    - EU directives support recycle and recovery
2. Control of product quality exists.
    - Quality control standards or guidelines exist.
3. Fuel quality is high.
    - Net calorific value (NCV)
    - Moisture content
    - Ash content
    - Cl, N, S, heavy metals
4. Policy incentives exist for the recovery of the waste stream.

The indicators proposed heavily depend on the availability and reliability of data at the EU level. No weighting has been used to judge whether one indicator or the other is more important for stream selection.

For the evaluation of the different waste-derived fuels, it is convenient to group the fuels into two categories: biomass combustibles (RDF, GWW, DSS) and petrochemical combustibles (NRP and TDF). The data used to assess the different waste fuels were all obtained from literature and are displayed in table 1.1. By observing Table 1.1, on the one hand, the supply of biomass combustibles is relatively abundant and reliable. Their high energy recovery rate of between 15 and 24 Mt/yr is mainly due to the Renewables Directive (2009/28/EC) which mandates levels of renewable energy use within the European Union. On the other hand, the petrochemical combustibles have a much lower generation rate as they are increasingly being re-used on a long term basis [22]. In addition, their

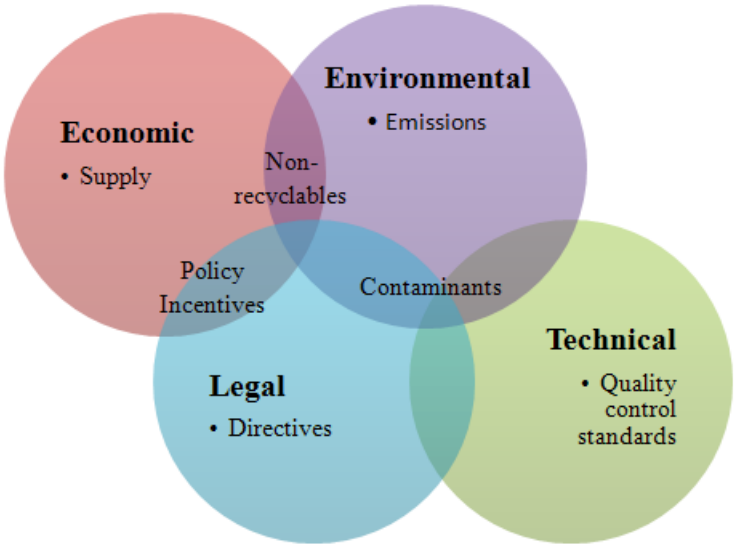

FIGURE 1.2: Waste selection criteria

energy recovery rates are relatively low because the Landfill directive (1999/31/EC), Packing and Packaging Waste Directive, PPW (1994/62/EC) and the End-of-life Vehicle Directive (2000/53/EC) have set high recycling targets for these combustibles.

Nonetheless, the petrochemical combustibles have markedly superior fuel qualities than their biomass counterparts. In particular, plastic waste generally has a high NCV (30-40 MJ/kg), low moisture content, (< 0.2 %) and low ash content (< 5 %). However mixed plastic waste also contains high concentrations of chlorine due to the presence of PVC. Although waste tyres have only slightly less superior fuel qualities, they often contain significant concentrations of Sulphur and Zinc which are added during the vulcanisation process. As discussed previously, these elements are detrimental to the effective clean-up and reforming of the gas produced.

A shortfall of using biomass combustibles for syngas production is their relatively significant moisture content which increases the energy requirement for drying in the gasifier. However GWW in classes A and B have an added advantage over sewage sludge in that they contain significantly lower concentrations of ash, N, S and the heavy metals, Hg, Cd, Zn and Pb and thus offer the potential for producing better quality syngas. RDF and SRF, tend to fall between these two extremes in terms of fuel quality. The only major advantage of using SRF over RDF is the existence of quality control standards for the former which definitely enhances the overall efficiency of the plant.

Thus the results show that of the biomass combustibles, SRF and GWW are the most suitable for syngas production. For the petrochemical combustibles, NRP is clearly the better fuel.

TABLE 1.1: Overview of the results of key criteria used for waste-derived fuel selection for syngas production. Reference to waste in EU27 [7, 8, 22, 33–35]

	Solid Waste Fuel (SWF)		**Graded wood waste (GWW)**		**Dried Sewage Sludge (DSS)**	**Non-recycled plastic waste (NRP)**	**Tyre derived fuel (TDF)**
	Refuse derived fuel (RDF)	**Solid recovered fuel (SRF)**	**Class A (AW)**	**Class B (BW)**			
Supply							
Quantity (Mt/yr, in 2004)	70.1		70.5		-	26.2	3.2
Energy recovery (Mt/yr, in 2004)	15.1		24		-	4.7	0.8
EU directives	Landfill, IED		Landfill, PPW		Landfill, IED	PPW, IED	Landfill, EVL, IED
Policy incentives	RED, EU ETS		RED, EU ETS		RED, EU ETS	-	-
Product quality control							
Existence of standards	No	Yes	Yes	Yes	No	Yes	No
Fuel quality							
NCV (MJ/kg d) (coal: 20-30 MJ/kg d.)	12-20	11-31	17-20	18.5-23	12-14	30-40	26-32
Moisture content (%) (coal: 3-10%)	15-25	24-32	10-15	10-20	~10-30	0.2	1.2 - 2
Ash content (%), (coal: 5-10%)	10-22	12 -15	1-10	0.4-1.8	30-40	5.3	10-20
Cl (%) (coal: ~0.04%)	0.4-0.6	0.07-0.88	0.01-0.05	0.01-0.03	-	2.4	-
N (%) (coal: 1-2%)	0.6	-	0.1-0.5	0.1-0.8	5	0.6	-
S (%) (coal: ~1%)	0.3	-	0.01-0.1	< 0.05	0.8	0.2	1
Hg (ppm) (coal: ~0.07 ppm)	0.2	0.25-0.45	0.02-0.05	-	0.2-1.8	-	0.17
Cd (ppm) (coal: ~0.01 ppm)	0.8	0.84-1.72	0.05-5	-	2-1500	-	8
Zn (ppm)	-	-	2-100	-	600-20000	-	2000
Pb (ppm) (coal:~3 ppm)	20	44-59.8	0.1-10	-	50-3600	-	410

Directives and Incentives

- Landfill : Landfill Directive, (1999/31/EC)
- IED : Industrial Emissions Directive, (2010/75/EU)
- RED : Renewables Directive (2009/28/EC)
- EU ETS : European Emissions Trading Scheme
- PPW : Packing and Packaging Waste Directive, (1994/62/EC)
- EVL: End-of-life Vehicle Directive, (2000/53/EC)

Colour coding

	Desirable
	Acceptable
	Undesirable

1.2 Pyro-gasification process and technologies

1.2.1 Pyro-gasification steps

There are four main steps in waste pyro-gasification: drying, pyrolysis, char gasification and oxidation. A general description of each process is given as follows:

Drying

Most pyro-gasification systems use waste biomass with a moisture content of 10 to 20 wt%. This moisture is trapped within the pores of the solid matrix in three forms: (1) Free water (above the fibre saturation point), (2) bound water (absorbed within the cell wall fibers - hemicellulose, cellulose and lignin), (3) water vapour (within the pores) [36]. The distribution of water in these three forms is governed by a liquid-vapour equilibrium. When the bio-waste feed enters the gasifier, it receives heat from the hot zone downstream. At about 100 °C and at ambient pressure, the free water inside the wood first evaporates, followed by the bound water.

Pyrolysis

Pyrolysis or devolatilization, is a thermal decomposition process that occurs in the absence of oxygen at temperatures between 300 °C and 800 °C. The three primary products of pyrolysis are: gas (mainly H_2, CH_4 CO, CO_2, C_xH_y (x = 2 or 3)), liquids (oils and tars), and char. The relative yields of these products depend mainly on the heating rate, pyrolysis temperature and residence time in the reaction zone, as well as the initial waste composition [37]. Generally, a low pyrolysis temperature, slow heating rate and long residence time increases biomass/waste conversion to char [38]. High temperature, slow heating rate and longer residence time favours conversion to gas [39], and finally, oil yield is maximised by operating at a moderate temperature, fast heating rate and short vapour residence time [18]. Regarding the initial waste composition, lignocellulosic waste with high lignin content tends to increase char yield, while high cellulose and hemicellulose content increases gas and oil (tar) yields [40, 41]. Furthermore, alkali salts in the bio-waste ash tends to catalyse pyrolysis reactions to favour CO_2 over CO production [40, 42].

Char gasification

At temperatures above 550 °C, char produced from pyrolysis can further react with gasification agents, mainly steam and/or carbon dioxide, to produce syngas which is rich in hydrogen and carbon monoxide. These key reactions are popularly known as Steam Gasification (Eq. 1.1), Boudouard (Eq. 1.2), Hydrogasification (Eq. 1.3) and Water-Gas Shift, WGS (Eq. 1.4). As can be seen in Equations 1.1 to 1.2, the combined heats of reaction ΔH_r is positive and thus heat is required for the gasification reactions to occur [43]. Walker et al. [44] have estimated the relative rates of the first three reactions, at 800 °C and 10 kPa, to be 10^3 for Steam gasification, 10^1 for Boudouard, and 3×10^{-3} for hydrogasification. As the rate of hydrogasification is much slower than the other reactions, it is not studied in most literature works

[45–49]. Moreover, it is only of importance when synthetic natural gas (SNG) is desired [36]

$$C + H_2O \rightarrow CO + H_2, \quad \Delta H_r = +131\ kJ/mol \tag{1.1}$$

$$C + CO_2 \rightarrow 2CO, \quad \Delta H_r = +172\ kJ/mol \tag{1.2}$$

$$C + 2H_2 \rightarrow CH_4, \quad \Delta H_r = -74.8\ kJ/mol \tag{1.3}$$

$$CO + H_2O \leftrightarrow CO_2 + H_2, \quad \Delta H_r = -41\ kJ/mol \tag{1.4}$$

Oxidation

To provide the heat required for drying, pyrolysis and char gasification, a certain amount of exothermic combustion is allowed in the gasifier, by injecting air or pure oxygen. The principal oxidation (combustion) reactions that occur between oxygen and the pyrolysis products are given by Equations 1.5 to 1.9 [50]. The main products of combustion, CO_2 and H_2O, serve as agents for the aforementioned char gasification reactions.

$$C + O_2 \rightarrow CO_2, \quad \Delta H_r = -394\ kJ/mol \tag{1.5}$$

$$CO + 0.5O_2 \rightarrow CO_2, \quad \Delta H_r = -283\ kJ/mol \tag{1.6}$$

$$CH_4 + 2O_2 \rightarrow CO_2 + 2H_2O, \quad \Delta H_r = -803\ kJ/mol \tag{1.7}$$

$$H_2 + 0.5O_2 \rightarrow H_2O, \quad \Delta H_r = -286\ kJ/mol \tag{1.8}$$

$$(tar)\ CH_{1.522}O_{0.0228} + 0.867O_2 \rightarrow CO + 0.761H_2O, \quad \Delta H_r = -243\ kJ/mol \tag{1.9}$$

To ensure that complete combustion does not occur in the gasifier, an important design parameter known as the equivalence ratio (ER) is evaluated. The ER is the ratio between the oxygen content in oxidant supply (air or pure oxygen) and that required for complete stoichiometric combustion as shown by the following equation

$$ER = \frac{\left(\frac{M_{O_2}}{M_{fuel}}\right)_{Actual}}{\left(\frac{M_{O_2}}{M_{fuel}}\right)_{Stoichiometric}} \tag{1.10}$$

The ER is very crucial because its higher value results in a lower concentration of H_2, CO and tars, and a higher CO_2 and H_2O content in syngas, thus decreasing the heating value of the gas [51]. For biomass gasification, values of ER between 0.25 and 0.35 are often used as they appear to maximize char conversion as shown in Figure 1.3 [43]. The actual ER value chosen depends on factors such as the fuel moisture content and tar yield [36, 43].

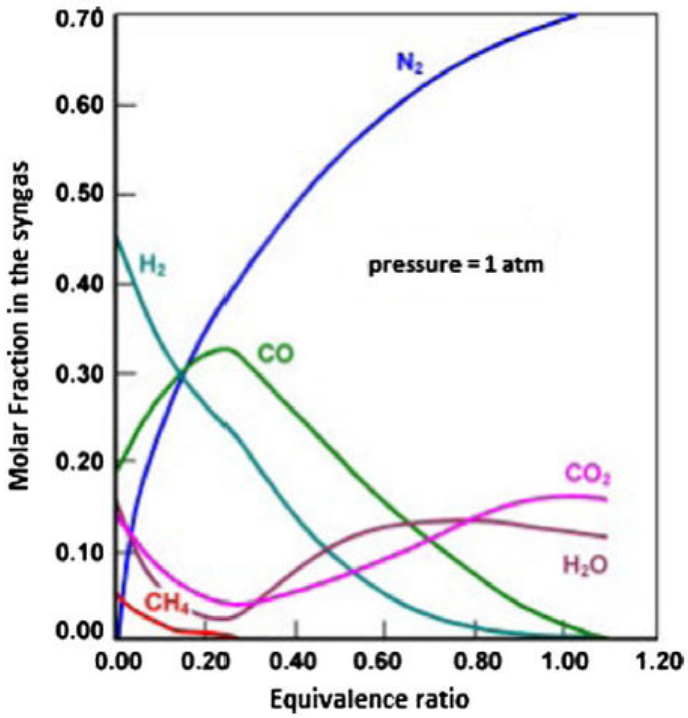

FIGURE 1.3: Syngas composition at chemical equilibrium as a function of ER, for wood gasification at 1 atm [43].

1.2.2 Pyro-gasification technologies

Currently, the reactors used for pyrolysis or gasification of biomass and waste are fixed beds, fluidised beds, rotary kilns, moving grate and plasma reactors. These reactors can be compared based on their fuel requirements, syngas quality, technical charateristics and cost as shown in Table 1.2. A brief description of each reactor type is presented as follows:

- Fixed bed reactors are also called moving-beds because the waste moves down the reactor as a plug and is supported on a grate. A major attraction of fixed beds gasifiers is that they can be built in small sizes at a relatively low cost which explains the large number of small-scale fixed-bed reactors in use world-wide [36]. The two main types of fixed gasifiers are the updraft (counter-current) and downdraft (co-current) reactors (Figure 1.4a).

  - In a counter-current gasifier, the feedstock is loaded from the top while the oxidising agent (air, oxygen or steam) is introduced from the bottom as shown in Figure 1.4a. In the reactor, the fuel is converted into combustible gas during its downward path. The feedstock is treated in the following sequence starting from the top: drying, pyroysis, reduction (gasification) and combustion (if air/oxygen is used). In the combustion zone, the highest temperature of the reactor is greater than 1200°C. As a consequence of the updraft configuration, the tar coming from the pyrolysis zone is carried upward by the flowing hot gas which results in the

production of a gas with a high tar content [52]. A high tar concentration causes several problems in the gasifier and the gas end-use applications because of its corrosive characteristics.

  - A downdraft gasifier is a co-current reactor where, the feedstock is fed in from the top, the oxidising agent is introduced at the sides above the grate while the product gas flows through a bed of hot ash and is withdrawn from under the grate (Figure 1.4a). Since the product gas passes through the high-temperature zone of the hot ash, this favours the cracking of tars in the product gas. Consequently, a downdraft gasifier has the lowest tar production rate of all types [36]. However, the internal heat exchange is not as efficient as in the updraft gasifier [52].

- Fluidised bed reactors are well known for their high-degree of mixing and temperature uniformity. A fluidised bed is composed of fine solids (normally char and sand), called bed materials, that are kept suspended in a liquid-like state (fluidised state) by contact with the upward flowing gasifiying medium. The advantages of a fluidised bed gasifier include its high tolerance to fuel quality due to its excellent gas-solid mixing and the large thermal inertia of the bed. The two main types of fluidised beds are the bubbling and circulating fluidised beds (Figure 1.4b) [53].

  - In a bubbling fluidised bed (BFB) reactor, the velocity of the upward flowing gasification agent is around 1-3 m/s and the expansion of the inert bed occurs only at the lower part of the gasifier as shown in Figure 1.4b [52]. The bed materials do not come out of the reactor because of the low velocity. Bubbling bed gasifiers can be grouped as low-temperature ($< 900°C$) and high-temperature (1000°C) types and can also operate at atmospheric or elevated pressure (10 bar). A low-temperature BFB is preferred in order to avoid ash fusion and consequent agglomeration however a high-temperature BFB minimises the production of methane and other hydrocarbons and thus produces a better-quality gas [36].

  - A circulating fluidised bed (CFB) gasifier provides a long gas residence time and is particularly suitable for fuels with high volatiles [36]. The velocity of the upward flowing gasification agent in a CFB reactor is around 5-10 m/s. Consequently, the expanded bed occupies the entire reactor and a fraction of sand and char is carried out of the reactor together with the gas stream. This fraction is captured and recycled in the reactor using an air cyclone that intercepts the gas stream as shown in Figure 1.4b. The gasification process occurs in the tall rise which allows a long residence time for the gas as well as for the fine particles.

- Rotary kilns are inclined slightly toward the discharge end and the axial movement of the feedstock is controlled by the speed of rotation (Figure 1.4c). The advantage of a rotary kiln over a fixed bed and fluidized bed reactor is that the feedstock properties (e.g. particle size and moisture content) are not design dependent and thus the kiln can use a variety of fuels over time. However, the major challenge in its use is the ability to control the flow of the oxidising medium, because air traditionally enters a rotary kiln through the low end, which tends to cause full combustion and hot spots near the air entrance [54]. Hence, some method of uniform and controllable air introduction throughout the length of the kiln is important.

- Moving grate systems place the fuel on a slopped grate with the oxidising medium provided both below and above the grate (Figure 1.4d). The gasification process in this reactor is divided into three stages namely a drying stage, a pyrolysis stage, and a char gasification stage. However, in practise, these operating zones are highly dependent on the fuel characteristics (e.g. fuel type, size and moisture content) and the operating parameters. Moving-grate gasifiers have an advantage over fluidized bed gasifiers as they accept a lumped feedstock and provide a longer residence time for the solid fuel. This makes moving-bed reactors more easily controlled and more tolerant of fuels with varying physico-chemical properties. A potential problem relating to the use of the moving-bed gasifier for the thermal treatment of mixed plastic wastes is the risk of plugging the feeding system due to the very low softening temperature of plastics [55].

- Plasma reactors use plasma torches, which generate an intensive electrical arc between two insulated electrodes (Figure 1.4e). The main advantage of the plasma reactor is that it provides high operating temperatures (2700-4500 °C), which when coupled with its relatively long gas residence time, generates reactive species (e.g. hydroxyl radicals) that crack the tar products and destroy toxic compounds (e.g. dioxin and furans). Furthermore, this technology is insensitive to the feedstock quality as a result of its independent energy source run by electricity instead of partial combustion of the gasification product [36, 56]. However, the plasma gasifier incurs very high costs due its large consumption of electricity which is in the order of 15-20 % of the gross power output of the plasma gasification plant [43, 57]. Thus the economic viability of this technology remains to be proven.

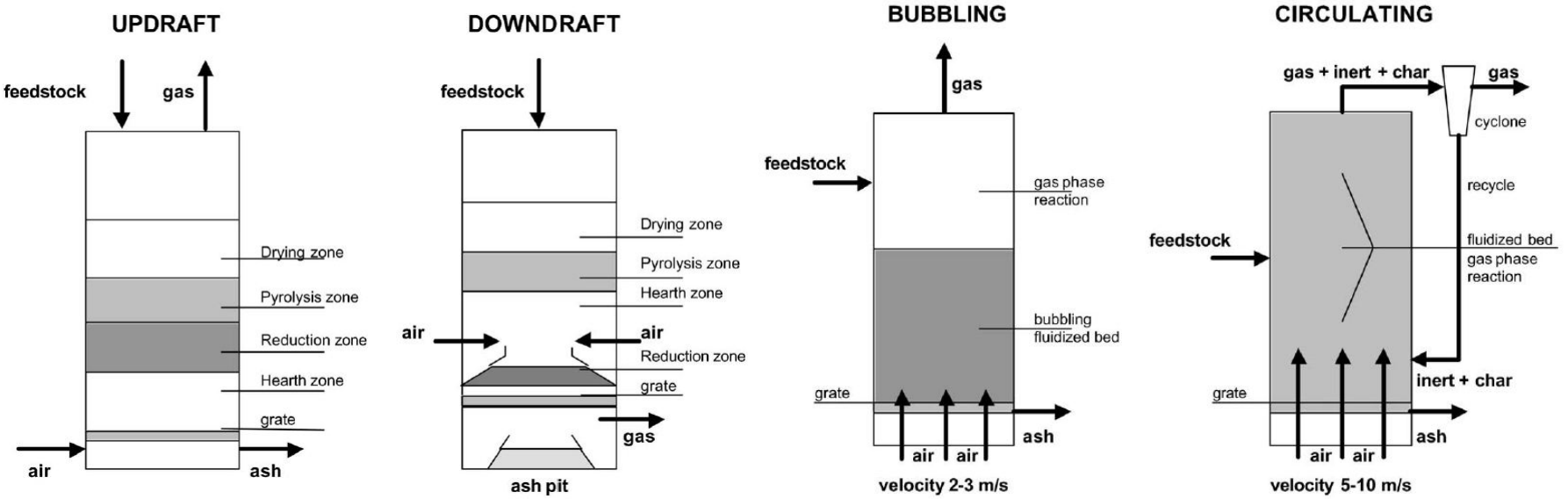

(A) Fixed bed reactors [53]

(B) Fluidised bed reactors [53]

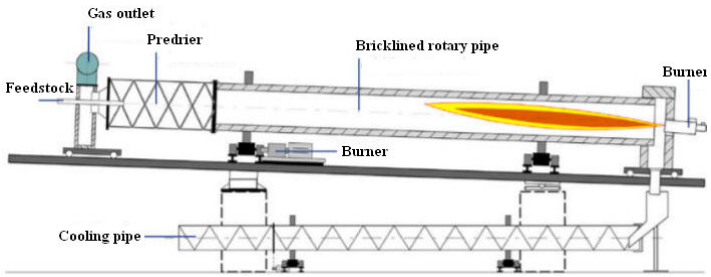

(C) Rotary kiln reactor [58]

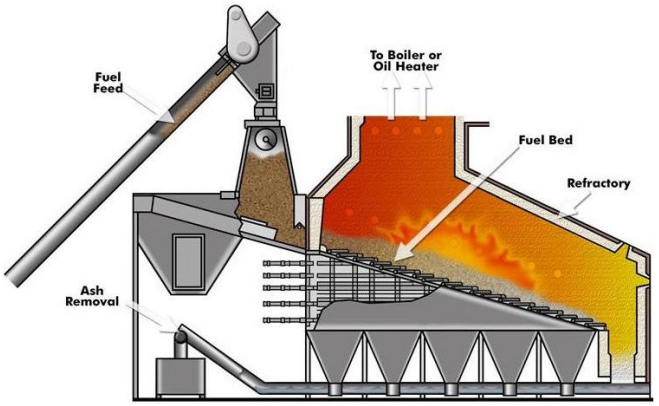

(D) Moving grate reactor [59]

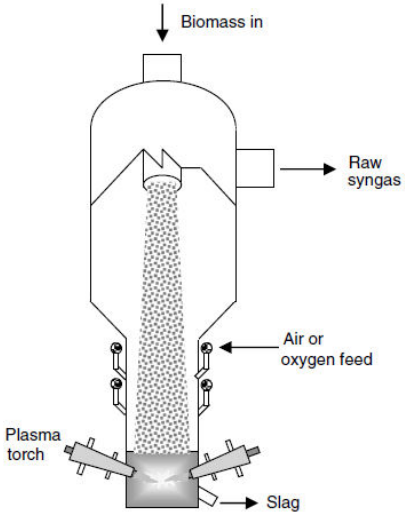

(E) Plasma gasifier [36]

FIGURE 1.4: Reactor types for waste pyro-gasification

TABLE 1.2: Comparison between different reactor designs for syngas production from solid waste pyro-gasification [24, 36, 52, 60–62]

	Downdraft Fixed Bed	**Updraft Fixed Bed**	**Bubbling Fluidized Bed**	**Circulating Fluidized Bed**	**Rotary Kiln**	**Moving Grate**	**Plasma**
Fuel requirements							
Particle size (mm)	< 100	< 100	< 150	< 100	No limit	< 200	No limit
Moisture content (%)	< 20	< 50	< 55	< 55	No limit	< 60	No limit
Ash content (% db)	< 5	< 15	< 25	< 25	< 40	< 20	No limit
Ash melting point (°C)	> 1250	> 1000	> 1000	> 1000	No limit	> 1200	No limit
Bulk density (kg/m^3)	> 500	> 400	> 100	> 100	> 100	250 – 450	> 100
Tolerance of composition variation	Moderate	Low	Very low	Very low	Very high	Very high	Very high
Syngas quality							
Tar content (g/Nm^3)	Low (< 3)	Very high (30-150)	High (~10)	High (~10)	High	-	Very low
Particulate matter	Medium	Low	High	High	High	-	Low
Technology							
Gasification temperature (°C)	700-900	700-900	550 - 1000	900 - 1000	750-1500	-	1,500-5,500
Temperature profile (gradient)	Large	Large	Small	Small	Large	Large	Large
Heat exchange and suspension-to-heat transfer coefficient (W/m^{2}K)	Inefficient (20-100)	Inefficient (20-100)	Very efficient (200-700)	Efficient (100-350)	Very poor (radiation)	Poor (radiation)	- (radiation)
Particle residence time	Particles stay in the bed until their discharge		Long (mins)	Short (seconds)	Very long (1-2 hours)	Very long (> 1 hour)	Long (mins)
Conversion	Very high	High	Intermediate	High	High	Very high (> 90 %)	Very high (can reach 100 %)
Control	Easy	Very easy	Intermediate	Intermediate	Intermediate	-	-
Process flexibility	Very limited	Very limited	Excellent	Excellent	Limited	Limited	Excellent
Scale-up potential	Very limited – low max size	Limited – low max size	Good	Good	Various size kilns available	Very good –long operating experience	Very limited -Small scale modules available
Scale	< 5 MWt	< 20 MWt	10< MWt<100	20 < MWt <300	5< MWt <50	-	> 2MWt
Economics							
Cost	Low	Low	Moderate	High	Moderate	High	Very high

Color codes

	Desirable
	Acceptable
	Undesirable

1.3 Modelling waste pyro-gasification

The design, operation and optimization of a gasifier require an extensive investigation of the operating parameters influence on the plant performance [21]. Conducting experiments at a large scale is often problematic because of their associated safety risks and high costs. Therefore, a mathematical model that is capable of describing, within a reasonable degree of deviation, the behaviour of a real gasifier operation is highly desirable. Such a model enables prediction of the evolution of the complex chemical and physical phenomena occuring in the gasifier which is beneficial for optimizing the reactor design and operating conditions at minimal temporal and financial costs [20]. The model types discussed in this section are grouped as equilibrium, kinetics, computational fluid dynamics (CFD) and artificial neural network (ANN) models.

1.3.1 Equilibrium models

Equilibrium models, also called zero-dimensional models, set relations between input and output variables of a gasifier without considering the details of the phenomena occuring inside the gasifier. Therefore, no description or evaluation of temperature, velocity, or concentration profiles in the gasifier is possible [21]. The concept of chemical reaciton equilibrium is based on the second law of thermodynamics, where species of a reacting system do not experience a net change in concentration over time [20, 63].

There are two widely used equilibrium modelling approaches for predicting the equilibrium composition of product gas : stoichiometric models, and non-stoichiometric models often referred to as "Gibbs free energy minimization approach". Stoichiometric models are based on equilibrium constants of an independent set of reactions which can be associated with a Gibbs free energy change (Eq 1.14). Examples of such models include works by [64–67]. The "Gibbs free energy minimization approach" concerns the direct minimization of the Gibbs free energy of reaction (Eq 1.15), which is popular among researchers [63, 68–73]. The stoichiometric approach requires a clearly defined reaction mechanism that includes all chemical reactions and species involved. However, the non-stoichiometric approach requires no particular reaction mechanism and the only input needed to specify the feed is its elemental composition, which can be readily obtained from ultimate analysis data [74]. The fundamental equations required to formulate an equilibrium model using either of the two modelling appraoches are given by Equations 1.11 - 1.15:

i. Overall mass balance:

$$F_{in} \sum_{in} n_{k,i} x_i = F_{out} \sum_{out} n_{k,i} x_i \tag{1.11}$$

where $n_{k,i}$ is the number of atoms k of a molecule i, and x_i is the molar fraction of a compontent i.

ii. Overall energy balance:

$$F_{in} \sum_{in} x_i H_i(T_{in}, P) = F_{out} \sum_{out} x_i H_i(T_{out}, P) \tag{1.12}$$

iii. Equilibrium constant of reaction j:

$$K_j = \prod_i \left(\frac{P_i}{P_o} \right)^{\nu_{i,j}} \tag{1.13}$$

which is related to temperature by:

$$- RT \ln K_j = \Delta G_j^{\circ} \tag{1.14}$$

where G_j° is the variation of the standard Gibbs free energy of reaction j as a function of temperature.

iv. Objective function to be minimized:

$$G_{total} = \sum_{i=1}^{N} n_i \Delta G_{f,i}^{\circ} + \sum_{i=1}^{N} n_i \, RT \ln \left(\frac{n_i}{\sum n_i} \right) \tag{1.15}$$

Equilibrium models are useful if an overall analysis of the system is desired. They are able to predict the highest gasification or thermal efficiency that can be possibly attained for a given feedstock [21, 67, 75, 76]. Furthermore, they possess the generic ability to simulate different reactor configurations as they are independent of the gasifier design and are not limited to a specified range of operating conditions [76, 77]. However, equilibrium models are based on assumptions that may oversimplify the process and lead to false conclusions [20, 21, 78, 79]:

- Equilibrium at exiting streams would require infinite residence time of the chemical components inside the reactor. Typical residence time in the different gasifer types are seconds to minutes, which may lead to conditions far from equilibrium.
- Perfect mixing and uniform temperature are assumed for the gasifier although different hydrodynamics are observed in practice, depending on the gasifier design.

Due to these assumptions, equiibrium models may have typical pitfalls at relatively low gasification temperatures (< 800 °C), whereby H_2 and CO yields are overestimated, and CO_2, methane, tars and char yields are underestimated [80]. Therefore, it is essential to develop detailed kinetics or computational fluid dynamics (CFD) models in order to estimate the product gas composition and the influence of various gasifier operating parameters at any point in space and time [20].

1.3.2 Kinetic models

Kinetic models take into account the kinetics of the main chemical reactions and the transport phenomena among phases in the gasifier. For homogeneous (gas-

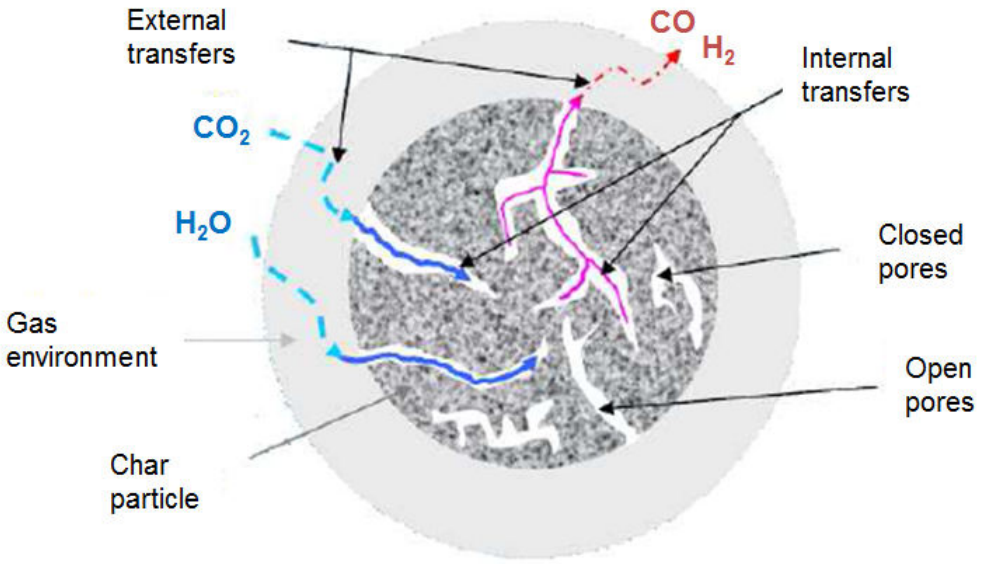

FIGURE 1.5: Schematic representation of mass transfer phenomena during gasification of a char particle [81].

gas) reactions (Eq. 1.4, 1.6-1.8) rate laws and kinetic parameters make up the kinetics model. However, for heterogeneous (gas-solid) reactions, such as pyrolysis (devolatilisation) and char gasification/combustion (Eq. 1.1-1.3, 1.5), mass transfer modelling are brought into play as these reactions involve at least two distinct phases [21]. Figure 1.5 gives an illustration of mass transfer phenomena that occur during gasification of char particles under O_2, H_2O, and CO_2 atmosphere to form H_2, CO and CO_2. The following mechanisms that can be observed are:

1. Diffusion/convection of the reactants in the gas layer that surrounds the particle (external transfers).
2. Internal diffusion of gas specie in the porous particle matrix (internal transfers).
3. Adsorbtion of gas species on the pore surface.
4. Chemical reactions between char and the oxidants (surface reactions).
5. Desorption of gaseous products from the pore surface.
6. Internal diffusion of gaseous products in the particle pore.
7. Diffusion/convection of the gas products at the particle surface towards the surrounding environment.

Hence, the apparent kinetics of biomass pyro-gasification involves strong interactions between chemical processes (adsorption, desorption and chemical reactions) and physical ones (heat and mass transfer). Models that can be found in literature for these heterogeneous reactions are discussed as follows.

Chemical kinetics

i. Pyrolysis

In literature, three classes of pyrolysis kinetic models are identified: 1) Global/ single-step models, 2) Multi-step models, 3) Structural models. For all three model classes, the temperature (T) dependence of the kinetic rate is normally given by a typical Arrhenius' form:

$$k = A\,exp\left(\frac{-E}{RT}\right) \tag{1.16}$$

Where k is the kinetics coefficient, A is the pre-exponential factor, E is the activation energy and R is the gas constant (8.314 J/K/mol).

Global/single-step models are the simplest pyrolysis models. They assume that volatile release can be represented by a single overall reaction such as [21]:

$$Biomass \rightarrow \nu_C CHAR + \nu_G GAS + \nu_T TAR \tag{1.17}$$

Where ν_C, ν_G, ν_T are the fractions of char, tar and gas, which are determined from experiments, under specified heating rates and temperatures. This is a major pitfall of single-step models as they cannot predict the relative amount of products and are dependent on the conditions in which the experiments were conducted. For example, such models may yield good predictions for slow, moderate temperature pyrolysis but may fail to do so for fast, high temperature pyrolysis. However, for engineering applications, these models can give reasonable results [82, 83].

To improve on the performance of global models, multi-step models involving series and/or parallel reactions have been developed. For lignocellulosic biomass or waste, a popular multi-step devolatilization mechanism is based on three parallel reactions (TPR) involving the release of volatiles from three pseudo-components: hemicellulose, cellulose and lignin [84–86]. Thus, the rate of pyrolysis of such biomass can be represented as the sum of the corresponding rates of its pseudo-lignocellulosic components. Gronli et al. [87] and [88] have shown that the TPR model better describe the decomposition behaviour of biomass than the single-step method. However the TPR method suffers from the same shortcoming as its counterpart in relation to its ability to predict the yields of pyrolysis products. Another important multi-step model is one that considers secondary reactions or cracking of tars to produce gases and char. Figure 1.6 gives an example the multi-step scheme used by Okekunle et al. [89] whose model gave good tar yield predictions. Procedures for determining TPR and global kinetic models using thermogravimetric techniques will be discussed in section 1.3.5.

Due to advances in analytical techniques such as Fourier transform infrared (FTIR) and thermogravimetry-mass spectrometry (TG-MS), more sophisticated models, known as structural models have been developed, which are capable of predicting the tar, gas and char yields as well as the gas composition by considering between 10

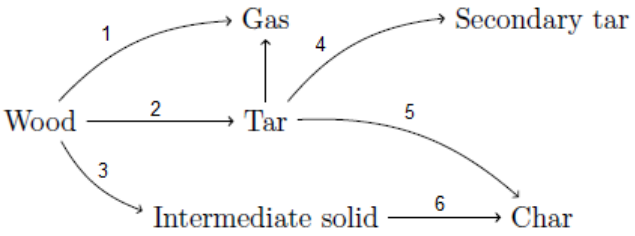

FIGURE 1.6: Multi-step reaction scheme for biomass pyrolysis [89].

and 50 chemical reactions. The most famous of which is the Ranzi model [90] which is based on FG-DVC (Functional Group-Depolymerization, Vaporization, Crosslinking) models. The Ranzi model describes the biomass components (cellulose, hemicellulose and lignin) as group monomers linked by chemical bonds, and can predict their depolymerisation and repolymerisation at different temperature and pressure conditions. Although structural models are able to predict pyrolysis product yields, their implementation in reactor-scale models demands signficant computational effort.

ii. Char gasification/combustion

The intrinsic reaction rate of char gasification or combustion reaction rates can be expressed as a variation of the char mass m_{char} with time t as shown in Equation 1.18.

$$\frac{dm_{char}}{dt} = k_{int}(T, P_i) S_r m_{char} \tag{1.18}$$

The parameter, k_{int} [$m^{-2}s^{-1}$] refers to the intrinsic kinetics of the reaction, which depends on the temperature T, and partial pressureP_i of the gaseous compounds involved in the reactions (H_2O, CO_2, O_2, etc). S_r [m^2] refers to the active (microporous) surface of the char and depends on the quantity and availability of the reactive sites [91]. As the active surface is very difficult to determine and it evolves as the char is converted, a new term can be introduced: the surface function, $f(\alpha)$. Hence, the reaction rate in Equation 1.18 can be re-written as:

$$\frac{d\alpha}{dt} = k_{int}(T, P_i) f(\alpha) \tag{1.19}$$

There are two main approaches to determining the intrinsic kinetic parameter, k_{int}. The first approach is the simpler one, based on the Arrhenius kinetic law and an n-order assumption with respect to the reactive gases (H_2O, CO_2, and O_2), which is given by [45]:

$$k_{int} = A\, exp\left(\frac{-E}{RT}\right) P_i^n \tag{1.20}$$

The second approach better describes the complexity of the phenomena involved such as the adsorption or desorption of molecules at the char active sites, as well as acceleratory or inhibitory effects of the presence of certain molecules on the reaction rate. The Langmuir-Hinshelwood form of the intrinsic kinetics most popularly used in literature. An example of the Langmuir-Hinshelwood rate of the Boudouard reaction

(Eq. 1.2), which takes into account CO inhibition [92] is expressed as follows:

$$k_{int} = \frac{k_1 P_{CO_2}}{1 + (k_2/k_3)\, P_{CO} + (k_1/k_3)\, P_{CO_2}} \tag{1.21}$$

where the constants k_j are given in the Arrhenius form (Eq. 1.16).

Three classic models for studying the evolution of the reactive surface function $f(\alpha)$ during heterogeneous reactions are: volume reaction model (VRM), shrinking core model (SCM) and random pore model (RPM). The VRM is also called the homogeneous model, as it assumes that the gasification or combustion reactions take place on all the active sites and that the char particle structure (density and size) is assumed not to change [21]. Equation 1.22 shows the surface function corresponding to the VRM model which decreases as the reactions progress.

$$f(\alpha) = 1 - \alpha \tag{1.22}$$

The SCM assumes that the reaction first occurs at the external surface of the particle and then gradually progresses inside it. In this case, the particle size reduces during conversion which in turn decreases the active surface, whereas the particle density remains unchanged. At the intermediate conversion stage, the char represents a shrinking core of unreacted solid [91]. The surface function is expressed in the SCM model as:

$$f(\alpha) = (1 - \alpha)^{2/3} \tag{1.23}$$

The RPM assumes that gasification occurs on the inside surface of the micropores, which occupy majority of the particle surface area. As the reaction proceeds, the active surface initially increases dure to pore growth, and then decreases as a result of coalescence of adjacent pores [91]. Equation 1.24 gives the expresion of the RPM.

$$f(\alpha) = (1 - \alpha)\sqrt{1 - \psi \ln(1 - \alpha)} \tag{1.24}$$

Where ψ is a parameter related to the pore structure of the unreacted sample ($\alpha = 0$), which can be calculated using Equation 1.25:

$$\psi = \frac{4\pi L_0 (1 - \epsilon_0)}{S_0^2} \tag{1.25}$$

Where S_0, L_0 and ϵ_0 are the pore surface area per unit volume [m^2/m^3], pore length [m] and solid porosity, respectively. However, because ψ is extremely difficult to measure, it has been determined empirically from experimental data by several authors [93–95].

Although VRM, SCM and RPM models are capable of predicting morphological changes of the char particle during gasification or combustion, they fail to predict other important mechanical phenomena such as fracturation or fragmentation of the particles (Fig.1.7) which may increase the char reactivity as a result of an increase

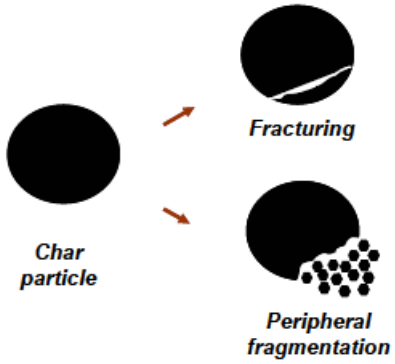

FIGURE 1.7: Schematic representation of fracturing and fragmentation of a char particle [91].

in active site concentration and gas diffusion through the char particle [96, 97]. This justifies the development of empirical $f(\alpha)$ functions for char gasification by several authors including Teixeira et al. [98], Guizani et al. [99], and Van de Steene et al. [100].

Transport phenomena

Heat and mass transport phenomena occur during the drying, pyrolysis and gasification stages of biomass/waste thermoconversion at both the particle and reactor scales. These phenomena are responsible for the biomass/waste particle bed heating up to the process temperature as well as the transport of volatiles and gasification agents between the particle and surroundings. Such phenomena are described using classic mass, momentum and energy conservation equations.

The external heat and mass transport can be modelled using exchange coefficients which is the most suitable for surrounding conditions and the particle characteristics. The internal mass transport inside the particles can be modelled using a combination of molecular diffusion and Knusden diffusion. The internal heat transport can be adequately described using conduction and internal radiation equations. Furthermore, because biomass/char particles are porous, Darcy's equation can be used to model laminar fluid flow through the porous media in order to obtain the pressure and velocity profiles in the solid [101].

$$u = -\frac{k}{\mu}\Delta P \tag{1.26}$$

Where u is the superficial gas velocity (m/s), k is the bed or particle permeability (m^2), and ΔP is the pressure gradient (Pa).

1.3.3 Computational fluid dynamics (CFD) models

Computational fluid dynamics (CFD) models predict fluid flow, heat and mass transfer, chemical reactions, solid and gas interactions, and other related phenomena [20, 101]. Regarding biomass/waste thermochemical conversion, CFD models may include submodels of complex chemical and physical processes such as vaporization,

devolatilization, volatile secondary reactions, and char oxidation, which are coupled with transport phenomena [82, 102–105].

The fundamental equations governing CFD models are the conservation laws of mass, momentum and energy. The most widely used numerical techniques to solve the CFD model equations are discretization methods, mainly finite difference (usually based on Taylor's series, polynomial expansions), finite elements (based on calculus of variations, and the method-of-weighted-residuals) and finite volumes method (based on control-volume formulation). Finite volumes are now the most commonly used approach in CFD code development because of its versatility and ease in understanding and programming [101]. The conservation laws are enforced over a discretized region in order to compute the flux of the fluid mass, momentum and energy, with suitable boundary conditions [36].

The benefits of CFD models are that they are safe, save cost and time, and are easy to scale-up compared to physical experiments [101]. However, CFD models use submodels, fitting parameters, or major assumptions in areas where precise information is not available, which may make the predicted results susceptible to the accuracy of these "weak links" [36]. Furthermore, CFD models can predict the behaviour of a given gasifier over a wide range of parameters using data from one experiment, but this prediction may not be accurate if the code is used for a different gasifier with substantially different input parameters [36]. Finally, CFD modelling for biomass thermochemical conversion still faces significant challenges due to the complexity of the biomass/waste feedstock and the thermochemical process, and thus, CFD modelling in this field needs further research and development [20].

1.3.4 Artificial neural network (ANN) models

Artificial neural network (ANN) is a mathematical modelling approach that uses regression to correlate input and output data of process units [20]. Although ANN has been extensively used in other fields, such as pattern recognition and signal processing, it has lately received attention as a tool in modelling renewable energy systems [106], and in particular, biomass/waste gasification [107–109].

The ANN model uses three hidden layers of neurons [106]: the first layer receives the input data (input layer), the second processes them (hidden layer), and the third delivers the outputs (output layer). An example of neuron layers and the connection patterns between them is shown in Figure 1.8, which was developed by Xiao et al. [108] to predict the gasification characteristics of MSW. The input layer has two values associated with it: inputs and weights [36]. Weights are used to transfer data from one layer to another. The network is trained by modifying the connection weights in some orderly fashion using learning methods [109]. It begins with a set of experimental data (with inputs and targeted outputs); the weights are adjusted until the difference between the neural network output and the corresponding target reaches a minimum [106]. When the process satisfies the required tolerance, the network holds the weights constant and makes output

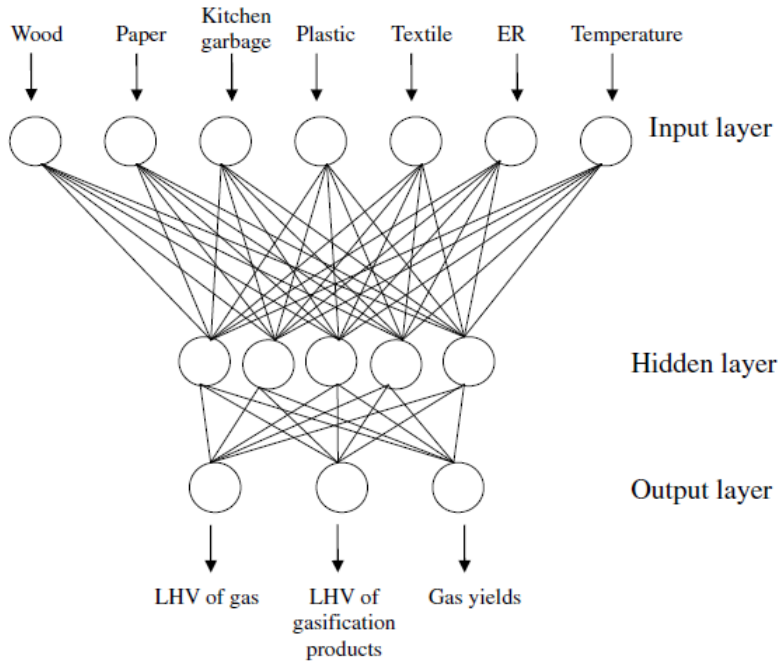

FIGURE 1.8: Schematic of a back propagating (BP) neural network [108].

predictions. A back-propagation algorithm (BP) is used to train the network, and multilayer feed-forward networks (MFNN) are used to approximate the function that correlates the input and output parameters. As shown in Figure 1.8, the ANN model developed by Xiao et al. [108] had an input layer consisting of seven neurons: the mass percentage of the five MSW components (wood, paper, kitchen garbage, plastic and textile), equivalence ratio (ER) and temperature. The output layer had three neurons: the lower heating value (LHV) of gas, LHV of gasification products, and the gas yield. Furthermore, five neurons were included in the hidden layer. The predicted results were acceptable, with relative errors below $\pm$ 25 %, when compared with industrial data.

A key advantage of ANN models compared to kinetic or CFD models is that ANN models demand less knowledge of phenomena occuring in the reactor. However, these models rely on a large number of experimental data, which are not readily available from biomass/waste gasification processes. Consequently, few works on neural networks model development in this field are reported in literature [20]. With limited data available to calibrate and evaluate the ANN model constants (weights), the neural network may return poor results from input data that differ from the original data it was trained with [110].

1.3.5 Kinetic modelling using thermal analysis data

This section discusses different procedures for determining kinetic models of biomass/waste thermochemical decomposition using data obtained from thermogravimetric analysis. The aim is to provide the relevant background information governing the pyrolysis modelling work performed in Chapter 4.

Rate equation

The reaction rate of solid waste pyrolysis, gasification or combustion can be parameterized in terms of three major variables: temperature T, extent of conversion α, and pressure P, as follows [111]:

$$\frac{d\alpha}{dt} = k\left(T\right) f\left(\alpha\right) h\left(P\right) \tag{1.27}$$

The pressure dependence, $h(P)$ is normally taken into account for gasification and/or combustion reactions, where P is the partial pressure of the gaseous reactant, which can be expressed in the form of the power law [100, 112, 113]:

$$h(P) = P^n \tag{1.28}$$

However, $h(P)$ is often ignored for pyrolysis reactions in literature where experiments are conducted under an inert atmosphere [111]. Hence, for pyrolysis kinetics, the rate is considered to be a function of only T and a. The dependence of the pyrolysis rate on temperature is represented by the rate constant, $k(T)$, and the dependence on the extent of conversion by the reaction model, $f(a)$:

$$\frac{d\alpha}{dt} = k\left(T\right) f\left(\alpha\right) \tag{1.29}$$

The temperature dependence of the reaction rate is typically parameterized through the Arrhenius equation:

$$k = A\, exp\left(\frac{-E}{RT}\right) \tag{1.30}$$

Where R is the gas constant (8.314 J/K/mol). Thus, a complete kinetic study of solid waste pyrolysis requires the determination of the kinetic triplet: namely, the activation energy E_α, the pre-exponential factor A, and the reaction model $f(\alpha)$. The determination of the latter constitutes, perhaps, the most delicate step, especially when dealing with highly complex reactions such as the decomposition of synthetic or natural polymers (e.g. plastics or wood), found in waste. Furthermore, knowledge of the kinetic model that drives the reaction provides an invaluable insight to the reaction mechanism [114].

Kinetic model determination

In literature, the most common technique for studying the thermal decomposition of solids is by thermogravimetric analysis (TGA). These studies can be conducted under either isothermal or dynamic (non-isothermal) conditions. In either conditions, there are two main procedures for determining the kinetic model governing the process: Model-fitting and model-free (isoconversional) methods in combination with master plots [115].

Model-fitting methods involve fitting different kinetic models, $f(\alpha)$, to the TGA data in order to choose the model that gives the best statistical fit, which in turn is used to estimate the arrhenius parameters, E_α and A via optimization algorithms

[114, 116]. In the case of lignocellulosic biomass such as wood, several authors have modelled the pyrolysis kinetics using three-parallel reaction (TPR) model via model- fitting methods [82, 85, 87, 117]. There are two main mechanisms for the TPR method in literature: Order-based mechanism, in which the reaction mechanisms of the pseudo wood components - hemicellulose, cellulose and lignin - are all assumed to follow n-order reaction (i.e. $f(\alpha) = (1-\alpha)^n$, where n=1 or n≠1, n>0); Distributed activation energy model (DAEM), in which each single reaction of pseudo components is considered to be a combination of infinite first-order (n=1) reactions and the activation energies can be represented by a continuous distribution function [118–120]. Although DAEM is helpful for engineering computation, it is week to interpret the reaction mechanism [119]. Furthermore, DAEM is complicated and introduces significant computational effort [120]. As a result of the difficulty in determining the proper kinetic model, most works found in literature resort to simply assuming first-order or "n-order" kinetic models without reporting arguments that support this assumption [121–123]. Nonetheless, recent works have proven that thermal decomposition of polymers does not necessarily take place through first - or n - order kinetics and other mechanisms such as diffusion or random scission can control the decomposition reaction [124].

Recently, the so-called "model-free" methods have attained great popularity because they allow determination of the activation energy of a process as a function of the degree of conversion without any previous assumption of the kinetic model, $f(\alpha)$. Among the 'model-free' (isconversional) methods, those developed by Flynn-Wall-Ozawa (FWO) [123], Kissinger [116], Friedmann, and Kissinger-Akahira-Sunose (KAS)[85] are widely used. However, these methods do not directly provide information regarding the decomposition mechanisms [111, 125], although this can be achieved with the use of master plots [124]. Master plots are reference theoretical curves that depend on the kinetic model, $f(\alpha)$, but are independent of the kinetic parameters, E_α and A. Experimental data can be easily transformed into experimental master plots and compared with the theoretical ones determined for different kinetic models [124]. This provides a simple graphical procedure for determining the kinetic model. The main advantage of the master plots approach is that no previous assumption regarding the reaction kinetic model is made, thereby avoiding errors that arise from the fit of inappropriate kinetic models. The only requirements of this method are, firstly, the activation energy should be previously known, and secondly, this parameter should be maintained roughly constant along the entire conversion range. Thus the master plots method is usually combined with isoconversional kinetic procedures, which serve to evaluate whether these requirements are met [114].

TGA curve deconvolution

The model-free procedure is only suitable for a single reaction [111]. As the decomposition of polymers, such as wood and plastics, involve multiple reactions, it would therefore be inappropriate to apply the model-free method to the whole pyrolysis process. A solution to this is to separate the reaction rate (DTG) curves obtained from TGA data into pseudo-component profiles, and then apply model-free procedures to each profile in order to study their decomposition kinetics [120]. In literature,

studies on slow pyrolysis kinetics using deconvolution methods are few. Regarding the deconvolution methods, the DTG profile of the polymer can be separated using symmetric functions such as Gaussian [126], Logistic and Lorentz functions [127], or assymetric functions such as Weibull [128], bi-Gaussian [129] and Fraser-Suzuki [130]. Assymetric functions are considered more suitable for deconvolution procedures in TGA, especially the Fraser-Suzuki function [131].

1.4 Syngas applications and cleaning processes

1.4.1 Syngas end-uses

Typically, a gasification system is made up of three fundamental units [52]:

- Gasifier, for syngas production.
- Syngas cleanup system, for contaminant removal.
- Energy recovery system, which is completed with suitable sub-systems for controlling environmental impacts (air pollution, solid waste production, and wastewater).

Figure 1.9 gives a schematic representation of the basic processes of a gasification plant. When syngas is combusted in a boiler (path in upper part), the plant is similar to a combustion plant, with the difference being that oxidation is divided into two steps (a.k.a. close-coupled combustion) [132]. The potential benefits of gasification is realised by following the 'full' gasification path in the lower part, where the syngas is properly cleaned before being fed into various end-use systems for the following applications [133, 134]:

- Electricity (and/or heat) production in steam cycles, gas engines, turbines (combined cycle), as well as fuel cells.
- Synthesis of hydrogen (used in refineries), Synthetic Natural Gas (SNG) and ammonia (mainly for fertiliser production).
- Transportation fuel synthesis from Gas-to-Liquids (GTL) processes including Fischer-Tropsch (FT) diesel and methanol/dimethyl ether (DME).

1.4.2 Syngas contaminants and quality requirements

According to Arena U. [5], the greatest technical challenges to be overcome in order to achieve wider market penetration of gasification technologies appear to be linked to improved and cheaper cleaning of syngas in order to meet defined specifications. Several contaminants may be found in waste-derived syngas including; particulate matter, tars, sulphur compounds (H_2S, COS), nitrogen compounds (NH_3, HCN) alkali metals (K, Na), hydrogen chloride (HCl) and trace heavy metals (Hg, Pb, Cd, Zn) [51, 135–137]. These contaminants can cause serious problems

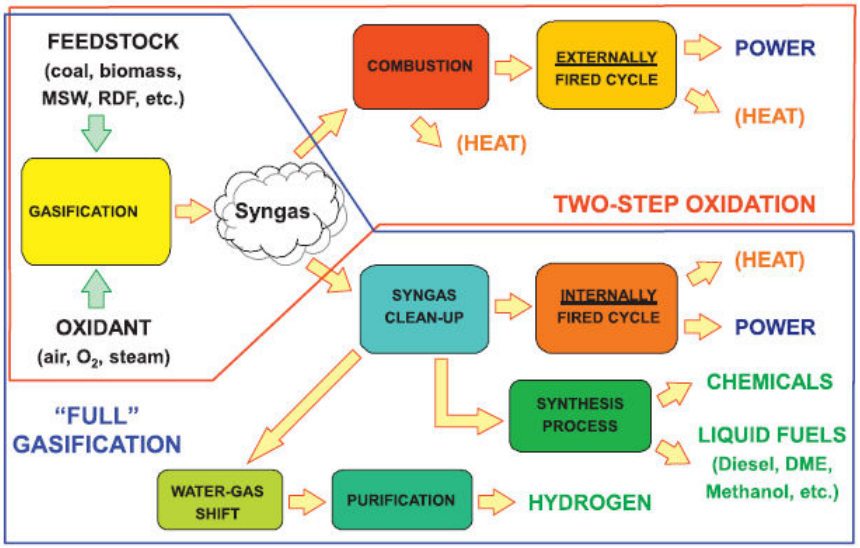

FIGURE 1.9: Schematic representation of the basic processes of a gasification plant [132]

in gasification systems such as fouling, clogging, corrosion, and catalyst poisoning which in turn can cause efficiency and safety concerns if not removed from the syngas. Furthermore, their presence in syngas strongly depend on the feedstock impurities and the gasification process parameters.

The level of syngas cleaning required is governed by the quality requirements of end-use applications and environmental emissions regulations [5]. As we can see in Table 1.3, the concentrations of different contaminants typically found in waste-derived syngas are significantly higher than those required for the various syngas applications and must therefore be removed [24, 60, 135]. Close-coupled combustion applications for electricity and heat production are relatively insensitive to syngas quality, although, HCl, dioxins, furans, SO_x and NO_x emissions may be an issue. Hence, the main concern for these applications is that the final combustion gas product (flue gas) meets environmental regulations (Table 1.3).

1.4.3 Syngas cleaning methods

Gas cleanup technologies can be classified according to the process temperature range; Hot gas cleanup (HGC), cold gas cleanup (CGC), or warm gas cleanup (WGC). These technologies can be distinguished based on the condensation temperatures of various compounds [135, 138]:

- Cold gas cleanup technologies, which often use water sprays, have exit temperatures near ambient conditions (< 100 °C) to enable water condensation.
- Warm gas cleanup typically occurs at temperatures higher than the boiling point of water up to temperatures of around 300 °C which allows for ammonium chloride condensation.

TABLE 1.3: Typical syngas contaminants and target levels of associated applications [24, 60, 135, 138]

Contaminant mg/Nm^3	Waste gasification	Gas engine	Gas turbine	Methanol synthesis	FT Synthesis	EU emissions standard*
Particulate	10^4 - 10^5	< 50	< 5	< 0.02	n.d	10
Tars	0 - 20000	< 100	< 10	< 0.1	< 0.01	n.s
Sulphur (H_2S, COS)	50 - 100	< 20	< 1	< 1	< 0.01	50 (SO_x)
Nitrogen (NH_3, HCN)	200 - 2000	< 55	< 50	< 0.1	< 0.02	200 (NO_x)
Alkali metals	0.5 - 5	n.s	< 0.2	< 0.2	< 0.01	n.s
Halides (HCl)	0 - 300	< 1	< 1	< 0.1	< 0.01	10
Heavy metals	0.005 - 10	n.s	n.s	n.s	< 0.001	0.03 (Hg)
Dioxins/Furans, n-TEQ/m^3	n.s	n.s	n.s	n.s	n.s	0.1

Note: n.d = not detectable, n.s = not specified, * = at 11% O_2

- Hot gas cleanup usually occurs in the temperature range of 400 to 700 °C. This results in the condensation of several alkali compounds. Higher temperatures are not usually employed in order to avoid using expensive piping material.

A recent review by Woolcock et al. [135] provides an excellent description of the different methods currently employed for syngas contaminant removal, which has been summarized in Table 1.4. It can be observed from this table that some methods are capable of removing several contaminants in a single process, such as wet scrubbing, while others focus on removing only one contaminant.

As the syngas exit temperature is usually in the range of 800 to 900 °C, which is well above the temperature required for many of the syngas end-use devices, it is therefore necessary that the gas be cooled before final use. Thus, it would seem that gas cleaning using CGC technologies, such as wet scrubbing, will be more appropriate. However, such techniques generate wastewater streams that contain dissolved tars, which must be removed, thereby adding to costs. Furthermore, CGC often suffer from energy inefficiencies [138]. These shortcomings of CGC may justify the use of HGC, however, if hot chemical conversion processes are employed, hot removal of particulates and aeorosols must be performed beforehand as they can cause catalyst fouling, poisoning or deactivation. In an attempt to meet these shortcomings of CGC and HGC, WGC is becoming increasingly important with respect to tar, particulate and HCl removal.

Table 1.4: Overview of different syngas cleaning technologies [135]

Contaminant	Hot gas cleanup	Warm gas cleanup	Cold gas cleanup
Particulate matter	Cyclones Barrier filtration Electrostatic separation Turbulent flow precipitator (TFP)	Cyclones Electrostatic separation Barrier filtration	Wet scrubbing
Tars	Thermal cracking Catalytic cracking Non-thermal plasma Physical separation	OLGA technique (Oil based gas washer)	Wet scrubbing Biological gas treatment
Sulphur (H_2S, COS)	Hot adsorption using metal oxides based on Zn, Fe, Cu, Mn, Mo, Co and V. etc	Semi-wet scrubbing	Chemical/Physical solvents Chemical redox Biological processes Physical absorption
Nitrogen (NH_3, HCN)	Catalytic selective oxidation Thermal catalytic decomposition	Semi-wet scrubbing	Wet scrubbing Adsorption Biological processing
Alkali	Hot adsorption using natural minerals, e.g. clays and kaolinite	Semi-wet scrubbing	Condensation Wet scrubbing
Chlorine	Hot adsorption using Na, Ca and Mg based minerals, etc	Semi-wet scrubbing using lime slurry	Wet scrubbing
Mercury	Hot adsorption using silica, bauxite kaolinite, zeolite, etc.		

Conclusion

This chapter has been dedicated to a literature study of the latest developments concerning waste-derived fuel classification and characteristics, pyro-gasification technologies and models, as well as waste-derived syngas applications and cleaning methods. Based on this literature review, the following decisions were made regarding this PhD work:

- Class B wood waste containing small amounts of plastics was selected as the

feedstock for pyro-gasification studies because of its abundant supply, low recycling rates and good fuel properties, as well as the many policy incentives and quality standards that support its energy valorization.

- Downdraft fixed bed reactor was the technology of choice for reactor-scale modelling and pilot-scale experiments, because it has relatively high fuel conversion rates and low tar yields, is easy to control, economical, and is suitable for small scale applications.

- Computational fluid dynamics (CFD) was the type chosen to model the pyro-gasification of class B wood waste in a downdraft fixed bed reactor. This CFD model was to consist of submodels that describe the drying, pyrolysis, char gasification, and combustion processes.

- Chlorine was the pollutant of interest, mainly for environmental reasons, as its concentration in class B wood waste may be significant due to the presence of PVC.

- As literature lacks reliable kinetics data for pyrolysis of wood/PVC mixtures, a solid-state kinetics model was to be developed for such a mixture using TGA data, and then incorporated in the CFD model.

- Different HCl sorbents were to be studied for syngas cleaning so that the flue gas generated from close-coupled combustion systems meets emissions standards for HCl.

CHAPTER 2

Characterisation of industrial and model waste

Introduction

The French regulation, ICPE - section 2910 [28], defines class B wood as industrial wood waste that has not been coated or treated with heavy metals (i.e. creosote and copper-chromium-arsenic (CCA)). Class B wood waste, managed by Suez Environnement, typically contains small amounts of plastics as shown in Figure 2.1. The presence of different plastics adds to the problem of heterogeneity of this wood type, thereby making it difficult to understand and predict its behaviour during pyro-gasification via experimental and modelling studies. Hence, for such studies, model wood waste consisting of virgin wood and plastic resins of known concentrations, are better-suited.

.

FIGURE 2.1: An example of Class B wood provided by Suez Environnement

In this work, poplar wood has been chosen as the model wood waste due to its high demand for industrial purposes and its extensive use in literature studies of pyro-gasification processes [139]. The plastic resins chosen are high density polyethylene (HDPE), polystyrene (PS) and polyvinyl chloride (PVC) because they are major plastic waste components [140] and they have sufficiently different characteristics to enable a study of the influence of plastic types on wood behaviour during pyro-gasification.

Characterisation of Class B wood waste and the model waste is key to understanding the role of their physical and thermo-chemical properties on their behaviour during pyro-gasification. Although specific standards for Class B wood waste characterisation do not currently exist, standards for solid recovered fuels (SRF) analysis can be used with a reasonable degree of confidence [36]. Hence, in this chapter, the characterisation of the waste samples is presented using European Standards for SRF prepared by Technical Committee CEN TC 343.

2.1 Materials

2.1.1 Industrial wood waste

Figure 2.2 shows the three samples of Class B wood waste provided by Suez for characterization purposes. These samples, in the form of chips, were obtained from industrial waste at a recycling center where they were pre-treated for use in a cement plant. Sample 1 (W1) and sample 2 (W2) are finished products that have been dried and ground, whereas sample 3 (W3) is wood waste rejected from the recycling centre before grinding due to its significant concentration of pollutants.

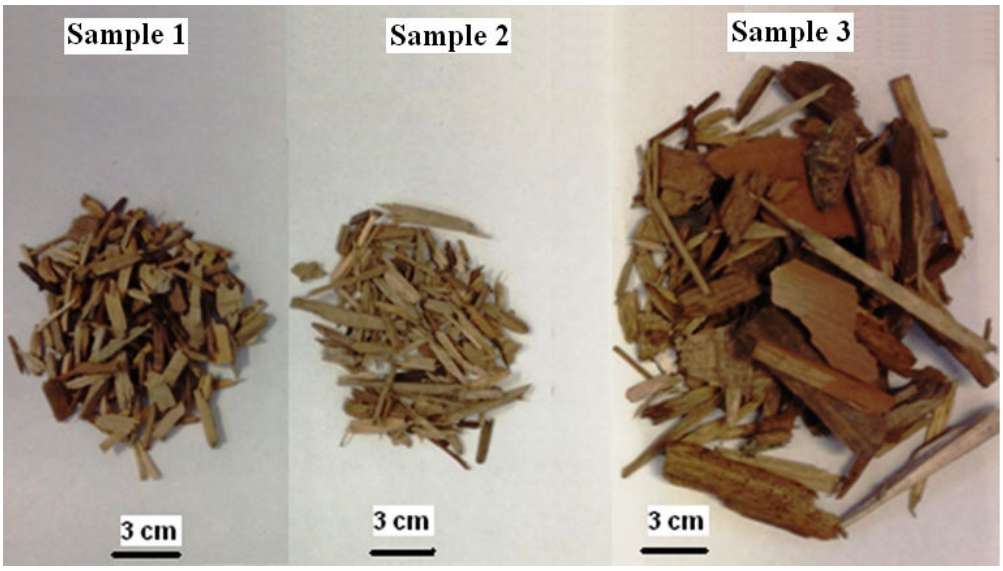

.

FIGURE 2.2: Class B wood waste samples

2.1.2 Model waste

The model waste used in this work consisted of poplar wood (PW), high density polyethylene (HDPE), polystyrene (PS) and polyvinyl chloride (PVC). Figure 2.3 shows the samples in their original form. PW was obtained from Special Diets Services (SDS) in the form of wood chips and the plastics were provided by Analytic Lab. HDPE and PS were received in the form of beads whereas PVC was obtained as fine particles (< 100 µm).

2.2 Characterisation methods

According to the European Standard, EN 15359 [27], three main characteristics of SRF are required for its classification: an economic characteristic (lower heating or net calorific value), a technical characteristic (chlorine content) and an environmental characteristic (mercury content). However, these characteristics of SRF are not in themselves sufficient to evaluate its suitability for energy purposes. Hence, EN 15359

.

FIGURE 2.3: Model waste samples

standard provides further properties of SRF that are obligatory and non-obligatory to specify which are listed in Table 2.1. In this work, the obligatory characteristics were specified for the three samples of Class B wood waste as well as the model waste, using European Standards as far as possible. Selected non-obligatory characteristics were determined based on their relevance to the experimental and modelling studies conducted in this work.

TABLE 2.1: Obligatory and non-obligatory specifications of solid recovered fuels (SRF) according to EN 15359 standard [27]

Obligatory	Non-obligatory
Particle form	Composition (wood, plastics, paper, textiles, etc)
Particle size	Bulk density
Ash content	Volatile content
Moisture content	Ash melting behaviour
Lower heating value	Major inorganic elements
Chlorine content	Trace in inorganic elements
Heavy metals content	Organic elements (C, H, O, N, S)

2.2.1 Particle size distribution

The particle size distribution of the three Class B wood waste samples (W1, W2 and W3) was determined using EN 15415-2 standard [141] for the large particles and EN 15415-1 [142] for the fines.

The large particle size distribution was analyzed based on a manual method for determining the maximum projected length, followed by a statistical evaluation. The following protocol was used according to EN 15415-2 standard [141]:

i. The total mass of the wood waste sample, MS, was weighed.

ii. The large particles were separated from the fines in the wood waste sample using a 3.15 mm sieve, also called the lower dimension of the format, LDF, sieve.

iii. The weight of the fine particles, MF, was taken.

iv. 200 of the particles that remained in the LDF sieve were randomly chosen and their respective maximum projected lengths were measured to within $\pm$ 5 mm using a ruler.

v. A higher dimension of the format, HDF, was fixed at 100 mm which is equivalent to the maximum particle size requirement of a fixed bed reactor [43].

vi. A histogram was then drawn to give an overview of the distribution of the maximum projected lengths, L, which is shown schematically in Figure 2.4. This histogram consists of the following characteristics:

   - The mass percentage of fine species, MPF, where $MPF = 100 \times MF/MS$.
   - The number percentage, NPC, of the particles in the number of central classes (NCC: 2, 3, 4, 5, 6) amongst the classes NCR = 7 between LDF and HDF.
   - The number percentage of large particles, NPL, corresponding to pieces larger than the HDF.
   - The number percentages of particle size classes '1' and '7', which are not specially labeled in the standard, and hence will not be commented on.

It should be noted that, instead of number percentages (i.e. NPC and NPL), mass percentages can be optionally used according to EN 15415-2 standard [141].

Concerning the particle size distribution of the weighed fines, a simple protocol provided by EN 15415-1 [142] was followed. The fines were subject to sieving using a mechanical oscillator with appropriate sieve sizes of decreasing order, ending with the collection pan (Figure 2.5). Sieve sizes of 3.15 mm, 1.6 mm, 1mm, 400 μm and 200 μm were used. The sieve operation was continued until the mass changes between two sequential sieves did not exceed the maximum of 0.3 % of the total

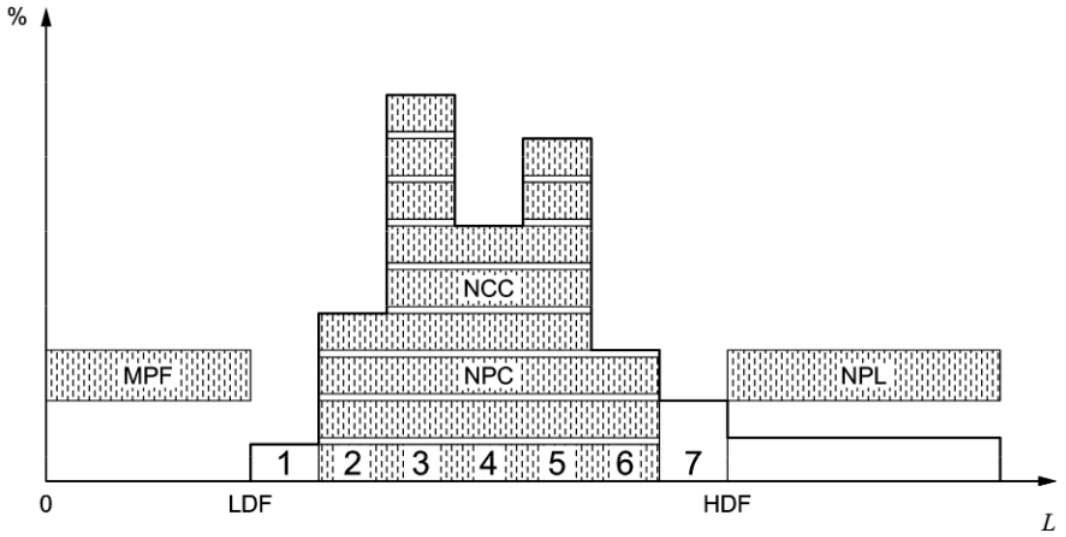

FIGURE 2.4: A schematic illustration of a histogram representing the maximum projected length distribution of large particles [141].

sample per minute of sieving operation. Finally, the weight of the retained wood particles in each sieve and in the collection pan was measured.

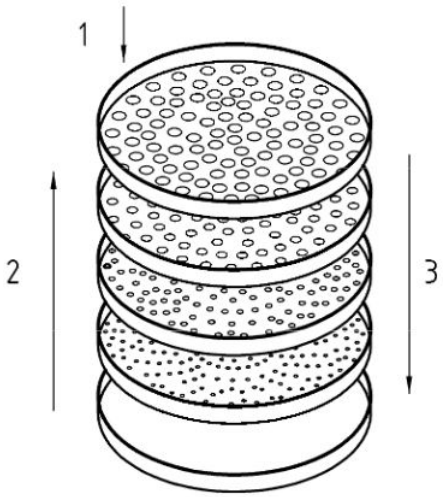

FIGURE 2.5: Principle of a mechanical oscillator: 1) Material addition, 2) Increasing hole diameters, and 3) Material flow direction [142].

2.2.2 Sample grinding

To perform the analyses outlined in the following sections, the Class B wood samples and the model samples were first ground into powder according to EN 15443 protocol [143]. A laboratory cutting mill (Fritsch Pulverisette 19) was used with a 0.5 mm sieve for the wood samples and 1 mm sieve for the plastics.

2.2.3 Densities

Two characteristic densities of the samples were of particular interest: the true and bulk densities. The true density is the weight per unit volume occupied by the solid fraction of the fuel. To measure the true density, a pycnometer (AccuPyc 1330TC) operating at 21 °C and 1.4 bar, was used. The bulk density is based on the overall volume occupied by the fuel particles. To determine its value, the sample was first placed in a graduated cylinder and the cylinder was tapped against a horizontal surface until the particles settled. The weight of the sample divided by its final volume gives its bulk density.

2.2.4 Moisture

Moisture content in wood is an important parameter because a high value increases the energy requirement for drying, hinders pyro-gasification, and consequently decreases the heating value of the product gas [144]. The moisture in biomass such as wood waste can be found in three forms: (1) Free water (above the fibre saturation point), (2) bound water (absorbed within the cell wall fibers - hemicellulose, cellulose and lignin), (3) water vapour (within the pores) [36].

In this work, the total moisture content in wood waste was determined using the protocol given in EN 15414-3 standard [145] which involves drying the sample in an oven and is applicable to all solid recovered fuels. A dry empty dish was first weighed and at least 1 g of the waste sample was added to the dish in an even layer. The weighed dish plus sample were then heated in an air oven at 105 °C for 24 h, transfered to a dessicator to avoid absorption of moisture by the sample from the atmosphere, and then left to cool to room temperature. The dish plus dried sample were weighed and the moisture content M_{ar}, in the sample, in wt% (as-received basis), was calculated by:

$$M_{ar} = \frac{m_2 - m_3}{m_2 - m_1} \times 100 \tag{2.1}$$

Where m_1 is the mass of the empty dish; m_2 and m_3 are the mass of the dish plus sample before and after drying respectively. Moisture was not determined for the plastic resins (HDPE, PVC and PS) used in this work as they are not hygroscopic [146].

2.2.5 Volatile Matter

The volatile matter of a fuel is the non-condensable (CO, CO_2, H_2 and light hydrocarbons) and condensable vapor (moisture and tars) released when the fuel is pyrolysed. Its yield depends on the temperature and heating rate of pyrolysis as well as the hydrogen content (H/C molar ratio) of the fuel [136].

The volatile content of the wood and plastic samples studied in this work were determined using the EN 15402 protocol [147]. The samples were first ground to

a particle size of less than 1 mm and then oven dried according to EN 15414-3 Standard [145]. Approximately 1 g of the sample was placed in a cylindrical crucible with a well-fitting lid so as to avoid contact with air during devolatilization. It was important that the crucible size was such that the sample layer did not exceed 0.2 g/cm^2. The covered crucible and its contents were placed in a furnace at 900 ± 10 °C for about 7 min. Next, the crucible was removed from the furnace, allowed to cool to room temperature, and then weighed. The volatile matter, V, expressed as percentage mass fraction of the dried sample, was calculated using the following equation:

$$V_{db} = \frac{m_2 - m_3}{m_2 - m_1} \times 100 \tag{2.2}$$

Where m_1 is the mass of the empty crucible and lid; m_2 and m_3 are the mass of the empty crucible and lid plus its contents before and after heating respectively.

2.2.6 Ash content and Inorganic elements

Ash is the inorganic solid residue left after complete combustion of wood fuel. It contains the bulk of the mineral fraction of the original biomass, primarily consisting of silica (Si), aluminium (Al), iron (Fe) and calcium (Ca), as well as small amounts of magnesium (Mg), titanium (Ti), sodium (Na) and potassium (P). Ash from wood waste may also contain halides such as chlorine and heavy metals including arsenic (As), cadmium (Cd), chromium (Cr), copper (Cu), lead (Pb) and mercury (Hg) which may cause serious corrosion and environmental problems in pyro-gasification systems [148].

EN 15403 standard [149] was used to determine the ash content of the dried wood samples. An empty crucible was first weighed and the dried analysis sample was added such that the sample layer did not exceed 0.1 g/cm^2 of the crucible surface. Afterwards, the weighed crucible plus sample was placed in a furnace whose temperature was initially raised to 250 °C at 5°C/min, and held there for 60 mins in order to eliminate the volatile components in the sample before combustion. Following this, the temperature was increased to 550 °C at 5°C/min and kept there for 130 mins to ensure that the carbon was completely burnt. The crucible plus its contents was then removed from the furnace, cooled in a dessicator, and weighed. To calculate the ash content in the sample (dry basis), the following equation was used:

$$A_{db} = \frac{m_3 - m_1}{m_2 - m_1} \times 100 \tag{2.3}$$

Where m_1 is the mass of the empty crucible; m_2 and m_3 are the mass of the empty crucible plus its contents before and after heating respectively.

The mineral species in wood were analysed using the protocols presented by EN 15410 [150] and EN 15411 [151] standards. A 200 mg sample of dried wood was first mineralized in an acid mixture consisting of 8 mL nitric acid (HNO_3) and 2 mL hydrogen peroxide (H_2O_2), heated at 200 °C for 4 h. After cooling, the

digestion solution was transfered to a volumetric flask and the digestion container was thoroughly washed with de-ionised water make up a 50 mL solution in the flask. Next, the solution was analysed using inductively coupled plasma with an atomic emission spectrometer (ICP-AES, HORIBA Jobin-Yvon Ultima 2), to determine the concentration in mg/L of mineral species in the solution. The following calculation was then made to obtain the results with respect to the initial wood sample.

$$C_{db} = \frac{C_{aq} V_{aq}}{m_s} \times 100 \tag{2.4}$$

Where C_{db} is the mineral specie content in the wood sample (wt%); C_{aq} and V_{aq} are the concentration of mineral specie in the solution and the total volume of solution respectively; m_s is the initial sample mass of dried wood.

2.2.7 Organic elements

The analysis of carbon (C), hydrogen (H), nitrogen (N) and sulfur (S) content in the fuel samples was performed using a CHNS analyzer (Flash 2000, ThermoFisher Scientific) according to EN-15407 standard [152]. The method was based on the complete oxidation of the sample in excess air in the presence of a catalyst layer. The combustion products, CO_2, NO_2, and SO_2 were then swept into a chromatographic column by the carrier gas (helium) where they were separated and detected quantitatively using a thermal conductivity detector (TCD). Since a few mg of sample was required, the CHNS analysis was repeated at least three times to improve its accuracy. The amount of oxygen was evaluated by difference.

2.2.8 Chlorine

Chlorine content in the wood and PVC samples were analyzed using X-ray fluorescence (XRF, PANanalytical). To perform the measurements, the empirical formula (matrix) of each sample was first determined from the mass percentages of C, H, O, N, S in the sample (see section 2.2.7). The samples were then placed in holders in the XRF chamber and were bombarded with high-energy X-ray beams. The ray of photons emitted from chlorine in the samples were detected and the concentration of chlorine was determined from the intensity of the emitted rays.

2.2.9 Heating value

The heating value is the amount of heat produced by the combustion of a unit quantity of a fuel. We differentiate between higher heating value (HHV) and lower heating value (LHV).

Higher heating value (HHV) is defined as the amount of heat released by the unit mass or volume of fuel (initially at 25 °C) once it is completely combusted and

the products have returned to a temperature of 25 °C. It includes the latent heat of vaporisation of water.

The temperature of the exhaust flue gas of a boiler is generally in the range of 120 to 180 °C. The combustion products are rarely cooled to the initial temperature of the fuel (∼ 25 °C). Hence, the water vapor in the flue gas does not condense, and therefore, its latent heat of vaporization is not recovered. As a consequence, the effective heat available for use in the boiler is a lower amount [36]. We therefore define a lower heating value (LHV) which is the amount of heat released by fully combusting a specified quantity of fuel less the heat of vaporization of water in the combustion product.

The HHV of the wood and plastic samples were determined at a reference temperature of 25 °C in a bomb calorimeter with an internal volume of 260 mL, according to the standard, EN 15400 [153]. A 10 mL solution of 0.5 M Na_2CO_3 (aq) was added to the combustion bomb to capture any acid gases released during combustion. The combustion process was performed using approximately 1 g sample under 30 bar of oxygen at about 25 °C.

With regards to the LHV, existing methods cannot directly determine this energy: this value can be calculated from the HHV of the analysed sample. The LHV requires information on the moisture and hydrogen content of the sample, which transform into water vapour during combustion of the sample. In our case, the sample is dried, hence only the hydrogen content of the sample is necessary to calculate the LHV. Information on the hydrogen content in the sample is determined by the CHNS analyser (see section 2.2.7). The LHV in MJ/kg is calculated using the following formula, according to standard EN 15400 [153]:

$$LHV = HHV - 0.206 \times \%H \tag{2.5}$$

Where %H is the hydrogen content in the dry sample.

2.2.10 Thermal behaviour

Two common techniques for studying the mass loss and reactions that occur during biomass pyrolysis or gasification are thermogravimetry (TG) and Differential scanning calorimetry (DSC). TG is a technique that analyses the change in mass of the biomass sample as a function of temperature and time whereas DSC analyses the difference between the heat flow rate to the sample and the reference sample while they are subject to a temperature alteration [115].

For the present work a simultaneous thermogravimetry-differential scanning calorimetry, going by the product name Setaram TG-DSC 111 was used (Figure 2.6). The analyses were conducted using 25 mg sample placed in a platinum crucible. The sample was heated to 800 °C at 5 °C/min under nitrogen atmosphere (4L/h).

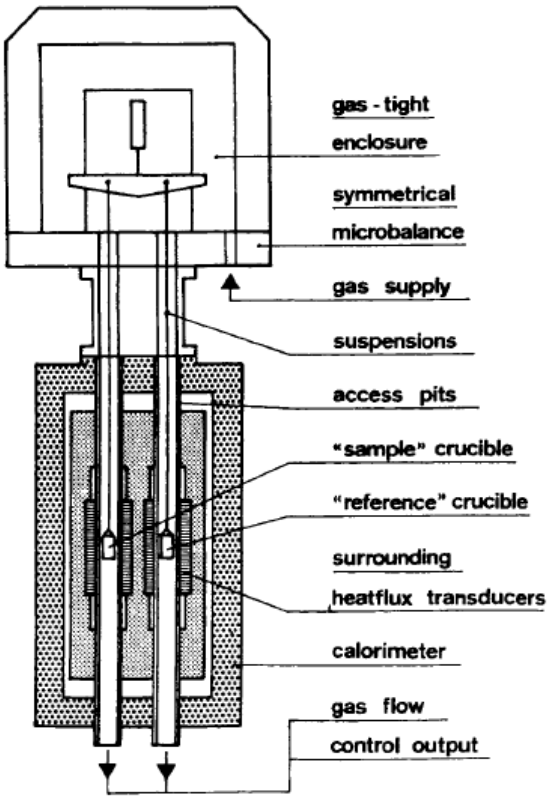

FIGURE 2.6: Schematic view of Setaram TG-DSC 111 [115]

2.3 Results

2.3.1 Thermo-physical properties

Particle size distribution

Figure 2.7 and Table 2.2 display the fines content, large particle size distribution and statistical analysis data of the three wood waste samples. It can be observed in Table 2.2 that samples W1 and W2 have a high fines content of 36 and 39 wt% respectively whereas W3 has a relatively low content of 8 wt%. This is expected as W1 and W2 have undergone pre-grinding.

By comparing the histograms of the maximum projected lengths of the wood waste samples in Figure 2.7, and the corresponding statistical data in Table 2.2, W1 can be seen to have a relatively narrow large particle size range (3 - 47 mm) with a normal distribution as the mean, median and mode are equal. W2 has a wider large particle size range (3 - 77 mm) and a slight right-skewed distribution. As for W3, a clear right-skewed distribution can be observed with 3 % of particles exceeding the threshold requirement as feed for fixed bed reactors (HDF = 100 mm).

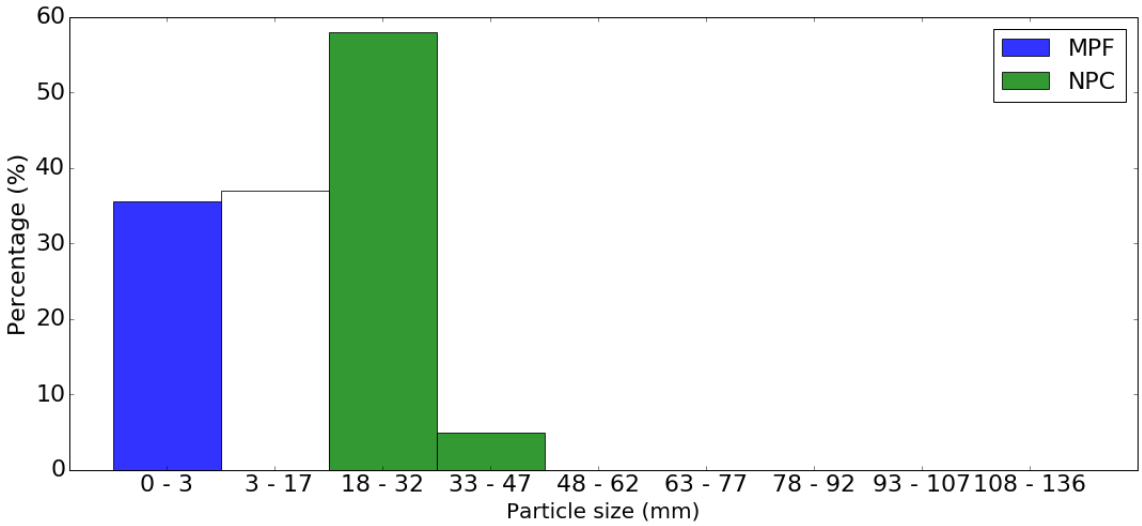

(A) W1 particles

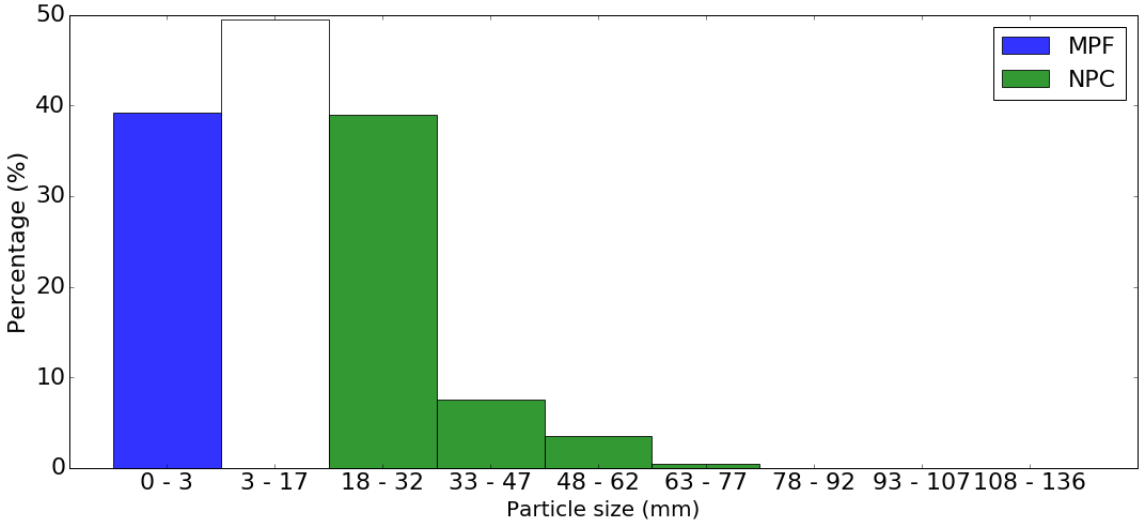

(B) W2 particles

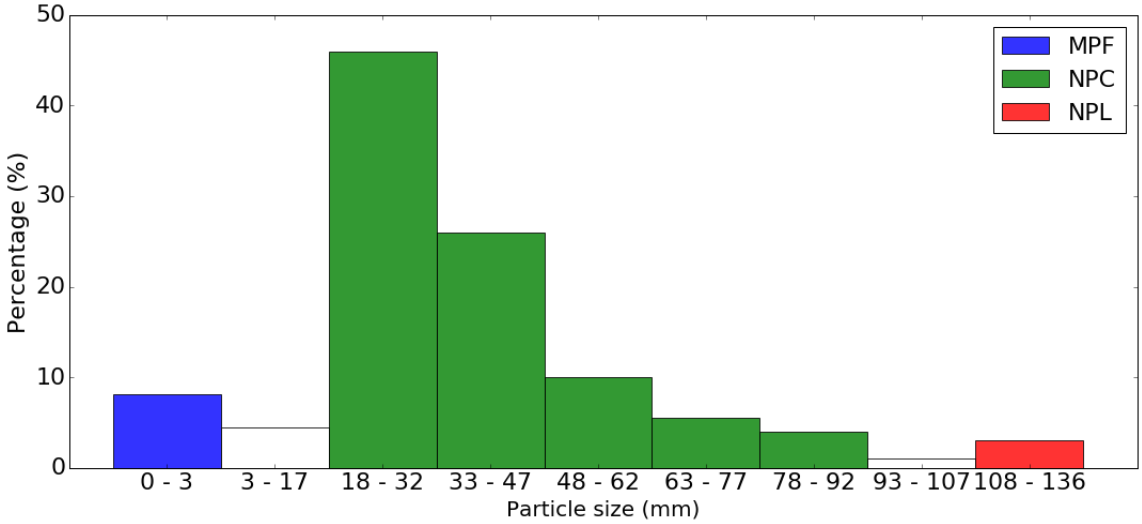

(C) W3 particles

FIGURE 2.7: Histogram of maximum projected length distribution of large Class B wood waste particles

TABLE 2.2: Data on the fines content and statistical analysis on the maximum projected lengths of Class B wood waste samples.

	W1	W2	W3
MS (g)	331.7	338.5	380.3
MF (g)	118.0	132.9	30.9
Mean size (mm)	20	21	40
Median size (mm)	20	18	32
Modal class (mm)	18-32	3-17	18-32

Concerning the particle size distribution of the fines, Figure 2.8 shows the mass percentage of fines with respect to the particle size class. It is clear that the modal class is 1.6 - 3.15 mm for all three wood waste samples. Furthermore, there is a significant weight fraction of fines (13 - 20 wt%) with a particle size below 0.4 mm which can play a major role in pyro-gasification reactons as they provide a high external surface to weight ratio.

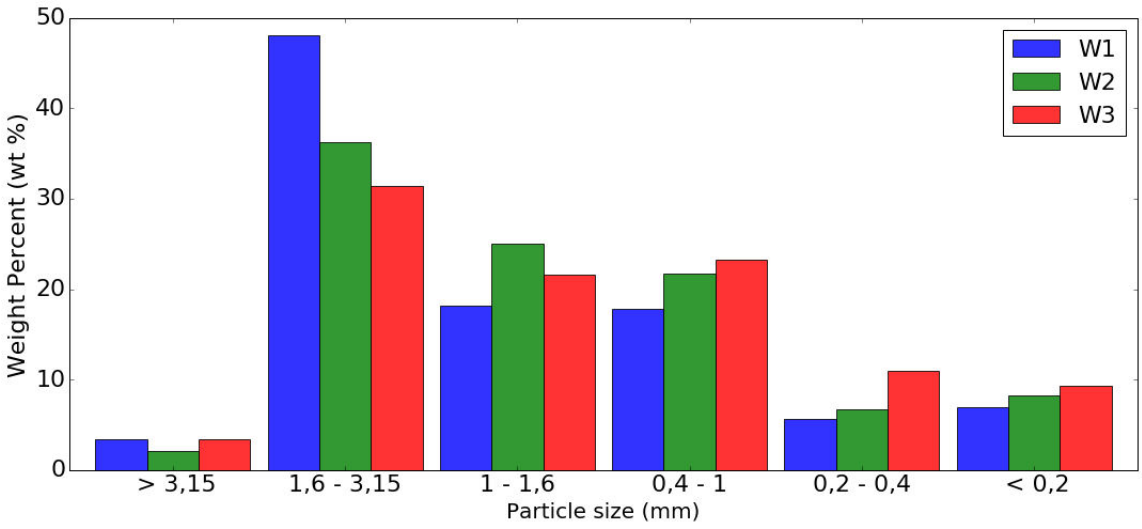

.

FIGURE 2.8: Histogram of fine particle size distribution of Class B wood waste particles

Density and heating values

Table 2.3 lists the true and bulk densities of the wood and plastic samples as well as their heating values (LHV and HHV). We can see that the true densities of the Class B wood waste samples are similar to that of poplar wood. This indicates that the wood waste is largely made up of hardwoods which are often used for construction, furniture making and flooring [154]. However, the bulk densities vary significantly between the wood samples. This may be mainly due to differences in particle packing. The true and bulk densities of PW, HDPE, PS and PVC correspond to those found

TABLE 2.3: Comparison of density and heating values of industrial and model waste

	True density (kg/m^3)	Bulk density (kg/m^3)	HHV (MJ/kg)	LHV (MJ/kg)
W1	1457.3	255.2	18.3	17.2
W2	1460.6	619.5	17.0	15.8
W3	1482.1	341.0	17.4	16.2
PW	1465.0	141.7	18.5	17.1
HDPE	947.0	426.2	46.5	43.5
PS	1064.0	560.6	41.4	39.8
PVC	1418.0	500.9	20.3	19.3

in literature [155].

The heating values of the class B wood waste and poplar wood samples are similar and are comparable to those of sub-bituminous/brown coal (17.4-23.9 MJ/kg) [156]. With regards to HDPE and PS, their high heating values are close to those of petrol/gasoline (44-46 MJ/kg) [156], whereas PVC has half as much. The observed variations in the heating values of the samples are linked to variations in their C, H, O and Cl content, which will be discussed in section 2.3.3.

2.3.2 Proximate Analysis

Table 3.1 shows the proximate analysis data which gives the composition of the fuel samples in terms of their contents of moisture, ash, volatile matter, and fixed carbon (determined by difference). By comparing the wood sample results, we can see that W1, W2 and W3 have higher moisture contents than PW, with W3 having the highest value of about 16 wt% which is within acceptable limits for pyro-gasification processes. With respect to ash content, W3 has a very high content of 5.7 wt% which is above the requirement (5 wt%) of a downdraft fixed bed reactor [43]. The volatile matter content of PW is slightly higher than those of the class B wood waste samples.

In Table 3.1, we can see that the plastics - HDPE, PS and PVC - have a significantly high volatile matter content ($>$ 95 wt%) with no ash measured. This indicates that the presence of these plastics in wood waste, may improve oil and gas yields from pyro-gasification. Of the plastics, only PVC has a significant fixed carbon content and thus may increase char yield from pyro-gasification when mixed with wood waste.

2.3.3 Ultimate Analysis

Organic element analysis

The ultimate analysis presented in Table 3.2 gives the contents of C, H, O, N, S and Cl in the wood and plastic samples. We can observe that W1, W2 and W3 have

Table 2.4: Comparison of proximate analysis (as-received basis) of industrial and model waste

	Moisture (%)	Ash (%)	Volatile Matter (%)	Fixed carbon (%)
W1	11.7	2.0	80.6	5.7
W2	12.5	2.2	82.0	3.3
W3	15.7	5.7	76.8	1.7
PW	8.0	2.0	85.1	4.0
HDPE	0.0	0.0	100	0.0
PS	0.0	0.0	99.6	0.4
PVC	0.0	0.0	95.8	4.2

Table 2.5: Comparison of ultimate analysis (dry ash-free basis) of industrial and model waste

	C (%)	H (%)	O (%)	N (%)	S (%)	Cl (%)
W1	47.4	5.2	45.7	1.7	0.0	0.06
W2	47.8	5.6	45.2	1.4	0.0	0.05
W3	46.2	5.7	46.5	1.7	0.0	0.07
PW	49.9	6.4	42.7	1.0	0.0	0.01
HDPE	86.1	14.5	0.0	0.0	0.0	0.0
PS	92.4	7.8	0.0	0.0	0.0	0.0
PVC	38.7	4.8	0.0	0.0	0.0	56.5

very similar compositions of C, H and O to that of PW which confirms that these wood waste samples do not contain significant amounts of organic preservatives (e.g. creosote). The wood waste samples also have low nitrogen and insignificant amounts of sulphur. Thus, they are likely to give low emissions of NO_x and SO_x when used for thermochemical processes. Compared to the wood samples, HDPE and PS have high C and H content and insignificant O content which contribute positively to their heating values as shown in Table 2.3. PVC, however, has a relatively low C and H content because of its high Cl composition, which consequently contributes negatively to its heating value (Table 2.3).

Although the chlorine content in the class B wood waste samples are low, are at least five times higher than in poplar wood. The main problems caused by Cl are the corrosive effect of chloride salts and HCl on metal parts in the pyro-gasifier and furnace [9, 157], emissions of HCl and particulate (KCl, NaCl, $ZnCl_2$, $PbCl_2$) as well as the influence of HCl on the formation of highly toxic polychlorinated dibenzo-p-dioxins (PCCD) and polychlorinated dibenzofurans (PCDF) when the contaminated syngas is combusted [158]. The higher chlorine content observed in the waste samples could be from the presence of small amounts of processed wood with PVC compounds such as wood with PVC-coatings, and wood pallets with PVC composite [159].

Inorganic element analysis

The analysis results of minerals in the wood samples are displayed in Table 2.6 and Figure 2.9. These elements are important with regards to ash melting, deposit formation, fly ash and aerosol emissions as well as corrosion (together with S and Cl) and the utilisation/disposal of ashes [136, 148].

During pyro-gasification, a fraction of the ash-forming elements in wood, especially K, Na, S, Cl, Zn, Pb, Cd and Hg are volatilised and combine with small particles to form fine fly ash or aerosols (1 nm to 1 μm) and coarse fly ash (5 to 100 μm) [148]. In Figure 2.9, we can see that the Class B wood waste samples have a significantly higher Na, Zn and Pb concentrations than PW. Na can combine with Cl (and S) in fly ash which increases corrosion risks. Furthermore, a higher Zn and Pb concentration in aerosols can become an important environmental pollution hazard. Coarse fly ash can be easily separated from the gas phase using cyclones, however aerosol precipitation requires much more cost intensive technologies such as Electrostatic Precipitators (ESP) or Bag House Filters (BHF) which are only economically viable for medium and large-scale units (> 20 MWe) [136].

Bottom ash is formed from wood pyro-gasification by non-volatile elements consisting mainly of refractory species such as Ca, Mg and Si, and smaller amounts of bound volatile compounds including K, Na and Al. These elements can have a strong influence on the ash melting temperature. Figure 2.9 shows that higher Ca, Mg, Si and Al are present in the class B waste samples (especially in W3) than in PW. High Si and Al content typically lowers the ash melting temperature while Mg and Ca increase it [160–162]. A lower ash melting temperature can cause ash sintering and slag formation which may result in deposits in syngas boiler tubes and may consequently reduce the plant availability and lifetime [148]. Hence, an appropriate temperature control technology may required.

As can be seen in Figure 2.9, PW has relatively low concentrations of heavy metals, and thus, if gasified, the coarse fly ash can be mixed with the bottom ash and then recycled to agricultural or forest soils in order to close the natural cycles of mineral constituents. However, the relatively high concentrations of the heavy metals, Ba, Pb and Zn, in class B wood waste may render its ash unsuitable for soil spreading. Hence, alternative ash recycling or disposal methods may be necessary.

2.3.4 Thermogravimetric Analysis

Figures 2.10 displays the TG, DTG and DSC (heat flux) curves as a function of temperature of the studied polymers. From these thermal decomposition curves, the following physical and chemical processes can be identified in the order of increasing temperature: water evaporation/desorption, melting, devolatilisation and charring. These processes are discussed as follows:

Table 2.6: Mean values of inorganic elements (as-received basis) of industrial and model waste

Element (mg/kg)	W1	W2	W3	PW
Al	820.21	542.41	1427.12	186.91
As	84.68	87.14	97.72	74.95
B	63.20	49.40	65.56	38.54
Ba	364.45	387.12	2296.90	28.45
Ca	4384.89	5314.03	11718.26	3981.09
Cd	30.58	30.20	31.18	28.95
Co	34.22	34.84	38.20	32.32
Cr	51.71	51.16	69.20	34.05
Cu	130.24	130.45	150.39	109.69
Fe	680.19	619.66	1841.79	80.49
Hg	14.38	14.82	15.42	14.15
K	451.02	423.12	741.49	655.03
Mg	401.50	428.15	734.06	384.25
Mn	114.47	109.15	125.48	45.05
Mo	41.20	42.21	42.00	40.04
Na	940.38	973.66	1108.84	382.21
Ni	39.85	43.37	42.33	37.84
P	221.40	277.84	312.09	339.98
Pb	377.77	362.89	1595.05	98.30
Sb	114.31	117.90	123.00	108.57
Se	132.71	137.97	144.07	129.70
Si	1326.05	1092.30	2402.63	189.95
Sn	287.04	296.86	312.16	271.04
Sr	43.24	51.35	116.33	30.55
Ti	430.74	394.07	776.31	36.71
V	41.99	43.93	75.16	36.63
Zn	281.89	315.27	1426.09	46.42
Zr	39.06	36.74	44.17	34.01

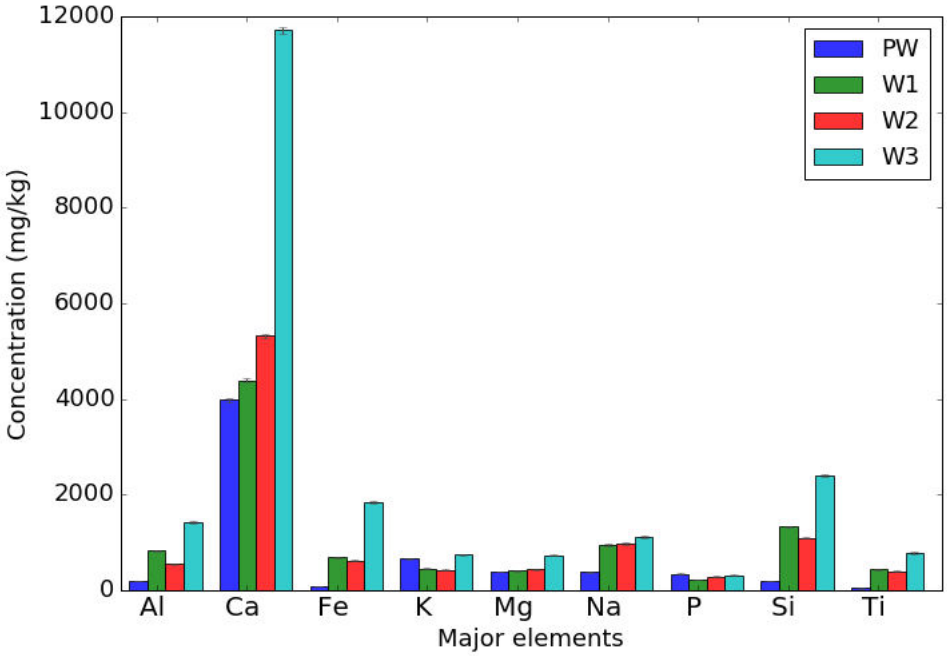

(A) Major inorganic elements

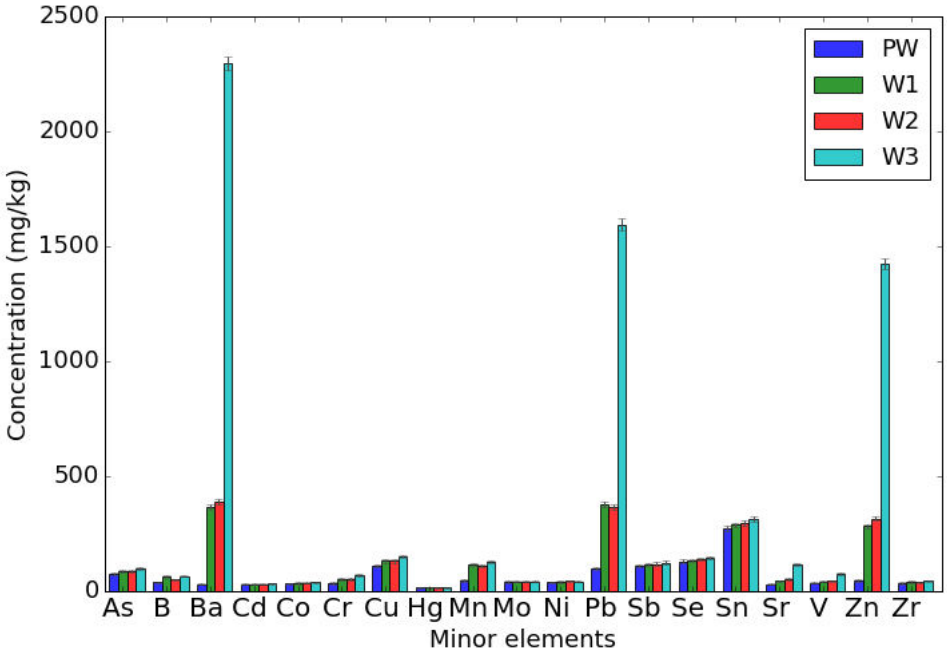

(B) Minor inorganic elements

FIGURE 2.9: Comparison of mineral concentrations in wood samples

- Physical desorption of water can be observed to start occuring below 100 °C for the wood samples (PW, W1, W2 and W3) which is represented by endothermic peaks and mass loss of approximately 6 wt%.

- HDPE melts at around 130 °C which results in a sharp endothermic peak. This well-defined melting temperature is characteristic of polymers with a high degree of order in molecular packing (i.e. degreee of crystallinity) [163]. HDPE is 95 % crystalline whereas PVC and PS are amorphous (< 15 % crystalline). Hence, no peak can be observed for PVC and PS because they melt over a wide temperature range. As for the wood samples, no fluid state is observed due to their highly complex structure which makes it impossible for wood to change state below temperatures at which devolatilisation occurs.

- The devolatilization phase for all the plastic and wood samples is generally characterized by a significant mass loss between 200 and 500 °C (Figure 2.10). However, the TG/DTG curves clearly show that the samples have different thermal stabilities which can be linked to their different polymer chain structures. By comparing the molecular unit structures of the plastics in Figure 2.11, we can see that PVC and PS are derivatives of HDPE with different substituents (Cl in PVC and benzene ring in PS). The dissociation energies of C-H, C-Cl and C-C bonds in the polymers are 414, 339 and 347 kJ/mol [164] respectively which can explain why HDPE has the highest thermal stability and PS is more stable than PVC. Concerning the wood samples (PW, W1, W2, W3), they can be observed to have very similar thermal decomposition behaviour in Figure 2.10. Wood is essentially made up of the three major components, cellulose, hemicellulose and lignin, whose molecular unit structures are displayed in Figure 2.11. Poplar wood contains roughly 42-29 wt% cellulose, 16-23 wt% hemicellulose and 21-29 wt% lignin [139]. On heating, hemicellulose decomposes first (190-290 °C) because of its weak branched-chain structure (Figure 2.10). This is followed by cellulose devolatilization (290-360 °C) because its thermally stable linear-chain structure. Finally, lignin decomposes (360-500 °C) over a broad temperature range as a result of its complex and highly cross-linked structure consisting of three building blocks: p-hydroxylphenyl, syringyl, and guaiacyl units.

- Charring is a process that occurs after the devolatilization stage whereby the remaining solid undergoes cross-linking and cyclization reactions to form a carbonaceous (char) residue [163]. In Figure 2.10, charring can only be observed for wood and PVC samples at temperatures above 350 °C. With regards to the wood samples, a char residue yield of 11.8, 34.0, 34.8 and 19.6 wt% where observed for W1, W2, W3 and PW respectively whereas 3.4 wt% char was seen for PVC. As for HDPE and PS, as a result the absence of cross-linking reactions during pyrolysis, these polymers were competely decomposed to yield volatiles.

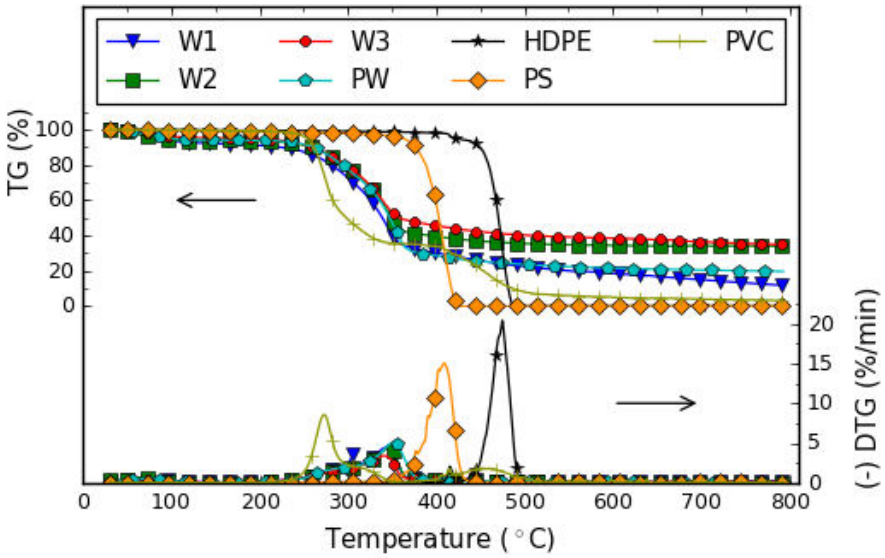

(A) TG and DTG curves

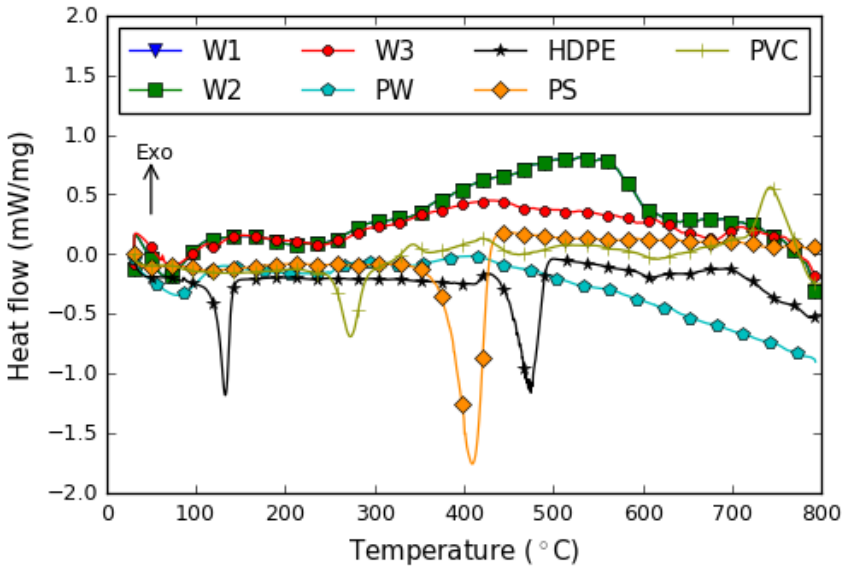

(B) DSC curves

FIGURE 2.10: Thermogravimetric analysis of plastic and wood samples at 5°C/min heating rate under N_2 atmosphere

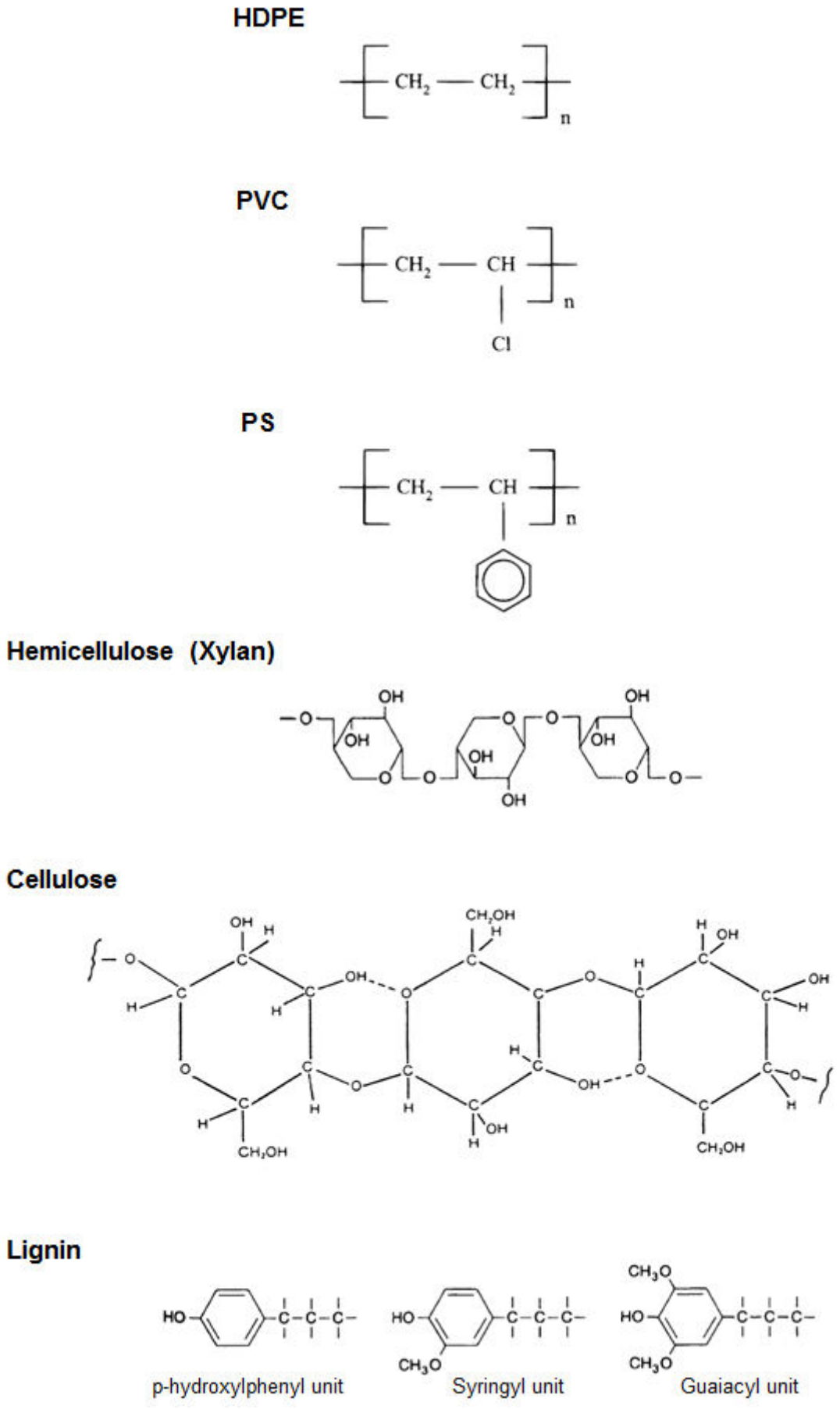

FIGURE 2.11: Molecular structural units of the plastics used and of wood components

Conclusion

This chapter presents the characteristics of Class B wood wastes (W1, W2 and W3), virgin poplar wood (PW), as well as the plastics, HDPE, PS and PVC. Several physical and thermo-chemical properties of these samples were analysed using European Standards for solid recovered fuels (SRF).

The particle size distribution of the three Class B wood waste samples was analysed, and W1 was found to have the highest fine particle (< 3 mm) content of 39 wt% while W3 had the least (8 wt%). Regarding large particles, W1 and W2 had normal and slightly right-skewed distributions respectively with similar mean sizes of 20 and 21 mm, whereas W3 had a strongly right-skewed distribution with a mean size of 40 mm as well as 3 % of particles exceeding the 100 mm limit requirement for fixed bed reactors.

The density and heating values of all three wood waste were similar to those of PW and PVC whereas HDPE and PS had heating values twice as high. Of the three wood waste samples, W3 had the highest moisture and ash content of 16 wt% and 5.7 wt% respectively. HDPE, PS and PVC were found to have at least 15 wt% more volatile matter content than the wood samples.

The class B wood waste and PW samples had similar C, H, and O content as well as low S and N concentrations. However, the Cl content in the wood waste samples were at least five times higher than in PW. Compared to the wood samples, HDPE and and PS had at least 36 wt% more C than the wood samples which resulted in the significantly higher heating values observed. Compared to the mineral content in PW, the class B wood samples has significantly higher concentrations of Na, Ca, Mg, Si and Al, as well as the heavy metals, Zn, Pb and Ba.

The themogravimetric analysis conducted on the samples showed that Class B wood wastes had similar thermal behaviour to PW: Water desorption below 100 °C; devolatization at 190-350 °C; and charring above 350 °C. The plastics showed different behaviour from the wood samples: HDPE melted at approximately 130 °C; PVC, PS and HDPE decomposed at 200-350 °C, 350-430 °C and 440-480 °C respectively, PVC underwent charring reactions at 350-500 °C.

The characteristics of the wood and plastics samples studied in this chapter will be relevant for the different experimental and modelling studies presented in the following chapters.

CHAPTER 3

Co-pyrolysis of wood and plastics

Introduction

This chapter presents a laboratory-scale experiment in a fixed bed reactor which investigates the co-pyrolysis of poplar wood (PW) and three different plastics: high density polyethylene (HDPE), polystyrene (PS) and polyvinyl chloride (PVC). The aim of this work is to study the influence of plastic type and content on the pyrolysis product yield, gas specie yields and gas heating value.

In recent years, co-pyrolysis of biomass and plastic waste has gained considerable research interest mainly due to the positive contribution of plastics to the product yield and the calorific value of the oil produced [17–19, 165, 166]. According to Johannes et al. [167], the interactions or synergy between biomass and plastics depends on various factors including the type and contact of the fuel components, pyrolysis duration, temperature and heating rate, and catalysts. Hence, it is not surprising that conflicting reports sometimes arise in literature concerning the differences between the actual and predicted yields of the pyrolysis products, where the predicted yields are calculated as linearly proportional to the contributions of the pure components. For example, Grieco and Baldi [168] observed insignificant interactions between low density polyethylene (LDPE) and beech wood during co-pyrolysis in a capsule at heating rates of 0.1 and 1 °C/s. However, Yang et al. [169] observed a significant synegistic effect on oil yield when LDPE and cedar wood were co-pyrolyzed at 600 °C in a dropdown tube reactor at rapid heating rates.

Research works on the co-pyrolysis of biomass and plastic waste have principally focused on the influence of temperature, heating rate and reaction time on product yield and quality [170–173]. Nonetheless, some authors, such as Oyedun et al. [174] have shown that the type and plastic content in the sample also play an important role. Unfortunately, the few studies on the influence of plastic content on product yield are narrowly-focused on polyolefins (polyethylene (PE) or polypropylene (PP)) because this plastic type generates high oil yields and is the most abundant in waste streams [168, 175, 176]. Consequently, the operating conditions chosen for these studies aim at maximising oil yields for liquid fuel production and involve low temperatures (400-500 °C), and short gas residence times (< 15 mins). Furthermore, with respect to research works on the influence of plastic content in biomass on gas composition and heating value, Grieco et al. [168] and Paradela et al.[172] have observed significant interactions. However, Paradela et al. [172] conducted their experiments with a fixed plastic waste mixture of 56 wt% PE, 17 wt% PS and 27 wt% PP and Grieco et al. [168] performed theirs using only PE as the plastic type. Hence, there remains a knowledge gap in literature about the contribution of non-polyolefins such as PS and PVC on the gas composition and heating value derived from co-pyrolysis with biomass.

Thus, in this work, we will investigate the influence of HDPE, PS and PVC content in wood on the co-pyrolysis product yields, gas specie yields and heating value, under conditions that favour gas production: high temperature, low heating

rate and long gas residence time.

3.1 Experimental methods

3.1.1 Wood and plastic samples

The materials used for the tests were poplar wood (PW), HDPE, PVC and PS, whose characterstics are displayed in Tables 3.1 and 3.2. The particle size of each pure material was less than 1 mm. Several wood/plastic mixtures for each plastic type were prepared having different plastic contents: 0-5-10-30-50-100 wt% plastic.

Table 3.1: Proximate analysis (as-received basis) of wood and plastic samples

	Moisture (%)	Ash (%)	Volatile matter (%)	Fixed carbon (%)	LHV (MJ/kg)
PW	8.0	2.0	85.1	4.0	17.1
HDPE	0.0	0.0	100	0.0	43.5
PS	0.0	0.0	99.6	0.4	39.8
PVC	0.0	0.0	95.8	4.2	19.3

Table 3.2: Ultimate analysis (dry ash-free basis) of wood and plastic samples

	C (%)	H (%)	O (%)	N (%)	S (%)	Cl (%)
PW	49.9	6.4	42.7	1.0	0.0	0.01
HDPE	86.1	14.5	0.0	0.0	0.0	0.0
PS	92.4	7.8	0.0	0.0	0.0	0.0
PVC	38.7	4.8	0.0	0.0	0.0	56.5

3.1.2 Pyrolysis reactor and procedure

Figure 7.1 gives a schematic representation of the experimental setup. For each test, 10 g of sample was placed in a quartz crucible. The sample was heated in a furnace to 750 °C at a heating rate of 20 °C/min under nitrogen atmosphere (33 mL/min) and was maintained at this temperature for 30 mins before being cooled to room temperature. These operating conditions allowed a reaction time of 66 mins which is sufficient for secondary cracking of volatiles to occur in order to form more gas and secondary char. At the reactor outlet, the volatile oil was condensed in an impinger bottle filled with cotton wool and cooled to 0 °C. Thus, in this case, the term 'oil' represents a mixture of bio-tar, oil, wax and small amounts of water produced from the pyrolysis process. For experiments with PVC, the oil condenser was replaced with two impinger bottles containing aqueous solutions of KOH to

trap HCl gas. Next, the total amount of the non-condensable gas produced from pyrolysis was collected in a Tedlar bag. Its composition was analyzed by a micro-gas chromatograph (Micro-GC, A3000 Agilent). The quantification of HCl concentration in the aqueous phase was conducted using X-ray fluorescence (XRF, PANanalytical).

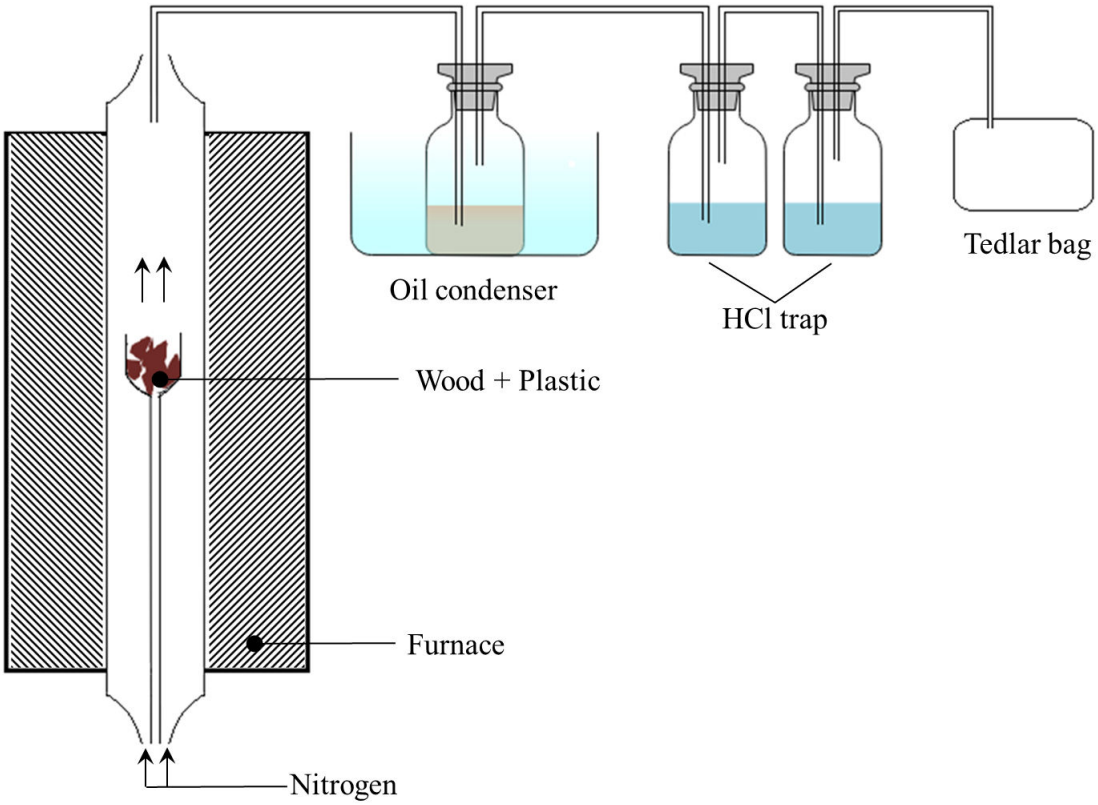

FIGURE 3.1: Experimental setup of pyrolysis equipments

The char yield was calculated by dividing the weight loss of the sample and crucible before and after pyrolysis by the total initial sample mass. The gas yield y_{gas}, was calculated based on the following equations:

$$V_{gas} = \frac{Q_{N_2}\, t}{x_{N_2}} \tag{3.1}$$

$$y_{gas} = \frac{\sum_i^n (\rho_i\, x_i)\, V_{gas}}{m_s} \tag{3.2}$$

Where V_{gas} is the total gas volume, Q_{N_2} and x_{N_2} are the volumetric flowrate and volume fraction of the nitrogen carrier gas respectively, t is the reaction time, ρ_i and x_i are the density and volume fraction of each gas specie i, measured at normal temperature and pressure, and m_s is the initial sample mass. To estimate the oil yield, the difference between the yields of char and gas was calculated.

The gas lower heating value LHV_{gas} in units of MJ/Nm^3 was estimated based on the lower heating values of each gas specie i (MJ/kg), using the following equation:

$$LHV_{gas} = \sum_{i}^{n} LHV_i \, \rho_i \, x_i \tag{3.3}$$

To evaluate the synergy between poplar wood and the plastic samples, the theoretical product yields were calculated according to the following formula:

$$y_{calc} = w_1 y_1 + w_2 y_2 \tag{3.4}$$

where y_1 and y_2 are the pyrolysis yields of pure wood and plastic; w_1 and w_2 are the mass proportions of wood and plastic in the sample respectively. Therefore, the interaction or synergy parameter Δy, is the difference between the experimental and calculated product yields from co-pyrolysis.

$$\Delta y = y_{exp} - y_{calc} \tag{3.5}$$

3.2 Results

3.2.1 Effect on char yield

Figure 3.2 and Table 3.3 present the yields of char, oil and gas with respect to the different plastic contents in the samples. It can be seen in Table 3.3 that the char yield from pure PW pyrolysis is 20.6 wt% whereas half as much char is produced from PVC (10.5 wt%) and virtually no char is produced from HDPE and PS. These results for the char yield of plastics are consistent with those of Williams et al. [164].

Regarding the co-pyrolysis of PW with HDPE and PS, a small positive synergy can be observed in Figure 3.2a with a maximum difference of approximately 2.5 wt% between the experimental and theoretical char yield. This indicates that the presence of HDPE and PS promotes secondary reactions of volatiles, such as condensation and repolymerisation, to form secondary char [38, 177]. Grieco and Baldi [168] and Bernado et al. [178] have made similar observations in this respect.

For co-pyrolysis with PVC, a strong positive synergy can be seen in Figure 3.2a, where the maximum synergy of 8 wt% occurs at a PVC content of 30 wt%. This corresponds to the findings of Cepeliogullar and Putun [179] who obtained significantly higher char yields compared with the theoretical yield for a mixture of 1:1 weight ratio of PVC and biomass (hazelnut shell, sunflower residues and E.rigida). An explanation for this phenomenon has been provided by Matsuzawa et al. [180, 181] who suggest that HCl produced from PVC pyrolysis promotes the dehydration and cross-linking of cellulose in biomass, which in turn promotes the charring of cellulose.

3.2.2 Effect on oil and gas yields

As shown in Table 3.3, the oil and gas yield of pure PW is 63.7 wt% and 15.7 wt%. On the one hand, pure HDPE and PS generate higher oil yields of 86.3 wt% and 99.5 wt% respectively, due to their relatively high volatile and low ash content (Table 3.1). Thus, HDPE and PS produce relatively small amounts of gas (13.7 and 0.5 wt% respectively). On the other hand, pure PVC has the lowest oil yield (30.3 wt%) and the highest gas yield (59.2 wt%), the latter of which is mainly composed of HCl gas (Table 3.4). These results are in accordance with those found in literature [182, 183].

In Figure 3.2b, it is clear that the presence of HDPE and PS increases oil yield relative to the pyrolysis of pure PW for all plastic contents, which is consistent with the reports of other authors [18, 184–187]. A slightly positive synergy can be observed at HDPE contents of less than 50 wt% whereas a negative synergy occurs for PS. The positive synergy associated with PE/biomass pyrolysis has also been recently observed by Yang et al. [169] and Onal et al. [175] who have suggested that more liquid organics are produced due to secondary reactions between the decomposition products of PE and biomass even at an ultra-short residence time of 30 s. However, the synergy of PS/biomass pyrolysis is not clear in literature. Oyedun et al. [174] have found from thermogravimetric analysis, that lower temperature and energy are required to pyrolyze PS/biomass blends than are required for HDPE/biomass pyrolysis. It is therefore possible, in our opinion, that the oil formed at lower temperatures in the presence of PS has more time to undergo secondary cracking reactions to produce more gaseous products, and thereby decrease the overall oil yield. This suggestion is supported by the observation, in Figure 3.2c, that the gas yield increases relative to the predicted yield for PS contents below 50 wt%.

With regards to co-pyrolysis with PVC, a significant positive synergy in oil yield can be observed in Figure 3.2b with a maximum difference of 11 wt% between the experimental and predicted yields at 50 wt% PVC content. A corresponding strongly negative synergy in gas (HCl) yield can be seen in Figure 3.2c, where the maximum synergistic difference of 18 wt% occurs at 30 wt% PVC content. This result is in agreement with Zhou et al. [188] who have recently observed a significant increase in oil yield for mixtures of PVC with three biomass components (hemicellulose, cellulose and lignin) during fast co-pyrolysis at 800 °C in a fixed bed reactor. They propose that the biomass and/or bio-char can act as a catalyst which promote chain scission of PVC, resulting in the increased production of chlorinated oil compounds. What this means in terms of HCl gas release will be discussed in the following section.

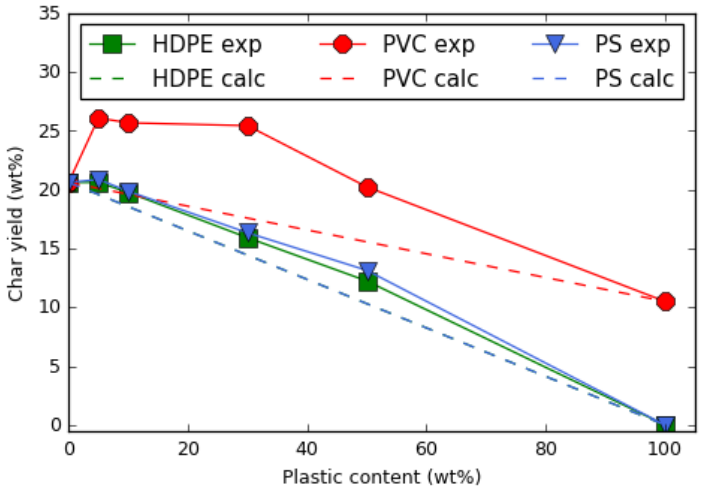

(A) Char yield

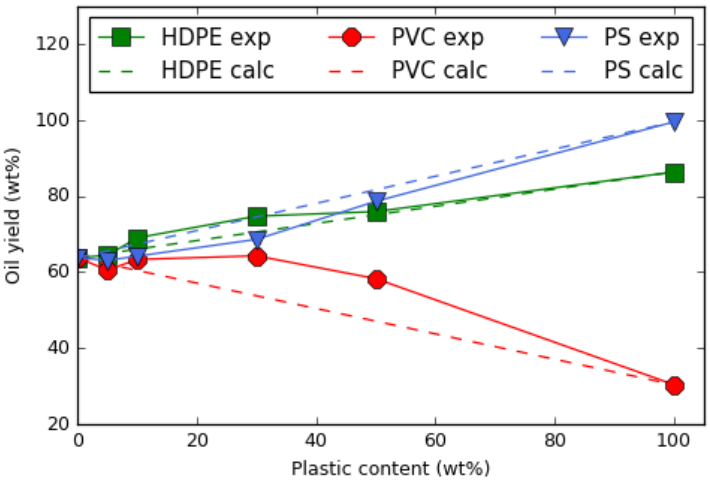

(B) Oil yield

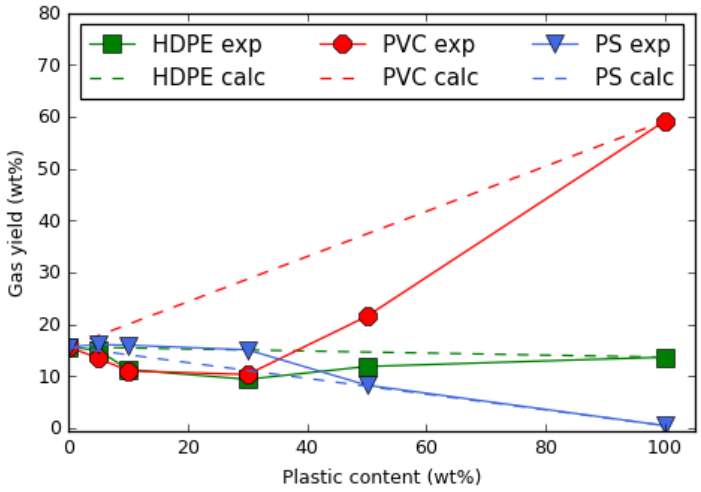

(C) Gas yield

FIGURE 3.2: Influence of plastic type and content on product yield

Table 3.3: Product yield from the pyrolysis of PW, HDPE, PVC, PS and their mixtures

	HDPE			PVC			PS		
Plastic Content (wt%)	Char (wt%)	Gas (wt%)	Oil* (wt%)	Char (wt%)	Gas (wt%)	Oil* (wt%)	Char (wt%)	Gas (wt%)	Oil* (wt%)
0 (100 wt% PW)	20.6	15.7	63.7	20.6	15.7	63.7	20.6	15.7	63.7
5	20.6	15.0	64.4	26.1	13.5	60.5	20.9	16.1	63.0
10	19.8	11.3	69.0	25.7	11.0	63.3	19.9	16.0	64.2
30	15.9	9.4	74.7	25.4	10.3	64.2	16.3	15.1	68.6
50	12.2	11.9	75.9	20.2	21.5	58.2	13.1	8.30	78.6
100	0.00	13.7	86.3	10.5	59.2	30.3	0.00	0.50	99.5

*Calculated by difference and represents a mixture of bio-tar, oil, wax and water

Table 3.4: Light gas yields from the pyrolysis of PW, HDPE, PVC, PS and their mixtures

	HDPE				PVC					PS			
Plastic Content (wt%)	H_2 (wt%)	CH_4 (wt%)	CO (wt%)	CO_2 (wt%)	H_2 (wt%)	CH_4 (wt%)	CO (wt%)	CO_2 (wt%)	HCl (wt%)	H_2 (wt%)	CH_4 (wt%)	CO (wt%)	CO_2 (wt%)
0 (100 wt% PW)	0.16	1.54	6.10	7.17	0.16	1.54	6.10	7.17	0.10	0.16	1.54	6.10	7.17
5	0.15	1.40	5.00	6.00	0.20	1.36	4.80	6.15	0.48	0.18	1.59	6.66	6.89
10	0.13	1.16	4.20	4.97	0.19	1.12	3.85	4.97	0.56	0.18	1.59	6.52	6.95
30	0.11	1.04	3.16	3.97	0.25	1.24	3.57	3.62	1.19	0.21	1.52	6.20	6.53
50	0.21	1.95	4.51	3.82	0.26	1.31	3.73	3.66	11.90	0.15	0.87	3.46	3.34
100	0.16	4.07	0.00	0.05	0.36	2.50	0.07	0.05	54.79	0.03	0.18	0.15	0.03

Table 3.5: Hydrocarbon gas (C_xH_y) yields from the pyrolysis of PW, HDPE, PVC, PS and their mixtures

	HDPE			PVC			PS		
Plastic Content (wt%)	C_2H_4 (wt%)	C_2H_6 (wt%)	C_3H_8 (wt%)	C_2H_4 (wt%)	C_2H_6 (wt%)	C_3H_8 (wt%)	C_2H_4 (wt%)	C_2H_6 (wt%)	C_3H_8 (wt%)
0 (100 wt% PW)	0.26	0.20	0.19	0.26	0.20	0.19	0.26	0.20	0.19
5	0.15	0.08	0.09	0.19	0.12	0.13	0.38	0.18	0.22
10	0.39	0.17	0.24	0.13	0.12	0.11	0.34	0.18	0.24
30	0.47	0.23	0.44	0.18	0.17	0.13	0.34	0.15	0.15
50	0.68	0.33	0.38	0.23	0.29	0.17	0.28	0.10	0.09
100	3.80	0.01	3.90	0.69	0.45	0.24	0.09	0.01	0.00

Table 3.6: Gas lower heating value (MJ/Nm3) from the pyrolysis of PW, HDPE, PVC, PS and their mixtures

	HDPE	PVC	PS
0 (100 wt% PW)	18.9	18.9	18.9
5	18.6	18.2	19.0
10	20.5	17.9	19.0
30	23.6	18.2	18.3
50	22.7	18.5	19.0
100	45.1	25.6	22.8

3.2.3 Effect on gas specie yields

Table 3.4 displays the yield of light gases derived from the co-pyrolysis of the different plastic and wood samples, and Table 3.5 shows the yield of the heavier hydrocarbon gases produced, which we will conveniently refer to as C_xH_y. In Figure 3.3, the variation of the various gas specie yields as a function of plastic content is presented, which reveals non-linear trends and therefore, the existence of interactions between PW and plastics.

Pure HDPE yields more hydrocarbons, CH_4 and C_xH_y, than pure PW although it generates a similar amount of H_2. Hence, the increase of HDPE content in the sample has a relatively insignificant effect on H_2 yield but increases CH_4 and C_xH_y yields. This may be due to the higher hydrogen content (H/C molar ratio) caused by the addition of HDPE in the sample. Thus, more H and OH radicals are released during co-pyrolysis, which act as hydrogen donor species, and therefore, promote the cracking of aromatic compounds in wood to produce more hydrocarbons in the gas and oil phases [18, 175, 189]. Nonetheless, the observed increase in hydrocarbon gas yield is much lower than the predicted value which indicates that interactions between HDPE and wood preferentially form hydrocarbons in the oil phase. CO and CO_2 yields decrease as more HDPE is added due to the lower oxygen content (O/C molar ratio) in the sample feed. In addition, a negative synergy can be observed for these gas species when the HDPE content is less than 50 wt% because more oxygenated oil compounds are formed [185, 187].

Concerning PS, the yields of the gas species generally decrease as PS content increases because oil production is favoured by this plastic (Figure 3.2b). However, positive synergies can be observed for H_2, CH_4, CO and CO_2, whereas insignificant interactions can be seen for C_xH_y compounds. This implies, in our opinion, that secondary reactions occur between PS and wood volatile products to promote lighter gases rather than heavier ones.

With regard to PVC, the evolution of CH_4, C_xH_y, CO and CO_2 yields as a function of PVC content follows the same trend as that of HDPE although the hydrocarbon yields are much lower because of the low hydrogen content in PVC. However, H_2 yield rises with higher PVC ratios and a positive synergy for H_2 can be seen at PVC contents below 50 wt%. This positive synergy in H_2 yield, in our opinion, may be due to enhanced condensation and cyclization reactions of polyene species produced from the dechlorination of PVC. These cyclization reactions of polyene take place via both radical and molecular mechanisms to form H_2, polycyclic aromatic hydrocarbons (PAH) and char [190]. Our proposed mechanism for enhanced H_2 production is supported by the recent works of Çepelioğullar et al. [179, 191] who obtained an increased amount of PAH from the co-pyrolysis of PVC and biomass mixtures.

It is interesting to observe in Figure 3.3b that although HCl yield increases as a function of PVC content, much lower yields of HCl are obtained compared to the predicted yields which suggests that HCl strongly interacts with poplar wood during

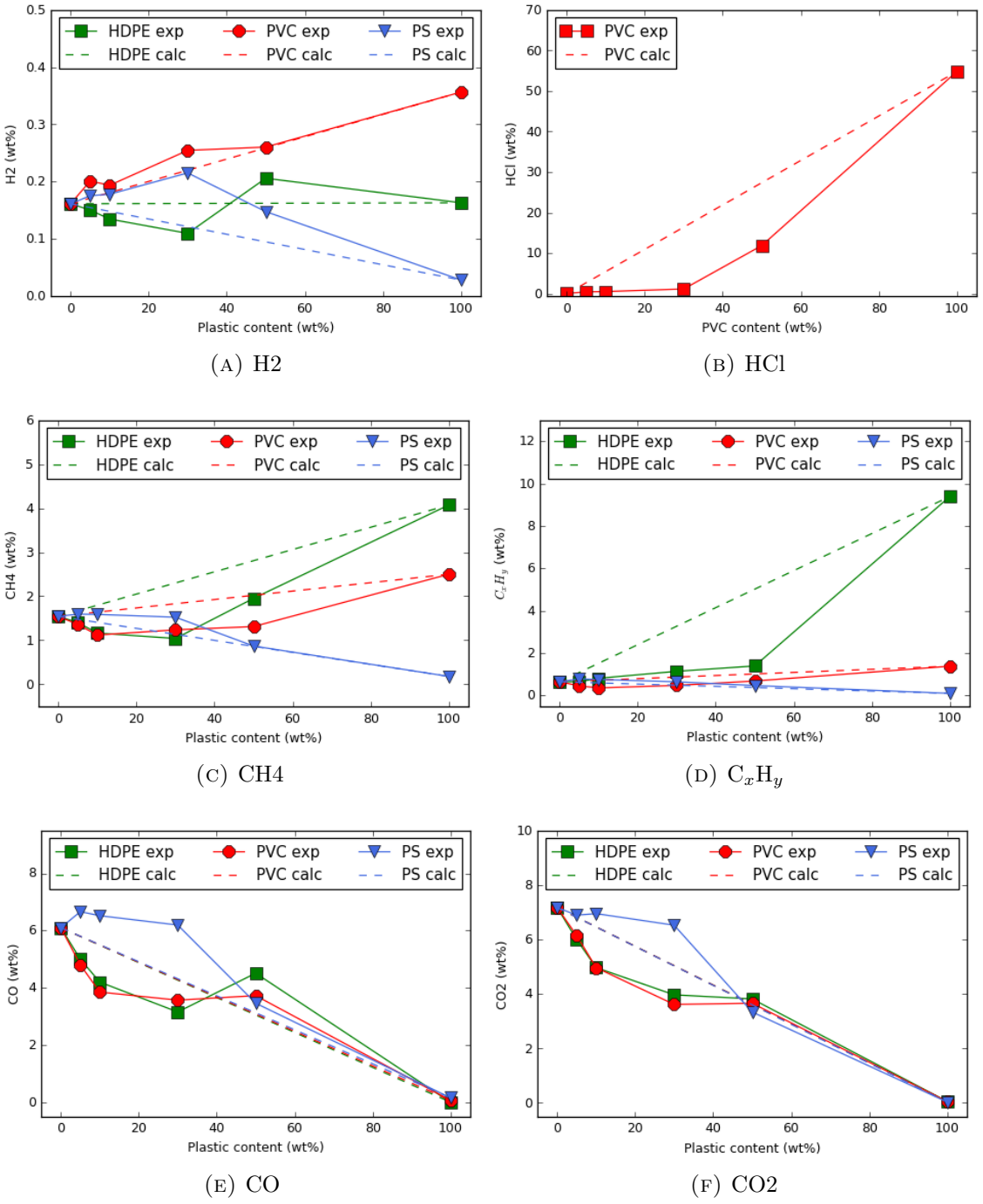

(A) H2 (B) HCl

(C) CH4 (D) C_xH_y

(E) CO (F) CO2

FIGURE 3.3: Influence of plastic type and content on gas composition

co-pyrolysis. This result is consistent with a recent TG-FTIR analysis by Zhou et al. [192] who report that, compared to pure PVC pyrolysis, the maximum HCl peak strongly weakens when PVC is co-pyrolysed with orange peel and tissue paper in a 1:1 weight ratio mixture. Furthermore, Kuramochi et al. [193] have reported a significant reduction in HCl emission when demolition wood is co-pyrolyzed with 1 wt% PVC film. However, the mechanism for HCl-biomass interaction is not well-defined in literature [194]. Kuramochi et al. [193] have pyrolyzed mixtures

of PVC with three constituents of biomass (cellulose, hemicellulose and lignin) separately. Their results show that cellulose has an insignificant effect on HCl emission, whereas hemicellulose, and lignin to a lesser extent, reduce HCl emissions by fixing most of the Cl molecules in the char product. A contradictory result has been presented by Zhou et al. [195] who have found that cellulose can also decrease HCl emission to a similar degree as hemicellulose and lignin. To further add to the confusion, another recent work by the same author suggests that the Cl molecules are fixed in the liquid product to form chlorinated oil compounds [188]. It is therefore evident that more investigations are needed to better understand the mechanisms that govern the interactions between HCl and biomass during co-pyrolysis with PVC. This point will be further addressed in section 3.2.5.

3.2.4 Effect on gas heating value

Table 3.6 and Figure 3.4 present the evolution of the gas lower heating value (LHV) with plastic content. Factors that can increase the LHV of a gas include high concentrations of hydrogen and hydrocarbons. Figure 3.4 shows that at conditions of normal temperature (20 °C) and atmospheric pressure, the LHV of gas derived from pure PW pyrolysis is about 19 MJ/Nm^3, while higher LHV values are observed for pure PS, PVC and HDPE in the order of 23, 26 and 45 MJ/Nm^3 respectively. It is therefore clear that the addition of HDPE contributes the most to the gas calorific value as a result of increased hydrocarbon formation. However, PS and PVC do not have a significant effect, because their hydrogen and carbon content preferentially distribute to the oil product of PS, and the char and HCl gas products of PVC.

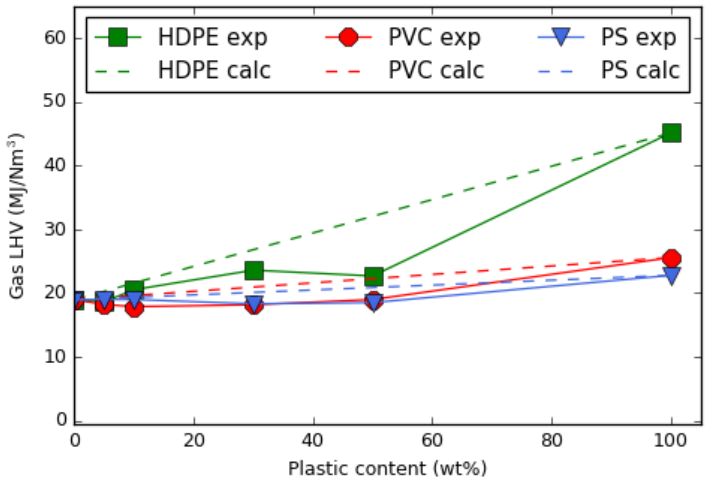

FIGURE 3.4: Influence of plastic type and content on gas heating value

3.2.5 Effect of PVC content on chlorine distribution

Figure 3.5 presents the yield of Cl molecules in the char, gas and oil products as a function of the PVC content in the sample mixture with PW. The Cl content in the char and gas products were analysed using X-ray fluorescence (XRF, PANanalytical) and the Cl content in oil was calculated by difference. The corresponding yields of Cl in the pyrolysis products were then determined on the basis of the initial mass of Cl in the PVC/PW samples. It can be observed in Figure 3.5 that products from pure PW pyrolysis contain insignificant amounts of Cl whereas for pure PVC, 96.98 wt% of Cl is released in the gas phase, thus leaving only 2.98 and 0.04 wt% Cl in the oil and char phase respectively. Compared to the products of pure PVC pyrolysis, the Cl yield decreases in the gas phase by 89.98 wt% when the PVC content is lowered from 100 wt% to 30 wt %, and the corresponding Cl yields in the oil and char products increase by 76.23 and 13.75 wt% respectively. Furthermore, even at a low PVC content of 5 wt%, the Cl distribution in oil is significantly higher than in the char and gas phases. Hence, it is clear that the Cl molecules from co-pyrolysis of PVC/PW are preferentially trapped in the oil product. Our result therefore supports the aforementioned hypothesis presented by Zhou et al. [188] that the Cl molecules are fixed in the oil product.

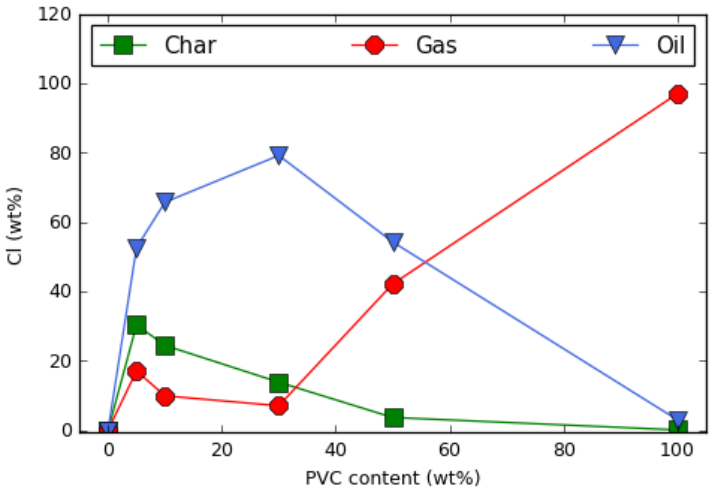

FIGURE 3.5: Influence of PVC content on distribution of chlorine in char, gas and oil products.

A further investigation was made to predict the maximum achievable yields of chloride species in the char, gas and oil products, using thermodynamic equilibrium calculations based on the Gibbs free energy minimization approach (see section 1.3.1). These calculations were performed using FactSage V.6.3. and a database developed by Said et al. [196]. The chosen input data for the calculations are:

- Feedstock: 10 g of 30 wt% PVC/PW, with its composition of organic and inorganic elements displayed in Table 3.7.
- Reactor temperature range : 150 - 750 °C.
- Reactor pressure: 1 atm

Table 3.7: Elementary composition of 30 wt% PVC/PW

	30 wt% PVC/PW
Organic elements (wt %)	
N	0,7
C	46,6
H	5,9
S	0,0
O	29,4
Cl	16,9
Inorganic elements (ppm)	
Al	131
As	52
B	27
Ba	20
Ca	2787
Cd	20
Co	23
Cr	24
Cu	77
Fe	56
Hg	10
K	459
Mg	269
Mn	32
Mo	28
Na	268
Ni	26
P	238
Pb	69
Sb	76
Se	91
Si	133
Sn	190
Sr	21
Ti	26
V	26
Zn	32
Zr	24

Figures 3.6a and 3.6b display, as a function of temperature, the equilibrium mass percentages of inorganic and organic chloride species in relation to the total mass of chloride species respectively. Figure 3.6a shows that above 200 °C, 95 wt% of chloride species is released into the gas phase as HCl. In addition, Cl is mainly trapped in the inorganic solid phase as $CaCl_2$ (4 wt%). It is interesting to observe in Figure 3.6b that organic chloride species are formed in trace amounts, the most abundant of which is dimethyl phosphinic chloride (C_2H_6ClOP), which forms a

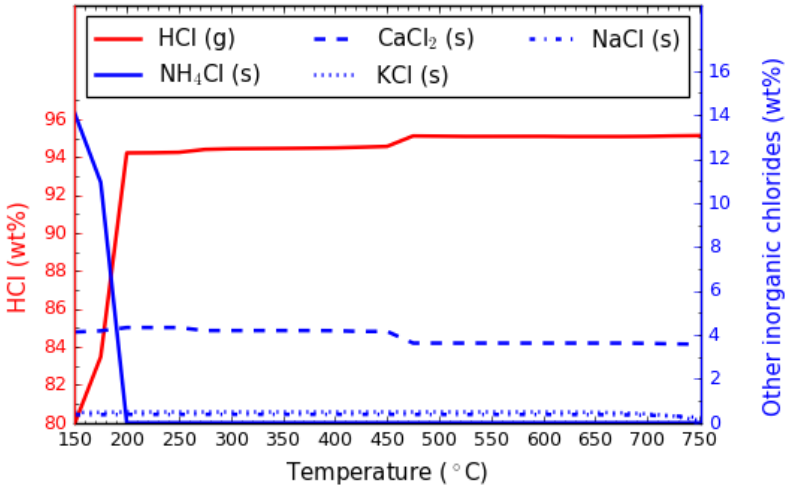

(A) Inorganic chloride species

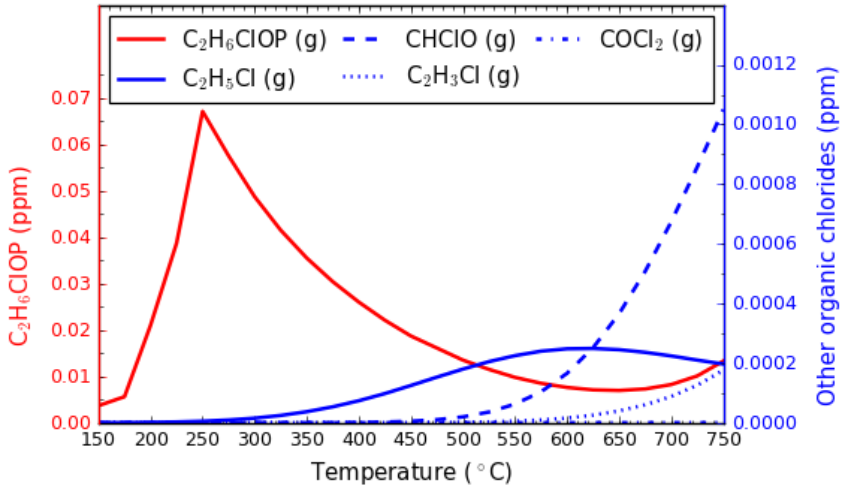

(B) Organic chloride species

FIGURE 3.6: Theoretical chloride species yield from the pyrolysis of 30 wt% PVC/PW between 150 °C and 750 °C, 1 atm

pinkish-white crystal at room temperature.

By comparing the predicted yields of chloride species from the thermodynamic equilibrium calculations, with those obtained experimentally from the pyrolysis of 30 wt % PVC/PW (Figure 3.5), we can first conclude that chlorinated hydrocarbons are only in trace amounts in the condensed oil phase (a mixture of bio-tar, oil, wax and water), which contradicts the proposal by Zhou et al. [188]. Secondly, we propose that the high chlorine content observed in the oil phase is mainly due to HCl gas dissolved in the water fraction of the oil upon condensation. This statement is supported by our observation in Figure 3.5 that HCl yield in the gas phase has a similar but opposite trend to the chloride species yield in the oil phase with respect to the initial PVC content in the sample. The pilot-scale experiments in chapter 4 will highlight this proposal.

Conclusion

Experimental work on the co-pyrolysis of poplar wood (PW) and plastics - HDPE, PS and PVC - has been presented in this chapter in which different synergistic effects of plastic type and content were observed on product yield, gas specie yield and gas heating value.

PVC was found to give the highest char yield with a maximum positive synergy of 8 wt% at 30 wt% PVC content. HDPE and PS showed a slightly positive synergy in char yield.

The addition of HDPE and PS generally increased oil yield and lowered gas yield relative to the pyrolysis of pure PW. However, for oil production, a slightly positive synergy was observed for HDPE contents below 50 wt% whereas a small negative synergy was seen for PS. The reverse effects on gas yields occured for these plastics. Interestingly, the presence of PVC had a significant positive synergy on oil yield with a maximum difference of 11 wt% between the experimental and predicted yields at 50 wt% PVC content. This was linked to a strong negative synergy in gas (mainly HCl) production, where a maximum synergy of 18 wt% was observed at 30 wt% PVC content.

With respect to the influence of plastic type and ratio on gas specie yield, the addition of HDPE significantly increased CH_4 and C_xH_y (x = 2 or 3) yields due to its high hydrogen content, but lowered CO and CO_2 yields as a result of the lower oxygen content in the sample mixture. In addition, negative synergistic effects were observed on the yields of these gas species below 50 wt% HDPE content. For PS, positive synergies occured for H_2, CH_4, CO and CO_2, whereas insignificant interactions were seen for C_xH_y compounds. With regard to PVC, an increase in H_2 yield was observed accompanied by a positive synergistic effect. Furthermore, HCl gas yield was found to decrease by 53.6 wt% when PVC content was decreased from 100 to 30 wt %. A further analysis of the distribution of Cl molecules in the char, gas and oil products using thermodynamic equilibrium calculations, revealed that Cl was largely fixed in the oil phase as dissolved HCl gas, although some chlorine was also trapped in the solid residue in the form of metal chloride salts.

The gas lower heating value (LHV) from HDPE co-pyrolysis with PW rose from 19 MJ/Nm^3 to 23 MJ/Nm^3 when the HDPE content increased to 50 wt%. However, an insignificant effect on gas LHV was observed from the addition of PS and PVC to the sample.

Our work bridges the knowledge gap that exists in literature about the synergistic effect between biomass and HDPE, PVC and PS, on product yield, gas specie yield and gas heating value under operating conditions that favor gas production. Moreover, by comparing the results of our work with literature, we have identified the need for a better understanding of the interactions involving HCl during co-pyrolysis

of biomass and PVC. Chapter 5 will therefore focus on modelling the kinetics of interactions between poplar wood and PVC during co-pyrolysis.

CHAPTER 4

Pilot-scale pyro-gasification of wood waste containing PVC

Introduction

Gas sampling and analysis during biomass/waste gasification are important steps to characterize and control the quality of syngas, as well as to regulate and optimize the gasifier operating parameters. The composition of syngas can be grouped as follows:

- Permanent gases: carbon monoxide (CO), hydrogen (H_2), methane (CH_4), carbon dioxide (CO_2) and light hydrocarbons (C_xH_y).
- Condensable gases: steam and tars (e.g. phenol, polycyclic aromatic compounds (PAHs), etc).
- Pollutants: Inorganic gases such as hydrogen chloride (HCl), ammonia (NH_3), hydrogen sulphide (H_2S), and carbonyl sulphide (COS).

Among the pollutants found in waste-derived syngas, Suez Environnement is particularly interested in monitoring HCl levels. HCl is considered a hazardous air pollutant (HAP) by the European IPPC (Integrated Pollution Prevention and Control) and US EPA (Environmental Protection Agency), and is also known to cause corrosion in the syngas end-use devices.

Hence, this chapter presents two air gasification tests in a pilot-scale downdraft reactor, located at PROVADEMSE platform at INSA-Lyon, as well as a series of analyses conducted at RAPSODEE on the product samples. The first test uses class B wood waste as feed whereas the second test involves wood waste containing 1 wt% PVC (0.57 wt% Cl). The aim of the first test is to analyze the syngas composition from the gasification of wood waste, including the contents of tar, HCl and permanent gas species in syngas.

For the second test, the principal objectives are to study the effect of a higher chlorine content in the feedstock on the syngas composition, and to provide experimental data for validation of the wood waste pyro-gasification model, which will be presented in chapter 6. Hence, in addition to analyzing the syngas composition, global mass, chlorine and energy balances on the gasifier will be presented for the second test, as well as proximate and ultimate analyses of the residual char from the pyro-gasification process.

4.1 Feedstock characteristics

For the first pyro-gasification test, only Class B wood waste, supplied by Suez, was used (Figure 4.1a). The proximate and ultimate analysis data for this wood waste is displayed in Table 4.1, which was determined by averaging the values obtained for samples W1 and W2 in chapter 2. For the second test, the wood waste was mixed with 10 wt% pellets of poplar wood (PW) containing 10 wt% PVC. Thus, the PVC content in the wood waste mixture was approximately 1 wt%, which increased

the chlorine content of the waste mixture to approximately 0.57 wt%. Figure 4.1b gives an image of the pellets which constitute the same PW and PVC that were individually characterised in chapter 2. These pellets were manufactured by RAGT Albi, through a process that involved drying and grinding PW, mixing the wood flour with PVC, and finally compacting and cutting the mixture to produce pellets with a diameter of 6.04 mm, length of 20-25 mm, and a bulk density of 684.45 kg/m^3. The proximate and ultimate analysis of the 10 wt% PVC/PW pellets is displayed in Table 4.1.

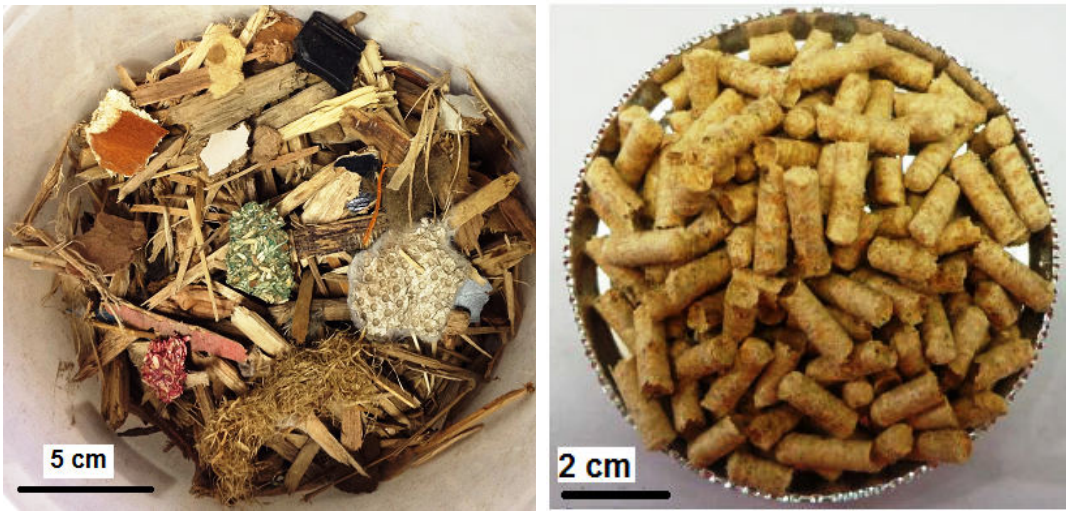

(A) Class B wood waste (B) 10 wt% PVC/PW pellet

FIGURE 4.1: Waste feedstock

4.2 Pilot-scale downdraft reactor

The pilot-scale downdraft gasifier located at PROVADEMSE was designed and patented by COGEBIO under the name Gasclean©. Figure 4.2 shows a schematic view of the pilot plant designed to produce 100 kW_{th} from the gasification of clean biomass or combustible waste. A reactive atmosphere is generated near the entrance to the gasifier by the combustion of propane with air (1) or, as was the case for our tests, by the partial combustion of the feedstock to provide heat for the pyro-gasification reactions. A hopper continuously feeds the gasifer with wood waste and the residual char (ash) is collected at the bottom of the gasifier by means of an automatic ash-removal system (2) and a cyclone (3). Meanwhile, the syngas produced is first cooled (4) and then pumped (6) to the boiler (8) where it is combusted in an air stream (5). Finally, the exhaust gas from the boiler is released to the atmosphere via a chimney (7).

An image of the gasifier is shown in Figure 4.3 and the steady-state operating conditions for the two tests are displayed in Table 4.2. During the tests, the reactor was fed with wood waste at a rate of 11-12 kg/h. Air was injected at three different

TABLE 4.1: Proximate and Ultimate analysis of class B wood waste and 10 wt% PVC/PW pellets

	Wood waste	10 wt% PVC/PW pellets
Proximate analysis (wt%, db)		
Moisture	12.10	6.04
Ash	2.10	0.75
Volatiles	81.30	83.50
Fixed carbon	4.50	9.71
LHV (MJ/kg d)	16.50	18.21
Ultimate analysis (wt%, db)		
C	47.60	46.27
H	5.40	5.75
O	45.45	42.34
N	1.55	0.00
S	0.00	0.05
Cl	0.03	5.65

zones of the gasifier: 1) At the reactor inlet (secondary air, Air_2) to partially oxidize the pyrolysis products in order to supply heat to the endothermic drying and pyrolysis processes, 2) At the side of the reactor (primary air, Air_1) to gasify the pyrolysis char and volatiles, and 3) At the reactor bottom (tertiary air, Air_3) to partially oxidize uncracked tars and remaining char. Both wood waste and air were fed to the reactor at room temperature, and as a result of the partial oxidation reactions, the reactor temperature increased from 83 °C near the top, to 630-660 °C near the bottom. The syngas produced had a flowrate of 30 Nm^3/h and an exit temperature of 530-580 °C.

TABLE 4.2: Steady-state operating conditions for the first pyro-gasification test with only wood waste feed, and for the second test with wood waste/PVC feed.

Parameters	1st test	2nd test
Wood waste flowrate (kg/h)	12	11
Air flowrates (Nm^3/h)		
Air_1	18.5	17.7
Air_2	1.2	1.1
Air_3	3.0	2.7
Reactor temperature (°C)		
T_{R1}	83.2	82.8
T_{R2}	661.6	629.2
Syngas flowrate (Nm^3/h)	32.0	28.9
Syngas temperature (°C)	580.0	529.0

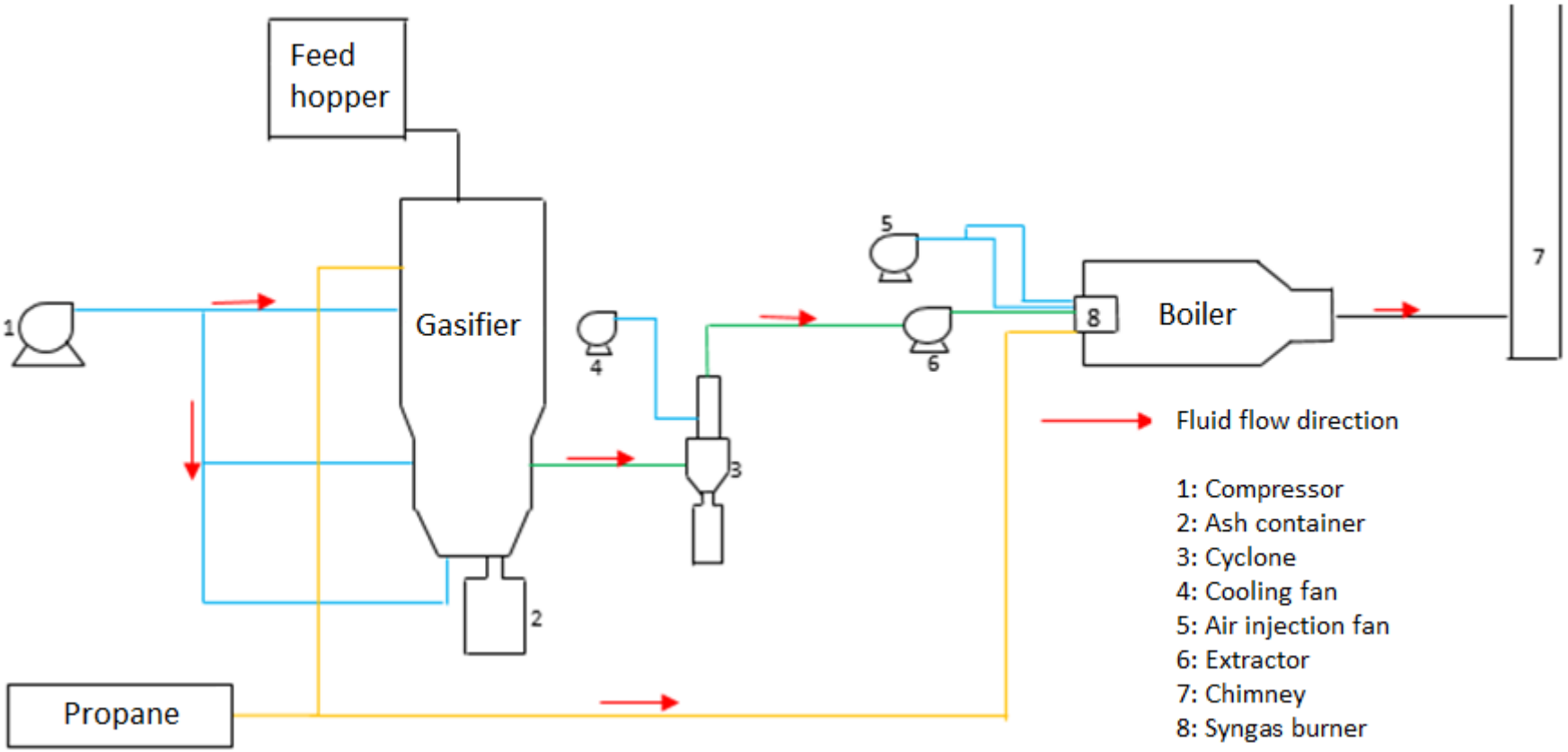

FIGURE 4.2: Schematic view of pilot gasification plant

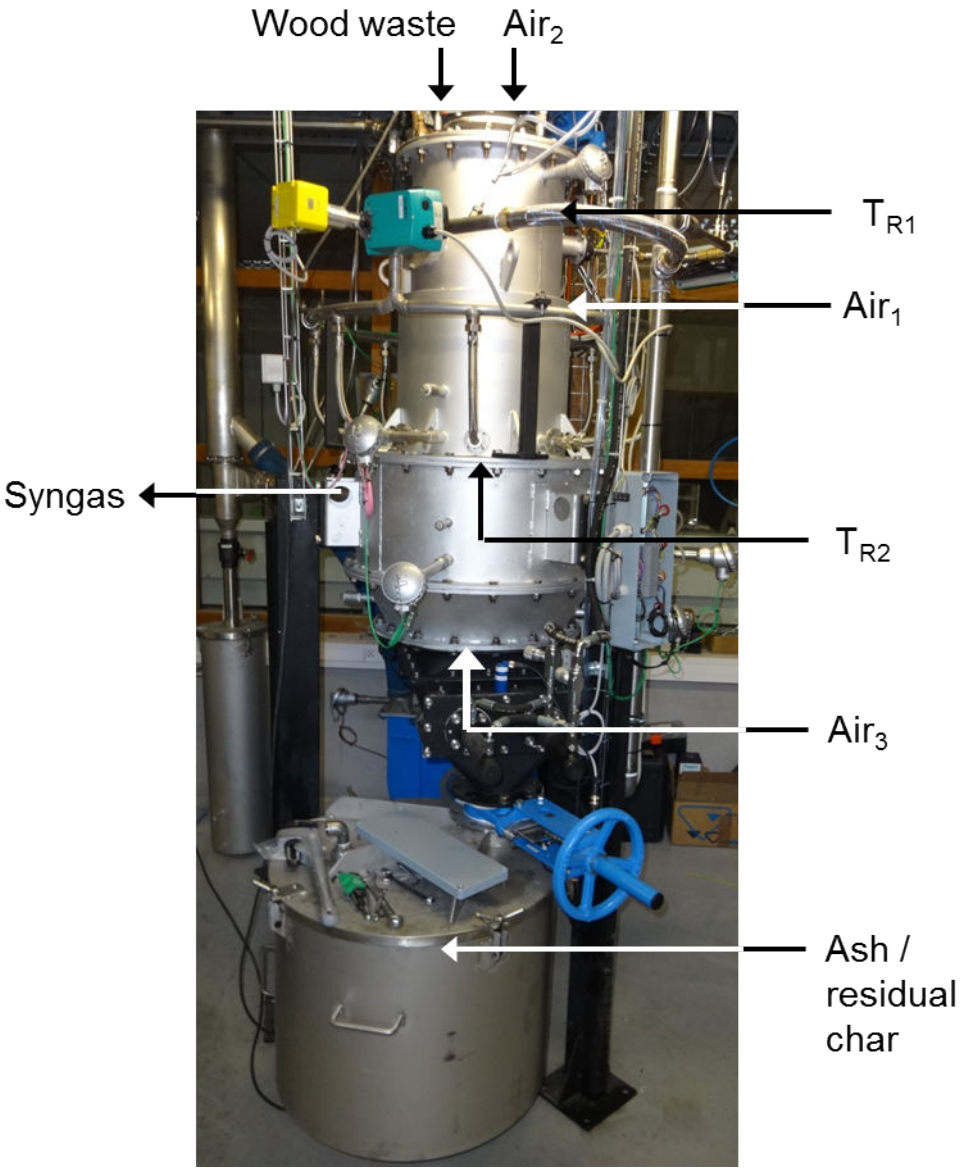

FIGURE 4.3: Pilot-scale downdraft gasifier

4.3 Syngas sampling and analysis

4.3.1 Gas sampling equipment

The equipment used for syngas sampling follows the CEN BT/TF 143 technical specification [197], and consists of a heated probe and particle filter, a tar condenser, and equipment for pressure and flowrate adjustment and measurement. This equipment is shown in Figure 4.4. The temperature of the heating probe, filter and tubes was kept at about 400 °C in order to prevent tar condensation and thermal decomposition.

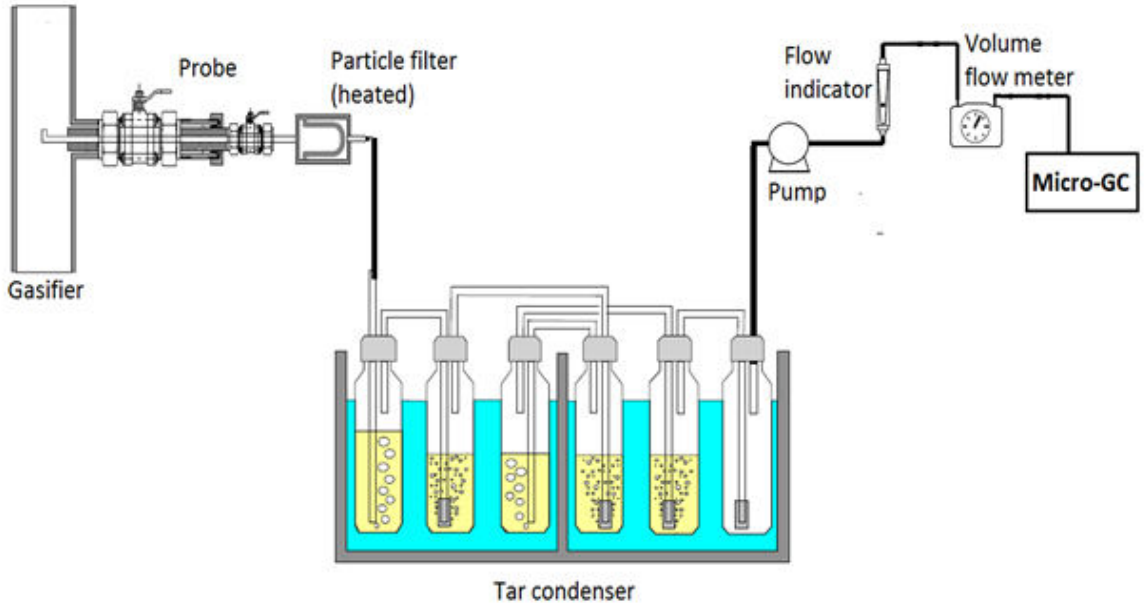

FIGURE 4.4: Gas sampling system according to the technical specification, CEN BT/TF 143 [197]

4.3.2 Tar sampling in syngas

The method used to sample tar in syngas was strictly based on the CEN BT/TF 143 technical specification [197]. As illustrated in Figure 4.4, tar collection was performed in a condenser containing six 250 mL impinger bottles, the first of which served as a condenser for water vapour in syngas. The first five bottles contained approximately 50 mL isopropanol solvent for tar absorption whereas the last bottle was kept empty. The temperature of the first three impingers was maintained at 35 °C and the last three bottles were cooled to - 20°C. After gas sampling, the solutions were kept in dark in storage bottles, for analysis using GC-MSMS.

4.3.3 HCl sampling in syngas

To sample HCl in syngas, the gas leaving the particle filter was bubbled through two impinger bottles containing an aqueous solution of KOH at a controlled flowrate for a specified time. The solution was then analyzed using ion chromatography to determine the chlorine content.

4.3.4 Analytical methods

Several analytical instruments were used to characterize the composition of syngas and residual char (ash):

- Micro gas chromatograph (micro-GC - Agilent) was used to analyse permanent gases found in syngas including H_2, CH_4, CO, CO_2, N_2, O_2, and light hydrocarbons (C_xH_y).
- Gas chromatography-mass spectrometry (GC-MSMS – TQ8030 Schimadzu) was employed to identify the organic compounds in tar.

- Ion Chromatography System (ICS - 3000 Dionex) enabled quantification of HCl concentration in the aqueous phase.
- Karl-Fischer titrator (KF- Mettler Toledo V30) was used to measure the concentration of condensed steam in syngas that is absorbed in the isopropanol solution. The titrant used in this method was a mixture of iodine and sulphur dioxide.
- Analysis of the organic and chlorine content in the residual char samples was performed using a CHNS analyzer (Flash 2000, ThermoFisher Scietific) and X-ray fluorescence (XRF - PANalytical) respectively, and its mineral composition was determined by an inductively coupled plasma with an atomic emissions spectrometer (ICP - AES, HORIBA Jobin-Yvon Ultima 2).

4.4 Results of wood waste pyro-gasification

4.4.1 Permanent gas analysis

The composition of the permanent gas species identified in syngas is displayed in Figure 4.5. It can be observed in this figure that the major gas species are H_2, CO, CO_2 and N_2, and that relatively small amounts of CH_4 and light hydrocarbons are produced.

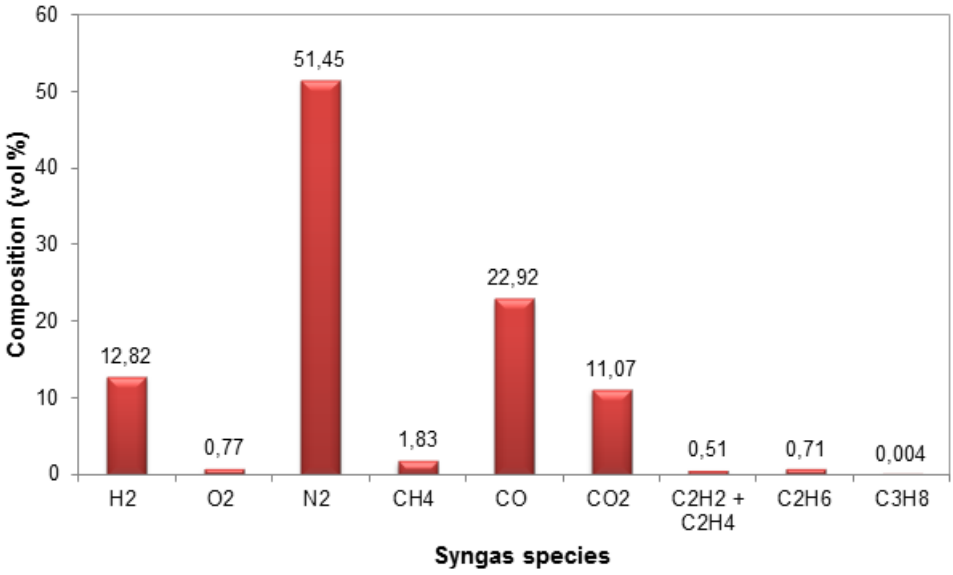

FIGURE 4.5: Composition of permanent species in syngas from wood waste gasification

4.4.2 Tar analysis

The family of organic compounds identified in the tar samples using GC-MSMS are displayed in Table 4.3 and a more detailed list of the tar species detected are shown in Table A.1. In total, a tar content of 1162.1 mg per Nm^3 syngas was measured,

which is within the typical tar composition range (500 - 2000 mg/Nm^3) of wood fuelled downdraft gasifiers [134]. It is clear that aromatic compounds, particularly Toluene, make up the majority of the tar components, followed by polycyclic aromatic hydrocarbons (PAHs) and nitrogen containing aromatics. It is also important to note that no organic chloride compounds were detected in the tar samples.

TABLE 4.3: Tar compounds analyzed in syngas from wood waste gasification

Group name	Concentration (mg/Nm^3)
Acids	33.7
Phenols	31.6
Furans	6.7
Aromatic compounds	823.9
PAHs	158.3
Alicyclic compounds	1.6
Nitrogen containing aromatics	102.9
Ketones	3.2
Mixed oxygenates	8.6

4.4.3 Chlorine analysis

Figure 4.6 presents a flow diagram that shows the chlorine content in the waste feedstock and products of the gasification system. The syngas and exhaust gas produced can be seen to contain trace amounts of chlorine, where the concentration of Cl in the exhaust gas is well below the EU emissions limit of 10 ppm. We can also see that the chlorine is concentrated in the residue char.

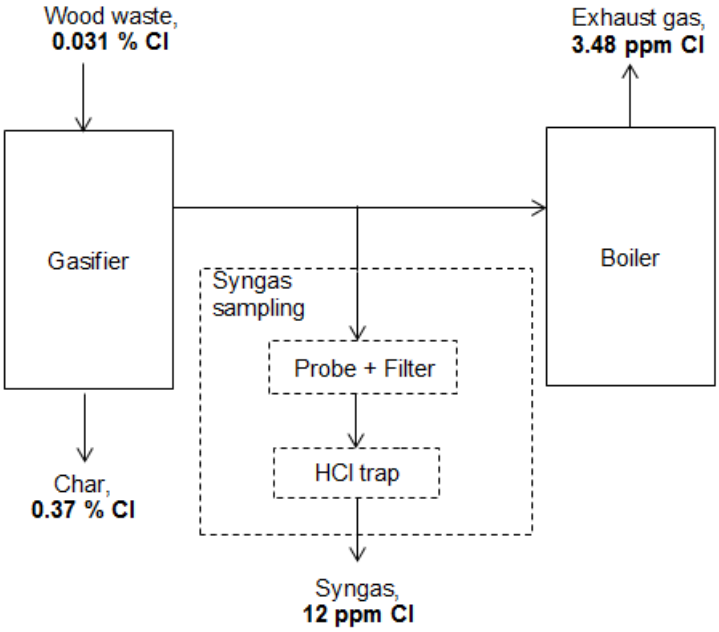

FIGURE 4.6: Schematic of chlorine content in wood waste and gasification products

4.5 Results of wood waste/PVC pyro-gasification

4.5.1 Permanent gas analysis

Figure 4.7 shows the composition of permanent gas species in the syngas produced from wood waste/PVC gasification. By comparing with the results obtained from the gasification of only wood waste in Figure 4.5, we can see that the gas composition in both tests are similar, although the concentration of CO decreased by 6 vol% and CO_2 slightly increased by 2 vol% for the second test with wood waste/PVC as feedstock. This could be linked to the slightly higher air inlet flowrate in the first test which may have increased the oxidation of char to produce CO_2 (Eq 6.53), which in turn reacted with char to produce more CO via the Boudouard reaction (Eq 4.2).

$$C + O_2 \rightarrow CO_2 \tag{4.1}$$

$$C + CO_2 \rightarrow 2CO \tag{4.2}$$

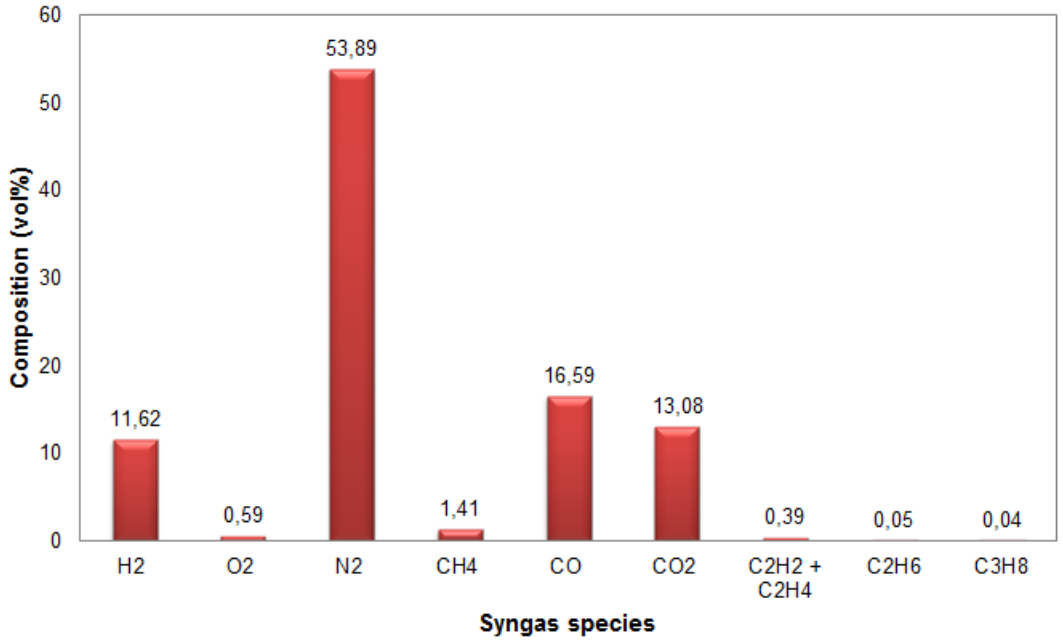

FIGURE 4.7: Composition of permanent gas in syngas from wood waste/PVC gasification

4.5.2 Steam and HCl analysis

The steam content in syngas was found to be 13.92 vol% using the titration method described in section 4.3.4. HCl concentration in syngas was 40.2 ppm or 65.5 mg/Nm^3, which is 5.5 times higher than the corresponding value for wood waste pyro-gasification, due to the presence of 1 wt% PVC.

4.5.3 Tar analysis

In Table 4.4, the measured concentration of groups of tar compounds are displayed and a list of the individual tar species is presented in Table A.2. The total tar content measured was 2471.6 mg/Nm^3 which is twice the concentration of tar measured in syngas from the gasification of wood waste without PVC addition. Furthermore, by comparing Tables 4.3 and 4.4, we can see that the presence of 1 wt% PVC in wood waste increases the concentration of aromatic compounds by 42.6 %, and also significantly raises the content of PAHs and Furans by a factor of 4.4 and 21.5 respectively. The observed increase in PAHs formation is in accordance with the experimental results of Çepelioğullar et al. [179, 191] and Zhou et al.[188] obtained from the co-pyrolysis of PVC and biomass. In addition, the chlorinated organic compound, 2-Chloro-4-aminopyrimidine, is detected in tar, although its concentration is much lower than those of the other family of tar compounds. This experimental data supports our proposed theory in chapter 3 - section 3.2.5 that a high chlorine content observed in the condensed oil phase is mainly due to the presence of dissolved HCl gas, as only trace amounts of chlorinated hydrocarbons are formed in the oil phase.

Table 4.4: Tar compounds analyzed in syngas from wood/PVC gasification

Group name	Concentration (mg/Nm^3)
Chlorinated compounds	11.5
Acids	28.8
Phenols	320.9
Furans	143.2
Aromatic compounds	1175.22
PAHs	690.92
Nitrogen containing aromatics	101.1

4.5.4 Residual char characteristics

Proximate and ultimate analyses were conducted on the residual char (ash) from the pyro-gasification of wood waste/PVC and the results are shown in Table 4.5. We can see from the proximate analysis that the residual char has a relatively high fixed carbon and LHV which indicates a significant loss of potential energy in the gasification plant. The char also has a relatively high ash content and low moisture and volatile content which is typical of unburnt char from gasification processes.

From the ultimate analysis, we can observe a chlorine concentration of 6 wt% in the char which represents an increase by a factor of 16 compared to the chlorine content in char from wood waste gasification in the absence of PVC (Fig. 4.6).

The composition of inorganic elements in the residual ash was also analyzed and the results are shown in Figure 4.8. We can see that Ca, Si and Ti are the

TABLE 4.5: Proximate and Ultimate analysis of residual char from wood/PVC gasification

	Residual char
Proximate analysis (wt%, db)	
Moisture	1.71
Ash	12.48
Volatiles	7.06
Fixed carbon	78.75
LHV (MJ/kg, db)	30.71
Ultimate analysis (wt%, db)	
C	46.06
H	0.93
O	46.70
N	0.02
S	0.00
Cl	6.29

most abundant elements in the residual ash with concentrations above 20000 mg/kg. These are followed by Al, Cu, Fe, K, Mg, Na and P, which have concentrations between 5000 and 15000 mg/kg. These relatively high concentration of ash minerals in the solid residue may be due to the presence of metal additives for preserving the wood.

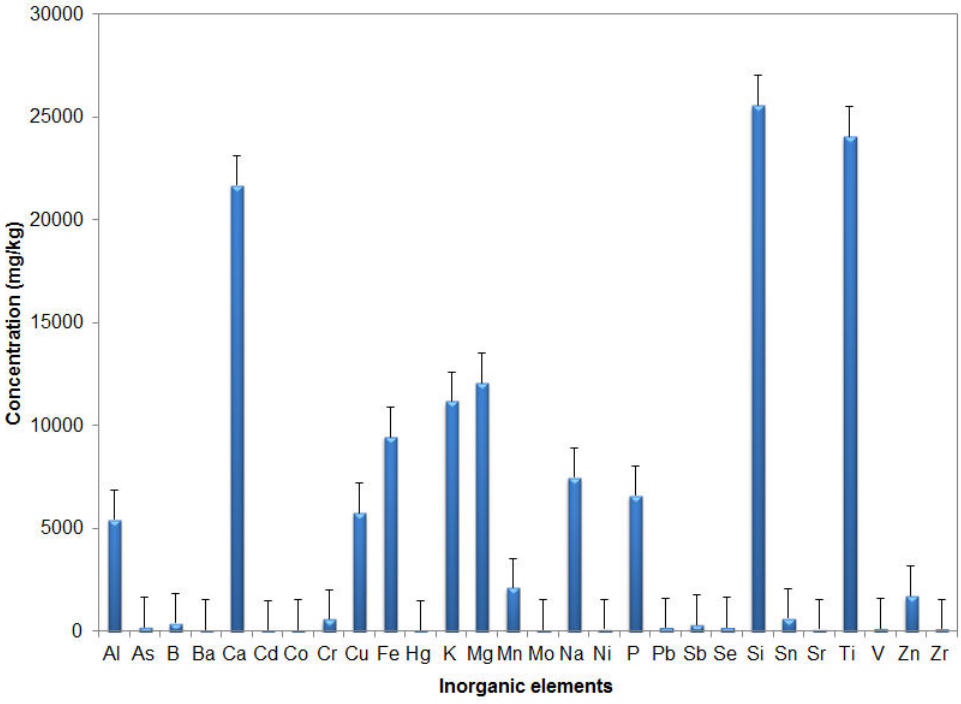

FIGURE 4.8: Mineral composition in residual char from wood/PVC gasification

4.5.5 Global mass balance

Based on the results of analyses conducted, a mass balance on the gasfier was conducted using the following inlet and outlet streams:

Inlet:

- Wood waste;
- N_2 and O_2 in air.

Outlet:

- Residual char
- Fine particles
- Condensable gases: Tar, steam (H_2O) and HCl.
- Non-condensable gases: H_2, O_2, N_2, CH_4, CO, CO_2, C_2H_2, C_2H_4, C_2H_6 and C_3H_8.

In Figure 4.9, the mass balance shows a difference of 1.42 % between the inlet and outlet flowrates of the streams. This may be mainly due to an error in nitrogen analysis, considering the inert property of this gas specie under the experimental conditions used. However, this mass balance result is very good and indicates that the syngas sampling methods for tar, steam and permanent gases are reliable.

4.5.6 Chlorine mass balance

A mass balance was also performed on chlorine at the gasifier entrance and exit. The result, shown in Figure 4.10, reveals a difference between the inlet and outlet flow of chlorine of 34 wt%. This large percentage of Cl that is unaccounted for, could be the result of several factors including:

- Lack of Cl content analysis of the particles trapped in the filter of the syngas sampling line.
- Dissolution of HCl in condensed steam and tars in the non-heated parts of the sampling tubes, which was not washed, collected and analyzed.
- Adsorption of HCl on the surface of the metal and plastic tubes in the sampling line.

In literature, significant mass fractions of Cl missing in the Cl mass balance closure when the batch sampling method was used have been reported, such as in the work of Kuramochi et al. [193] who observed up to 64.4 wt% of Cl content not accounted for after co-pyrolysis of wood and PVC. Thus, it is clear that the batch method for sampling and analyzing chlorine content in syngas should be either improved or an alternative method should be found. Over the course of this PhD, two Enveloppes Soleau have been deposited on new methods for sampling HCl in syngas in order to perform online measurements of HCl concentration. A patent on one of these methods is also currently underway.

4.5.7 Global energy balance

The overall energy balance on the autothermal gasifier was performed by considering the following:

Energy input: Enthalpy of (dry wood waste + moisture + air) at reference temperature (25 °C) + heating value (LHV) of wood waste + heating value of wood waste.

Energy output: Enthalpy of (syngas + char + fines) at outlet temperature (529 °C) + heating value (LHV) of (syngas + char and fines) + heat loss from the reactor.

The heat loss from the reactor was estimated to be 0.81 kW based on measurements of the average external wall temperature of the reactor (60 °C) and the ambient temperature (25 °C), and by taking 10 $W/m^2/K$ as the heat transfer coefficient value.

Figure 4.11 presents the result of the energy balance on the gasifier, which shows a difference of 1.45 % between the energy inputs and outputs. This balance is considered highly satisfactory.

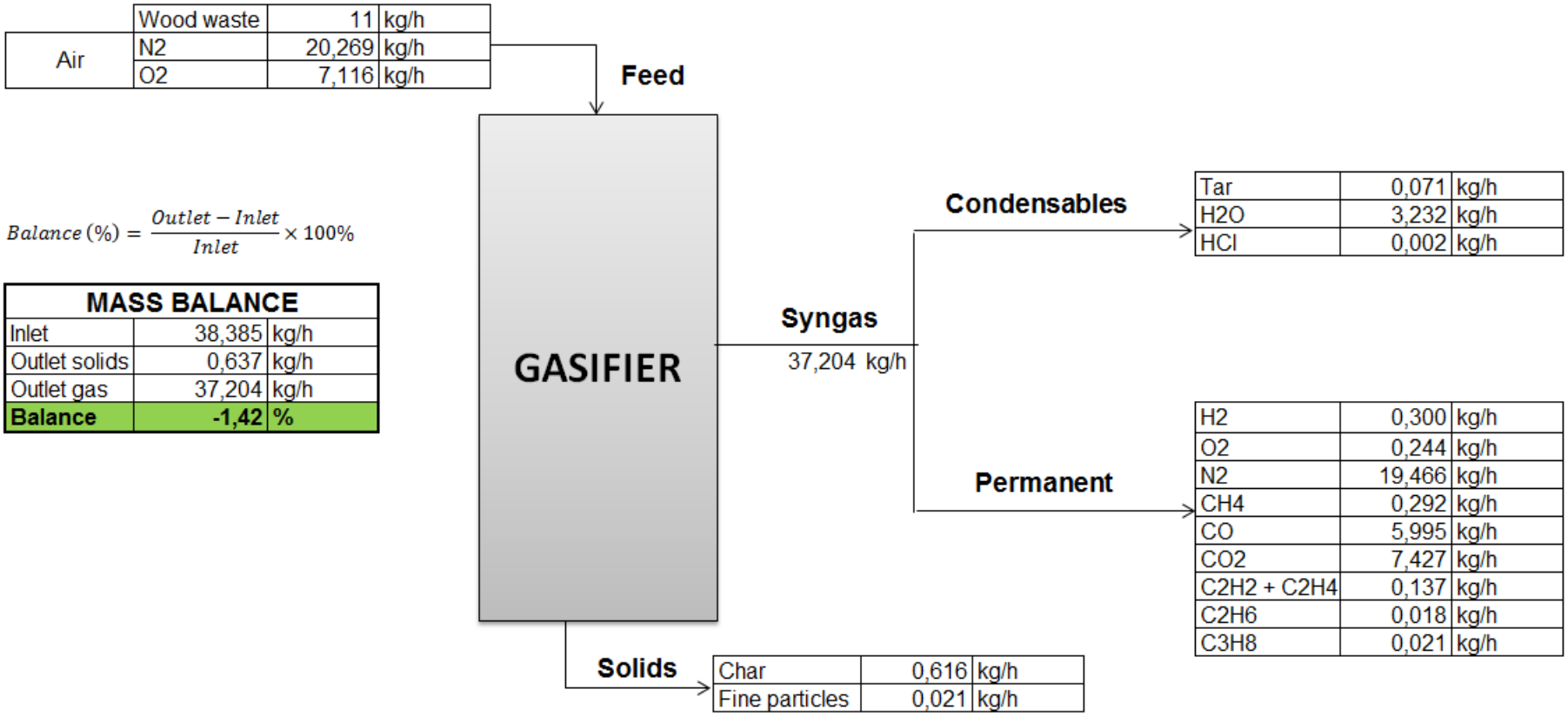

FIGURE 4.9: Global mass balance on gasifier for wood waste/PVC gasification

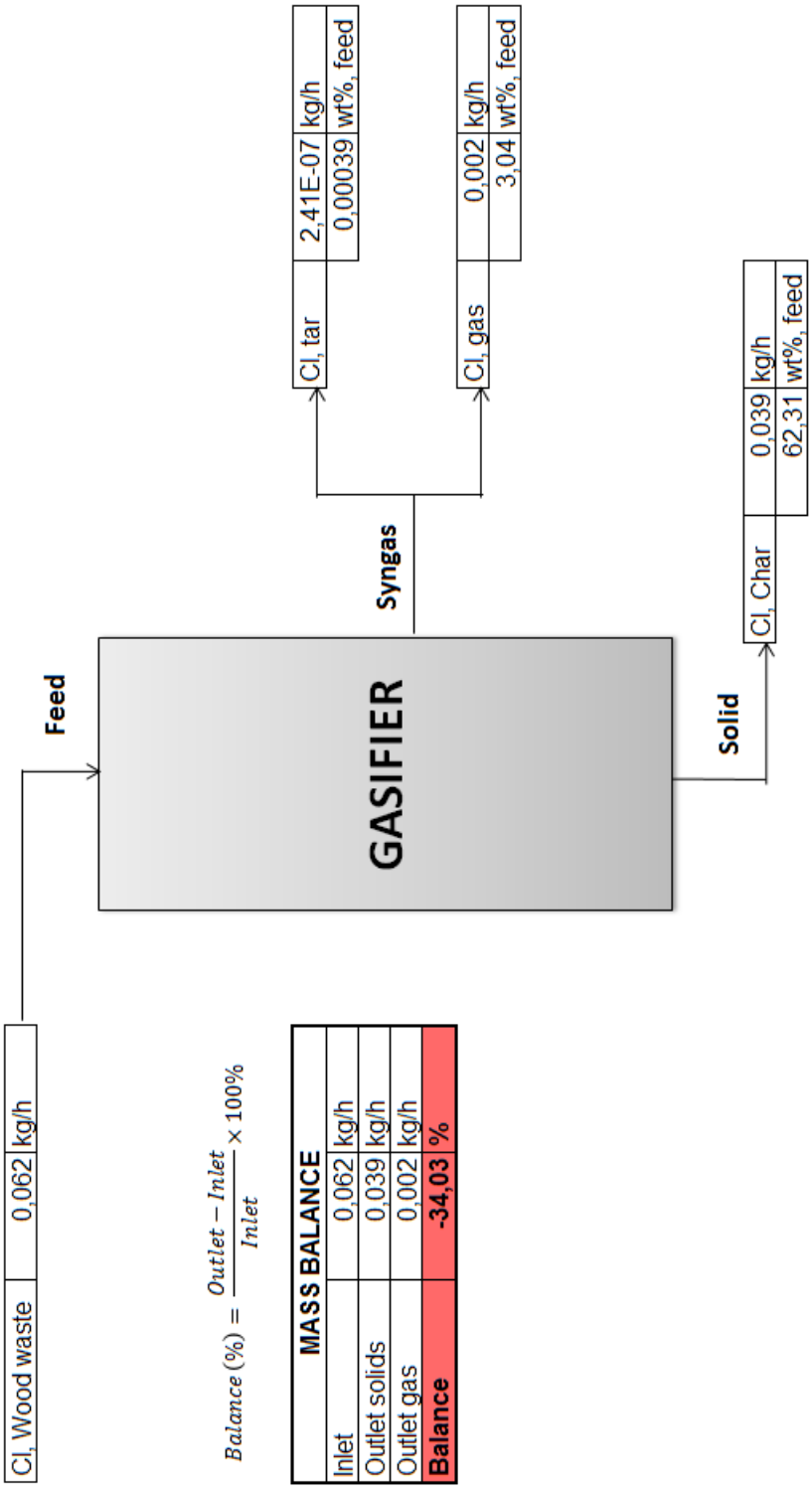

FIGURE 4.10: Chlorine mass balance from wood waste/PVC gasification

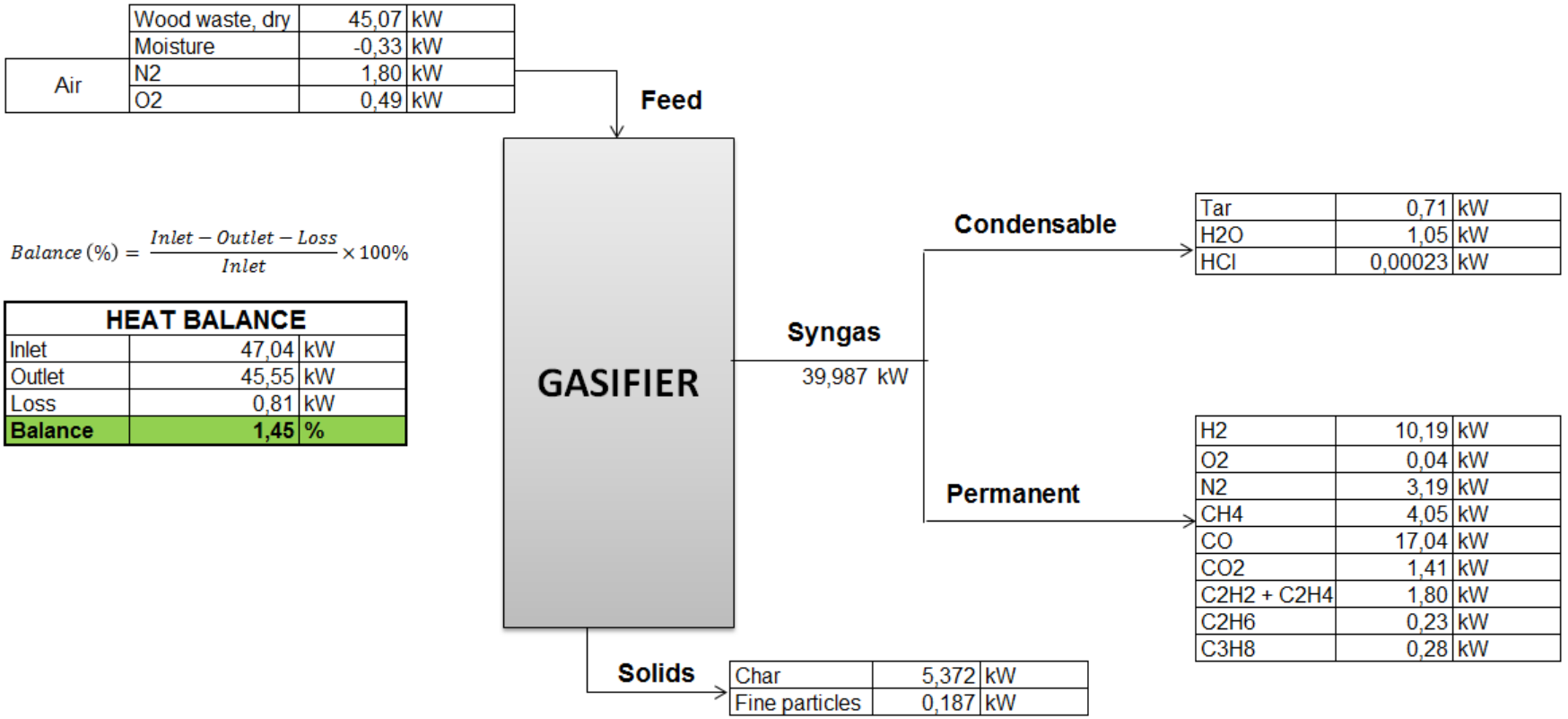

FIGURE 4.11: Overall energy balance from wood waste/PVC gasification

Conclusion

In this chapter, two pyro-gasification tests have been performed in a pilot-scale downdraft reactor. The first test involved Class B wood waste as feedstock, whereas in the second test, wood waste containing 1 wt% PVC was used. The results of the first test revealed that the main permanent species in syngas were H_2, N_2, CO and CO_2, with lesser concentrations of CH_4 and light hydrocarbons. Similar results were obtained for the second test, although the concentration of CO decreased by roughly 6 vol% due to the lower air inlet flowrate.

The tar content and composition in syngas were analysed in both tests and it was seen that the presence of 1 wt% PVC in wood waste doubled the concentration of tar in syngas, increased the concentration of aromatic compounds by 42.6 %, and also raised the content of PAHs and Furans by a factor of 4.4 and 21.5 respectively.

HCl was 5.5 times more concentrated in syngas, and chlorine in the residual char was 16 times higher in the second test than in the first, due to the presence of 1 wt% PVC (0.57 wt% Cl) in the feedstock. However, mass balance closure on chlorine was not achieved in the second test, whereas the opposite was true for the overall mass and energy balances.

Despite the lack of closure for Cl mass balance, mainly due to loss of HCl in the syngas sampling line, the overall mass balance results of the second test with wood waste/PVC feedstock will be used to validate the CFD model developed during this PhD, which will be presented in chapter 6.

CHAPTER 5

Focus on pyrolysis of wood-PVC pellets: Kinetic modelling

Introduction

This chapter aims at further investigating the interactions observed during co-pyrolysis of PVC and poplar wood (PW) in Chapter 3, by performing thermogravimetric analysis (TGA) and kinetic modelling. For more detailed description of the various kinetic analysis methods mentioned in this introductory section, refer to Chapter 1 - Section 1.3.

In the last decade, several authors have studied the co-pyrolysis of PVC and different biomass/waste using TGA, and all have observed strong interactions in terms of lower pyrolysis temperatures of biomass/waste in the presence of PVC [180, 192, 194, 198–202]. However, very few kinetic analysis of these interactions have been found in literature. A complete kinetic study of such a co-pyrolysis process requires the determination of the kinetic triplet: namely, the activation energy E_α, the pre-exponential factor A, and the kinetic model $f(\alpha)$ [114].

Abdoulkas et al. [200] have studied the reactivity of co-pyrolysed olive residue and PVC using the isoconversional Friedman method to determine E_α. The entire pyrolysis process was considered a single step reaction which led to a significant variation of E_α with conversion α. According to the Kinetics Committee of the International Confederation for Thermal Analysis and Calorimetry (ICTAC) [111], a significant variation of E_α with α indicates that the pyrolysis process is kinetically complex and thus, it is inappropriate to use a single-step rate equation to describe the kinetics of this process throughout the whole range of conversions and temperatures.

More recent kinetic analyses by Han et al. [198] and Cepeliogullar et al. [199] suffer from this flaw of a single-step co-pyrolysis model, and thus, the activation energy values they provide are highly questionable. Furthermore, these authors have assumed that the co-pyrolysis mechanism is first-order ($f(\alpha) = 1 - \alpha$) without reporting arguments that support this assumption. Recent works have proven that the pyrolysis of polymers does not necessarily take place through first - or n - order kinetics and that other mechanisms such as diffusion or random scission can control the decomposition reaction [123, 124, 203]. In such cases, this often yields higher A and E_α values than the true values and particularly give A values that are too large to be physically reasonable [203].

The objective of this work therefore, is to develop a multi-step apparent kinetic model for the co-pyrolysis of PVC and PW pellets and to identify the mechanisms that govern their interactions. This work combines the use of Fraser-Suzuki deconvolution and isoconversional Kissinger-Akahira-Sunose (KAS) methods to determine the apparent E_α for each pseudo-component in the PVC/PW mixture, as well as the master-plot procedure to determine the reaction mechanisms $f(\alpha)$, and eventually A.

5.1 Experimental methods

5.1.1 Preparation of poplar wood-PVC pellets

The poplar wood (PW) sample used in this study was obtained from Special Diets Services (SDS). It was first dried at 105 °C for 24 hours and then ground to into fine powder with a particle size < 100 μm. The PVC samples were provided by Analytic Lab with a particle size of approximately 130 μm. To prepare 0, 1, 5, 10 and 100 wt% PVC/PW pellets, the samples were first weighed and then mixed using pestle and mortar. The mixture was then pressed manually at 10 bar to produce 0.5 g pellets of < 3 mm thickness. Table 5.1 shows the proximate and ultimate analysis of the PW and PVC samples. The analytical methods used are detailed in Chapter 2.

Table 5.1: Proximate and Ultimate analysis of poplar wood (PW) and PVC

	PW	PVC
Proximate analysis (wt%, as-received basis)		
Moisture	8.4	0.0
Ash	2.0	0.0
Volatiles	85.1	95.8
Fixed carbon	4.5	4.2
Ultimate analysis (wt%, dry ash-free basis)		
C	49.9	38.7
H	6.4	4.8
O	42.7	0.0
N	1.0	0.0
S	0.00	0.00
Cl	0.01	56.5

5.1.2 Thermogravimetric apparatus and procedure

Thermogravimetric analysis of the samples was performed under atmospheric pressure using a TGA/DTA analyser (STA 409 PC, Netzsch). Samples of 0.5 g were placed in platinum crucibles and heated from 30 °C to 800 °C at rates of 5, 10 and 20 °C/min under nitrogen atmosphere (100 mL/min). Each heating rate run was repeated twice and the mass loss data were found to be repeatable (error < 1 %).

5.2 Experimental results

5.2.1 Pyrolysis of pure poplar wood

Figure 5.1(A) shows the TG/DTG curves for the pyrolysis of 100 wt% poplar wood (PW) at heating rates of 5, 10 and 20 °C/min. These curves show the typical

behaviour of wood pyrolysis : a shoulder appears at 190-290 °C which corresponds to hemicellulose decomposition; a sharp peak is observed at 290-360 °C owing to cellulose decomposition; and the broad, low magnitude tailing at 360-500 °C can be linked to lignin degradation. These results are similar to those reported in literature for other wood types [87, 116].

Hemicellulose, $(C_5H_8O_4)_n$, decomposes at a lower temperature than cellulose, $(C_6H_{10}O_5)_n$, because it is a branched-chain polymer composed of several monosaccharides, including glucose, xylose, mannose, galactose and arabinose [204]. Thus hemicellulose has a weak amorphous structure which decomposes at a lower and broader temperature range. However, cellulose has a long linear chain, principally made-up of D-glucose units [36]. Its crystalline, strong structure and high homogeneity, make it thermally resistant and decompose within a short temperature interval. Furthermore, lignin degrades slowly over a large range of temperature because it is a complex and highly cross-linked polymer consisting of three phenylpropane structures: p-hydroxylphenyl, syringyl, and guaiacyl units [205]. Lignin is the 'glue' that holds adjacent cellulosic fibers together and thus, it is the most difficult wood component to decompose [36].

5.2.2 Pyrolysis of pure PVC

The TG/DTG curves for the pyrolysis of PVC are presented in Figure 5.1(B). Two main degradation steps can be observed. The first step, which occurs at 200-350 °C, is the dehydrochlorination of PVC to form HCl and polyene [206]. Moreover in this phase, at temperatures of roughly 300-350 °C, the polyene molecules produced subsequently undergo condensation and de-alkylation reactions to form benzene and aromatic compounds. After dehydrochlorination, the second step in PVC pyrolysis (350-550 °C) is the cyclization and cross-linking of polyene molecules to form polyaromatic hydrocarbons (PAH) and char residues [207].

The effect of heating rate can be observed in both Figures 5.1(A) and 5.1(B). As the heating rate increases, the TG/DTG curves shift towards higher temperatures. This is due to heat transfer limitations resulting from the temperature difference between the sample and the furnace. In such instances, the thermal lag is more pronounced at higher heating rates, which in turn slows down the decomposition rate. [116, 120].

5.2.3 Co-pyrolysis of PVC and poplar wood

Figure 5.2 presents the TG/DTG curves for the pyrolysis of 1, 5 and 10 wt% PVC/PW pellet samples at heating rates of 5, 10 and 20 °C/min. By comparing these TG/DTG curves to those of 100 wt% PW and PVC in Figure 5.1, the following observations can be made :

- The presence of PVC shifts the DTG peaks of hemicellulose and cellulose decomposition in wood towards lower temperatures. For example, at a heating rate of 5 °C/min, cellulose in pure wood degrades with a DTG peak at approximately

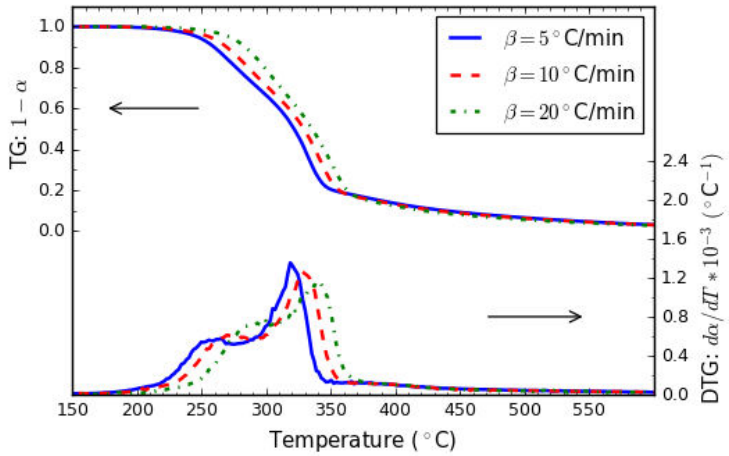

(A) 100 % PW

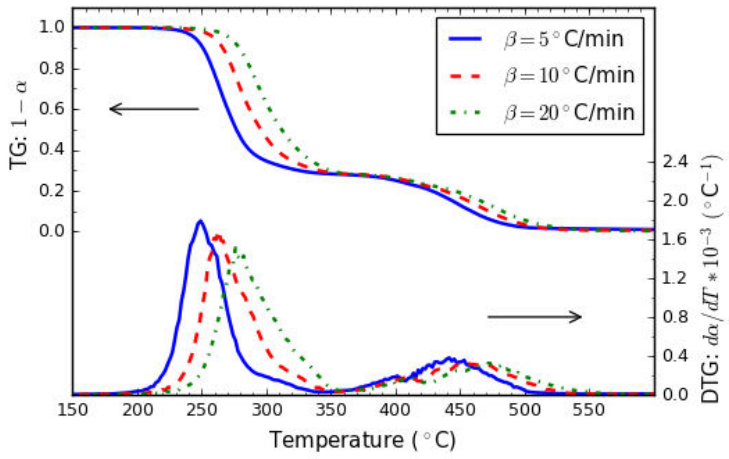

(B) 100 % PVC

FIGURE 5.1: TG and DTG curves of pure poplar wood (PW) and PVC pellets at heating rates of 5, 10 and 20 °C/min

332 °C. However, in the presence of 1, 5, and 10 wt% PVC, this temperature is lowered by 2, 55, and 60 °C respectively. These lower temperatures thus approach the DTG peak temperature of PVC dehydrochlorination (266 °C).

- With respect to pure wood, the addition of PVC significantly increases the height of the DTG peaks at 200-300 °C, which relates to cellulosic fibre degradation. For instance, at a heating rate of 5 °C/min, the corresponding DTG peak heights for 1, 5, and 10 wt% PVC increase by a factor of 2.10, 3.77 and 3.80 respectively compared to pure wood pyrolysis. Furthermore, in the case of 5 wt% and 10 wt% PVC/PW samples, the DTG peak heights increase by a factor of 1.19 and 1.20 respectively compared to pure PVC pyrolysis.

- At temperatures between 350 °C and 500 °C, the conversion of 10 wt% PVC/PW is only 4 % more than that of 100 wt% PW. Hence, lignin in PW can be considered largely unaffected by the cyclization/cross-linking step in PVC pyrolysis.

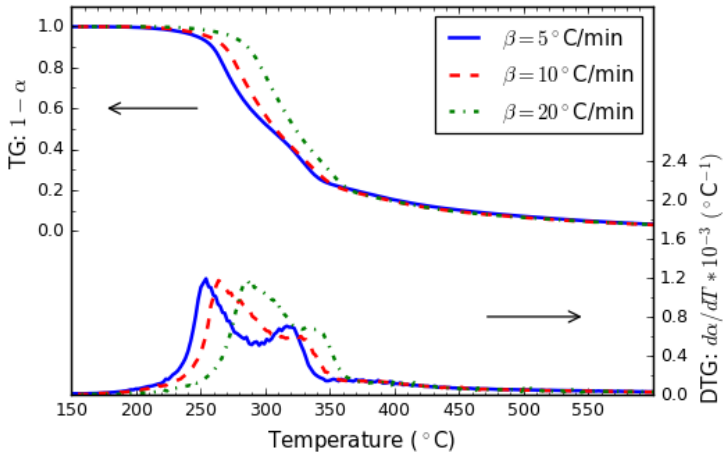

(A) 1 % PVC/PW

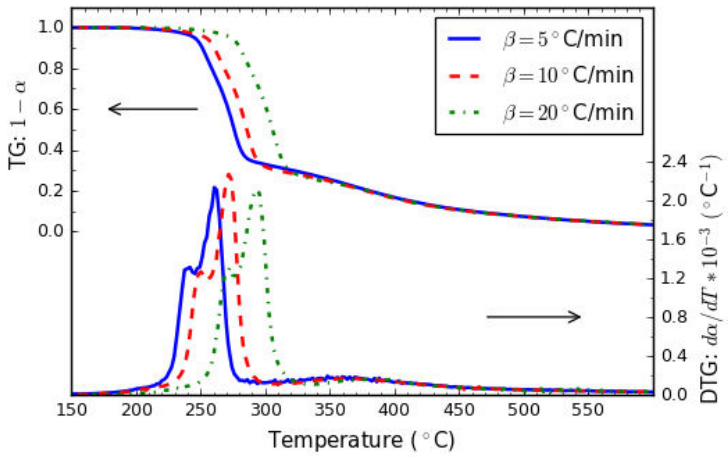

(B) 5 % PVC/PW

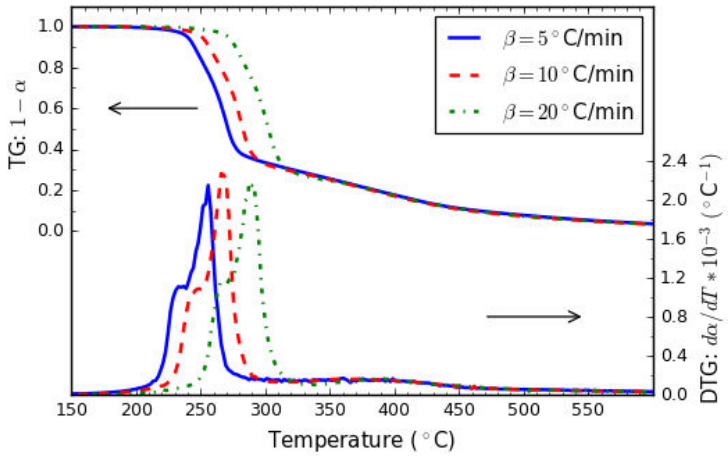

(C) 10 % PVC/PW

FIGURE 5.2: TG and DTG curves of pellets of 1, 5 and 10% PVC/poplar wood (PW) pellets at heating rates of 5, 10 and 20 °C/min

The above observations are indicative of the strong interaction between the cellulosic components of PW and HCl released during PVC dehydrochlorination. In literature, similar observations of such interactions have been made with other biomass types including straw, olive residue and municipal solid waste (MSW) [192, 202, 208].

Another point worth noting is the very small difference in the pyrolysis behaviour of 5 and 10 wt% PVC/PW. This implies that most, if not all, of the cellulosic fibres in wood react with the chlorinated species products during co-pyrolysis with PVC concentrations as low as 5 wt%. However, this is not the case for 1 wt% PVC, because a second DTG peak corresponding to cellulose decomposition appears at roughly 330 °C (Figure 5.2) and thus, not all the cellulose decomposes during the dehydrochlorination step. Matsuzawa et al. [180] also observed a second DTG peak at approximately 300 °C for a mixture of 2 wt% PVC and a pure cellulose polymer.

5.3 Kinetic modelling approach

5.3.1 Model assumptions and reaction scheme

To describe the TG/DTG curves of pure poplar wood, a three-component devolatilisation mechanism is proposed for the volatile fractions of its pseudo-components, hemicellulose (H), cellulose (C) and lignin (L). These pseudo-components decompose independently of each other as shown by Equations 5.1 - 5.3.

$$H \xrightarrow{k_{1,PW}} V_H \tag{5.1}$$

$$C \xrightarrow{k_{2,PW}} V_C \tag{5.2}$$

$$L \xrightarrow{k_{3,PW}} V_L \tag{5.3}$$

Where k refers to the reaction rate constant and V is the gas released from each devolatilisation reaction. Some mineral matter in wood may also volatilise during pyrolysis but they generally make up a small mass fraction of wood and are therefore not considered in this reaction scheme. A three-component mechanism is also proposed for PVC, involving the pseudo-components, HCl and polyene (P):

$$HCl \xrightarrow{k_{1,PVC}} V_{HCl} \tag{5.4}$$

$$P1 \xrightarrow{k_{2,PVC}} V_{P1} \tag{5.5}$$

$$P2 \xrightarrow{k_{3,PVC}} V_{P2} \tag{5.6}$$

Where P1 refers to the polyene molecules that volatilize as a result of condensation

and de-alkylation reactions, and P2 are the polyene molecules that degrade by cyclization and cross-linking reactions.

A global reaction scheme is also proposed for the interactions between the pseudo-components of PW and PVC during co-pyrolysis, (Equations 5.7 - 5.12). Here, only the dehydrochlorination phase in PVC pyrolysis is considered which, which for convienience sake, is represented by the volatalization of HCl pseudo-component. Hemicellulose and cellulose in PW decompose to release volatiles via two parallel reactions: thermal degradation and acid hydrolysis. Finally, lignin only undergoes thermal degradation because it mainly decomposes after HCl release.

$$H \xrightarrow{k_{1,PVC/PW}} V_H \tag{5.7}$$

$$C \xrightarrow{k_{2,PVC/PW}} V_C \tag{5.8}$$

$$L \xrightarrow{k_{3,PVC/PW}} V_L \tag{5.9}$$

$$HCl \xrightarrow{k_{4,PVC/PW}} V_{HCl} \tag{5.10}$$

$$H - HCl \xrightarrow{k_{5,PVC/PW}} V_{H-HCl} \tag{5.11}$$

$$C - HCl \xrightarrow{k_{6,PVC/PW}} V_{C-HCl} \tag{5.12}$$

With regard to modelling 1 wt% PVC/PW pyrolysis, all six reactions in Equations 5.7-5.12 are assumed to take place, thus leading to a six pseudo-component devolatilisation model. However, for 5 wt% and 10 wt% PVC/PW, a four pseudo-component model is considered because the hydrolysis rate of hemicellulose and cellulose is expected to be much faster than the thermal degradation rate in the presence of high HCl concentrations. Thus, in the case of high PVC concentrations (5 or 10 wt%), reactions 5.7 and 5.8 are assumed to be negligible.

5.3.2 TGA kinetics

The expression for the rate of solid-state reactions has the following form:

$$\frac{\mathrm{d}\alpha}{\mathrm{d}t} = k\left(T\right) f\left(\alpha\right) \tag{5.13}$$

The conversion, α , is the fraction of the initial sample decomposed:

$$\alpha = \frac{m_0 - m}{m_0 - m_\infty} \tag{5.14}$$

where m_0, and m_∞ are the initial and final mass of the sample, and m is the mass at a given time t of the analysis. According to the Arrhenius equation, the temperature dependence on the rate constant, k is given by:

$$k = A\,exp\left(\frac{-E}{RT}\right) \tag{5.15}$$

where A is the pre-exponential factor (min^{-1}), E is the activation energy (kJ/mol), R is the gas constant (8.314 J/K/mol) and T is the absolute temperature (K). Combining Eq. (5.13) and Eq. (5.15) gives the fundamental expression in Eq. (5.16) to determine the kinetic parameters that satisfactorily describe the TGA results.

$$\frac{\mathrm{d}\alpha}{\mathrm{d}t} = A\,exp\left(\frac{-E}{RT}\right) f(\alpha) \tag{5.16}$$

For non-isothermal TGA experiments at linear heating rate, $\beta = \mathrm{d}T/\mathrm{d}t$, Eq. (5.16) can be expanded to:

$$\frac{\mathrm{d}\alpha}{\mathrm{d}T} = \left(\frac{A}{\beta}\right) exp\left(\frac{-E}{RT}\right) f(\alpha) \tag{5.17}$$

5.3.3 Fraser-Suzuki deconvolution

Deconvolution of the DTG peaks can be performed using a Fraser-Suzuki Function (FSF) [120].

$$\left.\frac{\mathrm{d}\alpha}{\mathrm{d}T}\right|_i = H_{p,i}\,exp\left\{-\frac{ln2}{A_{s,i}^2}\,ln\left[1+2A_{s,i}\frac{T-T_{p,i}}{W_{hf,i}}\right]^2\right\} \tag{5.18}$$

The FSF parameters, H_p, A_s, T_p, and W_{hf}, represent height (K^{-1}), asymmetry (dimensionless), peak temperature (K) and half-width (K) of the $\mathrm{d}\alpha/\mathrm{d}T$ vs. T profile for the i-th pseudo component respectively. Hence, for wood and PVC pyrolysis, the deconvolution of the $\mathrm{d}\alpha/\mathrm{d}T$ vs. T profiles gives:

$$\frac{\mathrm{d}\alpha}{\mathrm{d}T} = \sum_{i=1}^{N_c} c_i H_{p,i}\,exp\left\{-\frac{ln2}{A_{s,i}^2}\,ln\left[1+2A_{s,i}\frac{T-T_{p,i}}{W_{hf,i}}\right]^2\right\} \tag{5.19}$$

Where c_i and N_c are the mass fraction of the i-th pseudo-component and the total number of pseudo-components of each sample respectively. To estimate the unkown parameters, c_i, H_p, A_s, T_p, and W_{hf} were initially guessed and then adjusted until the deviation between the calculated and experimental values for $\mathrm{d}\alpha/\mathrm{d}T$ was minimised. The deviation $Dev(\%)$ was calculated using Nonlinear Least Squares [120]:

$$Dev\,(\%) = \frac{\sqrt{\left(\sum_{j=1}^{N_d}\left[\left(\frac{\mathrm{d}\alpha}{\mathrm{d}T}\right)_{j,e} - \left(\frac{\mathrm{d}\alpha}{\mathrm{d}T}\right)_{j,c}\right]^2\right)/N_d}}{h} \times 100 \tag{5.20}$$

Where j denotes the j-th experimental point and N_d is the total number of data points. $(\mathrm{d}\alpha/\mathrm{d}T)_{j,c}$ and $(\mathrm{d}\alpha/\mathrm{d}T)_{j,e}$ are the calculated and experimental DTG data, and h is the maximum value of $(\mathrm{d}\alpha/\mathrm{d}T)$. Next, the separated $\mathrm{d}\alpha/\mathrm{d}T$ curves were

each integrated using the Middle Riemann Sum method [209] to obtain α values for each component i:

$$\alpha_i = \sum_{j=1}^{N_d} \frac{1}{2} \left[\left(\frac{\mathrm{d}\alpha}{\mathrm{d}T} \right)_j + \left(\frac{\mathrm{d}\alpha}{\mathrm{d}T} \right)_{j-1} \right] (T_j - T_{j-1}) \tag{5.21}$$

5.3.4 Activation energy determination using KAS method

The integral rearrangement of equation Eq. (5.16) gives:

$$g(\alpha) = \int_0^\alpha \frac{1}{f(\alpha)} d\alpha = \frac{A}{\beta} \int_{T_0}^{T} exp\left(\frac{-E}{RT} \right) dT \tag{5.22}$$

where $g(\alpha)$ is the integral form of $f(\alpha)$. $f(\alpha)$ is a function for the algebraic expression that represents the mechanism of the solid-degradation process. The most common forms of $f(\alpha)$ and corresponding $g(\alpha)$ are listed in Table 5.2.

Kissinger-Akahira-Sunose (KAS) method [111] linearizes Equation 5.22 to obtain the following expression:

$$\ln\left(\frac{\beta}{T_\alpha^2} \right) = \ln\left(\frac{A_\alpha R}{E_\alpha g(\alpha)} \right) - \frac{E_\alpha}{R T_\alpha} \tag{5.23}$$

The apparent activation energy can be obtained from the plot of $\ln(\beta/T_\alpha^2)$ versus $1000/T_\alpha$ for a given value of conversion, α, where the slope of the straight line is equal to $-E_\alpha/R$. Once the most suitable $f(\alpha)$ is known, the pre-exponential factor, A_α, can be calculated from the intercept.

5.3.5 Master plots

The most suitable reaction mechanism of pyrolysis, $f(\alpha)$, can be determined using the generalized master plots method [114].

$$\lambda(\alpha) = \frac{f(\alpha)}{f(\alpha)_{0.5}} = \frac{(\mathrm{d}\alpha/dt)_\alpha}{(\mathrm{d}\alpha/dt)_{0.5}} \frac{exp\left[E_0/(R T_\alpha)\right]}{exp\left[E_0/(R T_{0.5})\right]} \tag{5.24}$$

where $(\mathrm{d}\alpha/\mathrm{d}t)_{0.5}$, and $T_{0.5}$, are the conversion rate and temperature corresponding to $\alpha = 0.5$ respectively. E_0 is the average activation energy determined using the KAS method. The suitable pyrolysis reaction mechanism is obtained when the model $\lambda(\alpha)$ best matches the experimental $\lambda(\alpha)$.

TABLE 5.2: The most common reaction mechanism functions used in kinetic analysis of solid-state reactions [115, 120, 210]

Model		$f(\alpha) = (1/k)(d\alpha/dt)$	$g(\alpha) = kt$
Power law	Pn Power law	$n(\alpha)^{(n-1)/n}$	$-\alpha^{1/n}$
Nucleation and Growth	A2 Avrami-Erofeev	$2(1-\alpha)[-ln(1-\alpha)]^{1/2}$	$[-ln(1-\alpha)]^{1/2}$
	A3 Avrami-Erofeev	$3(1-\alpha)[-ln(1-\alpha)]^{2/3}$	$[-ln(1-\alpha)]^{1/3}$
	A4 Avrami-Erofeev	$4(1-\alpha)[-ln(1-\alpha)]^{3/4}$	$[-ln(1-\alpha)]^{1/4}$
	B1 Prout-Trompkins	$\alpha(1-\alpha)$	$ln[\alpha/(1-\alpha)]$
Geometrical models	R2 contracting area	$2(1-\alpha)^{1/2}$	$1-(1-\alpha)^{1/2}$
	R3 contracting volume	$3(1-\alpha)^{2/3}$	$1-(1-\alpha)^{1/3}$
Diffusion models	D1 one-dimensional	$1/2\,\alpha$	α^2
	D2 two-dimensional	$[-ln(1-\alpha)]^{-1}$	$(1-\alpha)ln(1-\alpha)+\alpha$
	D3 three-dimensional	$3/2(1-\alpha)^{2/3}\left[1-(1-\alpha)^{1/3}\right]$	$\left[1-(1-\alpha)^{1/3}\right]^2$
	D4 Ginstling-Brounshein	$3/2\left[(1-\alpha)^{-1/3}-1\right]^{-1}$	$1-(2\alpha/3)-(1-\alpha)^{2/3}$
Order-based models	F0 zero order	1	α
	F1 first order	$1-\alpha$	$-ln(1-\alpha)$
	F2 second order	$(1-\alpha)^2$	$[1/(1-\alpha)]-1$
	F3 third order	$(1-\alpha)^3$	$\left[1/(1-\alpha)^2\right]-1$
Random scission model	L2	$2\left(\alpha^{1/2}-\alpha\right)$	-

Note: $g(\alpha)$ is the integral form of $f(\alpha)$

5.4 Kinetic modelling results

5.4.1 Fraser-Suzuki deconvolution results

The Fraser-Suzuki deconvolution parameters for pure PW and PVC pyrolysis at 5, 10 and 20 °C/min are listed in Table 5.3 and those for 1, 5 and 10 wt% PVC/PW mixtures are shown in 5.4. The deconvolution models fit the experimental data satisfactorily with low deviation values ($< 10\,\%$) which were calculated using Equation 5.20. Figure 5.3 gives an example of the deconvolution curves of the samples at a heating rate of 5 °C/min.

Table 5.3: Fraser-Suzuki deconvolution results for pure PW and PVC at 5, 10 and 20 °C/min

		100 % PW			100 % PVC		
Component		5	10	20	5	10	20
H	H_p	0.5100	0.5300	0.5800	-	-	-
	T_p	275.00	287.75	300.50	-	-	-
	w_{hf}	53.00	53.00	51.00	-	-	-
	A_s	-0.06	-0.10	-0.10	-	-	-
	c_i	0.33	0.34	0.35	-	-	-
C	H_p	1.3000	1.2000	1.1	-	-	-
	T_p	332.00	341.75	351.90	-	-	-
	w_{hf}	25.00	27.00	29.00	-	-	-
	A_s	-0.40	-0.40	-0.40	-	-	-
	c_i	0.42	0.41	0.41	-	-	-
L	H_p	0.1100	0.1050	0.1000	-	-	-
	T_p	371.50	380.50	391.00	-	-	-
	w_{hf}	185.00	190.00	195.00	-	-	-
	A_s	0.20	0.31	0.45	-	-	-
	c_i	0.25	0.25	0.24	-	-	-
HCl	H_p	-	-	-	1.6000	1.5500	1.4000
	T_p	-	-	-	266.00	279.50	293.00
	w_{hf}	-	-	-	33.00	33.00	33.00
	A_s	-	-	-	0.00	0.00	0.00
	c_i	-	-	-	0.55	0.57	0.56
P1	H_p	-	-	-	0.3000	0.3000	0.3300
	T_p	-	-	-	290.00	306.00	322.00
	w_{hf}	-	-	-	50.00	50.00	50.00
	A_s	-	-	-	0.20	0.20	0.20
	c_i	-	-	-	0.16	0.16	0.18
P2	H_p	-	-	-	0.3500	0.3000	0.2800
	T_p	-	-	-	447.00	460.00	473.00
	w_{hf}	-	-	-	77.50	85.00	85.00
	A_s	-	-	-	0.00	0.00	0.00
	c_i	-	-	-	0.29	0.28	0.26
Dev (%)		1.99	1.63	2.23	1.48	1.99	2.85

Table 5.4: Fraser-Suzuki deconvolution results for of 1, 5 and 10 wt% PW/PVC pellets at 5, 10 and 20 °C/min

		1 % PVC/PW			5 % PVC/PW			10 % PVC/PW		
Component		5	10	20	5	10	20	5	10	20
H	H_p	0.1600	0.1800	0.2000	-	-	-	-	-	-
	T_p	275.00	287.75	300.50	-	-	-	-	-	-
	w_{hf}	53.00	53.00	51.00	-	-	-	-	-	-
	A_s	-0.06	-0.10	-0.10	-	-	-	-	-	-
	c_i	0.11	0.12	0.13	-	-	-	-	-	-
C	H_p	0.7200	0.6300	0.67	-	-	-	-	-	-
	T_p	332.00	341.75	351.50	-	-	-	-	-	-
	w_{hf}	25.00	27.00	29.00	-	-	-	-	-	-
	A_s	-0.40	-0.40	-0.40	-	-	-	-	-	-
	c_i	0.25	0.23	0.26	-	-	-	-	-	-
L	H_p	0.1100	0.1000	0.1000	0.1600	0.1400	0.1400	0.1500	0.1400	0.1400
	T_p	371.50	380.50	391.00	371.50	380.50	391.00	371.50	380.50	391.00
	w_{hf}	185.00	190.00	195.00	185.00	190.00	195.00	185.00	190.00	195.00
	A_s	0.20	0.31	0.45	0.20	0.31	0.45	0.20	0.31	0.45
	c_i	0.27	0.25	0.24	0.35	0.32	0.35	0.34	0.33	0.33
HCl	H_p	0.0128	0.0134	0.0140	0.0735	0.0730	0.0724	0.1370	0.1360	0.14300
	T_p	266.00	279.50	293.00	266.00	279.50	293.00	266.00	279.50	293.00
	w_{hf}	33.00	33.00	33.00	33.00	33.00	33.00	33.00	33.00	33.00
	A_s	0.00	0.00	0.00	0.00	0.00	0.00	0.00	0.00	0.00
	c_i	0.0055	0.0056	0.0056	0.0282	0.0289	0.0283	0.0552	0.0555	0.0559
H-HCl	H_p	0.9000	0.9300	0.9300	1.1000	1.1000	1.1000	0.9500	0.9500	1.0000
	T_p	267.00	280.00	298.50	255.00	268.50	286.00	250.00	264.00	282.00
	w_{hf}	20.00	20.00	20.00	20.00	20.00	20.00	20.00	20.00	20.00
	A_s	0.00	0.00	0.00	0.00	0.00	0.00	0.00	0.00	0.00
	c_i	0.23	0.23	0.22	0.25	0.26	0.26	0.22	0.22	0.24
C-HCl	H_p	0.5900	0.7200	0.7000	2.0000	2.0000	2.0000	1.9500	2.0000	2.0000
	T_p	284.00	301.00	318.00	275.00	288.00	307.00	270.00	283.00	303.00
	w_{hf}	16.00	16.00	16.00	16.00	16.00	16.00	16.00	16.00	16.00
	A_s	0.00	0.00	0.00	0.00	0.00	0.00	0.00	0.00	0.00
	c_i	0.13	0.15	0.14	0.38	0.39	0.38	0.39	0.39	0.38
Dev (%)		3.99	3.98	3.11	1.78	2.32	1.35	1.70	1.82	1.15

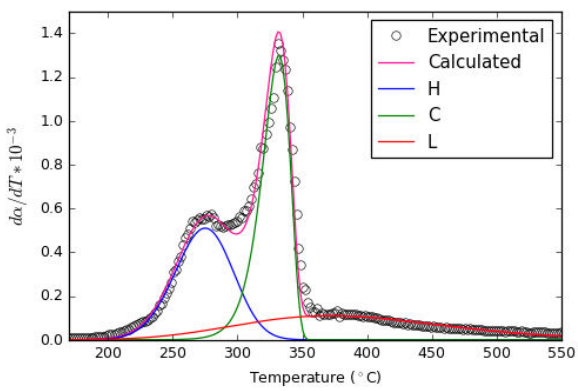

(A) 100 % PW

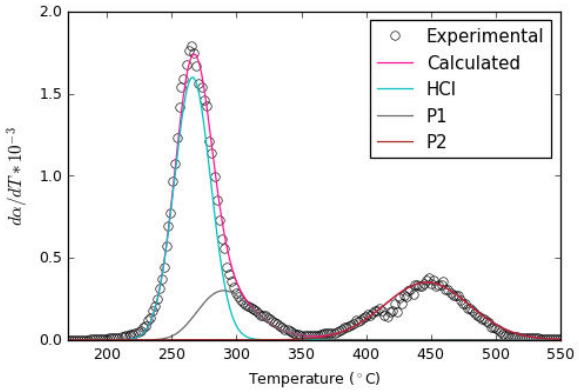

(B) 100 % PVC

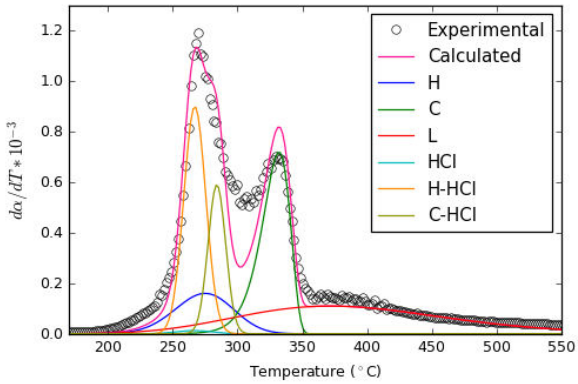

(C) 1 % PVC/PW

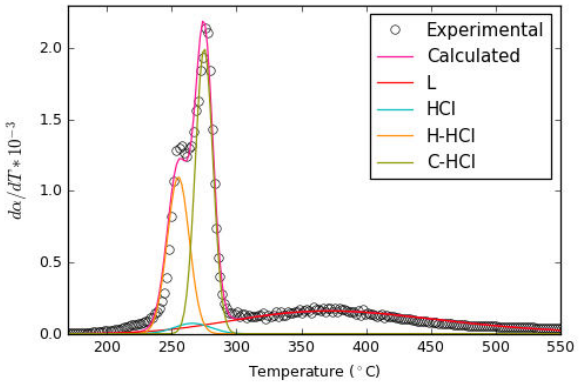

(D) 5 % PVC/PW

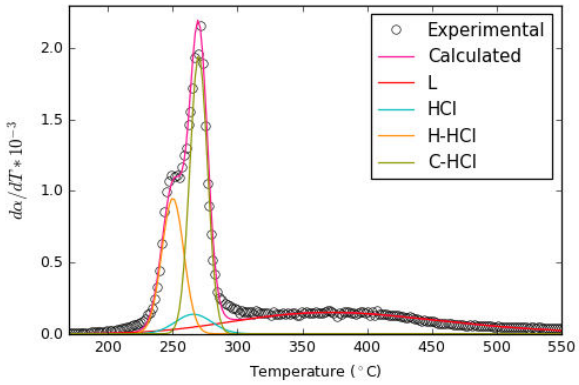

(E) 10 % PVC/PW

FIGURE 5.3: Deconvoluted DTG curves of pellets of Poplar wood (PW), PVC and their mixtures at 5°C/min

5.4.2 Isoconversional activation energy results

Following the separation of the DTG peaks (Figure 5.3), the Middle Riemmann Sum integral method (Equation 5.21) was employed to obtain the conversion values α, with respect to temperature for each pseudo-component at all three heating rates (5,

10, 20 °C/min). Next, the isoconversional activation energy of each pseudo-specie decomposition was evaluated at a given α from the slope of the KAS plot in Equation 5.23, i.e. $ln\,(\beta/T_\alpha^2)$ vs. $1/T_\alpha$ plot. As an example, Figure 5.4 presents the KAS plots for all six components of 1 wt% PVC/PW in the conversion range of 0.10 to 0.90. Correlation coefficient values (R^2) ranging between 0.9900 and 1 were obtained from linear regression analysis of these plots, which indicates that the activation energies calculated are relatively accurate.

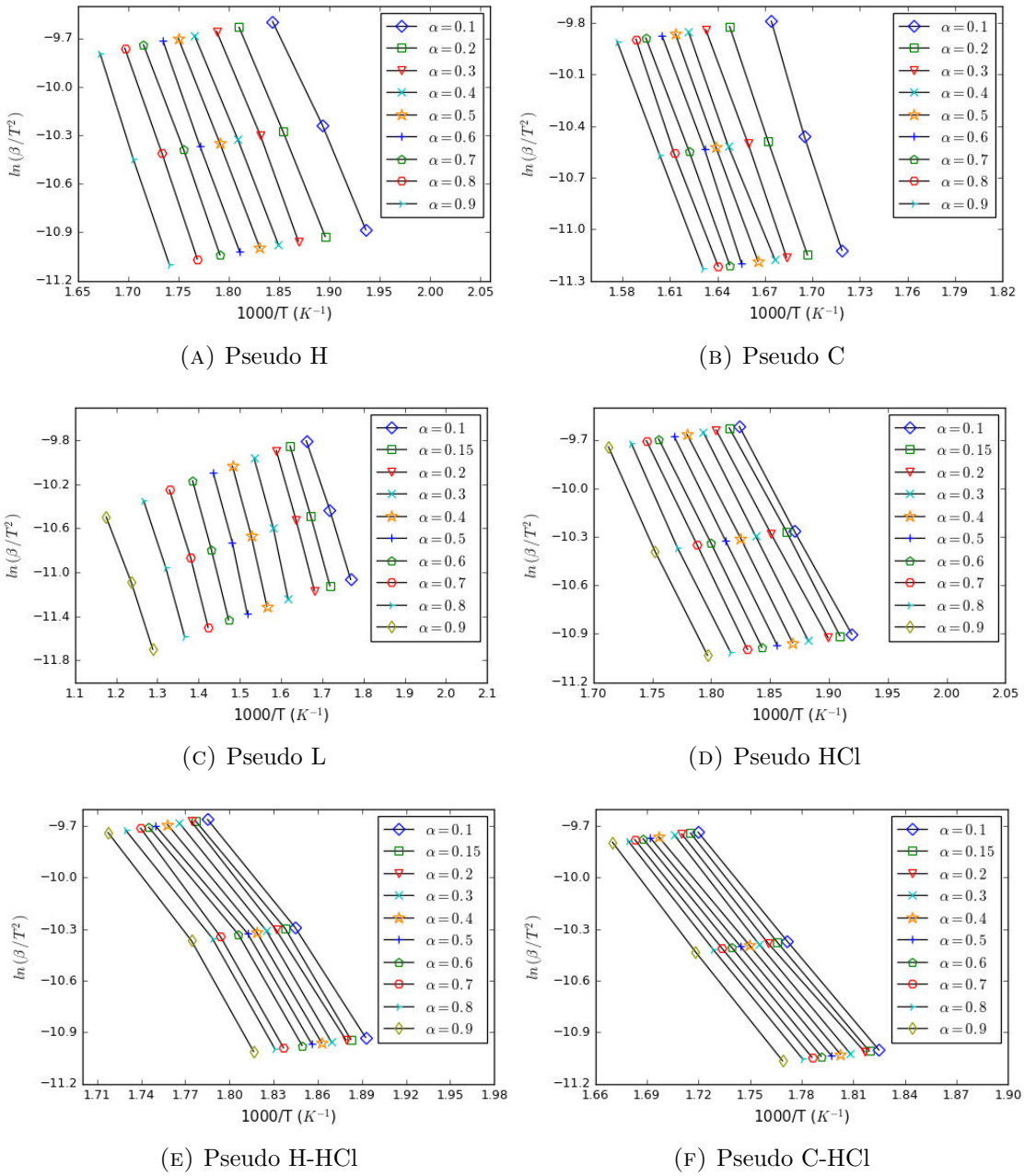

(A) Pseudo H

(B) Pseudo C

(C) Pseudo L

(D) Pseudo HCl

(E) Pseudo H-HCl

(F) Pseudo C-HCl

FIGURE 5.4: KAS plots for the pseudo-components between conversions of 0.1 and 0.9

Figure 5.5 displays the evolution of activation energy (E_α) with conversion α, calculated for the pseudo-components of pure PW and PVC as well as their

mixtures. According to the ICTAC Kinetics Committee [111], E_α values are considered to vary significantly with α if the difference between the maximum and minimum values of E_α is above 20-30 % of the average E_α. From Figure 5.5, it can be observed that E_α values for the co-pyrolysis pseudo-species (H-HCl and C-HCl) and those of pure PVC (HCl, P1 and P2), are roughly constant with variations of $<$ 16 % over the entire conversion range. Thus, it is likely that the decomposition of each of these pseudo-components is dominated by a single reaction mechanism and can therefore be adequately described by a single-step model [111]. However, higher E_α variations with α can be observed for hemicellulose (29 %), cellulose (22 %) and lignin (35 %) in pure PW as they are more kinetically complex. Because the pyrolysis of lignin takes place over several stages, and its decomposition occurs over a wide temperature range, it would therefore be more appropriate to apply multi-step kinetics to treat this process. However, this lies beyond the scope of the current work and thus, some loss of accuracy in lignin decompsition kinetics will be incurred in order to favour reliable kinetic predictions of the interactions between the cellulosic pseudo-components of PW and HCl from PVC.

The average apparent activation energies obtained for cellulose, hemicellulose and lignin in PW are 216, 136 and 112 kJ/mol respectively. These results fall within the range of activation energies in literature for biomass pseudo-components as shown by Figure 5.6 which was provided by Anca-Couce et al. [117] in a recent review on biomass pyrolysis. For PVC, the pseudo-species, HCl, P1, and P2, have an average E_α of 120, 112, and 226 kJ/mol. Similar to biomass pyrolysis, literature values for the activation energy of PVC vary considerably, possibly due to the different temperature programs used and the type of PVC sample studied. For example, Sanchez-Jimenez et al.[211] have reported an E_α of 114 kJ/mol for HCl-PVC whereas Miranda et al. [212] have obtained 198 kJ/mol. However, the trend in activation energies for the three pseudo-components agree with those generally found in literature : $E_{\alpha,P1} < E_{\alpha,HCl} < E_{\alpha,P2}$ [212–214]. Furthermore, the co-pyrolysis pseudo-components, H-HCl and C-HCl, have average E_α values of 97.9 and 101.7 kJ/mol respectively which are lower than those obtained for their pure-sample counterparts. This observed catalytic effect of HCl on cellulosic fibers is supported by the experimental work of Matsuzawa et al. [180] who have shown that HCl evolution from PVC catalyses the dehydration and charring of cellulose to form H_2O, CO, CO_2, char and other volatiles. In addition, new findings show that the depolymerisation of cellulose to produce levoglucosan during pyrolysis can be catalysed by H_2O or neighbouring OH groups [203, 215, 216]. Hence, HCl can also indirectly catalyse cellulose depolymerisation via the formation of more H_2O from the dehydration process.

5.4.3 Master plots for kinetic model determination

Figure 5.7 shows the experimental master plots for each pseudo-component which were constructed by inserting the average E_α values obtained in the previous section into Equation 5.24 and plotting $\lambda(\alpha)$ as a function of α. By comparing these experimental master plots against the theoretical ones of kinetic models in Table 5.2,

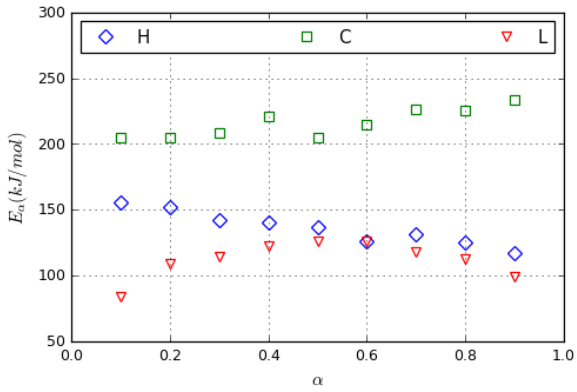

(A) 100 wt% PW

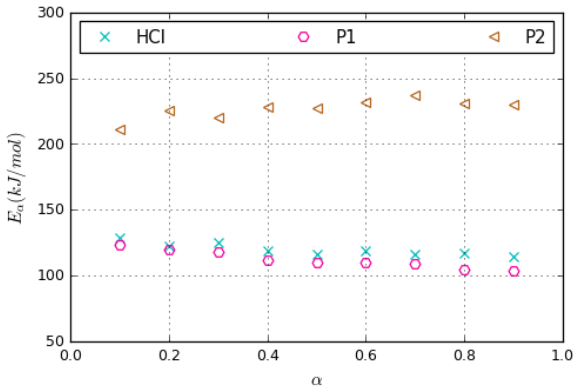

(B) 100 wt% PVC

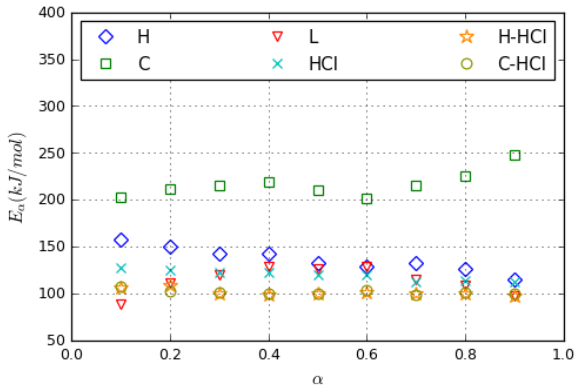

(C) 1 wt% PVC/PW

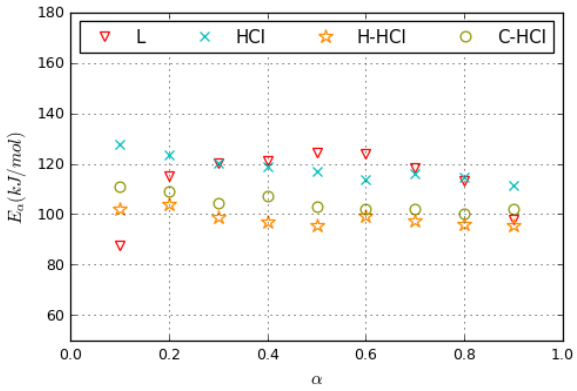

(D) 5 wt% PVC/PW

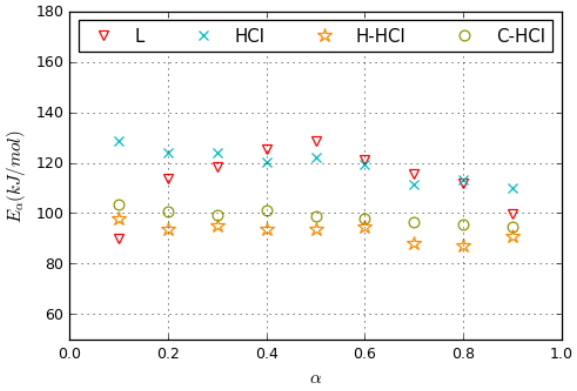

(E) 10 wt% PVC/PW

FIGURE 5.5: Activation energy distribution as a function of conversion of the pseudo-components in PW, PVC and PVC/PW pellets

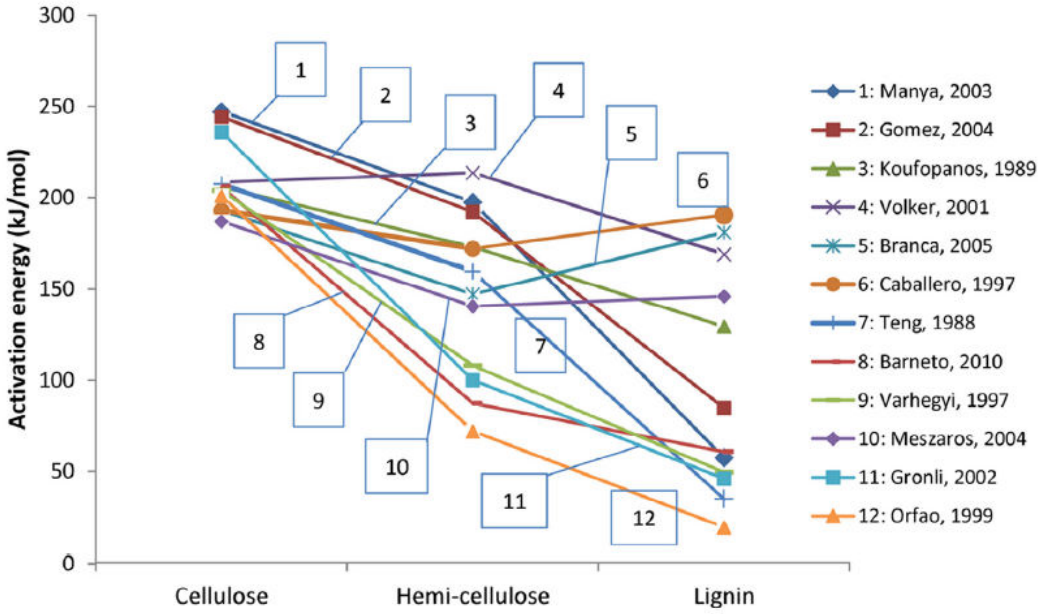

FIGURE 5.6: Activation energies reported in literature for biomass-components [117]. Data obtained with experiments formed at several heating rates (except 11): 1 [217], 2 [218], 3 [86], 4 [219], 5 [220], 6 [221], 7 [84], 8 [222], 9 [223], 10 [224], 11 [87], 12 [225]

the following suitable models have been identified below.

Order-based (F) models best describe pseudo hemicellulose (H), lignin (L), P1 and P2 pyrolysis. An order-based model with a reaction order other than $n = 0$, 1, 2 and 3, is semi-empirical in solid-state kinetics and hence, it may be a combined effect of other mechanisms such as Nucleation and Diffusion as is the case for hemicellulose pyrolysis [119, 226]. A reaction order of $n = 1.4$ was obtained for hemicellulose decomposition which is identical to the recently published result by Wang et al. [119] and also falls within the range, $n = 1$ - 2, reported in literature [122, 123, 227]. As for pseudo-lignin, a high reaction order between $n = 4$ and $n = 5$ was reached when matched with the experimental results. This behaviour of lignin may be linked to its highly complex phenylpropane composition whose degradation may involve several mechanisms occuring simultaneously. Furthermore, for P1 and P2, reaction orders of $n = 1$ and $n = 2.5$ can be observed. Solid-state kinetic mechanisms for these two pseudo-components have not yet been found in literature in order to compare with our results.

The Random scission (L2) function most adequately models cellulose (C) and HCl degradation. Random scission is an "acceleratory" type model which assumes that bond-breaking occurs randomly along the polymer chains, producing fragments of progressively shorter length that eventually evaporate when they are small enough [124, 228]. This mechanism for cellulose pyrolysis has recently been reported by several authors [114, 120, 203, 229] and can be associated with intra-ring scission of the glucose unit in the cellulose chain during dehydration and charring reactions [180]. Regarding pseudo HCl-PVC decomposition via dehydrochlorination, the

observed random scission mechanism may stem from β-scission reactions that occur along the polymer chain leading to the reduction in chain length and the formation of polyene molecules [190].

Avrami-Erofeev (A) equations best model H-HCl and C-HCl pseudo-components. An Avrami-Erofeev model is also an "acceleratory" type model and is based on nucleation and growth of crystals formed from chemical reactions [115, 230]. Both pseudo H-HCl and C-HCl have an n value of 2, representing two-dimensional growth of crystal nuclei, assuming that the number of nuclei remains constant. This A2 reaction mechanism for H-HCl and C-HCl decomposition signals a rate-limiting reaction between HCl and basic minerals in wood to form metal chloride salt crystals. Examples of metal chlorides formed from reactions between HCl and minerals in PW during pyrolysis have been previously given in Figure **??**. In this Figure, $CaCl_2$ is the most abundant metal chloride crystal, which may formed from the reaction between calcium carbonate $CaCO_3$ and HCl:

$$CaCO_3 + 2HCl \leftrightharpoons CaCl_2 + H_2O + CO_2 \tag{5.25}$$

This acid-base reaction is slow because of its low chemical potential energy ΔG_c, which increases from -30 to 0 kJ/mol as the temperature rises from 25 to 800 °C [231]. Thus, the nucleation and growth of $CaCl_2$ crystals may be the rate limiting step in the reactions between HCl and wood.

A summary of the kinetic model results for PW, PVC and PVC/PW pyrolysis are presented in Tables 5.5 and 5.6. With regards to pseudo-lignin (L), a new kinetic model, F3*: $f(\alpha) = (1-\alpha)^{2.9577}\alpha^{-0.008}$, was determined using the Nonlinear Least Squares regression and the Evolutionary Solver in Excel to fit the experimental data via minimising the deviation parameter in Equation 5.20. The optimal pre-exponential factors A, were also determined using this method. It can be seen in Tables 5.5 and 5.6 that the deviation between the predicted DTG data and the experimental ones is less than 4.5 % for all samples, which is considered to be a good fit.

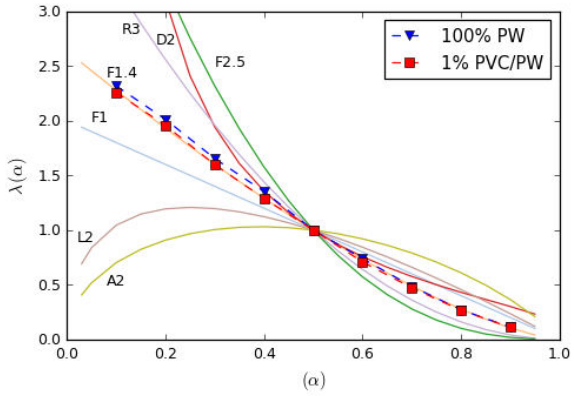

(A) Pseudo H

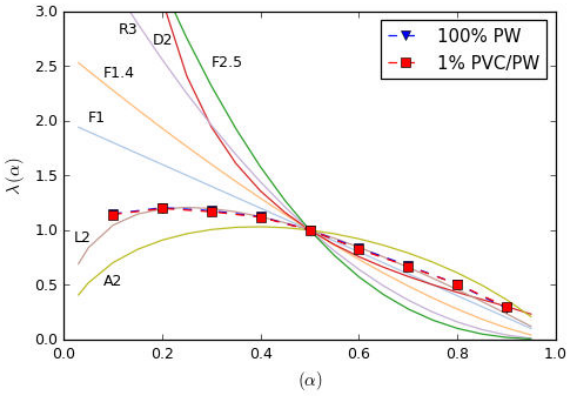

(B) Pseudo C

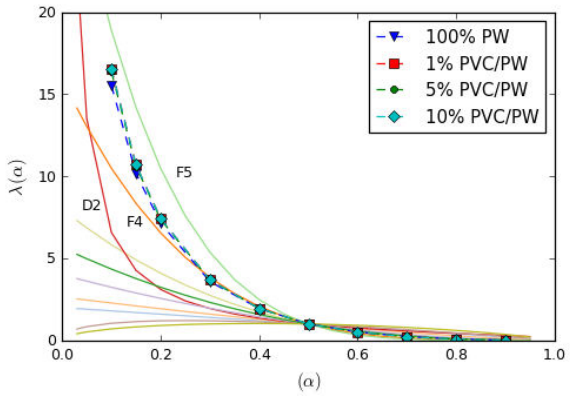

(C) Pseudo L

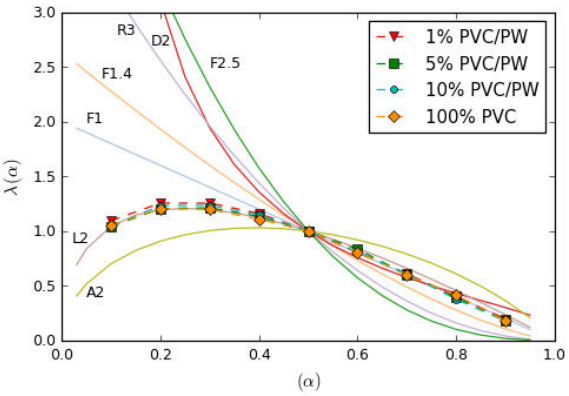

(D) Pseudo HCl

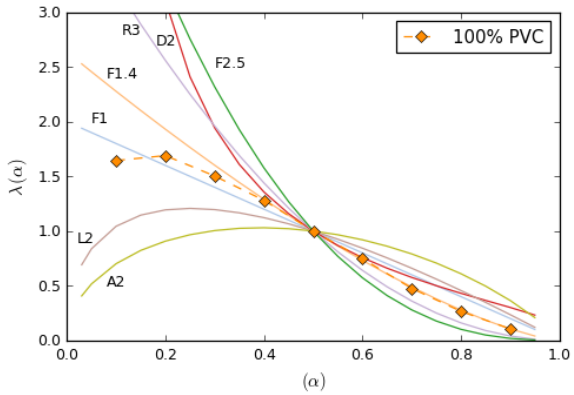

(E) Pseudo P1

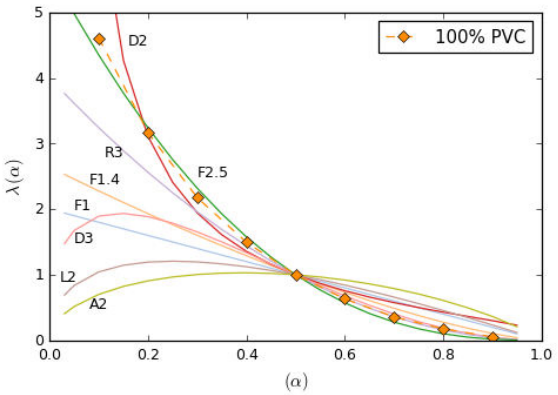

(F) Pseudo P2

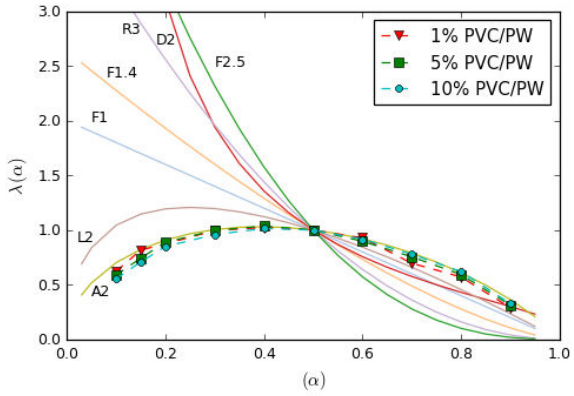

(G) Pseudo H-HCl

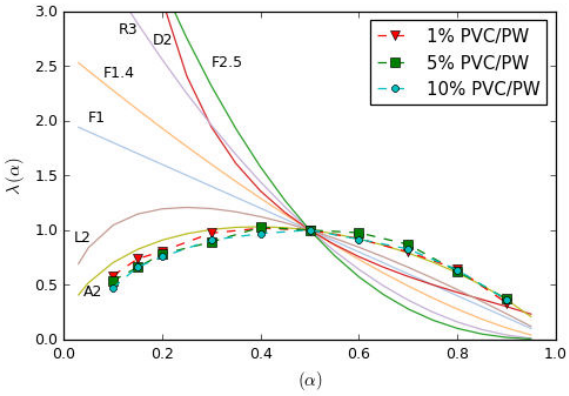

(H) Pseudo C-HCl

FIGURE 5.7: Comparisons between experimental and theoretical mechanistic models according to the generalised master plot procedure.

TABLE 5.5: Kinetic parameters for the pyrolysis of pure PW and PVC pellets. Values have been averaged over heating rates of 5, 10 and 20 °C/min

Component		100 % PW	100 % PVC
H	E (kJ/mol)	136.2	-
	A (min^{-1})	7.7 x 10^{13}	-
	Model	F1.4	-
	c	0.37	-
C	E (kJ/mol)	215.9	-
	A (min^{-1})	8.3 x 10^{19}	-
	Model	L2	-
	c	0.42	-
L	E (kJ/mol)	110.7	-
	A (min^{-1})	2.7 x 10^{09}	-
	Model	F3*	-
	c	0.24	-
HCl	E (kJ/mol)	-	119.7
	A (min^{-1})	-	7.5 x 10^{12}
	Model	-	L2
	c	-	0.56
P1	E (kJ/mol)	-	112.2
	A (min^{-1})	-	6.8 x 10^{10}
	Model	-	F1
	c	-	0.23
P2	E (kJ/mol)	-	225.9
	A (min^{-1})	-	2.5 x 10^{17}
	Model	-	F2.5
	c	-	0.21
Dev (%)		4.1	3.2

F3*: $f(\alpha) = (1-\alpha)^{2.9577}\alpha^{-0.008}$

TABLE 5.6: Kinetic parameters for the pyrolysis of PVC/PW pellets. Values have been averaged over heating rates of 5, 10 and 20 °C/min

Component		1 % PVC/PW	5 % PVC/PW	10 % PVC/PW
H	E (kJ/mol)	136.3	-	-
	A (min^{-1})	2.6 x 10^{13}	-	-
	Model	F1.4	-	-
	c	0.12	-	-
C	E (kJ/mol)	216.7	-	-
	A (min^{-1})	5.6 x 10^{19}	-	-
	Model	L2	-	-
	c	0.25	-	-
L	E (kJ/mol)	112.6	112.2	112.6
	A (min^{-1})	3.6 x 10^{09}	5.4 x 10^{09}	5.5 x 10^{09}
	Model	F3*	F3*	F3*
	c	0.21	0.29	0.29
HCl	E (kJ/mol)	120.1	119.0	119.9
	A (min^{-1})	6.4 x 10^{10}	3.2 x 10^{11}	7.5 x 10^{11}
	Model	L2	L2	L2
	c	0.0053	0.0301	0.0583
H-HCl	E (kJ/mol)	101.6	98.8	93.3
	A (min^{-1})	3.8 x 10^{10}	4.1 x 10^{10}	1.3 x 10^{10}
	Model	A2	A2	A2
	c	0.25	0.27	0.25
C-HCl	E (kJ/mol)	108.2	104.6	98.7
	A (min^{-1})	1.4 x 10^{10}	1.2 x 10^{11}	3.8 x 10^{10}
	Model	A2	A2	A2
	c	0.16	0.41	0.41
Dev (%)		4.5	1.9	2.0

F3*: $f(\alpha) = (1-\alpha)^{2.9577}\alpha^{-0.008}$

Conclusion

The work presented in this Chapter concerns the development and validation of a multi-step kinetic model that predicts the pyrolysis behaviour and reaction mechanism of poplar wood (PW) pellet containing different concentrations of PVC. Thermogravimetric experiments at different heating rates were conducted and apparent kinetic parameters were determined by combining Fraser-Suzuki deconvolution, isoconversional ("model-free") methods and master plot procedures. Our model fits the experimental data well with a deviation of less than 4.5 %.

The model results show that at a low PVC concentration of 1 wt%, the apparent activation energies of the pseudo-components of PW, hemicellulose and cellulose, decrease from 136.3 to 101.6 kJ/mol and from 216.7 to 108.2 kJ/mol respectively. Moreover, increasing the concentration of PVC by a factor of 5 and 10 further decreases the activation energy of hemicellulose by 2.8 kJ/mol and 8.3 kJ/mol and that of cellulose by 3.6 and 9.5 kJ/mol respectively. The observed decrease in activation energies is due to acid hydrolysis of the cellulosic fibres by HCl which is formed from the dehydrochlorination of PVC during pyrolysis.

The reaction mechanism or rate-limiting step for the interaction between PVC and PW was identified to be a Nucleation and Growth mechanism that follows the Avrami-Erofeev model with n=2 (A2). This kinetic model has been linked to the formation and growth of metal chloride crystals as a result of reactions between HCl and minerals in PW.

Our results are signficant because the few kinetic models currently in literature on the co-pyrolysis of biomass and PVC assume a single-step co-pyrolysis model and/or first-order reaction mechanism. These assumptions have been shown by several authors to often give inaccurate kinetic parameters. Thus, our work is an improvement on current kinetic models for co-pyrolysis of biomass and PVC.

A key advantage of our model is in its relative simplicity which makes it readily usable in a reactor-scale model of a pyro-gasifier. This point will be further exploited in the next chapter.

CHAPTER 6

Modelling pyro-gasification of wood waste in a downdraft reactor

Introduction

This chapter presents work that has been previously published by the author in *AIChE Journal* [232]. It discusses the steps taken to develop a one dimensional (1D), steady-state, computational fluid dynamics (CFD) model in order to simulate the pyro-gasification of wood waste in a downdraft reactor. Two key stages in the development of the model are presented as follows :

The first stage involves modelling the char-gasification zone of the reactor. The model assumptions are first discussed, and then the governing mathematical equations are presented. Next, the model is validated against experimental data found in literature. After validation, sensitivity analysis is performed on the model in order to evaluate the influence of key operating parameters on the model output. A heat duty analysis is also conducted to determine the conditions at which the gasifier can operate adiabatically or autothermally.

The second modelling stage incorporates submodels of other important processes that occur during biomass pyro-gasification, namely, drying, pyrolysis and combustion. The model assumptions are presented, as well as the governing mathematical equations. Furthermore, the difficulties encountered during model simulation tests are briefly discussed.

6.1 Wood char gasification modelling approach

A schematic view of a downdraft reactor is shown in Figure 6.1a. The wood particles are fed at the top of the reactor and slowly flow to the bottom where the residual ash is withdrawn. The gasification agents are injected through the sides of the reactor. During their downward flow, the particles undergo the following main processes: drying, pyrolysis, combustion and reduction. Finally, the produced gas is withdrawn from the bottom of the reactor.

This section is focused on modelling the gasification of char produced from the pyrolysis of wood by considering reactions of char with the gasification agents: air (O_2, + N_2), steam (H_2O) and carbon dioxide (CO_2). The reactions considered in this model and their associated heats of reaction at 25 °C are [36]:

$$C + O_2 \rightarrow CO_2, \text{ Combustion, } \Delta H_r = -394\ kJ/mol \tag{6.1}$$

$$C + CO_2 \rightarrow 2CO, \text{ Boudouard, } \Delta H_r = +172\ kJ/mol \tag{6.2}$$

$$C + H_2O \rightarrow CO + H_2, \text{ Steam gasification, } \Delta H_r = +131\ kJ/mol \tag{6.3}$$

$$CO + H_2O \leftrightarrow CO_2 + H_2, \text{ Water-gas shift (WGS), } \Delta H_r = -41\ kJ/mol \tag{6.4}$$

where N_2 in air has been assumed to remain inert.

Figure 6.1b shows the char bed in the gasification zone of the reactor in which

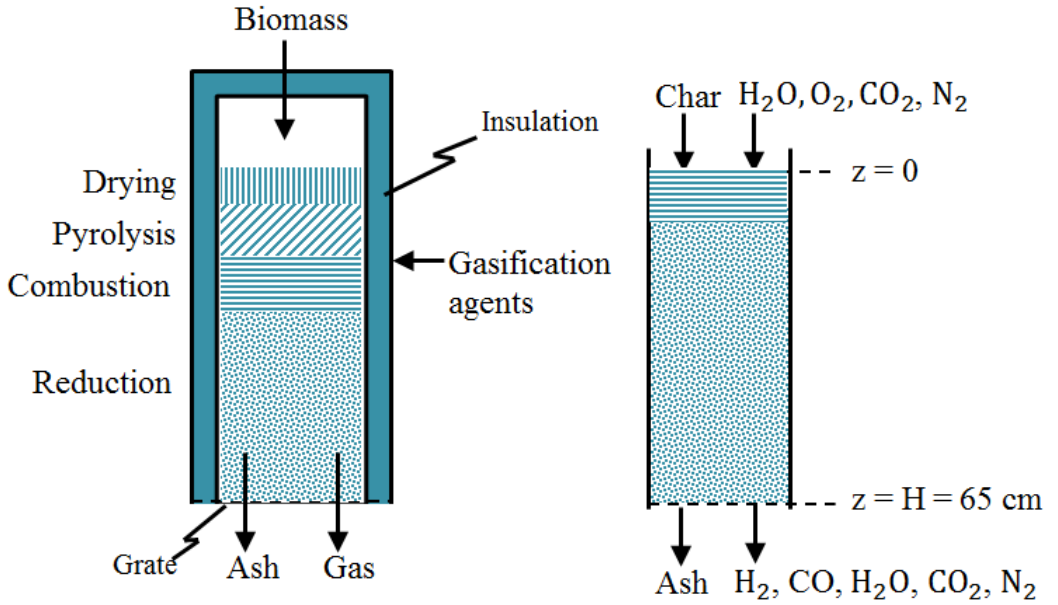

(A) Schematic view

(B) Model representation of char gasification zone

FIGURE 6.1: Downdraft fixed bed reactor

the equations of mass, heat and momentum are solved. The boundary conditions for these equations are applied at the bed inlet and outlet (z = 0 and z = H, respectively).

6.1.1 Assumptions

The following assumptions were made to model the gasification of wood char in the downdraft reactor:

1. Steady-state operation as most industrial downdraft gasifiers operate over long periods with few interruptions and the feed and withdrawal rates of the solid and gas phases have relatively low fluctuations.

2. Laminar flow regime for the gas phase due to the low velocities usually encountered in fixed bed reactors.

3. Ideal gas mixture as most downdraft gasifiers operate at atmospheric pressure.

4. Char bed is a homogeneous porous media so that all variables are assumed continuous in space and time.

5. At the pore scale, there is no heat transfer resistance between the solid and the gas phases. This assumption is based on the experimental findings of Van de Steene et al. [100]. The complex medium can therefore be represented with a single temperature field ($T_g = T_c = T$).

6. Heat transfer by radiation is neglected due to the relatively large flows of gas and solid which renders convective and conductive heat transfer predominant.

7. Constant bed porosity, tortuosity and particle diameter are assumed constant along the bed as the evolution of these parameters with conversion is very difficult to determine.

6.1.2 Mathematical equations and boundary conditions

Continuity equation of gas phase coupled to momentum balance (Darcy's law)

The continuity equation for the gas phase is written as:

$$\nabla \left(U_g C_g \right) = \sum_{j=1}^{6} r_j \tag{6.5}$$

where U_g is the superficial gas velocity (m/s), C_g is the total gas concentration (mol/m^3) and r_j is the mass source of gas species j (mol/m^3/s), where j belongs to CO, CO_2, H_2O, O_2, H_2.

By considering the gas as an ideal mixture, C_g can be expressed as a function of bed pressure P, and temperature T, by:

$$C_g = \frac{P}{RT} \tag{6.6}$$

where R is the universal gas constant.

As with several other fixed bed models [85, 233, 234], Darcy's law is used to describe the average flow of gas through the porous char bed:

$$U_g = -\frac{K}{\mu} \nabla P \tag{6.7}$$

where K is the bed permeability (m^2) and μ (kg/m.s) is the gas dynamic viscosity.

Darcy's law can be coupled to the continuity equation by substituting Equations 6.6 and 6.7 into Equation 6.5 to finally give:

$$\nabla \left(-\frac{P}{RT} \frac{K}{\mu} \nabla P \right) = \sum_{j=1}^{6} r_j \tag{6.8}$$

The bed permeability K, is calculated using Blake and Kozeny correlation [235]:

$$K = 150 \, \frac{(1-\epsilon)^2}{\epsilon^3} \frac{\mu}{d_{p,0}} \tag{6.9}$$

where ϵ is the bed porosity, and $d_{p,0}$ is the average particle diameter.

Mass balance equation for each gas species

The mass balance for each chemical species j in the gas phase is given by :

$$\nabla \left(U_g C_{g,j} \right) = \nabla \left(D^*_{j,N_2} \nabla C_{g,j} \right) + r_j \tag{6.10}$$

The left-hand side of Equation 6.10 represents the contribution of convective mass transfer and the first term on the right-hand side represents diffusive transfers. Here we have assumed that since N_2 is the dominant gas in the gas phase, the effective diffusion coefficient in species j in the gas phase is equivalent to the effective diffusion coefficient D^*_{j,N_2} of species j in pure N_2 (m^2/s). This effective diffusion coefficient is a function of the bed porosity ϵ and the bed tortuosity τ [81] as well as the bulk diffusion coefficient between species j and N_2.

$$D^*_{j,N_2} = \frac{\epsilon}{\tau} D_{j,N_2} \tag{6.11}$$

The dependence of the bulk diffusion coefficient D_{j,N_2} on temperature and pressure is expressed according to the Chapaman-Enskog formula:

$$D_{j,N_2} = D_{j,N_2} \left(T_{ref} P_{ref} \right) \left(\frac{P_{ref}}{P} \right) \left(\frac{T}{T_{ref}} \right)^{3/2} \tag{6.12}$$

where $(T_{ref} P_{ref})$ is the diffusivity of species j in nitrogen (N_2) gas solvent under reference conditions. Table B.1. lists the expression for the diffusion coefficient for each gaseous species j. The bed tortuosity is approximated by [81]:

$$\tau = 1 - 0.41 \ln \left(\epsilon \right) \tag{6.13}$$

Finally, the last term r_j in the right-hand side of Equation 6.10 is the production rate of species j , and will be detailed hereafter.

Mass balance equation for the solid phase (char)

The mass balance equation for the solid phase is given by:

$$\nabla \left(U_c C_c \right) = r_c \tag{6.14}$$

where U_c and C_c are the velocity and concentration of char, respectively, and r_c is the sink term for the consumption of char by the chemical reactions.

The velocity of char in the downdraft reactor can decrease significantly as a result of bed compaction. Bed compaction is a consequence of the reduction in particle size due to carbon conversion and various mechanical phenomena such as fragmentation and particle arrangement [236]. Equation 6.14 can be coupled to the char bed compaction equation which expresses the solid phase velocity as a function of char conversion X:

$$U_c \left(X \right) = U_{c,0} f \left(X \right) \tag{6.15}$$

where $U_{c,0}$ is the initial char superficial velocity (m/s), and $f(X)$ is an empirical

function developed by Teixeira et al. [237] and determined for wood char chips:

$$f(X) = -1.03 \cdot 10^{-4} X^2 + 4.25 \cdot 10^{-4} X + 1 \tag{6.16}$$

The conversion of char is calculated from the molar flowrates of the gaseous carbon species produced (CO and CO_2):

$$X = \frac{\dot{n}_{c|_{z=0}} - \dot{n}_c}{\dot{n}_{c|_{z=0}}} = \frac{\dot{n}_{CO} + \dot{n}_{CO_2} - \dot{n}_{CO_2|_{z=0}}}{\dot{n}_{c|_{z=0}}} \tag{6.17}$$

Reaction kinetics

The reaction rates for the heterogeneous reactions υ_i (Eq. 6.1-6.3) are determined by,

$$\upsilon_i = \omega_i C_{c,0} \tag{6.18}$$

where $C_{c,0}$ is the initial concentration of char and the notation ω_i denotes the char conversion rate for each heterogeneous reaction in Equations 6.1-6.3. The char conversion rates have been correlated by Teixeira and co-workers to the experimental parameters, temperature T and partial pressure of the reactant gas P_j (i.e. H_2O, CO_2 and O_2), as well as the other char properties, porosity ϵ_p, particle thickness e_p and reaction pre-exponential factor A_i, by three functions that take the form [238]:

$$log_{10} w_1 = f(T, P_j, e_p, \epsilon_p, A_i) \tag{6.19}$$

The functions of the char particle conversion rates in the three reactant gases are given in Equations 6.20-6.22, and the coefficient values are listed in Table B.2

Combustion function

$$\begin{aligned} log_{10} w_1 =& a + bT + cP_{O_2} + de_p + e\epsilon_p + fA_{O_2} + gT^2 + hP_{O_2}^2 + ie_p^2 \\ &+ j\epsilon_p^2 + kTP_{O_2} + lTe_p + mTA_{O_2} \end{aligned} \tag{6.20}$$

Boudouard function

$$\begin{aligned} log_{10} w_2 =& a + bT + cP_{CO_2} + de_p + e\epsilon_p + fA_{CO_2} + gT^2 + hP_{CO_2}^2 + iTe_p \\ &+ jT\epsilon_p + kTA_{CO_2} + le_p\epsilon_p + me_pA_{CO_2} + n\epsilon_pA_{CO_2} \end{aligned} \tag{6.21}$$

Steam gasification function

$$\begin{aligned} log_{10} w_3 =& a + bT + cP_{H_2O} + de_p + e\epsilon_p + fA_{H_2O} + gT^2 + hP_{H_2O}^2 \\ &+ iTe_p + jT\epsilon_p + kTA_{H_2O} \\ &+ lP_{H_2O}A_{H_2O} + me_p\epsilon_p + ne_pA_{H_2O} \\ &+ o\epsilon_pA_{H_2O} \end{aligned} \tag{6.22}$$

The properties of wood char used in this model are $e_p = 5.5 \times 10^{-3}$, $\epsilon_p = 0.75$, and the pre-exponential factors are $A_{O_2} = 1.1 \times 10^9$ $s^{-1}atm^{-0.6}$, $A_{CO_2} = 1.2 \times 10^8$ $s^{-1}atm^{-0.7}$ and $A_{H_2O} = 3.55 \times 10^3$ $s^{-1}atm^{-0.8}$, respectively [237].

For the water-gas shift reaction (WGS), we used a simple reversible rate expression for CO conversion which was proposed by Moe [239].

$$\nu_4 = k_{WGS} P_{CO} P_{H_2O} \left(1 - \frac{P_{CO_2} P_{H_2}}{K_{eq,WGS} P_{CO} P_{H_2O}}\right) M_{CO} \tag{6.23}$$

$$k_{WGS} = 1.85 \times 10^{-5} exp\left(12.88 - \frac{1855.5}{T}\right) \tag{6.24}$$

$$K_{eq,WGS} = exp\left(\frac{4577.8}{T} - 4.33\right) \tag{6.25}$$

where k_{WGS} (mol.g^{-1}.min^{-1}) and $K_{eq,WGS}$ are the rate constant and equilibrium rate constant respectively.

From the knowledge of the reaction rates $\nu_i, i = 1 \cdots 4$, the production term r_j of chemical species j appearing in Equations 6.10 and 6.14 can be expressed by:

$$r_j = \sum_{i=1}^{4} \nu_{ij}\, \nu_i \tag{6.26}$$

where ν_i denotes the (algebraic, positive for product, negative for reactants) stoichiometric coefficients of j in reaction i. Table B.3 details the expression for the production terms of the chemical species.

Energy balance equation

With the assumption of local thermal equilibrium between the gas and solid phases, the energy conservation equation write:

$$\left(\mathbf{U}_g C_g c_{p,g} M_g + \mathbf{U}_c C_c c_{p,c} M_c\right) \nabla T = \nabla \left(\lambda_b \nabla T\right) + \dot{Q}_r + \dot{Q}_{loss} \tag{6.27}$$

where convective heat transfer is represented by the term on the left-hand side of Equation 6.27 and conductive heat transfer by the term on the right-hand side. The effective thermal conductivity λ_b, in the porous media is evaluated by assuming that heat conduction in the solid and gas phase takes place in parallel which follows from the fifth assumption that no heat transfer occurs between the solid and gas phases [240]:

$$\lambda_b = (1 - \epsilon)\, \lambda_c + \epsilon \lambda_g \tag{6.28}$$

Table B.4 details the expression of the thermal conductivities of the chemical species in the two phases as a function of temperature. In Equation 6.27, $\dot{Q}_r$ is the heat source term which can be expressed as a function of the heats of reactions $\Delta H_{r,i}$ of Equations 6.1 to 6.4:

$$Q_r = -\sum_{i=1}^{4} \nu_i \Delta H_{r,i} \tag{6.29}$$

On the other hand, the heat lost to the surrounding by convection from the outer wall of the reactor Q_{loss}, was estimated to be 37.7 kWm^{-3} by Teixeira et al. [81]

which was determined from Newton's law of cooling as:

$$Q_{loss} = \frac{hA(T_w - T_\infty)}{V} \tag{6.30}$$

where A and V denote the outer surface area and volume of the reactor, respectively. The average wall temperature T_w and ambient temperature T_∞ were experimentally found to be 62 °C and 20 °C respectively, and the heat transfer coefficient h, is 10 $\mathrm{Wm^{-2}K^{-1}}$.

Boundary conditions

The system of differential equations formed from Equations 6.5 to 6.27 can be solved with the following boundary conditions to specify concentration, temperature and pressure values or their derivatives at the inlet (z=0) and outlet (z=H) of the char bed:

- Concentration of species in gas and solid phases

$$\text{Inlet} \quad C_j|_{\text{z=0}} = C_{j,0} \tag{6.31}$$

$$\text{Outlet} \quad \mathbf{n} \cdot \nabla C_j|_{\text{z=}H} = 0 \tag{6.32}$$

- Bed temerature

$$\text{Inlet} \quad T|_{\text{z=0}} = T_0 \tag{6.33}$$

$$\text{Outlet} \quad \mathbf{n} \cdot \nabla T|_{\text{z=}H} = 0 \tag{6.34}$$

- Bed pressure

$$\text{Inlet} \quad -\frac{K}{\mu} \cdot \nabla P|_{\text{z=0}} = \mathbf{U}_{g,0} \tag{6.35}$$

$$\text{Outlet} \quad \nabla P|_{\text{z=}H} = P_{atm} \tag{6.36}$$

6.1.3 OpenFOAM simulation

The system of partial differential equations discussed in the previous section was solved using the finite volume discretization method employed by the open source CFD software, OpenFOAM. The chemical and thermal properties data were obtained from NIST-JANAF Thermochemical Tables [241] and Teixeira [81]. A mesh convergence study was performed and an optimum value of 325 cells were found.

6.2 Simulation results

6.2.1 Validation of char gasification model

The model predictions have been validated against three different experimental results: two different feedstock with the same operating conditions (Table 6.1), and two different experimental conditions with the same feedstock (Table 6.2). The

results are presented in Table (Table 6.3). It can be seen that the model predictions are in good agreement with all three experimental observations remain regarding CO and H_2 concentrations at the bed outlet; nevertheless the model captures the trend well.

A more detailed evaluation of the model's ability to predict the evolution of the bed behaviour along the bed height was made by comparing the predicted results with the experimental ones for char chip gasification provided by Teixeira et al. [237]. The results are displayed in Figure 6.1 which reveal a highly reactive zone at the top of the bed (z < 10 cm) where the bed temperature decreases sharply to 875 °C due to the predominant endothermic char gasification reactions involving H_2O and CO_2. Below this zone, the low temperatures slow down the char gasification reactions which in turn decrease the production rate of H_2 and CO. To estimate the accuracy of our simulation results (w_{is}) with respect to the experimental data (w_{ie}), the sum squared method was used:

$$\text{Mean error } (\%) = 100\sqrt{\frac{\sum_{i=1}^{N}\left(\frac{w_{ie}-w_{is}}{w_{ie}}\right)^2}{N}} \tag{6.37}$$

The error analysis on our simulation results reveal a discrepancy of 4 % for char conversion, 2 % for bed temperature, 11 % for H_2 and 4 % for CO. These discrepancies are satisfactory given that the experimental error reported by Teixeira et al. [237] is 11 %.

Table 6.1: Composition and properties of char from Maritime Pine wood chips and pellets

	Van de Steen et al. [242] Char chips	Teixeira et al. [237, 243] Char chips	Teixeira et al. [243] Char pellets
Proximate analysis (wt % dry basis)			
Ash	1.4	1.7	1.4
Volatile Matter	4.9	4.0	2.0
Fixed carbon (by difference)	93.7	94.3	96.6
Ultimate analysis (wt % dry basis)			
C	89.8	92.6	92.8
H	2.2	1.0	1.3
N	0.1	0.2	0.3
O	6.1	3.8	3.1
S	0.001	< 0.2	> 0.2
LHV (MJ kg^{-1} dry basis)	-[a]	33.4	33.1
Char bed bulk density g cm^{-3}	-[a]	0.13	0.37
Particle density g cm^{-3}	-[a]	0.33	0.66
Particle porosity (-)	-[a]	0.74	0.51
Particle average thickness (mm)	-[a]	5.2	4.2

[a] Value not provided by the author and hence is estimated to be the same as that for char chips used by Teixeira.

Table 6.2: Operating conditions at the bed inlet for char gasification experiments

	Van de Steen et al. [242] Char chips	Teixeira et al. [237, 243] Char chips and pellets
Gas (%; mol/min)		
H_2O	19; 2.35	28; 32
CO_2	9; 1.12	8.2; 0.9
O_2	2; 0.25	2.7; 0.3
N_2	59; 7.31	61.1; 7.0
CO	59; 7.31	0
H_2	4; 0.5	0
Solid char (g/min)	28	28
Temperature (°C)	950	1028
Total pressure (atm)	1.01	1
Gas velocity (m/s)	0.68	0.7
Bed height (cm)	65	65

Table 6.3: Experimental and predicted results for char bed outlet conditions.

	Van de Steene et al. [242] Char chips		Teixeira et al. [237, 243] Char chips		Teixeira et al. [243] Char pellets	
	Exp.	Num.	Exp.	Num.	Exp.	Num
T (°C)	700	688	770	731	730	692
H_2O (vol%)	9.8	8.2	11.5	11.2	11.5	9.5
CO_2 (vol%)	10.8	10.2	10.0	11.0	9.0	11.1
O_2 (vol%)	0.6.	0.2	0.0	0.0	0.0	0.0
H_2 (vol%)	15.9	15.5	14.0	13.4	13.5	14.8
CO (vol%)	9.8	12.4	11.2	10.5	11.5	11.4
N_2 (vol%)	52.9	53.7	53.3	53.9	54.6	53.1
Solid (g/min)	3.1	3.6	2.5[a]	2.3	2.8[b]	2.9
Char conversion, X	89.0	71.0	95.0	87.0	95.0	99.0

[a] Calculated at a bed height of 50 cm.

[b] Calculated at a bed height of 15 cm

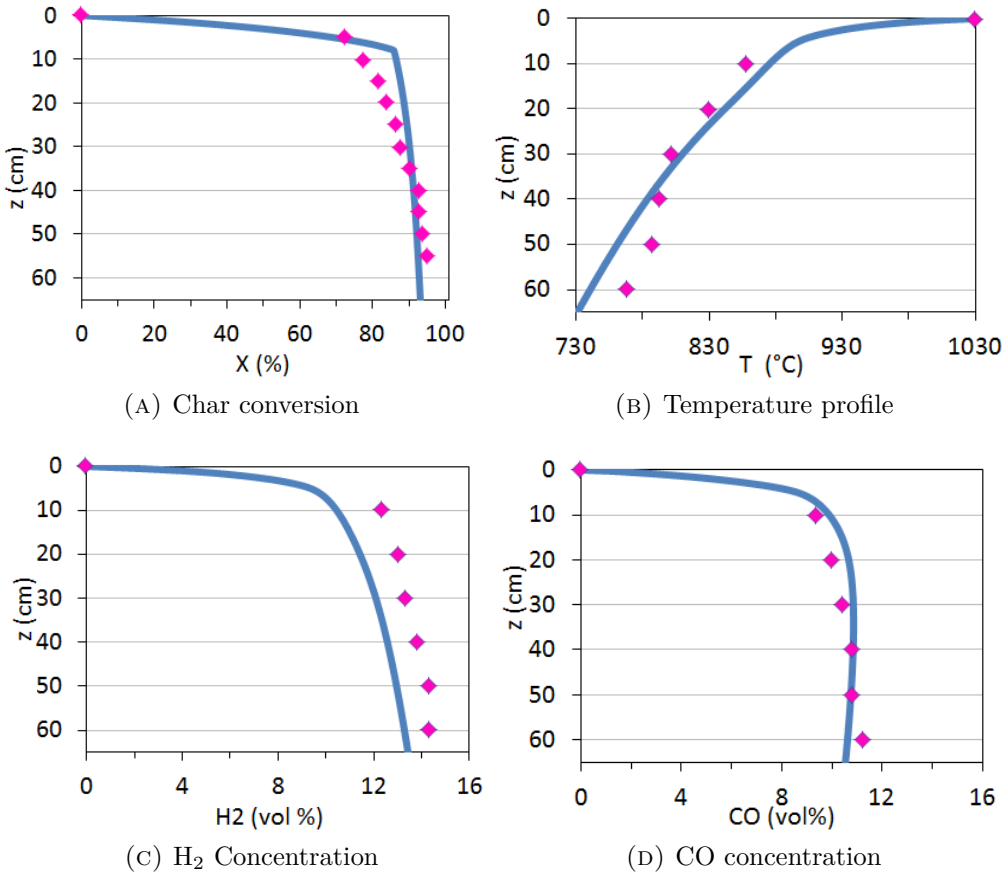

(A) Char conversion (B) Temperature profile

(C) H_2 Concentration (D) CO concentration

FIGURE 6.2: Experimental vs. numerical results for char conversion. In all graphs the experimental data are represented by diamonds and the simulation results are represented by solid lines.

6.2.2 Sensitivity analysis

Effect of bed porosity

In this model, several parameters depend on the bed porosity (ϵ) including the bed permeability, diffusivity, tortuosity and conductivity. Hence, it is important that we test the sensitivity of the model to changes in the bed porosity, since we have assumed that this parameter is constant (see section 6.1.1).

The test was conducted by varying the bed porosity 0.25 to 0.70. Char from maritime pine wood chips was chosen as the feedstock for this analysis whose properties are provided by Teixeira et al. [237, 243] and are shown in Table 6.1. We can see from the results in Figure 6.3 that a decrease in bed porosity by 64% (0.70 to 0.25) leads to a decrease in overall char conversion by 3% and a less than 1% variation in outlet temperature, H_2 and CO concentrations. Hence we can conclude that our model is relatively insensitive to changes in bed porosity and thus insensitive to the other coefficients mentioned above. Thus the assumption of a constant bed porosity remains valid for this model.

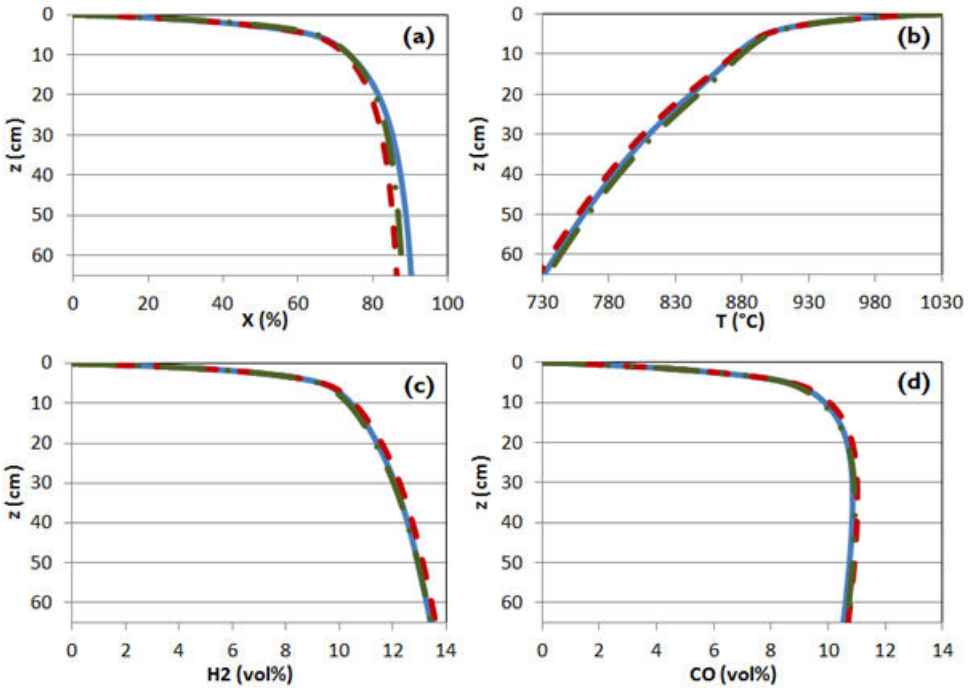

FIGURE 6.3: Influence of char bed porosity (0.25 – dash-dotted line, 0.50 – dashed line, 0.70 - solid line) on char conversion (a), temperature profile (b), H_2 concentration (c) and CO concentration (d).

Effect of inlet bed temperature and gas composition

The aim of this analysis is to study the effect of the bed inlet temperature and gas composition on the syngas H_2/CO ratio and to compare our results with those obtained experimentally in literature. The operating conditions used for this study are displayed in Table 6.4 and were varied as follows:

- Inlet bed temperature, T_0 : 900 - 1000 °C
- O_2 concentration, C_{O_2} : 0 - 3 vol%
- Steam concentration, C_{H_2O} : 5 - 20 vol%
- CO_2 concentration, C_{CO_2} : 5 - 20 vol%

The results, in Figure 6.4, shows that a rise in the inlet bed temperature from 900 to 1000 °C favours the production of CO to the detriment of H_2 by lowering the H_2/CO ratio by 17 %. This is because, the increase in bed temperature increases the rate of the endothermic steam gasification (Eq. 6.3) and Boudouard reactions (Eq. 6.2) which leads to a more CO production and an insignificant rise in H_2 production. This enrichment in CO caused by bed temperature increase is consistent with the experimental observations by Yang et al [244], who have reported that a temperature rise from 600 to 700 °C during steam gasification of biomass char, decreased the H_2/CO ratio from 0.23 to 0.07. Producing CO-rich syngas (low H_2/CO ratio) is desirable for Fischer-Tropsch (FT) synthesis of diesel fuels. However, this may not

TABLE 6.4: Operating conditions for sensitivity analysis of gasifier temperature and inlet gas composition

T_0 (°C)	O_2 (vol%)	H_2O (vol%)	CO_2 (vol%)	N_2 (vol%)
900	1.5	10	10	78.5
1000	1.5	10	10	78.5
950	0.0	10	10	80.0
950	3.0	10	10	77.0
950	1.5	20	10	68.5
950	1.5	5	10	83.5
950	1.5	10	20	68.5
950	1.5	10	5	83.5

justify the indirect heating of the reactor to temperatures above 900 °C due to the associated high energy costs and the relatively small gain in H_2/CO ratio.

A small increase in O_2 concentration from 0 to 3 vol % lowers the H_2/CO ratio by 50 wt% (Figure 6.4), and thereby produces a syngas rich in CO. This is due to the increase in char combustion rate (Eq. 6.1) when more O_2 is added, which produces more CO_2 and raises the bed temperature, which in turn boosts the Boudouard reaction (Eq. 6.2) to produce more CO. Yang and co-workers [245] have experimentally observed that when the air velocity is increased from 31 g/m^2/s to 112 g/m^2/s in a fixed bed reactor, the concentration of CO increases from 4 to 17 vol% which follows a similar tendency as our predicted results. Thus, our results show that raising the O_2 concentration is beneficial to provide direct heat to the reactor and to produce syngas with a low H_2/CO ratio for FT synthesis. Of course, a trade-off must be found between this benefit of increasing O_2 and the additional costs incurred from operating at higher air flow rates or producing oxygen-rich air from air separating units.

Regarding the influence of steam, an increase in H_2O concentration from 5 to 20 vol% results in a significant H_2 production leading to an increase in H_2/CO of 330 %. More H_2O in the gasifier boosts the steam gasification reaction (Eq. 6.3), thereby producing more CO and H_2. Much of this CO produced is consumed by the WGS reaction to favour H_2 production (Eq. 6.4). This corresponds to the trend revealed from steam gasification experiments by Yan et al. [246] in a similar reactor configuration, who revealed that a steam flowrate rise from 0 to 0.165 g/min per gram of biomass char, increased the H_2/CO ratio from 0.88 to 3.74. Consequently, syngas produced from steam gasification can be used in applications requiring high H_2 concentrations such as in gas turbine combustion and solid oxide fuel cells (SOFC).

Finally, when the inlet CO_2 concentration is elevated from 5 to 20 vol%, this lowers H_2/CO by 41 % due to the increase in the Boudouard reaction rate (Eq. 6.2). Butterman and Castaldi [247] have revealed similar results, where introducing 5 to 50 vol% CO_2 during biomass gasification at 900 °C, increased CO by a factor of

3 and decreased H_2 by the same factor. Thus, although increasing the inlet CO_2 concentration from 5 to 10 vol % increases the char conversion and CO production, further increasing the inlet CO_2 concentration from 10 to 20 vol % actually lowers the syngas quality because the net increase of CO is small and H_2 production is further decreased. Hence, in view of recycling large streams of CO_2 produced from industrial processes, our results show that low concentrations of CO_2 should be used if CO_2 were to serve as a gasifying agent for controlling syngas composition.

Further discussion on the reaction rate profiles as well as interactions between the different gasification reactions can be found in the published journal article of this work [232].

The sensitivity analysis of the above operating parameters are not only in good agreement with the trends reported by experimental works in literature, but they also reveal that the inlet concentration of O_2 and H_2O have the strongest influence on syngas composition. By adjusting these parameters in order to achieve the desired syngas composition for various applications, the feedstock will thus have a lesser impact on the syngas produced and therefore increase the fuel flexibility of the gasifier.

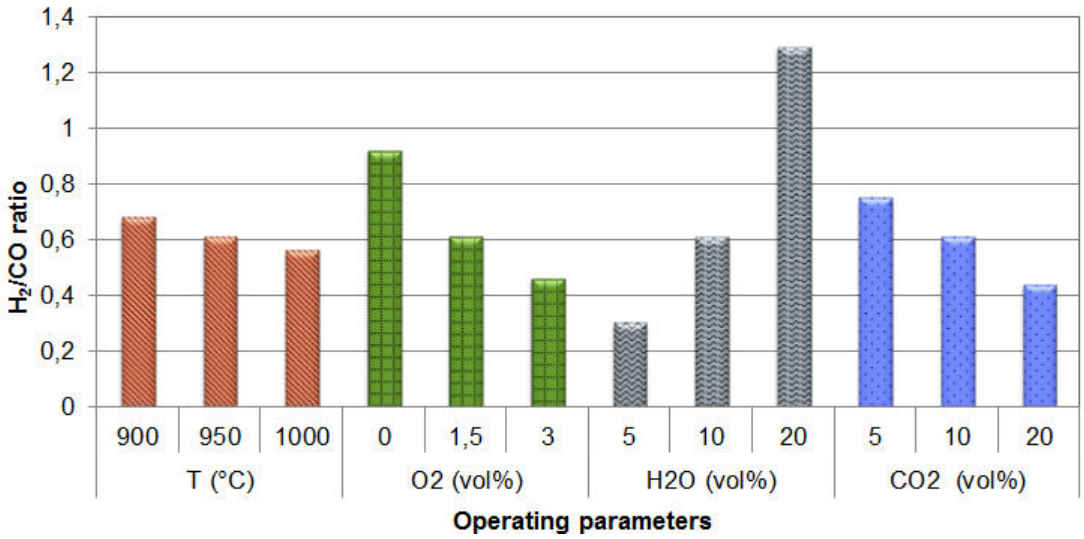

FIGURE 6.4: Effect of inlet bed temperature and gas composition on syngas H2/CO ratio. Reference condition: T = 950 °C, O_2 = 1.5 vol%, H_2O = 10 vol%, CO_2 = 10 vol%

6.2.3 Heat duty analysis

The gasifier heat duty is the external heat added to heat the feedstock up to the gasification temperature, to meet any shortfall in the gasification reaction heat requirement, and for wall losses from the reactor. As shown in Figure 6.5, char enters with its chemical energy and sensible heat; the gasifying agents enter with sensible heat at the reference temperature (25 °C); the product gas, with its chemical energy, leaves at the gasifier temperature; unburnt char (ash) leaves with a potential energy in it; and the unutilized steam and other gases also leave the at the gasification temperature.

The heat duty is calculated by performing an overall energy balance on the gasifier as shown below:

Energy input: Enthalpy of (char + steam + oxygen + nitrogen + carbon dioxide) at reference temperature + heating value of char + external heat (heat duty).

Energy output: Enthalpy of product gas at gasifier temperature + heating value of product gas + heat in residual char/ash + heat of gasification reaction + heat loss from the reactor.

If A and W are the flowrates of air and steam respectively needed to gasify 1 mol/s of char (C), we can calculate the heat duty Q_{duty} (kJ/kg) by performing an energy balance on the gasifier, taking 25 °C as the reference:

$$\begin{aligned} Q_{duty} = 1/C \Big[& \Big(c_{p_{CO}} \dot{n}_{CO} + c_{p_{CO_2}} \dot{n}_{CO_2} + c_{p_{CH_4}} \dot{n}_{CH_4} + c_{p_{H_2}} \dot{n}_{H_2} + c_{p_{O_2}} \dot{n}_{O_2} + c_{p_{N_2}} \dot{n}_{N_2} \Big) T_g \\ & + (1 - X_g)\, W H_g + P_a\, q_a + Q_r + Q_{loss} + Q_{syngas} \\ & - (A c_{p_a} T_0 + c_{p_C} T_0 + W H_0 + HHV) \Big] \end{aligned} \tag{6.38}$$

Where H_0 and H_g are the enthalpies of steam at the reference temperature and the gasifier exit temperature; c_{p_j} and $\dot{n}_j$ are the molar specific heat and molar flowrate of species j, at temperature T_g leaving the gasifier; $(1 - X_g)\, W$ is the net molar flowrate of steam remaining in the syngas; P_a is the flowrate of the residual char (ash); and q_a is the heating value of the ash. Q_{loss} is the total heat loss through the wall Q_{syngas} is the amount of energy in the syngas, and Q_r is the net heat of reaction.

The heat duty analysis was performed with the aim to determine the temperature at which the gasifier could operate adiabatically or autothermally (i.e. $Q_{duty} \simeq 0$) under different inlet steam concentrations (Reference condition: T = 950 °C, O_2 = 1.5 vol%, H_2O = 10 vol%, CO_2 = 10 vol%). The gasifier temperature was fixed in the range of 700 - 950 °C, and the steam concentration was varied between 5 and 20 vol%. Figure 6.6 shows the results of the analysis, which reveals that the gasifier achieves near adiabatic conditions at a temperature of 760 °C. This is close to the exit-gas temperature of a typical downdraft gasifier, which is about 700 °C [36].

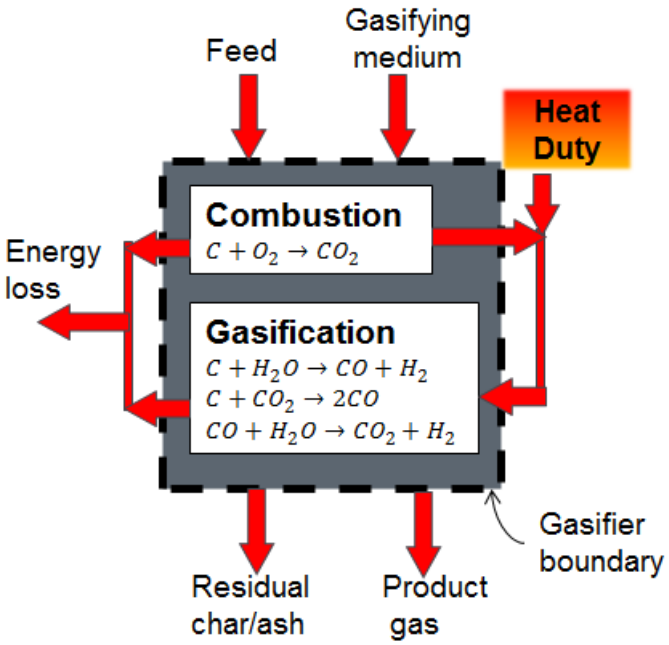

FIGURE 6.5: Energy flow in and out of a gasifier

6.3 Wood waste pyro-gasification model

6.3.1 Gasifier model and general assumptions

Following the development and validation of the char gasification model, submodels for wood drying, pyrolysis and combustion were added. A representation of the complete model for wood waste pyro-gasification is shown in Figure 6.7, where air is injected from the top and side of the reactor in order to combust part of the pyrolysis volatiles and char so as to provide heat for the endothermic drying, pyrolysis and gasification processes.

Generally, the model assumptions made for the char gasification model (see section 6.1.1) were retained for the pyro-gasification model. Most importantly, the single temperature field treatment of the gas and solid phases was maintained, especially as the wood waste and air were assumed to enter the reactor at ambient temperature (i.e. no pre-heating).

For the char gasification and combustion models, it was assumed that the residual chlorine in the char after pyrolysis of wood/PVC, did not have a significant effect on the reaction rates. This assumption was verified by performing thermogravimetric tests on char from wood/PVC pellet pyrolysis under different oxidising atmospheres and temperatures as shown in Figure 6.8. The results show that the residual chlorine in char from the pyrolysis of 5 wt% PVC/poplar wood (PW) (Cl = 2.85 wt%), does not have a significant influence on the rate of char combustion and gasification. Thus, the correlation functions developed by Teixeira et al. [98] of char conversion rates during during reactions with H_2O, CO_2 and O_2 were retained. However, it

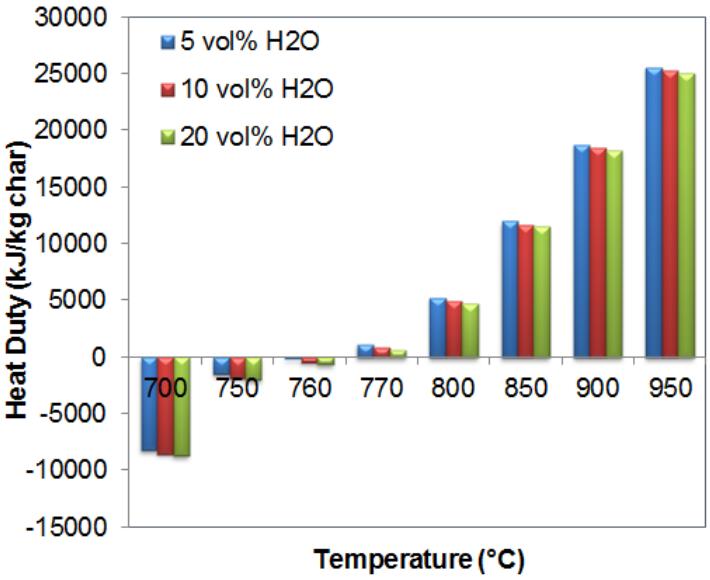

FIGURE 6.6: Gasifier heat duty (Reference condition: T = 950 °C, O_2 = 1.5 vol%, H_2O = 10 vol%, CO_2 = 10 vol%)

is clear in Figure 6.8a. that chlorine content has a significant influence on wood pyrolysis rate, and hence, the apparent kinetics model developed in Chapter 5 for wood/PVC pyrolysis was used in this model.

6.3.2 Drying model

To model the drying of wood particles in the bed, an Arrhenius type drying model featuring vaporization and condensation was used [248]. This model uses a temperature threshold of 95 °C above which water evaporates and below which it condenses (Eq. 6.39 and 6.40).

Moisture $\xrightarrow{k_{d1}}$ water vapour,

$$\omega_{vap} = A_{d1} exp\left(\frac{E_{d1}}{RT}\right) \rho_w \quad \text{if T} > 95\ ^\circ\text{C} \tag{6.39}$$

Water vapor $\xrightarrow{k_{d2}}$ moisture,

$$\omega_{cond} = k_{d2} \left\|\mathbf{U_g}\right\| \rho_g\, y_{steam} \quad \text{if T} < 95\ ^\circ\text{C} \tag{6.40}$$

6.3.3 Pyrolysis model

Assumptions

- Although for the overall pyro-gasification process, the particles are assumed to be thermally thin due to the steep temperature profile along the downdraft gasifier, apparent kinetics will be used for the pyrolysis process.

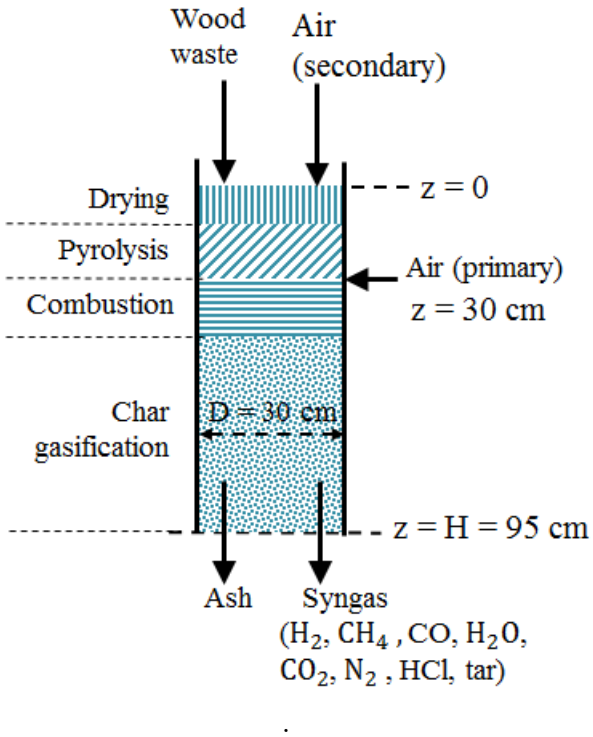

FIGURE 6.7: Model representation of wood waste pyro-gasification in a downdraft reactor

- A six-step parallel reaction scheme is considered for the wood waste containing PVC. The fractions of gases, tars and chars produced, as well as the gas composition, are determined experimentally.
- Tars undergo secondary cracking in one-step process to produce secondary gases, whose composition are also determined experimentally.

Reaction scheme

The primary pyrolysis of wood waste containing PVC (B) to produce char, primary gas and tar is given by the global reaction in Equation 6.41.

$$B \xrightarrow{k_{p1.i(i=1,\ldots6)}} y_c CHAR + y_g GAS_1 + y_T TAR, \quad \Delta H_{r,p1} = -420\ kJ/kg \tag{6.41}$$

Where y_j is the mass fraction of the product species j. The tar product under goes thermal cracking to produce secondary gases in a one-step reaction:

$$TAR \xrightarrow{k_{p2}} GAS_2, \quad \Delta H_{r,p2} = +42\ kJ/kg \tag{6.42}$$

By considering that the volatile fraction of wood waste contains six pseudo-components - hemicellulose (H), cellulose (C), lignin (L), HCl, hemicellulose-HCl (H-HCl) and cellulose-HCl (C-HCl), that decompose independently of each other, their devolatilization reactions are represented by Equations 6.43 - 6.48:

$$y_H H \xrightarrow{k_{p1.1}} V_H \tag{6.43}$$

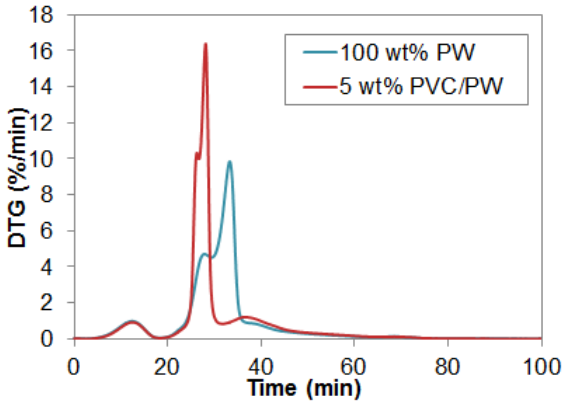

(A) Pyrolysis: N_2, 10 °C/min

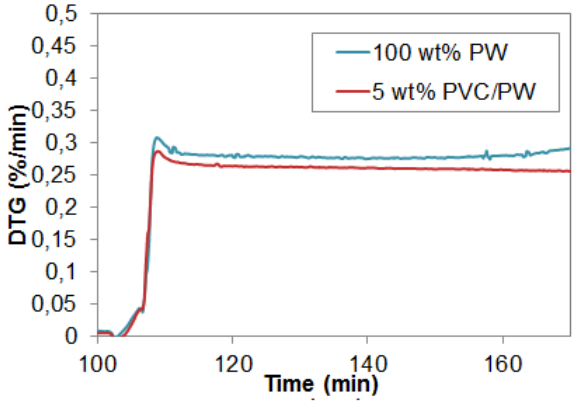

(B) Combustion: 8 vol% O_2/N_2, 900 °C

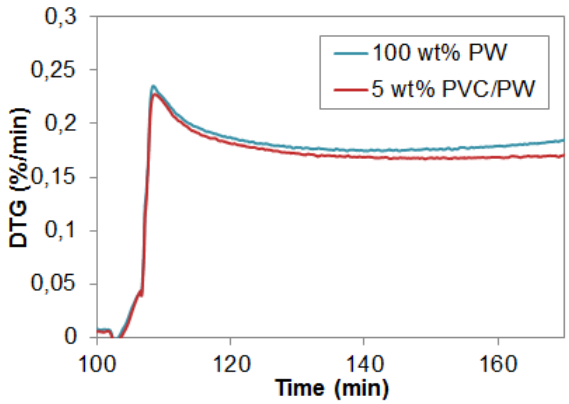

(C) Boudouard: 20 vol% CO_2/N_2, 900 °C

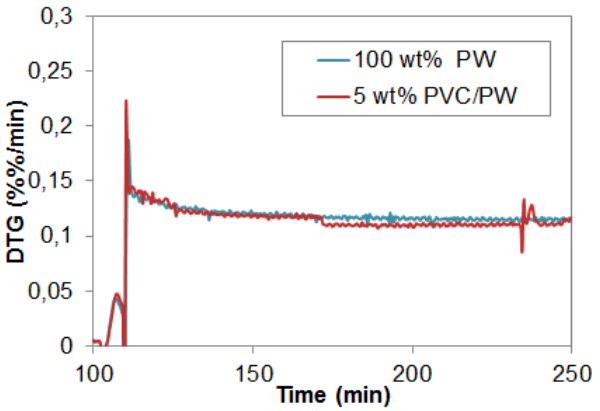

(D) Steam gasification: 60 % RH at 400 °C, 1000 °C

FIGURE 6.8: Comparing DTG curves of char pellets of 100 wt% Poplar wood (PW) and 5 wt% PVC/PW at different pyro-gasification conditions

$$y_C C \xrightarrow{k_{p1.2}} V_C \tag{6.44}$$

$$y_L L \xrightarrow{k_{p1.3}} V_L \tag{6.45}$$

$$y_{HCl} HCl \xrightarrow{k_{p1.4}} V_{HCl} \tag{6.46}$$

$$y_{H-HCl} H - HCl \xrightarrow{k_{p1.5}} V_{H-HCl} \tag{6.47}$$

$$y_{C-HCl} C - HCl \xrightarrow{k_{p1.6}} V_{C-HCl} \tag{6.48}$$

where V_j are the volatiles released from the decomposition of the pseudo-components.

Reaction kinetics

Equation 6.49 gives the reaction rate $y_{p1.i}$ (kg/m^3/s), for the pyrolysis of each pseudo-component (Eq. 6.43 - 6.48), in terms of its conversion rate $\omega_{p1.i}$ (s^{-1}) and

initial wood density $\rho_{B,0}$ (kg/m^3).

$$y_{p1.i} = \omega_{p1.i}\,\rho_{B,0} \tag{6.49}$$

The Arrhenius parameters ($A_{p1.i}$, $E_{p1.i}$) and kinetic model $f(\alpha_j)$, for determining the pseudo-component conversion rates $\omega_{p1.i}$ (Equation 6.50), have been determined in Chapter 5 for wood and PVC pellets. The parameters obtained for 1 % wood/PVC pyrolysis are summarized in Table 6.5 and will be used as the reference parameters.

$$\omega_{p1.i} = A_{p1.i}\exp\left(\frac{-E_{p1.i}}{RT}\right) f\left(\alpha_j\right) \tag{6.50}$$

By taking the sum of the pseudo-component reaction rates $y_{p1.i} = 1, 2...6$, the production term for wood waste r_B can be expressed as:

$$r_B = \sum_{j=1}^{6} y_{p1.ij} y_{p1.i} \tag{6.51}$$

where $y_{p1.ij}$ denotes the stoichiometric coefficient (mass fraction) of each pseudo component species j in reaction $p1.i$. The initial values $y_{p1.ij,0}$ are equivalent to those of c_j determined in Chapter 5, and are displayed in Table 6.5 for 1 % wood/PVC pyrolysis.

As for tar secondary cracking, the production term for this reaction is given by [50]:

$$r_T = \epsilon A_{p2}\, exp\left(-\frac{E_{p2}}{RT}\right)\rho_T \tag{6.52}$$

where ϵ is the bed porosity.

6.3.4 Combustion model

The combustion reactions employed in this model are those involving the volatile and char products from pyrolysis [50]. These reactions given in Equations 6.53 - 6.57, with their corresponding kinetic parameters in Table 6.6. The inclusion of tar combustion posed the greatest difficulty in converging the model as the quantity of tar produced from pyrolysis is significantly higher than that of the other volatile products and thus, its combustion is highly exothermic. To resolve this problem, the molar stoichiometric coefficient of oxygen ($\nu_{k_{c5},O_2} = 0.867$) was raised to a value of 6 in order decrease the amount of tar consumed by oxidation, and thus reduce the quantity of heat released.

Indeed, we have henceforth designated ν_{k_{c5},O_2} as our model adjustment parameter, which is valid because in any case, its value in Equation 6.57 was determined empirically for virgin wood, and we expect the composition of tar to vary a lot from one feedstock to another. For instance, we have clearly shown in chapter 4 - section 4.5.3 that the addition of 1 wt% PVC to wood waste significantly increases the concentration of aromatic compounds, PAHs and furans in the tar product, and therefore, we expect the combustion stoichiometry of this tar to be very different from

Table 6.5: Kinetic parameters for the pyrolysis of 1% PVC/wood, and tar cracking.

Specie	Parameter	Value/Expression	Ref.
H	$E_{p1.1}$ (kJ/mol)	136.34	chapter 5
	$A_{p1.1}$ (min^{-1})	2.62 x 10^{13}	
	$f(\alpha_H)$	$(1-\alpha_H)^{1.4}$	
	$y_{p1.1H,0}$	0.12	
C	$E_{p1.2}$ (kJ/mol)	216.71	chapter 5
	$A_{p1.2}$ (min^{-1})	5.60 x 10^{19}	
	$f(\alpha_C)$	$2\left(\alpha_C^{0.5}-\alpha_C\right)$	
	$y_{p1.2C,0}$	0.25	
L	$E_{p1.3}$ (kJ/mol)	112.56	chapter 5
	$A_{p1.3}$ (min^{-1})	3.60 x 10^{09}	
	$f(\alpha_L)$	$f(\alpha_L)=(1-\alpha_L)^{2.9577}\alpha_L^{-0.008}$	
	$y_{p1.3L,0}$	0.21	
HCl	$E_{p1.4}$ (kJ/mol)	120.13	chapter 5
	$A_{p1.4}$ (min^{-1})	6.38 x 10^{10}	
	$f(\alpha_{HCl})$	$2\left(\alpha_{HCl}^{0.5}-\alpha_{HCl}\right)$	
	$y_{p1.4HCl,0}$	0.0053	
H-HCl	$E_{p1.5}$ (kJ/mol)	101.56	chapter 5
	$A_{p1.5}$ (min^{-1})	3.84 x 10^{10}	
	$f(\alpha_{H-HCl})$	$2\left(1-\alpha_{H-HCl}\right)\left[-ln\left(1-\alpha_{H-HCl}\right)\right]^{0.5}$	
	$y_{p1.5H-HCl,0}$	0.25	
C-HCl	$E_{p1.6}$ (kJ/mol)	108.18	chapter 5
	$A_{p1.6}$ (min^{-1})	1.42 x 10^{10}	
	$f(\alpha_{C-HCl})$	$2\left(1-\alpha_{C-HCl}\right)\left[-ln\left(1-\alpha_{C-HCl}\right)\right]^{0.5}$	
	$y_{p1.6C-HCl,0}$	0.16	
Tar	E_{p2} (kJ/mol)	107	[249]
	A_{p2} (s^{-1})	4.28 x 10^{6}	[249]

Table 6.6: Kinetic parameters for combustion reactions

Specie	Parameter	Value	Ref.
Char	E_{c1} (kJ/mol)	160	[250]
	A_{c1} (min^{-1})	5.67 x 10^9	[250]
CO	E_{c2} (kJ/mol)	166	[251]
	A_{c2} ($(m^3/mol)^{0.75}/sK$)	$10^{17.6}$	[251]
CH_4 = Tar	$E_{c3} = E_{c5}$(kJ/mol)	80	[251]
	$A_{c3} = A_{c5}((m^3/mol)^{0.5}/sK)$	9.2 x 10^6	[251]
H_2	E_{c4} (kJ/mol)[a]	42	[251]
	A_{c4} (m^3/s mol)[a]	10^{11}	[251]

[a] Estimated by Di Blasi [50]

the tar of wood waste pyro-gasification without added PVC. Thus, an interesting perspective for this modelling work is to experimentally determine ν_{k_{c5},O_2} for the combustion of tars produced from the pyrolysis of different wood waste feedstock.

$$C + O_2 \xrightarrow{k_{c1}} CO_2, \quad \Delta H_{r,c1} = -394\ kJ/mol \tag{6.53}$$

$$CO + 0.5O_2 \xrightarrow{k_{c2}} CO_2, \quad \Delta H_{r,c2} = -283\ kJ/mol \tag{6.54}$$

$$CH_4 + 2O_2 \xrightarrow{k_{c3}} CO_2 + 2H_2O, \quad \Delta H_{r,c3} = -803\ kJ/mol \tag{6.55}$$

$$H_2 + 0.5O_2 \xrightarrow{k_{c4}} H_2O, \quad \Delta H_{r,c4} = -286\ kJ/mol \tag{6.56}$$

$$(tar)\ CH_{1.522}O_{0.0228} + 0.867O_2 \xrightarrow{k_{c5}} CO + 0.761H_2O, \quad \Delta H_{r,c5} = -243\ kJ/mol \tag{6.57}$$

6.3.5 Boundary conditions

The boundary conditions were the same as those for the char gasification submodel, except that the reactor inlet temperature T_0 for the solid and gas phase was fixed at ambient temperature, T_0 = 25 °C. A mesh convergence study was conducted and 2000 cells were found to be the optimum value.

6.4 Validation of wood waste gasification model

The model predictions have been validated against the experimental results of the pilot-scale gasification of Class B wood waste containing 1 wt% PVC ($\simeq$ 0.6 % Cl), which has been previously discussed in Chapter 4. The feedstock characteristics are displayed in Table 4.1. Table 6.7 shows the operating conditions at the reactor inlet, where the primary and secondary air injection points are schematically represented in Figure 6.7. To obtain data on the primary pyrolysis products of Class B wood waste containing 1 wt% PVC, an experiment was performed in a fixed bed reactor under conditions typically encountered in downdraft pyro-gasification (Table 6.8). The results of the primary pyrolysis product yields and gas composition are presented in Table 6.9, which also displays literature data [252] on the secondary gas composition (GAS_2) from tar cracking, obtained for wood.

Table 6.7: Reactor inlet operating conditions for the pilot-scale gasification of Class B wood containing 1 wt% PVC

Operating parameters	
Wood waste flowrate (kg/h)	11
Primary air flowrate (Nm^3/h)	17.7
Secondary air flowrate (Nm^3/h)	3.8
Temperature at reactor inlet (°C)	25
Total pressure (atm)	1.01

Table 6.8: Operating conditions for the primary pyrolysis of Class B wood containing 1 wt% PVC in a fixed bed reactor

Operating parameters	
Pyrolysis temperature (°C)	500
Heating rate (°C/min)	20
Duration of plateau at 500 °C (min)	30
Nitrogen flowrate (Nm^3/h)	0.3
Gas residence time in reactor (s)	14
Total pressure (atm)	1.0

6.4.1 Reactor outlet conditions

Table 6.10 compares the experimental and predicted reactor outlet conditions. The predicted outlet temperature is 767 °C which is 22 % higher than the measured temperature. This error can be improved in the following way:

- Account for the partial oxidation of char to produce CO and CO_2 by replacing Equation 6.53 with Equation 6.58. This will decrease the heat of combustion by 178 kJ/mol and thus decrease the reactor outlet temperature.

TABLE 6.9: Pyrolysis data for Class B wood waste containing 1 wt % PVC: gas composition is expressed as a mass percentage of the initial waste feedstock.

Pyrolysis products		Yield
	y_C	0.24
	y_G	0.51
	y_T	0.25
GAS_1	H_2	0.1 %
	CH_4	1.2 %
	CO	11.1 %
	CO_2	13.6 %
	H_2O	25 %
	HCl	0.2 %
GAS_2	CO_2	9.5 %
	CO	5.7 %
	CH_4	3.8 %

- Increase the molar stoichiometric coefficient of oxygen (ν_{k_{c5},O_2}) in Equation 6.57. As previously discussed in Section 6.3.4, the value of ν_{k_{c5},O_2} was raised from 0.867 to 6 in order to decrease the extent of tar oxidation and thus decrease the heat generated from this reaction. Hence, the predicted reactor temperature can be reduced by further increasing the value of ν_{k_{c5},O_2}, or better still, by determining its value experimentally so as to have a more realistic reaction exothermicity.

As seen in Table 6.10, the model results for overall wood waste conversion and tar composition in syngas are similar to the experimental measurements. Regarding HCl composition in syngas, the model predicts 450 ppm as opposed to 54 ppm HCl analysed in the syngas. Given that 34 % error was obtained in relation to the chlorine balance on the pilot reactor due to HCl loss in the sampling line(see Chapter 4), we can assume that the maximum concentration of HCl in the syngas is 538 ppm. Thus, the deviation of 16 % between the model result and the maximum HCl concentration in syngas is considered to be satisfactory.

TABLE 6.10: Experimental and predicted results for the reactor outlet conditions of wood waste pyro-gasification.

	Model	Experiment
Temperature, T(°C)	767	629
Wood waste conversion, X	97.8	94.4
Tar in syngas (wt %)	0.0	0.2
HCl in syngas (ppm)	450	54 (max = 538)

6.4.2 HCl gas concentration and reactor temperature profiles

To further investigate the model's ability to predict the behaviour of the gasifier, the evolution of HCl concentration and temperature along the reactor bed were studied. We can observe in Figure 6.9, four distinct zones. Firstly, at the reactor inlet, a flat temperature profile can be seen which corresponds to an almost instantaneous drying at temperatures below 100 °C. As the temperature increases to 265 °C near the reactor inlet, the pyrolysis of the wood waste occurs which releases HCl gas. In the pyrolysis zone (bed height $<$ 22 cm), the HCl concentration reaches 950 ppm. At a bed height of 30 cm, air is injected, which partially oxidises the pyrolysis char and volatile products. As this reaction is highly exothermic, high temperatures can be observed near the air injection point (Figure 6.9). Furthermore, due to the large increase in gas production in this zone, the concentration of HCl decreases sharply. In the gasification zone (bed height $>$ 30 cm), the temperature decreases owing to the endothermic char gasification and tar cracking reactions. Based on this analysis, we can conclude that our model gives coherent results for the profiles of HCl concentration and reactor temperature, considering the complexity of the reactions involved.

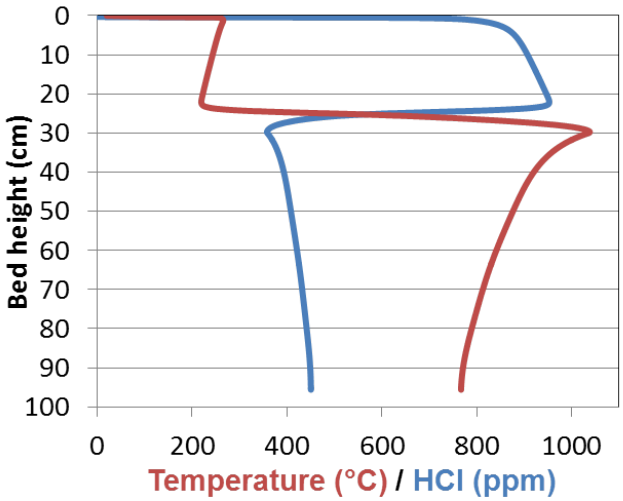

FIGURE 6.9: Model results for the profiles of HCl gas concentration and reactor bed temperature in wood waste pilot gasifier.

6.4.3 Syngas composition

Figure 6.10 displays the model prediction and experimental results of the exit syngas composition. We can observe that the model makes satisfactory predictions of N_2, CO_2, O_2 and CH_4 content in syngas whereas discrepancies can be seen in the results for H_2, CO and H_2O composition.

To improve the syngas composition prediction, the following modifications to the model's gasification reaction scheme may be required:

- Introduce the partial oxidation of char in order to increase the concentration of CO in syngas [253].

$$\Omega C + O_2 \overset{k_{c1}}{\rightarrow} 2\,(\Omega - 1)\,CO + (2 - \Omega)\,CO_2, \quad \Delta H_{r,c1} = -216\ kJ/mol \tag{6.58}$$

where Ω represents the number of moles of C consumed by one mole of O_2.

- Lower the oxidation kinetic rates of CO and H_2 in order to increase the content of these syngas components as well as lower CO_2 and H_2O compositions respectively:

$$CO + 0.5O_2 \overset{\beta k_{C2}}{\rightarrow} CO_2 \tag{6.59}$$

$$H_2 + 0.5O_2 \overset{\gamma k_{C4}}{\rightarrow} H_2O \tag{6.60}$$

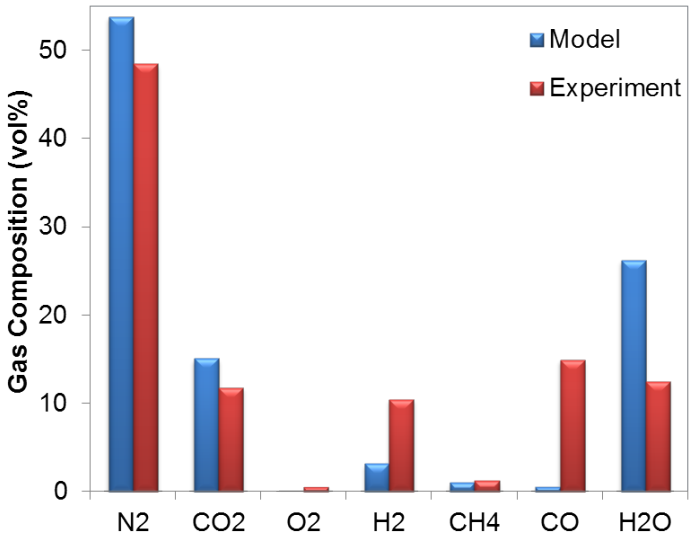

FIGURE 6.10: Experimental vs. numerical results for the composition of syngas at the wood waste pilot gasifier outlet.

Conclusion

In this chapter a 1D, CFD model has been developed to simulate the pyro-gasification of wood waste contaminated with a small amount of PVC (chlorine) in a downdraft gasifier at study state. The char-gasification zone of the reactor was first modelled and was found to be in good agreement with experimental data found in literature. Sensitivity analyses on the influence of bed porosity, inlet temperature and gas composition on the gasifier output data were performed. The results showed that the bed porosity had an insignificant influence on the bed behaviour and therefore could be rightly assumed constant, whereas the concentration of oxygen and steam in the inlet gas had the strongest influence on the syngas H_2/CO ratio. Furthermore, a heat duty analysis was conducted by performing an overall energy balance on the gasifier, which revealed that the downdraft gasifier was able to operate under autothermal conditions when the gasifier temperature was fixed at 760 °C.

In the second part of the model development work, submodels of drying, pyrolysis and combustion were added to the char-gasification model in order to simulate the complete pyro-gasification process of wood waste. For the pyrolysis model, the kinetic parameters obtained in Chapter 5 for the conversion rate of wood containing small amounts of PVC, were used. Furthermore, the tar oxidation reaction in the combustion submodel created stability problems during model simulation runs due to the combined high reaction exothermicity and tar content in the gasifier. A solution was eventually found by increasing the stoichiometric coefficient of oxygen in the reaction.

The complete model was validated using data obtained from a pilot-scale pyro-gasification test, which was performed with Class B wood waste feedstock containing 1 wt% PVC (0,6 wt% Cl). The model results were found to be in good agreement with experimental data in relation to the reactor outlet conditions (i.e. waste conversion, HCl and tar composition in syngas) as well as the profiles of temperature and HCl concentration along the reactor bed. However, improvements to the model are required in order to better predict the permanent gas composition and reactor outlet temperature.

CHAPTER 7

Syngas cleaning: HCl removal using inorganic sorbents

Introduction

Dry adsorption has been proposed as a promising method for removal of acid gases (e.g. SO_2 and HCl) in pyro-gasification and combustion processes based on chemical reactions with particulate basic solids (sorbents) [16, 254–257]. In literature, various sorbents for HCl removal have been studied, and can be classified into three groups: alkali-based sorbents, alkaline-earth based sorbents and other metal based sorbents.

- Alkali-based sorbents studied by researchers are mostly sodium and potassium compounds due to their strong HCl binding capabilities [258–261]. For example, Krishnan et al. [262] have shown that Nahcolite ($NaHCO_3$) can remove HCl from a gas mixture to concentrations as low as 1 ppm in the temperature range of 525 - 650 °C.

- Although the performance of alkaline earth-based sorbents is lower than that of alkali-based sorbents, they are significantly cheaper, and thus have attracted the attention of many researchers.[263–267]. Slaked lime ($Ca(OH)_2$), limestone ($CaCO_3$) and quicklime (CaO) are the most commonly studied, which have been shown to strongly bind to HCl in temperature range of 500-600 °C [268–271].

- Other metal based sorbents containing aluminium, iron, and zinc have also received considerable research interest.[263, 272, 273]. As an example, studies by Ohtsuka et al. [274] have shown that the addition of Al_2O_3 to Na_2CO_3 can reduce HCl in syngas to less than 1 ppm at 400 °C.

In this work, four different sorbents will be evaluated for their performance in HCl capture: CCW-S, CCW-D, Bicar and Lime. CCW-S and CCW-D are solid wastes recovered from an industrial process for producing sodium carbonate. CCW-S is a calcium carbonate residue that has been carbonated naturally for a long time by carbon dioxide in the atmosphere. On the other hand, CCW-D has been produced by a fast artificial carbonation process. In contrast to CCW-S and CCW-D, Bicar and Lime are commercial products, which are used for flue gas treatment of acid gases at industrial level. The experiments conducted with these sorbents will involve the adsorption of HCl in nitrogen and syngas atmospheres at ambient conditions, in order to study the influence of gas matrix on the sorbent performance. Various physico-chemical characterisation methods will be conducted on the sorbents before and after the tests and will be linked to the sorbent adsorption behaviour.

7.1 Experimental methods

7.1.1 Sample characterization

The physico-chemical properties of CCW-S, CCW-D, Bicar and Lime were analyzed before and after the tests using various techniques. Their mineral content was determined using an inductively coupled plasma with an atomic emissions spectra (ICP-AES, HORIBA Jobin-Yvon Ultima 2). Fourier transform infrared spectrometry

(FTIR, 8400S - Shimadzu) and thermogravimetric analyses (TGA, SDTQ600) were employed to indentify molecular bonds and semi-quantify the mineral compounds in the sorbents, respectively. Furthermore BET analyses were performed to determine the specific surface are of the particles, using Micromeritics 3Flex analyzer. The structures of the crystalline phases were studied using X-ray diffraction (XRD, Philips Panalytical X'pert Pro MPD diffractometer) and environmental scanning electron microscopy (ESEM, XL30 ESEM aparatus - FEI Company) in order to obtain information related to the particles' morphology. A Transition electrion microscope coupled to an energy dispersive X-ray (TEM-EDX) was employed to perform imaging and elemental mapping of chemical species in the samples.

Before characterization and tests, all four sorbents were sieved to obtain samples with particle sizes below 315 μm, and then dried at ambient temperature for 48 hours. For analyses with FTIR, reference samples of calcium carbonate ($CaCO_3$ - calcite, from Fisher Scientific), slaked lime ($Ca(OH)_2$, from Acros Organics) and sodium bicarbonate ($NaHCO_3$, from Acros Organics) were used, with each sample having more than 98 % purity.

7.1.2 Experiments with HCl in nitrogen

Gas matrix

The first set of experiments were performed with a 500 ppmv mixture of hydrogen chloride in nitrogen (HCl/N_2). These tests were peformed with all four sorbents, CCW-S, CCW-D, Bicar and Lime, in order to compare their HCl adsorption performance under ambient conditions (25 °C, 1 atm).

Reactor and operating conditions

Figure 7.1 gives a schematic representation of the experimental setup for the tests. A glass fixed-bed reactor (height = 120 mm, internal diameter = 10 mm), was equipped with a porous glass disc to hold the sorbent particles and allow the passage of gas through the sorbent bed. The bed height was kept at 7.58 mm for all sorbents by adjusting the mass of sorbent used for the experiments (0.3 - 0.5 g) according to their bulk densities. After placing the sorbents in the reactor, glass beads (4.2 g, 1 mm size) were added as inert particles to maintain the bed height. The 500 ppmv HCl/N_2 gas passed through the sorbent bed in a downward flow at a flowrate of 50 mL/min which was controlled by a mass flow meter. Thus, the gas residence time in the sorbent bed was maintained at 0.714 s.

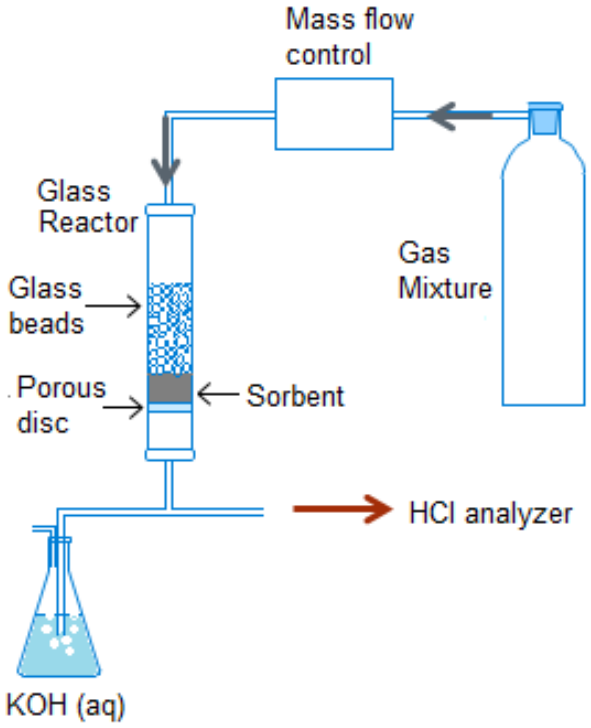

FIGURE 7.1: Experimental setup

Gas sampling and analysis

A sample of gas was collected at the reactor outlet using a gas cell, and then analyzed for its HCl content using FTIR. Figure 7.2 gives an example of the infrared spectrum of HCl in 500 ppmv HCl/N_2 gas mixture, which appears as a series of regular peaks between 2650 cm^{-1} and 3100 cm^{-1}. The residual HCl gas was scrubbed in an aqueous solution of KOH as shown in Figure 7.1.

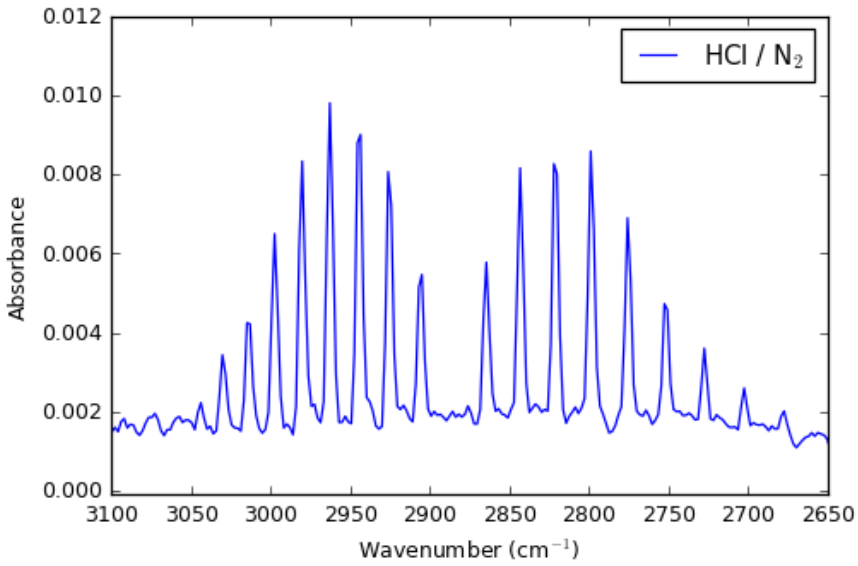

FIGURE 7.2: Infrared spectrum of 500 ppmv HCl/N_2 (25 °C, 1 atm)

7.1.3 Experiments with HCl in syngas

Gas matrix

The second set of experiments involved the use of 200 ppmv HCl in a simulated syngas matrix (HCl/Syngas), whose composition is shown in Table 7.1. These experiments were performed under ambient conditions (25 °C, 1 atm).

Table 7.1: Composition of syngas mixture used in experiments

Components	Nominal value	Analytical value
Hydrogen chloride, HCl (ppmv)	200	232
Methane, CH_4 (vol%)	5	4.96
Carbon dioxide, CO_2 (vol%)	25	24.9
Hydrogen, H_2 (vol%)	30	30.6
Carbon monoxide, CO (vol%)	Balance	Balance

Reactor and operating conditions

For experiments with HCl/Syngas, an online HCl analyzer named ProCeas was used which will be further described in the next section. In order to minimize the response time of this analyzer, a higher gas flowrate of 500 mL/min was used. Thus, to maintain the gas residence time in the sorbent bed at 0.714 s, a larger reactor (height = 168 mm, internal diameter = 14 mm) was used and a bed height of 39 mm was fixed. For these experiments, a sorbent mass of 4-5 g was used depending on the sorbent bulk density.

Gas sampling and analysis

FTIR technique could not be used to analyze the concentration of HCl in the syngas matrix because the infrared spectrum of methane, CH_4, overlapped that of HCl as shown in Figure 7.3. Hence, a new HCl analyzer called ProCeas was employed, which was manufactured by AP2E. ProCeas uses an enhanced IR laser technology called Optical Feedback Cavity Enhanced Absorption Spectroscopy (OFCEAS), which enables simultaneous online analysis of HCl and CH_4. During the experiments, the analyzer was directly connected to the reactor outlet and the HCl gas concentration was recorded at 1-second intervals.

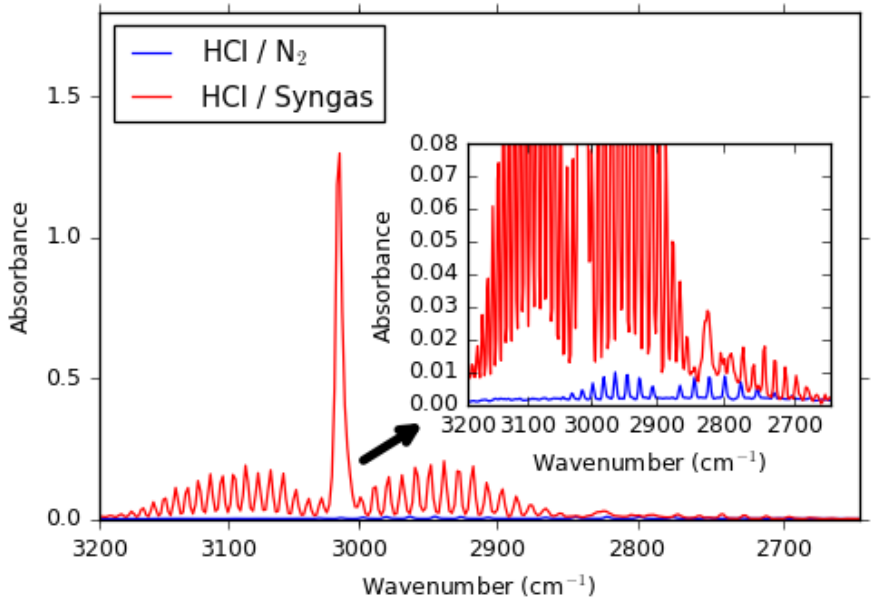

FIGURE 7.3: Zoom of infrared spectrums of 500 ppmv HCl/N_2 and 200 ppmv HCl/Syngas (25 °C, 1 atm)

7.2 Results and discussions

7.2.1 Characteristics of sorbents before experiments

Physical characteristics

Table 7.2 displays the bulk density, surface area and particle diameter of the sorbents before the experiments were performed. The BET results revealed the absence of mesopores and micropores in the sorbents, thus resulting in low values of surface area.

TABLE 7.2: Physical characteristics of sorbents before tests

Sorbent	Bulk density (kg/m^3)	Surface area (m^2/g)	Particle diameter, d_{50} (μm)
CCW-S	839.9	5	113
CCW-D	1149.6	7	348
Bicar	985.7	13	136
Lime	528.9	1	350

ICP

Table 7.3 displays the composition of inorganic elements in the sorbents before the tests. It can be observed that CCW-S, CCW-D and Lime mainly contain Ca, whereas majority of Bicar is composed of Na. CCW-S and CCW-D also have a

significant concentration of contaminants (Al, Fe and Mg) due to their waste origin. Furthermore, although Bicar and Lime are both commercial products, Bicar has a considerably higher purity.

TABLE 7.3: ICP results of sorbent materials before tests

Sorbent	Ca (g/kg)	Na (g/kg)	Al (g/kg)	Fe (g/kg)	Mg (g/kg)
CCW-S	454.76	-	1.81	3.97	2.68
CCW-D	388.77	-	1.36	2.54	4.21
Bicar	1.60	192.86	0.22	0.07	0.05
Lime	453.72	0.47	1.00	1.14	2.93

FTIR

Figure 7.4 shows the infrared spectra of CCW-S, CCW-D, Bicar and Lime as well as the reference spectra of pure $CaCO_3$, $NaHCO_3$ and $Ca(OH)_2$. Compared to pure $CaCO_3$, CCW-S and CCW-D show similar peaks at 1404, 873 and 713 cm^{-1}, which correspond to C-O bonds [275]. This suggests that calcium carbonate (calcite) is a major compound in these two industrial wastes. Furthermore, the spectrum of Bicar is almost identical to that of pure $NaHCO_3$, with peaks appearing between 600 and 1926 cm^{-1}. Regarding Lime, a peak appears at 3600 cm^{-1} due to vibrations of the O-H bond in $Ca(OH)_2$. A small peak also appears at 1404 cm^{-1} which shows that a small amount of $CaCO_3$ is present in Lime as a result of the spontaneous reaction between $Ca(OH)_2$ and CO_2 in air, at ambient conditions [275].

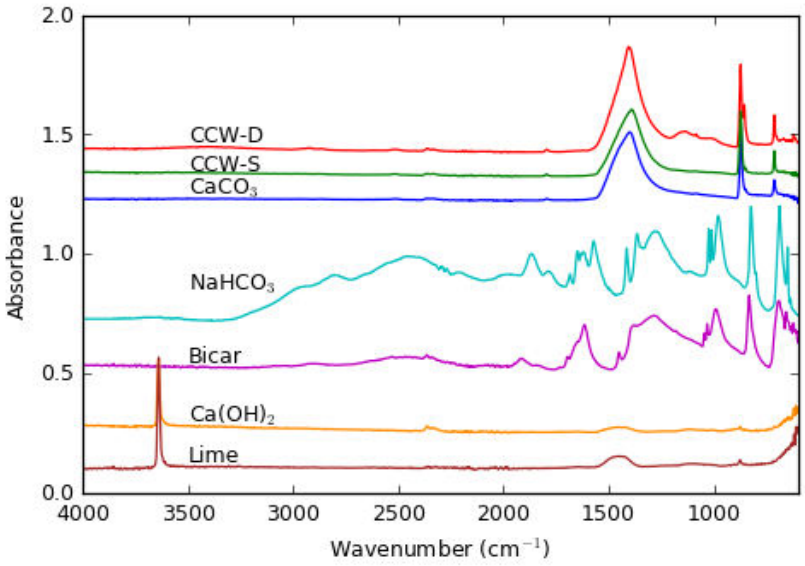

FIGURE 7.4: Infrared spectra of sorbents and reference compounds before tests

XRD

XRD analysis was performed in order to identify the crystalline structure of the inorganic compounds in the sorbents. The results are displayed in Table 7.4 and Figure 7.5. For CCW-S, the XRD analysis shows that calcium carbonate is the main component of this material, which has a rhombohedral structure that characteristic of calcite. In contrast, the XRD results reveal that CCW-D is a mixture of calcite (rhombohedral structure) and aragonite (orthorhombic structure). The presence of aragonite is explained by the fast artificial carbonation of CCW-D. For Bicar, we can observe the presence of only $NaHCO_3$ with a monoclinic crystalline structure, whereas in the case of Lime, two crystalline phases are observed: calcium hydroxide with a hexagonal structure, and calcite with a rhombohedral crystal shape. These results are in agreement with the observations made using the FTIR technique. Crystals of the impure elements detected by ICP (Al, Fe and Mg) have not been identified by XRD possibly because their concentrations are below the instrument's detection limit.

Table 7.4: XDR results of sorbents before tests

Sorbent	Reference code	Compound name	Chemical formula	Crystal system
CCW-S	00-047-1743	Calcium carbonate	$CaCO_3$	Rhombohedral
CCW-D	00-047-1743	Calcium carbonate	$CaCO_3$	Rhombohedral
	96-900-0227	Aragonite	$CaCO_3$	Orthorhombic
Bicar	00-021-1119	Sodium hydrogen carbonate	$NaHCO_3$	Monoclinic
Lime	01-081-2041	Calcium hydroxide	$Ca(OH)_2$	Hexagonal
	00-047-1743	Calcium carbonate	$CaCO_3$	Rhombohedral

TGA

Thermogravimetric analysis (TGA) was performed on the sorbents in order to semi-quantify their composition. Samples of the sorbents (20-30 mg) were heated from 30 °C and 1200 °C at a heating rate of 5 °C/min, under nitrogen atmosphere (100 mL/min). The TG and DTG curves obtained are shown in Figure 7.6. We can see that CCW-S decomposes in a one-step process between 556 and 743 °C with a corresponding mass loss of 40.4 wt%. Based on the results from ICP, FTIR and XRD analysis, we know that CCW-S is largely composed of $CaCO_3$, which decomposes by the following reaction:

$$CaCO_3(s) \rightarrow CaO(s) + CO_2(g) \tag{7.1}$$

Thus, the observed mass loss of 40.4 wt% in Figure 7.6a corresponds to the release of CO_2. Therefore, based on stoichiometric calculations, the content of $CaCO_3$ in CCW-S is estimated to be 91.8 wt%.

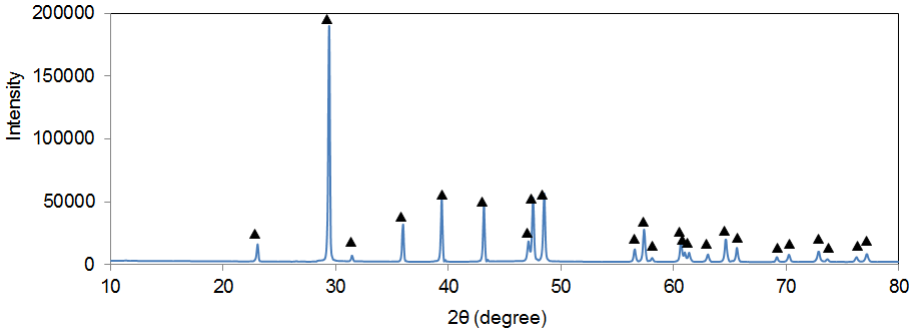

(A) CCW-S

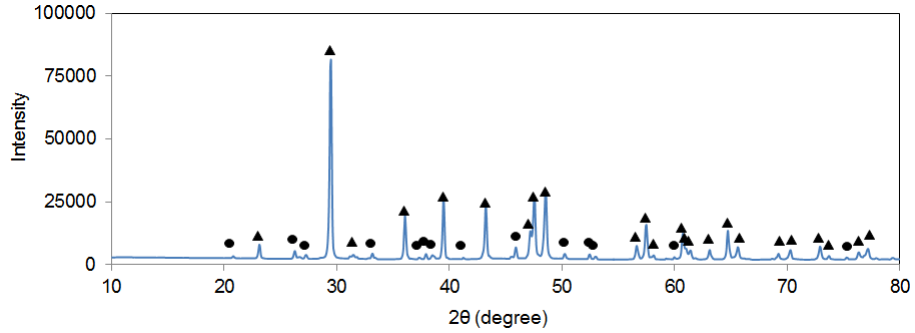

(B) CCW-D

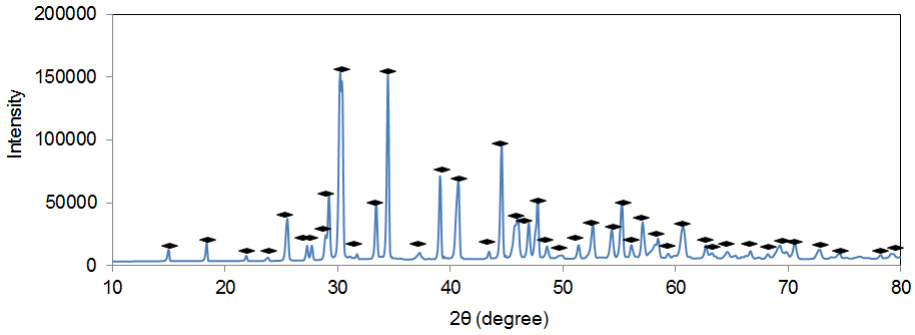

(C) Bicar

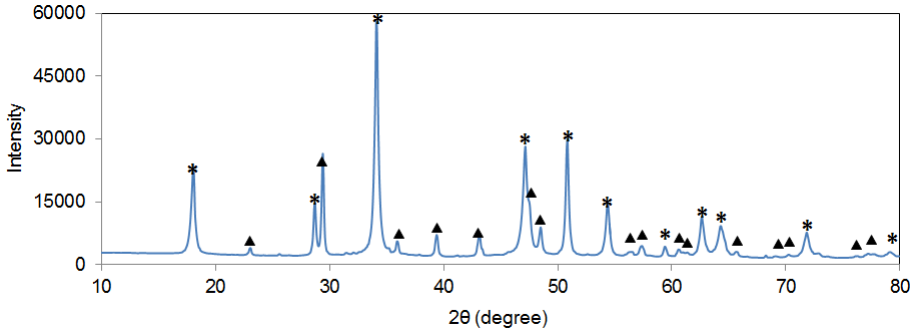

(D) Lime

FIGURE 7.5: XDR results of sorbents before tests. (▲) Calcium carbonate - rhombohedral, (●) Aragonite-orthorhombic, (⧫) Sodium hydrogen carbonate - monoclinic, (∗) Calcium hydroxide - hexagonal

By repeating this same analysis for CCW-D, we can observe in Figure 7.6b, a large DTG peak at 558-766 °C and a small peak at 760-891 °C. This corresponds to the decomposition of $CaCO_3$ (Eq. 7.1), and possibly $MgCO_3$ (7.2), respectively.

$$MgCO_3(s) \rightarrow MgO(s) + CO_2(g) \tag{7.2}$$

Based on this decomposition scheme, the composition of CCW-D was calculated to be 86 wt% $CaCO_3$ and 4 wt% $MgCO_3$. For both CCW-S and CCW-D a mass loss of 3 wt% and 6 wt% respectively can be observed at temperatures below 600 °C, which can be attributed to surface water evaporation and the decarbonation of impurities.

Figures 7.6c and 7.6d display the TG/DSC curves for Bicar and Lime respectively. Regarding Bicar, the decomposition of $NaHCO_3$ occurs at 90-163 °C, and based on stoichiometric calculations using Equation 7.3, the weight content of $NaHCO_3$ is calculated to be 99.9 wt%. In the case of Solid Lime, its thermal decomposition was divided into two steps. The first one occurs in the range of 300-425 °C, which involves the dehydration of $Ca(OH)_2$ (70 wt%) via the reaction in Equation 7.4. The second decomposition step occurs at 530-690 °C which corresponds to the decomposition of $CaCO_3$ (21.6 wt%) (Eq. 7.1). This confirms the FTIR and XRD results which show that $Ca(OH)_2$ was initially partially carbonated to form $CaCO_3$. A summary of the estimated mass composition of the sorbents is provided by Table 7.5.

$$2NaHCO_3 \rightarrow Na_2CO_3 + H_2O + CO_2 \tag{7.3}$$

$$Ca(OH)_2 \rightarrow CaO + CO_2 \tag{7.4}$$

Table 7.5: Composition of materials calculated from TG results

Sample	CCW-S	CCW-D	Bicar	Lime
$CaCO_3$ (wt%)	91.8	86.0	-	21.6
$MgCO_3$ (wt%)	-	4.0	-	-
$NaHCO_3$ (wt%)	-	-	99.9	-
$Ca(OH)_2$ (wt%)	-	-	-	70.0

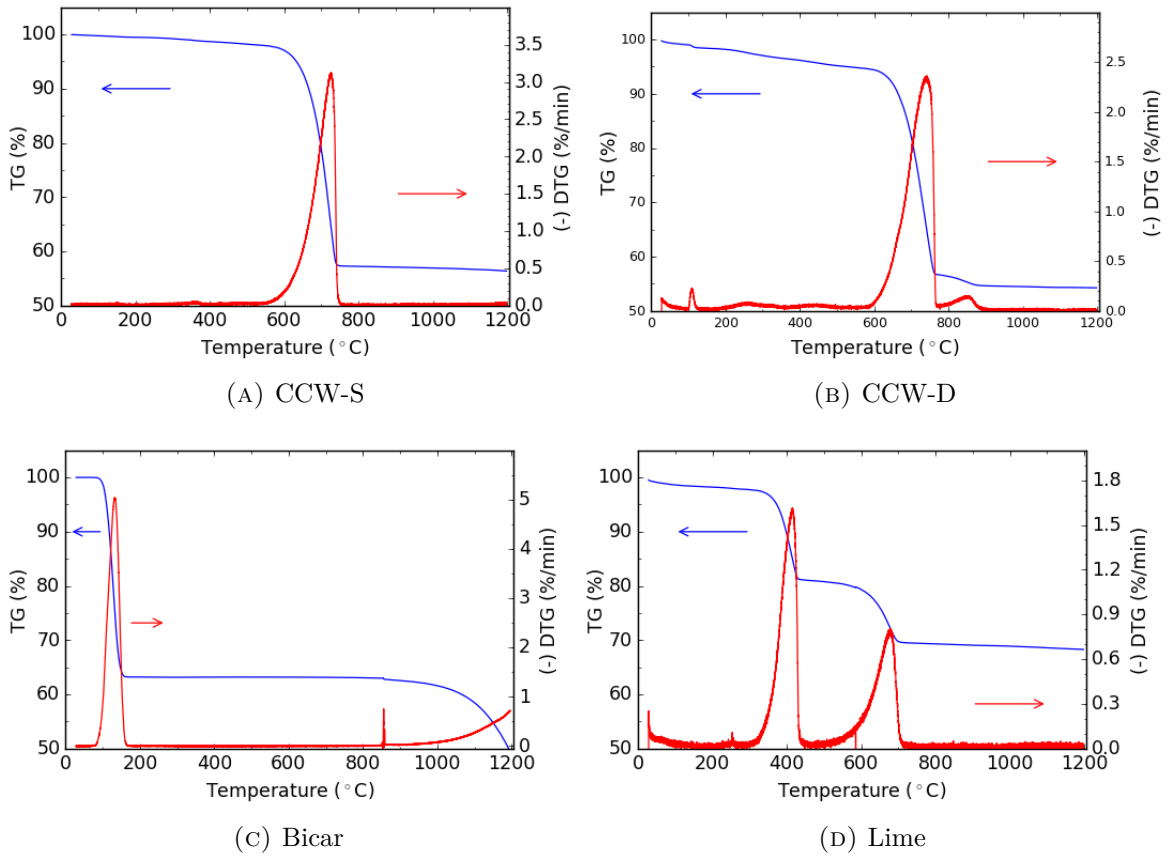

(A) CCW-S (B) CCW-D

(C) Bicar (D) Lime

FIGURE 7.6: Thermogravimetric curves of sorbents before tests

7.2.2 Adsorption of HCl in nitrogen

Breakthrough curves

Figure 7.7 displays the breakthrough curves obtained for the tests with 500 ppmv HCl/N_2 gas, which shows the evolution of the exit HCl concentration with time. Henceforth, we will define the breakthrough time t_b as the duration for which the exit HCl concentration is zero. The corresponding t_b value for each sorbent is displayed in Table 7.6. The tests were repeated at least twice for each sorbent, and the results show that adsorption tests with Bicar and CCW-S are repeatable with a deviation in t_b of 2.4 % and 6.5 % from the mean value respectively. However, the tests with CCW-D and Lime produce non-repeatable results which could be due to several reasons including heterogeneity of the samples and gas by-pass of the sorbents during the tests due voids created as a result of particle settling [276]. Further examination will be required to adequately explain these discrepancies in repeatability.

Nonetheless, it is obvious from Figure 7.7 and Table 7.6 that Bicar has the longest breakthrough time of 64 h and the highest HCl adsorption capacity of 26.8 wt%, where the HCl adsorption capacity was calculated by dividing mass of adsorbed HCl by the initial sorbent mass. Thus, we can see in Table 7.6 that the sorbents' performance in decreasing order is, Bicar > Lime > CCW-S > CCW-D.

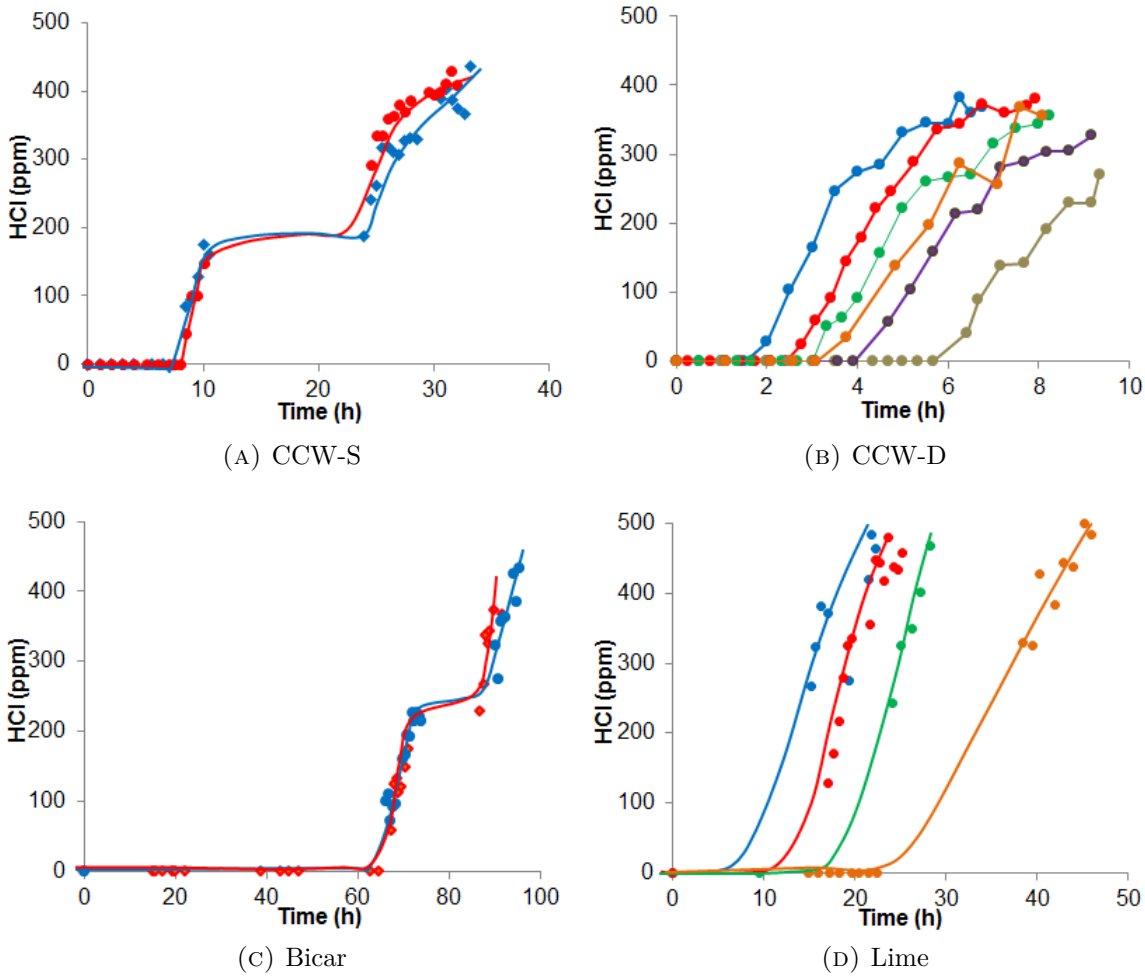

(A) CCW-S (B) CCW-D

(C) Bicar (D) Lime

FIGURE 7.7: Breakthrough curves for tests under HCl/N_2 gas conditions (25 °C, 1 atm)

A low adsorption capacity is undesirable because this means a low efficiency of HCl removal or a high consumption of sorbents is achieved. These results are coherent with those of several authors who have found calcium-based sorbents to be less reactive with HCl than sodium-based sorbents [259–262, 274, 277]. An explanation for the relatively slow reactions of $CaCO_3$ (CCW-S, CCW-D) and $Ca(OH)_2$ (Bicar) with HCl gas has been provided by Duo et al. [231] who compare their thermodynamic properties and mass transfer limitations. For $CaCO_3$ and HCl reactions, chemical free energy ΔG_c, at 25 °C is only -30 kJ/mol, which provides a very low driving force for the reaction to occur. Although $Ca(OH)_2$ + HCl reaction has a very high ΔG_c of -130 kJ/mol, and is thus expected to achieve high conversion rates, a dense and non-porous product layer is formed around the $Ca(OH)_2$ particle which limits the transfer of HCl to the reaction interface, and thus drastically slows down the reaction. This mechanism will be explained in more detail in section 7.2.2. Furthermore, although CCW-S and CCW-D are both $CaCO_3$ - based sorbents, CCW-S is seen to have a higher breakthrough time than CCW-D, which may be mainly because CCW-S contains roughly 16 % more Ca than CCW-D in Table 7.3.

Table 7.6: Break through times and HCl adsorption capacities of CCW-S, CCW-D, Bicar and Solid Lime in HCl/N_2 atmosphere (25 °C, 1 atm)

Sorbent	t_b (h)	Chloride capacity (wt %)
CCW-S	7.5 - 8.0	3.9
CCW-D	1.5 - 5.7	0.5 - 2.0
Bicar	64.7 - 66.3	26.8
Lime	8 - 24	6.2 - 18.6

In Figure 7.7, a plateau can be osberved for tests with CCW-S and Bicar at an outlet HCl concentration of at 200 - 250 ppm which does not appear for CCW-D and Lime. This may require further investigation but is currently out of scope of this work.

TEM-EDX

TEM-EDX analysis was performed on CWW-S and Bicar particles to qualitatively investigate the effect of the major elements - Ca, C, O, Na - and inorganic elements - Ca, Na, Al, Fe and Mg - on the formation of new products at the sorbent surface. Figure 7.8 displays the cartographic pictures of the distribution of inorganic elements on the surface of a CCW-S particle after the test with HCl/N_2 gas. The particle in this figure clearly shows Cl (HCl) fixed on its surface. In addition, the cartographs of Ca and Cl are almost identical which implies that a chlorinated product is formed on the particle. The elements, O and C, also have a similar distribution on the particle surface as Ca which indicates that not all of $CaCO_3$ in the particle is converted. Furthermore, the impurities - Al, Fe and Mg - appear to also adsorb HCl although in relatively small amounts because of their low content in the CCW-S sample.

Figure 7.9 displays the TEM-EDX cartograph of a Bicar particle. As seen by the brightness of the cartograph, Cl (HCl) is strongly fixed onto a portion of the Bicar particle surface to form a chlorinated product. It is also obvious that not all of $NaHCO_3$ is converted because the elements, O and C, are present and have a similar distribution as Na on the particle. As a result of the high purity of Bicar (Table 7.3), a small scatter of Al, Fe and Mg can be seen on the particle surface, in the same region as Cl, which indicates that these impurities also adsorb HCl just as they do for CWW-S. The adsorption of HCl by Mg and Al has been well documented in literature [272, 278–280].

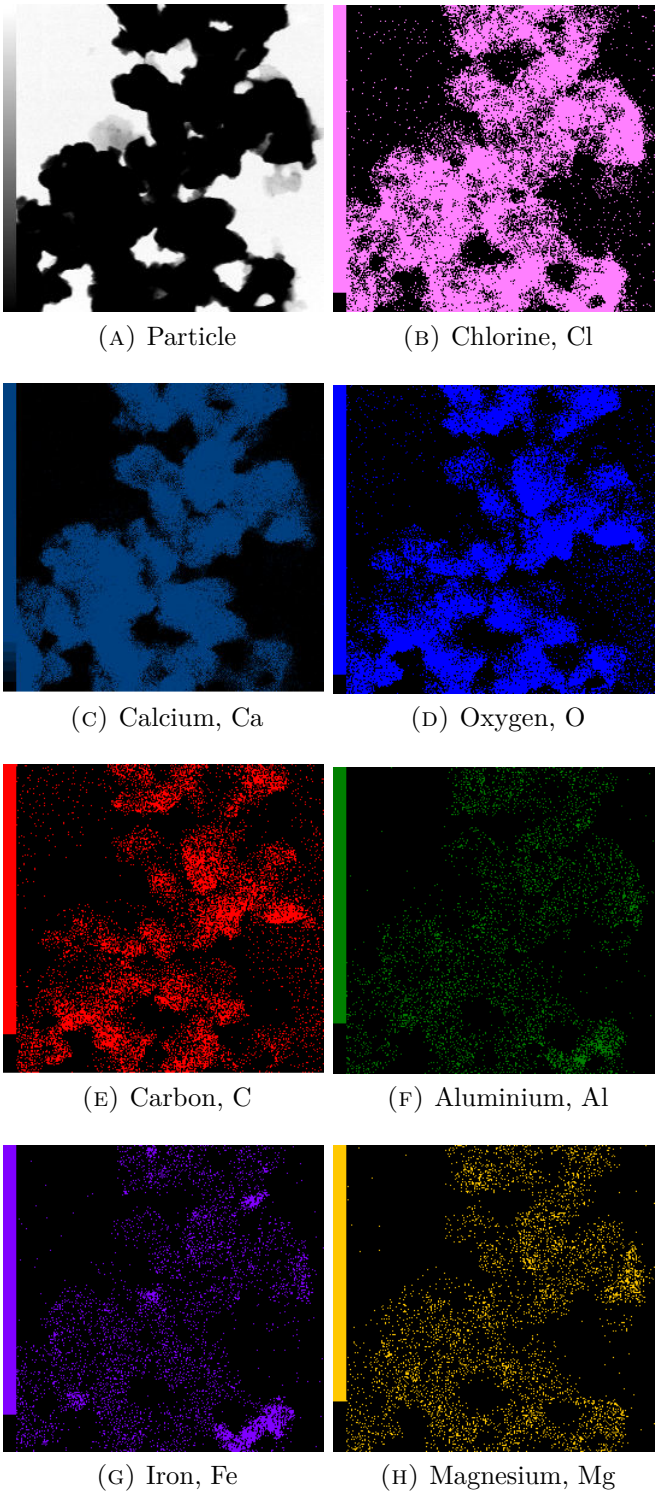

(A) Particle (B) Chlorine, Cl

(C) Calcium, Ca (D) Oxygen, O

(E) Carbon, C (F) Aluminium, Al

(G) Iron, Fe (H) Magnesium, Mg

FIGURE 7.8: TEM-EDX cartographic photos of CCW-S particles after tests under HCl/N_2 gas conditions (25 °C, 1 atm)

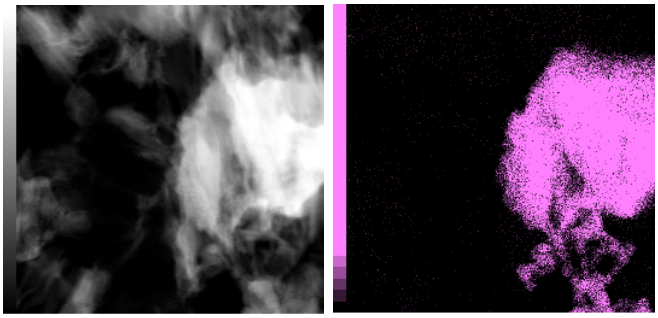

(A) Particle (B) Chlorine, Cl

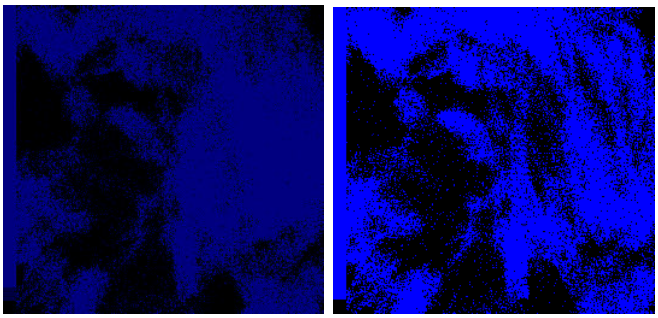

(C) Sodium, Na (D) Oxygen, O

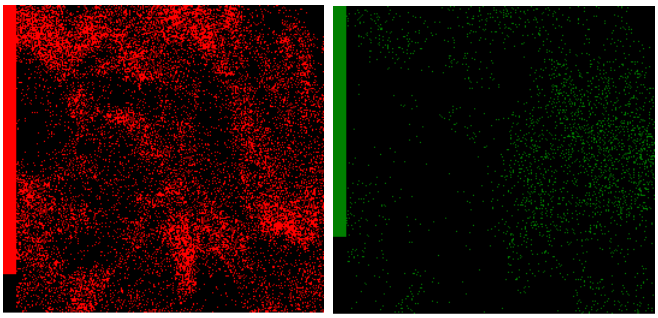

(E) Carbon, C (F) Aluminium, Al

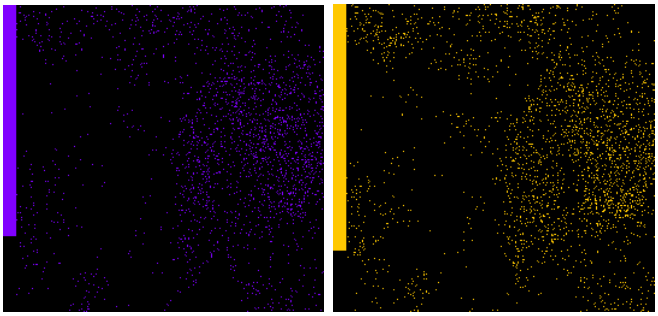

(G) Iron, Fe (H) Magnesium, Mg

FIGURE 7.9: TEM-EDX cartographic photos of Bicar particles after tests under HCl/N_2 gas conditions (25 °C, 1 atm)

XRD

The crystalline structures of all four sorbents after tests with HCl/N_2 gas are displayed in Table 7.7 and Figure 7.10. The results show that the CCW-S and CCW-D sorbents after the tests largely contain the same $CaCO_3$ crystal structures as before the tests (Table 7.5), and therefore, the content of any chlorine-containing crystal in the sorbent is below the detection limit of the XRD analyzer. This is expected due to the low reactivity of CCW-S and CCW-D observed in Table 7.6, implying that the CCW-S particle analysed using the TEM-EDX technique was one of the few that actually adsorbed HCl to form chlorinated products via the following possible reactions.

$$CaCO_3 + 2HCl \leftrightharpoons CaCl_2 + H_2O + CO_2 \tag{7.5}$$

$$CaCO_3 + HCl \leftrightharpoons CaClOH + CO_2 \tag{7.6}$$

For Bicar, NaCl crystals of cubic structure were detected alongside $NaHCO_3$. This indicates that Bicar adsorbed HCl via the chemical reaction:

$$NaHCO_3 + HCl \leftrightharpoons NaCl + CO_2 + H_2O \tag{7.7}$$

In the case of Lime, calcium chloride hydroxide, CaClOH, was detected along with the main crystals, $Ca(OH)_2$ and calcium carbonate $Ca(CO)_3$. Thus, CaOHCl might be the product of the reactions in Equations 7.6 and 7.8.

$$Ca(OH)_2 + HCl \leftrightharpoons CaClOH + H_2O \tag{7.8}$$

According to Partanen et al. [281], Tongamp et al. [282] and Chyang et al. [266], CaClOH initially forms from the reaction of lime and HCl at low temperatures, but it decomposes at higher temperatures (> 200 °C) to form the more stable $CaCl_2$ product.

Table 7.7: XRD results of crystalline structures present in sorbents after tests with HCl/N_2

Sorbent	Reference code	Compound name	Chemical formula	Crystal system
CCW-S	00-047-1743	Calcium carbonate	$CaCO_3$	Rhombohedral
CCW-D	00-047-1743	Calcium carbonate	$CaCO_3$	Rhombohedral
	96-900-0227	Aragonite	$CaCO_3$	Orthorhombic
Bicar	00-021-1119	Sodium hydrogen carbonate	$NaHCO_3$	Monoclinic
	96-900-8679	Halite	NaCl	Cubic
Lime	01-081-2041	Calcium hydroxide	$Ca(OH)_2$	Hexagonal
	00-047-1743	Calcium carbonate	$CaCO_3$	Rhombohedral
	00-036-0983	Calcium chloride hydroxide	CaClOH	Hexagonal

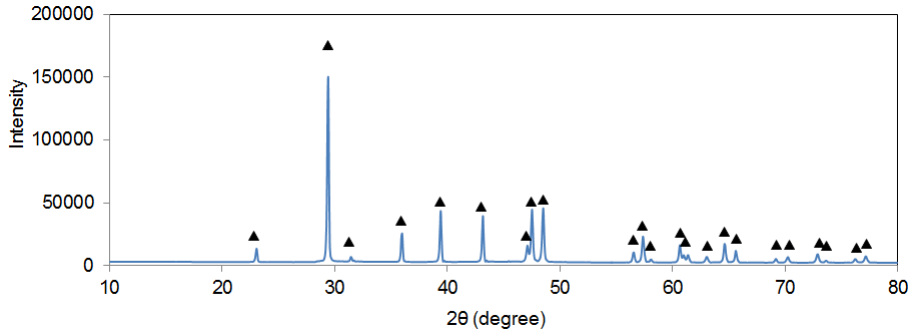

(A) CCW-S

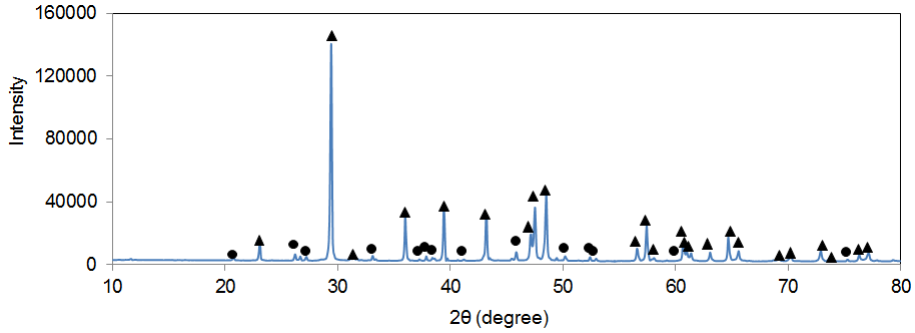

(B) CCW-D

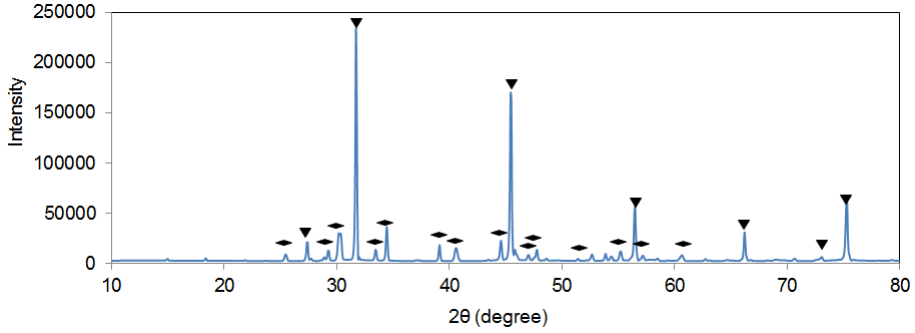

(C) Bicar

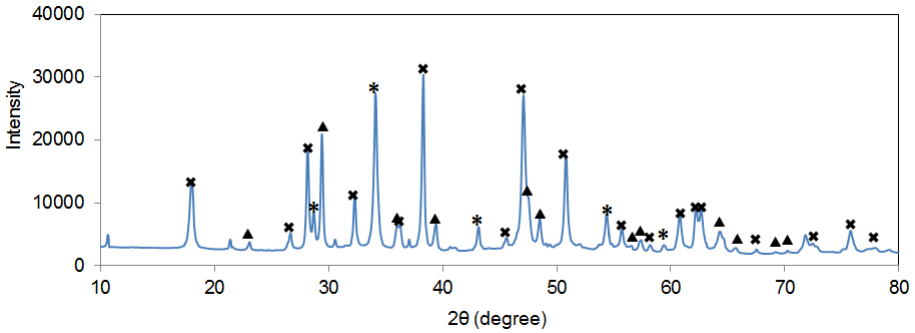

(D) Lime

FIGURE 7.10: XDR results of sorbents after tests under HCl/N_2 gas conditions (25 °C, 1 atm). (▲) Calcium carbonate - rhombohedral, (●) Aragonite-orthorhombic, (⧫) Sodium hydrogen carbonate - monoclinic, (∗) Calcium hydroxide - hexagonal, (×) Calcium chloride hydroxide - hexagonal

ESEM

ESEM analysis of the particle surfaces of all four sorbents, before and after the tests, are shown in Figure 7.12. There are no significant differences in the surface structures of CCW-S and CCW-D before and after the tests under HCl/N_2 atmosphere. This confirms the XRD results in Tables 7.4 and 7.7 that showed no changes in the crystal system of these sorbents.

Bicar particles after HCl adsorption, are seen to have deposits of cubic crystals on their surface which are not present on the original particles. These cubic crystals correspond to the NaCl crystals detected using XRD (Table 7.7). With regards to Lime, deposits of CaClOH crystals on the smoother surface of the Lime particles can be observed in the photo taken after the test. These results as well as those of the XRD analysis, confirm the formation of a chlorinated-product layer on particles of Bicar and Lime as a result of chemisorption of HCl on the particles. Furthermore, by taking a closer look at the product layer structure, we can see that the NaCl particles formed on Bicar are large and well spaced out, whereas the CaClOH crystals are small and form a dense layer on the Lime particles. This observation confirms the aforementioned model developed by Duo et al. [231]. that predicts that the high chemical potential energy of the reaction between HCl and the $Ca(OH)_2$ particles in Lime will result in a dense non-porous layer, and thus lead to a low reaction rate. The mechanism of this model will be briefly explained below using the illustration provided by Duo et al. [231] in Figure 7.11.

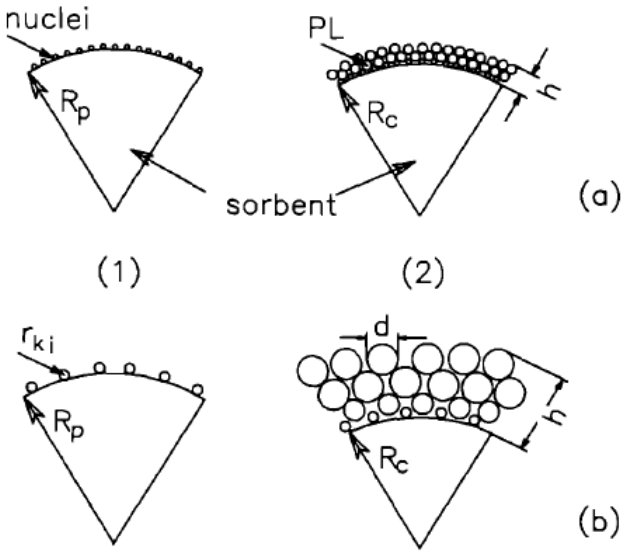

FIGURE 7.11: Schematic presentation of the mechanism of product layer formation: (row a) lower conversion; (row b) higher conversion; (column 1)initial nucleation: (column 2) structure of product layer (PL) (where r_{ki}= critical radius of initial nuclei; d= size of developed crystals; h = PL thickness; R_p = initial radius of reacting particle; R_c = radius of unreacted core) [231]

Consider a reaction of a gas with a non-porous particle, which can be described by a shrinking unreacted core model, where a product layer (PL) is formed as a shell outside the unreacted core (radius R_c), the reaction occurs at the interface between the unreacted core of the sorbent and the product layer, and the gases

diffuse through the PL of thicknes h, (Figure 7.11). In the initial reaction, the total free energy change ΔG, for the formation of a spherical nucleus is expressed as [231]:

$$\Delta G = 4\pi r^2\sigma + (4/3)\pi r^3\rho\Delta G_c \tag{7.9}$$

Where ΔG_c is the chemical free energy change of reaction per mol of the solid product formed, ρ is the molar density of the solid product, r is the radius of the nucleus, and σ (>0) is the surface energy per unit area. There is a critical radius r_{ki}, at which ΔG reaches a maximum. Thus, a nucleus with a radius exceeding r_{ki} tends to grow in order to reduce its total free energy, and eventually leads to a stable nucleus. For a forward reaction, $\Delta G_c < 0$, and thus a large ΔG_c leads to a small r_{ki} and subsequently to the formation of a dense and non-porous product layer as shown in Figure 7.11a. A small ΔG_c leads to a value of $r_k i$ too large for the nuclei to be formed. This model, also called the 'crystallisation and fracture' model, suggests the existence of optimum values of ΔG_c (i.e. ΔG_c between -30 kJ/mol and -130 kJ/mol), which generate well-spaced out and porous product layer as displayed in Figure 7.11b. Therefore, given that the NaCl particles formed on Bicar are large and well spread in Figure 7.12f., we can expect that its ΔG_c is closer to the optimum value than that of the reaction to form CaClOH crystals on Lime particles.

7.2.3 Adsorption of HCl in syngas

Due to their good adsorption test repeatabilities under HCl/N_2 atmosphere, CCW-S and Bicar were chosen as sorbents for experiments using 200 ppmv HCl/Syngas mixture. The breakthrough curves and sorbent performance results for these tests are shown in Figure 7.13 and Table 7.8. We can see that the breakthrough times, t_b, for CCW-S and Bicar are 2.7 h and 48.2 h respectively, which in comparison to their corresponding values under HCl/N_2 gas, is a significant decrease of 5.3 h and 16.5 h respectively. Furthermore, the HCl adsorption capacities of the two sorbents dramatically decrease in the presence of syngas.

To verify that this decrease in performance of CCW-S and Bicar was not due to reactor scale-up and the change in HCl analyzer, an adsorption test was repeated with CCW-S in the 'large' reactor configuration using 500 ppm HCl/N_2 gas. The results were then compared with those obtained with the 'small' reactor set-up under the same atmosphere. Figure 7.14 shows that, despite the difference in reactor scale and HCl analyzer, the value of t_b remained 8 h, and thus, the breakthrough time was unaffected by the reactor and HCl analyzer used. We can therefore attribute the reduced performance of CCW-S and Bicar to competitive interactions that occured between HCl and the syngas components at the active sites of the sorbents.

In literature, several authors have studied the influence of gas atmosphere composition on HCl adsorption capacity of carbon-based and sodium-based sorbents [271, 283–285]. All authors agree that the presence of CO_2 and H_2O significantly lowers the performance of the sorbents and they attribute this to the shift of the equilibrium position to the left in the reversible reactions in Equations 7.5, 7.6 and 7.7 due to the increase in the partial pressures of CO_2 and H_2O. However, CO_2 has

much more influence of this shift in equilibrium position than H_2O, and hence, the mechanism is called sorbent recarbonation.

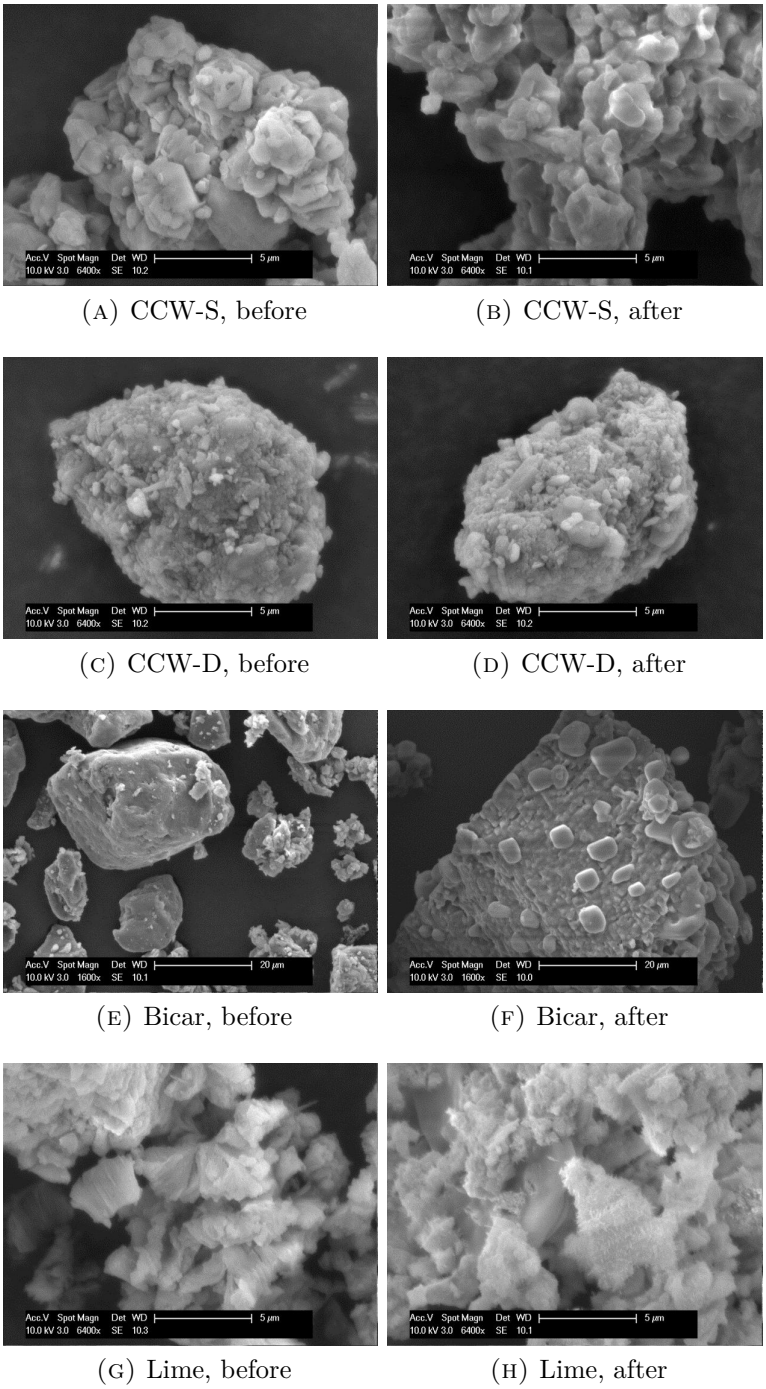

(A) CCW-S, before (B) CCW-S, after

(C) CCW-D, before (D) CCW-D, after

(E) Bicar, before (F) Bicar, after

(G) Lime, before (H) Lime, after

FIGURE 7.12: ESEM photos of sorbents before and after tests under HCl/N_2 gas conditions (25 °C, 1 atm).

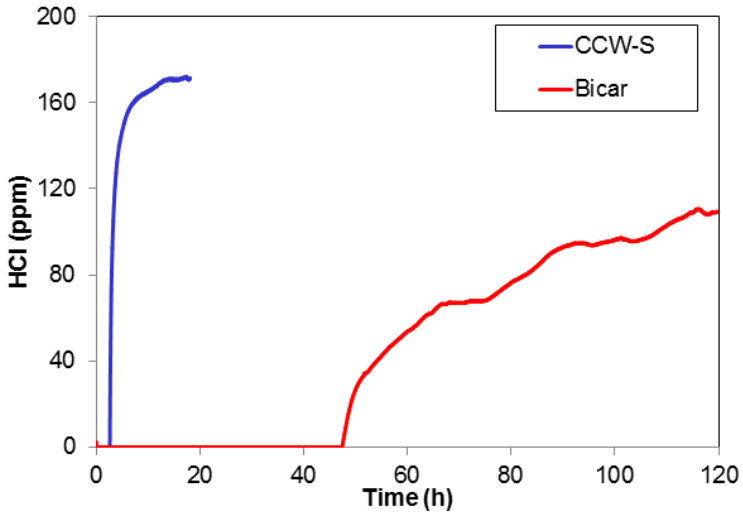

FIGURE 7.13: Breakthrough curves for HCl/Syngas conditions (25°C, 1 atm)

TABLE 7.8: Breakthrough time and HCl adsorption capacities of CCW-S and Bicar in HCl/syngas atmposphere (25 °C, 1 atm)

Sorbent	t_b (h)	Chloride capacity (wt %)
CCW-S	2.7	0.5
Bicar	48.2	6.7

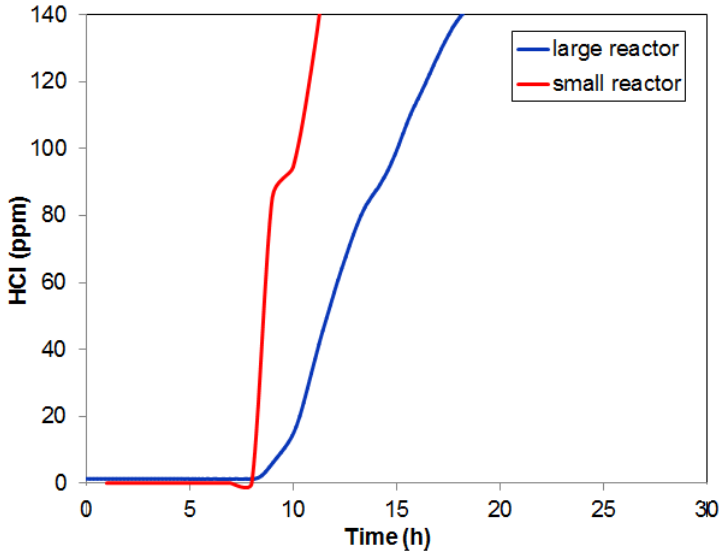

FIGURE 7.14: Comparing breakthrough curves for adsorption tests with CCW-S in small and large reactor, under 500 ppmv HCl/N_2 conditions (25°C, 1 atm)

Conclusion

In this chapter, the dry adsorption potential of four sorbents were studied: two solid wastes - CCW-S and CCW-D, and two commercial sorbents - Bicar and Lime. Various physico-chemical analyses were performed on each sorbent before the tests, including ICP, FTIR, XRD and TGA. The analysis results revealed that CCW-S and CCW-D were largely composed of $CaCO_3$, Bicar was purely $NaHCO_3$, and Lime contained both $Ca(OH)_2$ and small quantities of $CaCO_3$. The impurities - Al, Fe and Mg - were also detected in CCW-S, CCW-D and Lime.

The first set of adsorption tests were performed using a gas mixture of HCl and nitrogen (HCl/N_2) at ambient conditions. The results revealed that Bicar was the best performing sorbent. The average breakthrough times (h) and HCl adsorption capacities (wt%) of the sorbents were in the following decreasing order: Bicar (66 h, 26.8 wt%) > Lime (12.4 h, 16 wt%) > CCW-S (7.8 h, 3.9 wt%) > CCW-D (3.6 h, 1.3 wt%). Furthermore, TEM-EDX images of CCW-S and Bicar particles revealed the participation of the impurities - Al, Fe, and Mg - in HCl capture. In addition, XRD and ESEM analyses showed the formation of new crystals on the surface of Bicar and Lime particles, although no new crystals were observed on the particles of CCW-S and CCW-D.

The second set of adsorption experiments were conducted with CCW-S and Bicar sorbents, using a simulated HCl/Syngas atmosphere at atmospheric conditions. The breakthrough times and HCl adsorption capacities of the sorbents were, respectively, 48.2 h and 6.7 wt% for Bicar, and, 2.7 h and 0.5 wt% for CCW-S. This significant decrease in the sorbent performance in the presence of syngas highlights important interactions between HCl and syngas components, which deserves further investigation. A future study on the effect of different partial pressures of CO_2 (present in syngas) on the sorbent performance, could be performed.

Conclusion

Conclusion

This three-year PhD work has been dedicated to: 1) Studying the pyro-gasification of wood waste containing small amounts of plastics, 2) Developing a CFD model of wood waste pyro-gasification, and 3) Investigating methods for removing HCl from waste-derived syngas. Based on a literature review and evaluation of various waste-derived fuels available on the market, Class B wood waste containing small amounts of plastics was chosen as the feedstock for studies in this PhD work mainly due to its good fuel properties, low recycling rates and abundant supply. However, the heterogeneity of this industrial wood waste made it difficult to understand and predict its behaviour during pyro-gasification. Hence, a model waste was used, which consisted of virgin poplar wood and the plasic resins: high density polyethylene (HDPE), polystyrene (PS) and polyvinyl chloride (PVC). The physico-chemical and thermal properties of the model waste as well as Class B wood waste were analysed using European Standards for solid recovered fuels (SRF). These properties were relevant for the experimental and numerical work performed in this thesis.

In literature, a knowledge gap exists regarding the effect of non-polyolefins on the pyrolysis behaviour of wood. Hence, a laboratory-scale experiment was performed in a fixed bed reactor to study the pyrolysis of poplar wood in a mixture PS and PVC, as well as with the polyolefin, HDPE, for the sake of comparison. The results showed that PVC had a strong positive synergy on char yield with a maximum yield at 30 wt% PVC content. Both HDPE and PS significantly decreased gas yield in favour of oil production at all plastic contents in the sample. Furthermore, HDPE significantly increased methane and light hydrocarbon gas yields due to its high hydrogen content. For PS, positive synergies were observed for H_2, CH_4, CO and CO_2 yields whereas insignificant interactions were seen for hydrocarbon gas yields. The yield of HCl gas was found to decrease by 53.6 wt % when PVC content was decreased from 100 to 30 wt%, because the Cl molecules were trapped in the condensed oil product. With respect to the gas lower heating value (LHV), the increase in HDPE content from 0 to 50 wt% increased the LHV from 19 MJ/m^3 to 23 MJ/Nm^3, whereas an insignificant effect on the LHV was observed in the presence of PS and PVC.

Two pilot-scale waste pyro-gasification tests were also performed in a downdraft reactor, in order to analyze the syngas and residual char produced to perform mass and energy balances, and to provide relevant data to validate the CFD model developed in this PhD work. The first test involved Class B wood waste as feedstock, and for the second test, wood waste containing 1 wt% PVC was used. In both experiments, the results revealed that the main permanent species in syngas were H_2, N_2, CO and CO_2, with lesser concentrations of CH_4 and light hydrocarbons. However, the results showed that the addition of 1 wt% PVC to wood waste strongly influenced the tar content and composition in syngas by doubling the tar content and increasing the aromatic compound concentration by 42.6 % as well as the content of PAHs and furans by a factor of 4.4 and 21.5 respectively. Furthermore, HCl was 5.5 times more concentrated in syngas, and chlorine in the residual char was 16 times higher in the second test than in the first, due to the presence of 1 wt% PVC (0.57 wt% Cl) in the waste feedstock. Although a closure on chlorine mass balance was not achieved, due to loss of HCl in the gas sampling line, both mass and energy balance closures were attained.

Due to the significant interactions observed between PVC and poplar wood, in combination with scarce literature data on the kinetics of these interactions, a kinetic study was performed using thermogravimetric analysis as well as 'model-free' and master-plot procedures. A multi-step kinetic model was developed that correctly predicted the pyrolysis conversion rates of poplar wood (PW) pellet containing different concentrations of PVC. The results show that even at a PVC content as low as 1 wt%, the apparent kinetic energies of the pseudo-components in poplar wood decrease from 136 to 102 kJ/mol for hemicellulose, and from 217 to 108 kJ/mol for cellulose. This decrease in activation energy showcases the acid hydrolysis of the cellulosic fibres by HCl, which was released from the dehydrochlorination step of PVC pyrolysis. Thanks to master-plots, a Nucleation and Growth mechanism that follows an Amravi-Erofeev type model was found to be the rate limiting step for the interaction between poplar wood and PVC.

A 1D, computational fluid dynamics (CFD) model was then developed to simulate the pyro-gasification of wood waste in a downdraft reactor. The numerical results of the char-gasification submodel was found to be in good agreement with literature data and sensitivity analysis revealed that the inlet concentrations of oxygen and steam had the strongest influence on syngas composition. Furthermore, a heat duty analysis showed that the downdraft gasifier could operate autothermally when the gasifier temperature was fixed at 760 °C. Subsequent submodels of drying, pyrolysis and combustion processes were incorporated into the model, and have been validated against data obtained from tests conducted during this PhD work on a pilot scale downdraft reactor.

Syngas cleaning experiments based on dry adsorption at ambient temperature were also conducted in this work. Four solid sorbents were used: two solid wastes -CCW-S and CCW-D, and two commercial sorbents -Bicar and Lime. The first set of experiments, which were performed with HCl in nitrogen gas, revealed that

Bicar was the best performing sorbent. The performance of the sorbents in terms of breakthrough times (h) and HCl adsorption capacities (wt%) were in the following decreasing order: Bicar (66 h, 26.8 wt%) > Lime (12.4 h, 16 wt%) > CCW-S (7.8 h, 3.9 wt%) > CCW-D (3.6 h, 1.3 wt%). The second set of experiments where performed using simulated HCl/Syngas atmosphere and the adsorbents, CCW-S and Bicar. The breakthrough times and HCl adsorption capacities of the sorbents were respectively, 48.2 h and 6.7 wt% for Bicar, and, 2.7 h and 0.5 wt% for CCW-S. These results signaled a competitive interference of syngas in the adsorption of HCl. Furthermore, the solid wastes showed potential as HCl sorbents although more work is needed to determine the optimum operating conditions for these sorbents.

Perspectives

The results obtained in this PhD work have brought into light new ideas for further study of wood waste pyro-gasification and syngas cleaning, which will be discussed as follows.

- Co-pyrolysis experiments on the effect of different degrees of contact of wood and PVC on the pyrolysis products would be an interesting study, which has not yet been seen in literature. In this PhD work, pellets of wood and PVC mixtures were used, which is equivalent to a composite wood/PVC material in real waste. However, PVC may be present in wood waste in other forms such as a film covering on wood or as a material entirely separate from wood. A composite wood/PVC material presents the closest form of contact throughout the volume of the particle, whereas for a PVC film on wood, the close contact is only on the outer surface of the particle. If, however, PVC is entirely separate from wood, the only effect that PVC would have is the formation of HCl during pyrolysis which will in turn attack the outer surface of the wood particle. Therefore, co-pyrolysis experiments in the latter case could involve the pyrolysis of a wood particle in an atmosphere of HCl.

- Co-gasification of wood and plastics for syngas production has only recently received some research attention [189, 286, 287]. Alvarez et al. [189] have shown that co-gasification with polypropylene (PP) gives the highest yield of hydrogen compared to high density polyethylene (HDPE) and polystyrene (PS). However, HDPE produced the highest gas yield, whereas PS had the highest oil and char yields. Ahmed et al. [286] and Pinto et al. [287] have reported a significant significant increase in hydrogen, methane and light hydrocarbons in the presence of HDPE. Hence an interesting new study would be the co-gasification of wood and a mixture of plastics to investigate the influence of different plastic mixtures on wood gasification.

- In the CFD model work performed, the introduction of tar oxidation reaction posed a major problem in stabilising the oxidation fronts as this exothermic reaction combined with a high tar concentration, produced a large heat flux.

A solution was eventually found by increasing the stoichiometric coefficient of oxygen in the reaction so as to reduce the amount of heat produced. Thus, an analysis of the stoichiometric amount of oxygen needed to oxidize tar produced from the pyrolysis of Class B wood waste, would be helpful to improve the model predictions.

- With regards to HCl removal from syngas using dry adsorption methods, higher temperatures are known to improve sorbent performance. Hence, experiments could be performed to determine the optimum adsorption temperatures for the four sorbents used in this work under HCl/N_2 atmosphere. Once, the optimum temperature is determined, experiments could be performed with different partial pressures of CO_2 (present in syngas) to study its effect on the sorbent performance. Furthermore, regeneration tests using different heating cycles could be performed to study their effect on the sorbents' HCl adsorption performance and their thermal stability. In addition, the possibility of introducing the sorbents in the wood waste feed before pyro-gasification could be explored by performing in-situ HCl adsorption tests during pyro-gasification of wood/PVC samples. Under such conditions, the sorbent performance could be evaluated and the syngas can be analysed for metals that may have volatilised from the sorbents during the process.

- Apart from studying operating conditions that optimize the sorbents' performance in capturing HCl, investigations can also be undertaken to study the influence of the sorbents' physico-chemical or surface properties on its performance. For instance, effects of particle size and sorbent activation could be studied. Physical activation of a sorbent by heating may increase its porosity and hence its HCl adsorption capacity. Likewise, chemical activation of the sorbent by impregnating elements such as phosphate, iron and Na_2CO_3 onto its surface may also improve its performance.

Scientific production and intellectual property

Scientific Publications

1. A. EPHRAIM, V. POZZOBON, O. LOUISNARD, D. PHAM MINH, A. NZIHOU, P. SHARROCK: “Simulation of Biomass Char Gasification in a downdraft reactor for syngas production”, AIChE Journal, 62: 1079-1091, 2016.

2. A. EPHRAIM, D. PHAM MINH, D. LEBONNOIS, C. PEREGRINA, P. SHARROCK and A. NZIHOU, “Co-pyrolysis of wood and plastics: Influence of plastic type and content on product yield, gas composition and quality” (In preparation).

3. A. EPHRAIM, V. POZZOBON, D. PHAM MINH, D. LEBONNOIS, P. SHARROCK and A. NZIHOU, “Pyrolysis of wood treated with PVC: Kinetic modelling” (In preparation).

4. A. EPHRAIM, V. POZZOBON, D. PHAM MINH, D. LEBONNOIS, P. SHARROCK and A. NZIHOU, “Modelling pyro-gasification of wood waste in a downdraft gasifier” (In preparation).

5. TLD. NGO, A. EPHRAIM, D. PHAM MINH, D. LEBONNOIS, C. PEREGRINA, P. SHARROCK and A. NZIHOU, “HCl removal from syngas using inorganic sorbents” (In preparation).

Intellectual property

Enveloppes Soleau

1. A. EPHRAIM, D. PHAM MINH, D. LEBONNOIS, JM. AUDIC, P. SHARROCK and A. NZIHOU: "Apparatus and procedure for removal of tar in producer gas for continuous sampling of hydrogen chloride," INPI, 2016, 3 pages, N°574264

2. A. EPHRAIM, D. PHAM MINH, D. LEBONNOIS, JM. AUDIC, P. SHARROCK and A. NZIHOU: "Zeolite material for hot gas drying of wet producer gas for continuous sampling of hydrogen chloride," INPI, 2016, 2 pages. N°574263

Patent

1. A. EPHRAIM, D. PHAM MINH, D. LEBONNOIS, JM. AUDIC, P. SHARROCK and A. NZIHOU: "Méthode et dispositif pour l'élimination des goudrons de la phase gazeuse et pour la mesure de chlorure d'hydrogène," (In preparation)

Conferences

1. A. EPHRAIM, V. POZZOBON, D. PHAM MINH, D. LEBONNOIS, C. PEREGRINA, P. SHARROCK, A. NZIHOU: "Behaviour of chloride pollutants in syngas from wood waste pyro-gasification: a modelling approach", 6th international conference on energy from biomass and waste, Venice, 2016 (Oral presentation).

2. A. EPHRAIM, V. POZZOBON, O. LOUISNARD, D. PHAM MINH, A. NZIHOU, P. SHARROCK: "Simulation of biochar gasification in a downdraft reactor for syngas production", 6th International conference on engineering for waste and biomass valorization, Albi, 2016 (Oral presentation).

3. A. EPHRAIM, D. PHAM MINH, D. LEBONNOIS, C. PEREGRINA, P. SHARROCK and A. NZIHOU, "Co-pyrolysis of wood and plastic wastes: Influence of plastic type and content on product yield and quality", 3rd International conference, WASTES: Solutions, Treatments and Opportunities, Viana do Castelo, 2015 (Oral presentation).

4. A. EPHRAIM, D. PHAM MINH, A. NZIHOU, P. SHARROCK, "Valorisation of wood and plastic waste by pyro-gasification and syngas cleaning", The BRISK Open Workshop / TOTeM 40, 2015 (Poster presentation).

5. Nordic biogas conference, Reykjavik, 2014 (only attended).

Appendices

APPENDIX A

Tar analysis

Table A.1: List of tar compounds analyzed in syngas from wood waste gasification

Group / Common name	Concentration (mg/Nm^3)
Acids	**33.68**
Phosphonic acid, (p-hydroxyphenyl)-	27.71
Carbonic acid, phenyl propyl ester	4.73
Benzoic acid, diphenylmethyl	1.24
Phenols	**31.63**
Phenol, 2-methyl-	10.16
Phenol, 3-methyl-	17.38
Phenol, 2,5-dimethyl-	2.31
Phenol, 2,6-dimethyl-	0.53
p-Cresol	1.26
Furans	**6.66**
Benzofuran, 7-methyl-	1.15
Benzofuran, 2-methyl-	1.83
Dibenzofuran	1.45
Benzofuran, 2,3-dihydro-	1.51
Benzofuran, 4,7-dimethyl-	0.72
Aromatic compounds	**823.98**
Toluene	601.75
Ethylbenzene	13.10
o-Xylene	19.69
Benzene, 1-ethyl-2-methyl-	6.36
Benzene, 1-ethenyl-3-methyl-	3.68
Benzene, 1-ethenyl-4-methyl-	31.12

Benzene, 1,1'-(1-ethenyl-1,3-propanediyl)bis-	5.30
Benzene, cyclopropyl-	0.71
Indane	0,38
Benzene, 1-propynyl-	48.86
1,3,5,7-Cyclooctatetraene	73.72
Benzene, 1,3-diethenyl-	1.71
Cycloprop[a]indene, 1,1a,6,6a-tetrahydro-	12.46
Biphenyl	4.14
4H-Cyclopenta[def]phenanthrene	0.60
1H-Cyclopropa[l]phenanthrene,1a,9b-dihydro-	0.41
PAHs	**158.34**
Phenylethyne	1.82
Acenaphthene	5.76
Naphthalene, 1,8-dimethyl-	3.07
Acenaphthylene	12.55
1-Isopropenylnaphthalene	3.56
2-Naphthalenol	2.08
1-Naphthalenol	0.95
Naphthalene, 2-methyl-	22.97
1,4-Methanonaphthalene, 1,4-dihydro-	1.58
Naphthalene, 2-ethyl-	1.70
1-Isopropenylnaphthalene	0.75
Fluorene	5.98
1H-Phenalene	0.85
Fluoranthene	1.37
Pyrene	1.44
Anthracene, 1,2-dihydro-	0.89
Phenanthrene	7.05
Anthracene, 9-methyl-	0.83
Azulene	82.30
5,16[1',2']:8,13[1",2"]-Dibenzenodibenzo[a,g]cyclododecene, 6,7,14,15-tetrahydro-	0.84
Alicyclic compounds	
Tetracyclo[5.3.0.0<2,6>.0<3,10>]deca-4,8-diene	1.63
Nitrogen containing aromatics	**102.93**
Benzonitrile	2.41
Benzenepropanenitrile, .beta.-oxo-	2.19
5-Methylbenzimidazole	6.18
Iodoacetonitrile	0.29
Tetrahydro-2H-thiopyran-4-ylidenemalononitrile, 5,5-dioxide	1.17
5H-Cyclopentapyrazine, 6,7-dihydro-2,5-dimethyl-	3.08
Quinoline	3.88
1H-Indazole, 4-methyl-	0.99

2-Phenyl-4-methylimidazole	0.82
1,8-Diazacyclotetradecane-2,9-dione	81.92
Ketones	
5,9-Undecadien-2-one, 6,10-dimethyl-	3.22
Mixed oxygenates	
Triphenylphosphine oxide	8.57

Table A.2: List of tar compounds analyzed in syngas from wood waste/PVC gasification

Group / Common name	Concentration (mg/Nm^3)
Chlorinated compounds	
2-Chloro-4-aminopyrimidine	11.49
Acids	
Thiocyanic acid, phenylmethyl ester	28.79
Phenols	**320.96**
Phenol	193.24
Phenol, 3-methyl-	72.90
Phenol, 2-methyl-	50.64
Phenol, 3,4-dimethyl-	4.17
Furans	**143.15**
Benzofuran	126.08
Benzofuran, 2-methyl-	14.46
Dibenzofuran	2.61
Aromatic compounds	**1175.22**
Toluene	469.96
Benzene, propoxy-	11.93
Benzene, 1,1'-(1-ethenyl-1,3-propanediyl)bis-	44.35
Benzene, 1-propynyl-	199.67
Biphenyl	26.65
Ethylbenzene	54,04
1,3,5,7-Cyclooctatetraene	357.76
Phenylethyne	10.87
PAHs	**690.93**
Naphthalene	17.25
Naphthalene, 2-methyl-	118.46
1,4-Methanonaphthalene, 1,4-dihydro-	2.76
1-Isopropenylnaphthalene	3.36
Phenanthrene	26.05
Azulene	398.20
Acenaphthene	3.21
Acenaphthylene	44.13
Cycloprop[a]indene, 1,1a,6,6a-tetrahydro-	43.53
2-Methylindene	22.90
Fluorene	4.87
Fluoranthene	6.21
Nitrogen containing aromatics	**101.05**
Benzonitrile	21.23
5-Methylbenzimidazole	12.16
2-Phenyl-4-methylimidazole	13.22
5-Methylbenzimidazole	29.29
Benzenepropanenitrile, .beta.-oxo-	12.89
5H-Cyclopentapyrazine, 6,7-dihydro-2,5-dimethyl-	12.26

APPENDIX B

CFD model correlations

TABLE B.1: Expression for diffusion coefficient of gaseous species as a function of temperature and pressure (Chapaman-Enskog formula) [81]

Chemical Species, j	Diffusion Coefficient, D_{j,N_2} (m^2/s)
N_2	$1.39 \times 10^{-4} \left(\frac{1.013 \times 10^5}{P}\right) \left(\frac{T}{1173}\right)^{3/2}$
CO_2	$1.13 \times 10^{-4} \left(\frac{1.013 \times 10^5}{P}\right) \left(\frac{T}{1173}\right)^{3/2}$
H_2O	$2.11 \times 10^{-4} \left(\frac{1.013 \times 10^5}{P}\right) \left(\frac{T}{1173}\right)^{3/2}$
CO	$1.40 \times 10^{-4} \left(\frac{1.013 \times 10^5}{P}\right) \left(\frac{T}{1173}\right)^{3/2}$
H_2	$5.11 \times 10^{-4} \left(\frac{1.013 \times 10^5}{P}\right) \left(\frac{T}{1173}\right)^{3/2}$
O_2	$1.43 \times 10^{-4} \left(\frac{1.013 \times 10^5}{P}\right) \left(\frac{T}{1173}\right)^{3/2}$

TABLE B.2: Coefficient values of the apparent kinetic functions for the three heterogeneous reactions [49]

Reaction	Steam Gasification	Boudouard	Oxidation
a	-2.38×10^{1}	-3.30×10^{1}	-7.83
b	2.92×10^{-2}	4.18×10^{-2}	8.65×10^{-3}
c	2.63	2.86	2.32×10^{1}
d	3.72×10^{2}	6.01×10^{2}	-2.89×10^{2}
e	-4.33	-6.42	-3.52
f	3.32×10^{-6}	1.48×10^{-8}	1.13×10^{-10}
g	-1.02×10^{-5}	-1.45×10^{-5}	-3.12×10^{-6}
h	-2.88	-2.90	-6.59×10^{1}
i	-4.08×10^{-1}	-5.86×10^{-1}	2.85×10^{4}
j	3.39×10^{-3}	4.86×10^{-3}	3.78
k	-2.59×10^{-9}	-1.12×10^{-11}	-4.95×10^{-3}
l	8.38×10^{-7}	1.34×10^{2}	-9.54×10^{-2}
m	1.19×10^{2}	-2.87×10^{-7}	-8.36×10^{-14}
n	-8.17×10^{-5}	-4.04×10^{-9}	
o	1.05×10^{-6}		

TABLE B.3: Expression for production term r_j, of each chemical species

Chemical Species, j	Expression for production term
r_C	$C_{c,0}\,[-\omega_1 - \omega_2 - \omega_3]$
r_{CO_2}	$C_{c,0}\,[\omega_1 - \omega_2] + \nu_4$
r_{H_2O}	$-C_{c,0}\,\omega_3 - \nu_4$
r_{O_2}	$-C_{c,0}\,\omega_1$
r_{CO}	$C_{c,0}\,[2\omega_2 + \omega_3] - \nu_4$
r_{H_2}	$C_{c,0}\,\omega_3 + \nu_4$

Table B.4: Expression of the thermal conductivity of gaseous species and char as a function of temperature.

Reaction	Thermal Conductivity (mW/m/K)	Temperature Range (K)	Refs.
N_2	$-0.3721 + 0.10977T - 9.42549 \times 10^{-5}T^2 + 8.05548 \times 10^{-8}T^3 - 3.35367 \times 10^{-11}T^4 + 5.15605 \times 10^{-15}T^5$	65-2500	[288]
O_2	$-1.7536 + 0.1224T - 1.322444 \times 10^{-4}T^2 + 1.7804 \times 10^{-7}T^3 - 1.200176 \times 10^{-10}T^4 + 2.9817302 \times 10^{-14}T^5$	70-1500	[288]
CO_2	$-0.341914 + 0.0314T + 1.170458 \times 10^{-4}T^2 - 1.281 \times 10^{-7}T^3 + 5.7923 \times 10^{-11}T^4 - 9.72044 \times 10^{-15}T^5$	190-2000	[288]
H_2	$-4.0803 + 0.9858T - 1.330466 \times 10^{-3}T^2 + 1.1217 \times 10^{-6}T^3 - 3.25582 \times 10^{-10}T^4$	16-1500	[288]
CO	$-0.42832 + 0.09941T - 5.96573 \times 10^{-5}T^2 + 3.81583 \times 10^{-8}T^3 - 1.43131 \times 10^{-11}T^4 + 2.56748 \times 10^{-15}T^5$	80-2200	[288]
H_2O	148	1500	[288]
C	95.8	307	[289]

APPENDIX C

French extended abstract / Résumé Long

Introduction

La gestion efficace de déchets est encore un grand challenge de notre société. Selon un rapport récent de la Banque Mondiale, 1,3 Mt/an de déchets municipaux est actuellement généré au niveau mondial et ça devrait doubler d'ici 2025 [1]. Cela entraine des coûts financiers élevés et des impacts environnementaux importants. C'est pour cette raison que beaucoup de pays, particulièrement ceux en Europe ont comme objectif de devenir des « Sociétés du Recyclage », c'est-à-dire des pays qui non seulement minimise la production de déchet mais aussi l'utilise comme ressource [2]. Par contre, dans la réalité, ce n'est pas possible de recycler infiniment des déchets car certains matériaux sont non-recyclables en raison de la présence des impuretés toxiques. Au lieu de mettre en décharge ces déchets, leurs fractions combustibles peuvent être valorisées comme une source d'énergie.

La pyro-gazéification est un procédé thermochimique prometteur pour la récupération d'énergie qui se trouve dans le déchet solide combustible. Ce procédé a lieu à haute température ($>$ 800 °C) et utilise un oxydant, comme l'air ou la vapeur d'eau, pour transformer le déchet en gaz de synthèse (syngaz). Le syngaz, qui est un gaz combustible riche en hydrogène (H2) et monoxyde de carbone (CO), est un vecteur énergétique important parce que la demande d'énergie mondiale est prévu d'augmenter jusqu'à 865 EJ en 2040, ce qui représente une hausse de 56 % par rapport à l'année 2010 [4]. Le syngaz est également considéré comme un mélange plate-forme important pour différents procédés de synthèse chimique tels que la synthèse Fisher-Tropsh, la synthèse du méthanol. Cependant, pour le syngaz dérivés de déchets, une contrainte technique majeur à surmonter est de développer des méthodes de purification de gaz qui sont à la fois plus efficaces et moins chères afin de pouvoir répondre aux exigences strictes des réglementations environnementales

ainsi que les exigences techniques de l'usage final.

Parmi des nombreux types des déchets combustibles, les déchets du bois et des matières plastiques sont bien adaptés pour la production du syngaz grâce à leurs quantités abondantes, associé à leurs faible taux de recyclage, leurs valeurs énergétiques intéressantes, ainsi que l'existence des législations et des normes de contrôle de qualité. Pourtant, les déchets de bois et plastiques sont hétérogènes et peuvent avoir des teneurs en impuretés significatives, telles que le chlore. La présence du chlore peut provenir du chlorure de polyvinyle (PVC) qui se trouve souvent dans le déchet de bois et des plastiques. En effet, PVC est un des plastiques les plus utilisés. La thermo-conversion des déchets contenant du chlore conduit à la formation du chlorure d'hydrogène (HCl), qui se trouve dans le syngaz et qui peut créer des problèmes de corrosion, et des problèmes liés à la santé et l'environnement. Etant donné que la contamination de déchets par le PVC est difficile à éviter, c'est alors nécessaire d'enlever du HCl dans le syngaz avant toute utilisation.

Dans ce contexte, les objectifs globaux de cette thèse sont les suivants :

- Etudier la pyro-gazéification des déchets de bois, contaminés par des plastiques, à l'échelle laboratoire et pilote afin de comprendre l'influence de la composition de ces déchets sur les produits du procédé.
- Modéliser et simuler le processus de pyro-gazéification du déchet de bois dans un réacteur à lit fixe continu pour prédire l'influence des paramètres opératoires et de la composition de déchet sur la quantité et qualité du syngaz produit.
- Etudier, à l'échelle laboratoire, le traitement du HCl dans le syngaz en utilisant des adsorbants inorganiques.

État de l'art

Une étude bibliographique a été effectuée dans le cadre de cette thèse pour examiner les développements récents au sujet de la classification et caractérisation des combustibles dérivés des déchets, les technologies et modèles du processus de pyro-gazéification, ainsi que les applications et méthodes de purifications du syngaz dérivés des déchets. Sur la base de cette étude, les décisions suivantes ont été prises :

- Le bois de catégorie B (bois B) contenant une faible quantité de plastiques a été sélectionné comme le déchet à étudier pour les études de pyro-gazéification en raison de leurs quantités abondantes, associées à leurs faible taux de recyclage, leurs valeurs énergétiques intéressantes, ainsi que l'existence des législations et des normes de contrôle de qualité et qui favorise la valorisation énergétique de ces déchets.
- Un réacteur à lit fixe co-courant (downdraft) a été choisi comme la technologie à modéliser. Les expériences de pyro-gazéification à l'échelle pilote sont également effectuées avec ce type de réacteur. Ce choix se base sur le fait que les taux de

conversions des combustibles solides dans ce réacteur sont relativement élevés et les rendements en goudrons sont faibles. De plus, ce réacteur est facile à contrôler, rentable et bien adapté aux applications à petite échelle.

- Un modèle du type mécanique des fluides numériques (computational fluid dynamics, CFD, en anglais) pour modéliser la pyro-gazéification du bois B dans un réacteur downdraft a été choisi. Ce modèle CFD se compose des sous-modèles qui décrivent les processus de séchage, pyrolyse, oxydation et gazéification.

- Le chlore (Cl) est le polluant qu'on s'intéresse dans cette thèse pour des raisons essentiellement environnementales parce que la concentration du chlore dans le bois B peut atteindre un niveau significatif à cause de la présence du PVC.

- Des données cinétiques sur la pyrolyse des mélanges du bois et du PVC n'étant pas disponibles, des analyses thermogravimétriques (ATG) sont réalisées afin d'obtenir des données pour ensuite développer et valider un modèle cinétique. Ce modèle cinétique sera intégré au modèle CFD global.

- En visant une application du syngaz en cogénération, la méthode d'adsorption en voie sec, utilisant des différents adsorbants inorganiques, semble la plus adaptée pour le traitement de HCl dans le syngaz.

Caractérisation de déchet industriel et modèle

Le bois B utilisé dans ce travail est un déchet d'origine industriel fourni par la société SUEZ et qui est destiné pour l'utilisation dans une cimenterie. Figure C.1 présente trois échantillons de déchet de bois B : Sample 1 (W1) et sample 2 (W2) sont des produits finis qui sont séchés et broyés, tandis que sample 3 (W3) est la fraction rejetée du centre de recyclage à cause de sa teneur en polluant élevée. La présence d'une faible quantité des plastiques dans le bois B pose un problème d'hétérogénéité du déchet, ce qui rend difficile la compréhension et la prédiction de son comportement lors des études expérimentales et de la modélisation. Donc on a choisi de travailler aussi avec un déchet modèle composé de bois peuplier vierge (PW), et de différents plastiques : polyéthylène haute densité (HDPE), polystyrène (PS) et chlorure de polyvinyle (PVC). L'image illustrative de chacun de ces composés se trouve dans la Figure C.2.

La caractérisation du bois B et le modèle représentatif de ce déchet est importante pour aider à comprendre le rôle de leurs propriétés physiques et thermochimiques sur leur comportement lors du processus de pyro-gazéification. Pour cela, des normes Européen pour les combustibles de récupération solides (CSR) rédigées par le comité technique CEN TC 343 sont utilisées.

Premièrement, la distribution de la taille des particules des trois échantillons du bois B a été analysée. Les résultats ont montré que W1 a la teneur en particules fines (< 3 mm) la plus élevée soit 39 % en masse, alors que celle de

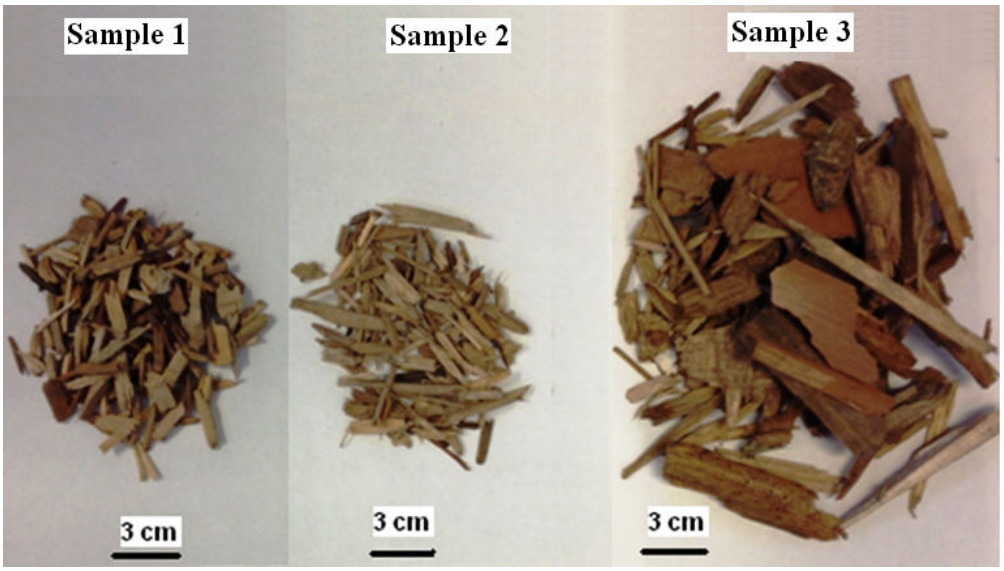

FIGURE C.1: Echantillons de déchet de bois industriel (bois B).

FIGURE C.2: Déchet modèle de bois B.

W3 a été la plus faible. Par rapport à l'analyse de la distribution de grandes particules, W1 et W2 sont respectivement une distribution normale et une distribution avec une asymétrie légèrement positive. De plus, ces échantillons ont des

tailles de particules moyennes similaires de respectivement 20 et 21 mm. Pour W3, on a obtenu une distribution avec une asymétrie fortement positive et une taille moyenne de 40 mm. On a aussi découvert que 3 % des particules de W3 ont une taille plus grosse que la limite exigée pour les réacteurs à lit fixe, soit 100 mm.

La masse volumique et la valeur calorifique des trois échantillons du bois B ont été analysées. Les valeurs obtenues sont similaires à celles de PW et PVC, alors que HDPE et PS aient des valeurs deux fois plus élevées. Parmi les trois échantillons du bois B, W3 a eu les taux d'humidité et de cendres les plus élevés de respectivement 16 % et 5,7 % en masse. De plus, HDPE, PS et PVC ont environ 15 % en masse de plus en matières volatiles que tous les échantillons du bois.

Le bois B et PW ont des teneurs similaires en C, H et O, ainsi qu'une faible concentration en S et N. Cependant, on a trouvé que la teneur en Cl dans le bois B est au moins cinq fois plus élevée que celle du PW. Au contraire, le PW contient plus de Na, Ca, Mg, Si et Al, ainsi que les métaux lourds, Zn, Pb et Ba que les bois B.

Pour les analyses thermogravimétriques, les trois échantillons de bois B ont un comportement thermique similaire à PW : désorption de l'eau aux températures au-dessous de 100 °C ; dévolatilisation à 190-350 °C ; et la graphitisation au-delà de 350 °C. Par contre, les plastiques ont montré un comportement diffèrent que les bois B : HDPE s'est fondu à environ 130 °C ; PVC, PS et HDPE se sont décomposés respectivement à 200-350 °C, 350-430 °C et 440-480 °C ; et PVC a subi des réactions de graphitisation à 350-500 °C.

Ces caractéristiques des échantillons de bois et de plastiques analysés ont été importantes pour les études expérimentales et de modélisations effectuées dans le cadre de ce travail de thèse.

Co-pyrolyse de bois et plastiques

Dans cette partie, une étude expérimentale à l'échelle laboratoire a été réalisée sur la co-pyrolyse du bois peuplier (PW) et les plastiques HDPE, PS et PVC. L'objectif est d'étudier l'effet de type et teneur en plastique dans un mélange avec du bois sur le rendement en produits de pyrolyse, le rendement en espèces gazeux et le pouvoir calorifique du gaz produit. On a préparé des échantillons contenants du bois et différents teneurs en plastiques de chaque type : 0 – 5 – 10 – 30 – 50 – 100 % en masse.

La Figure C.3 présente schématiquement l'installation expérimentale pour effectuer les expériences de pyrolyse. Pour chaque test, 10 g d'échantillon sont mis dans un creuset en quartz. Ensuite l'échantillon est chauffé dans un four jusqu'à 750 °C à une vitesse de chauffe de 20 °C/min sous atmosphère d'azote (33 mL/min). A la sortie du réacteur, la phase condensable du gaz a été piégée dans un récipient rempli de coton et refroidi jusqu'à 0 °C. Ce gaz condensé appelé « huile », est un mélange de l'eau, des goudrons, de l'huile et de la cire. Pour les tests avec les échantillons contenant du PVC, le condenseur d'huile a été remplacé par deux bouteilles qui contiennent des

solutions de KOH pour piéger le HCl dans le gaz. Ensuite, le gaz non-condensable a été récupéré dans un sac Tedlar et analysé par la µ-GC. De plus, la concentration du HCl dans la phase aqueuse a été mesurée avec un analyseur fluorescence X.

Suite à ces analyses, les rendements en char, huile, gaz, composés gazeux et le pouvoir calorifique du gaz ont été calculés pour chaque test. De plus, les synergies entre le bois peuplier et les plastiques ont été déterminées.

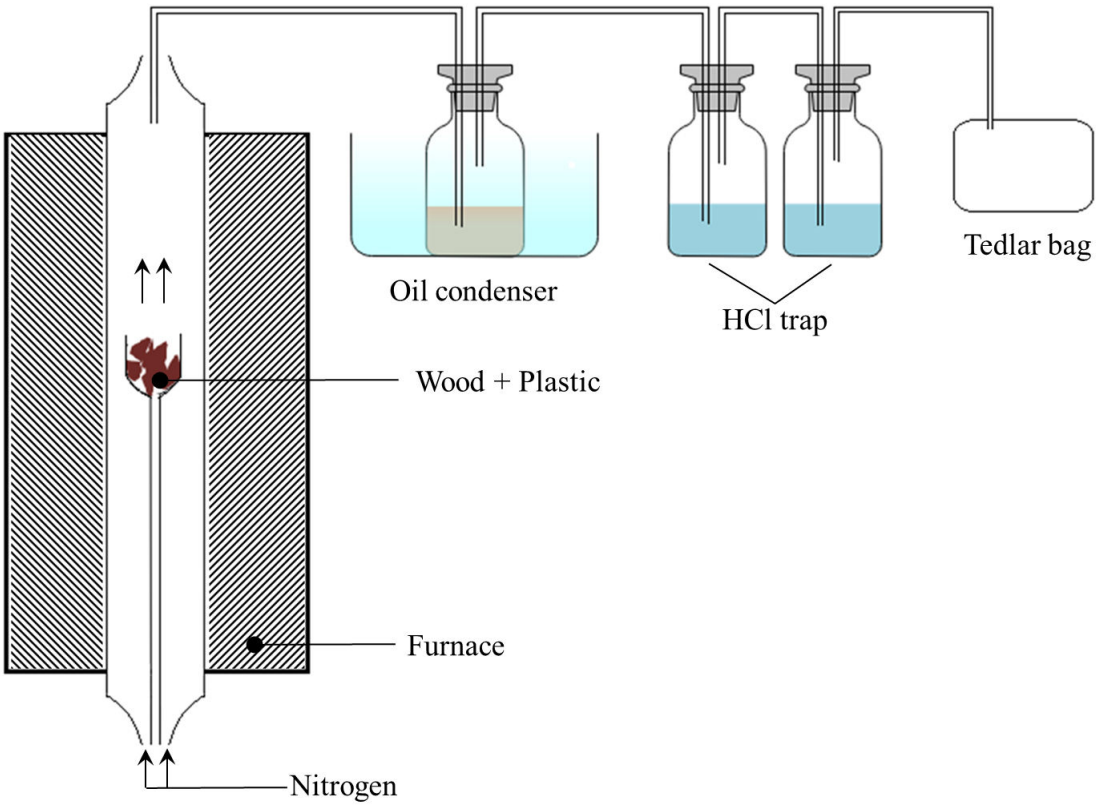

FIGURE C.3: Installation pour les expériences de pyrolyse.

Les résultats ont montré que la présence du PVC dans l'échantillon donne le meilleur rendement en char comparé aux autres plastiques avec une synergie dont le maximum est de 8 % en masse à un teneur en PVC de 30 % en masse. Par contre, un effet de synergie plus faible sur le rendement en char a été observé pour HDPE et PS.

D'une manière générale, l'ajout de HDPE et PS a augmenté le rendement de l'huile de pyrolyse et a diminué celui de gaz par rapport aux rendements observés pour la pyrolyse de PW pur.

L'ajout de PVC favorise fortement la formation de l'huile. Cela a également haussé la production de H_2. L'augmentation de a teneur en PVC conduit à une augmentation de la formation de HCl. Une étude supplémentaire a été effectuée pour déterminer la distribution du chlore dans les trois phases de produits, en faisant

des calculs d'équilibre thermodynamique (FactSage). Cette étude a montré que la majorité du chlore initialement dans l'échantillon a été trouvé dans la phase huileuse sous forme de HCl dissous, et qu'une petite quantité du chlore a été piégé dans le résidu solide sous forme des chlorures inorganiques.

L'ajout de HDPE au bois a augmenté d'une manière remarquable le rendement en CH_4 et C_xH_y (x=2 ou 3) grâce à sa structure chimique riche en hydrogène. Toutefois, le rendement en CO et CO_2 a baissé à cause de la baisse de la teneur en oxygène de l'échantillon quand la teneur en HDPE augmente. De plus, au-delà de 50% en masse en HDPE, le rendement en espèces gazeuses diminue.

L'ajout de PS est favorable pour la production de H_2, CH_4, CO et CO_2, mais a peu d'influence sur la production des espèces C_xH_y.

En ce qui concerne le PCI du gaz produit de la pyrolyse des mélanges du HDPE et PW, on a observé une hausse de 19 MJ/Nm^3 à 23 MJ/Nm^3 quand le teneur en HDPE a augmenté de 0 % à 50 % massique. Cependant, un effet négligeable sur le PCI a été observé pour l'ajout de PS et PVC à l'échantillon.

Les résultats de ce travail ont contribué à la compréhension du comportement thermo-chimique des mélanges bois/plastique. Les conditions opératoires favorables pour la formation des produits gazeux ont été déterminées. La formation du HCl comme polluant gazeux du syngaz est également mise en évidence.

Pyro-gazéification de déchet du bois contenant du PVC à l'échelle pilote

Dans ce travail, deux essais de pyro-gazéification ont été effectués dans un réacteur downdraft à l'échelle pilote. Pour le premier essai, le déchet de bois B a été utilisé tandis que pour le deuxième essai, le déchet de bois B contenant 1 % en masse de PVC (0,57 % en masse de Cl) a été utilisé.

Le pilote utilisé se trouve à la plate-forme PROVADEMSE (INSA de Lyon). Sa capacité de production de chaleur à partir de la pyro-gazéification de la biomasse est d'environ 100 kWth. Une image du gazéifieur est montrée dans la Figure C.4. Durant les tests, le réacteur a été alimenté avec le déchet à 11-12 kg/h. L'air a été injecté à trois différents zones du réacteur afin d'oxyder partiellement les produits de la pyrolyse du déchet. Au régime permanent, le réacteur fonctionne en auto-thermicité, sans ajout énergétique pour maintenir la température du four. Le syngaz et char résiduel (cendres) ont été analysés afin de pouvoir faire un bilan matière, bilan énergétique et un bilan sur le chlore.

Les résultats du premier test ont montré que H2, N2, CO et CO2 sont les espèces majeures dans le syngaz et qu'on retrouve des concentrations plus faibles de CH4 et des hydrocarbures légères. On a obtenu des résultats similaires pour le deuxième test,

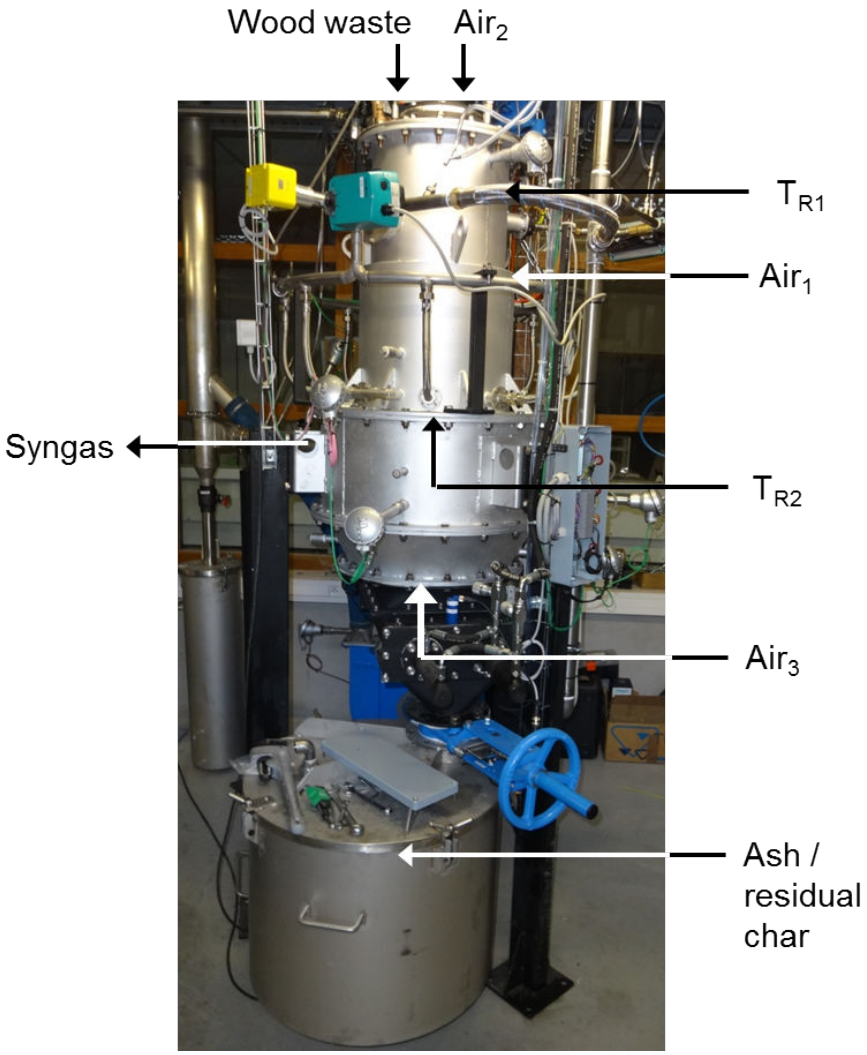

FIGURE C.4: Gazéifieur pilote de type downdraft.

tandis que la concentration du CO a diminué par 6 % en volume à cause d'un plus faible débit d'air injecté. Les résultats pilote ont confirmé ceux obtenus au laboratoire.

La composition de goudrons dans le syngaz a été analysée pour les deux essais et, par comparaison, on a constaté que la présence de 1 % massique de PVC dans le déchet de bois a augmenté la concentration des composés aromatiques dans les goudrons par 42,6 %, ainsi que la teneur en HAP et Furanes par un facteur respectivement de 4,4 et 21,5. Par contre, la formation des composées chlorées organiques dans le goudron est par contre négligeable.

Quant à la distribution du chlore dans les produits de pyro-gazéification, l'ajout de 1 % en masse de PVC dans le déchet de bois a rendu le syngaz 5,5 fois plus concentré en HCl et le char résiduel 16 fois plus concentré en chlore. Par contre, le bilan matière sur le chlore pour le deuxième essai n'a pas été bouclé, probablement due à la condensation de HCl dans la ligne d'échantillonnage. Au contraire, les bilans

massiques et énergiques globaux ont bien été bouclés. Ces résultats permettent de valider le modèle CFD qu'on a développé.

Focus sur la pyrolyse des pellets du bois-PVC : Modélisation cinétique

Il s'agit du développement et de la validation d'un model cinétique à étapes multiples qui sert à prédire le comportement pyrolytique de pellet de bois peuplier (PW) contenant des différentes teneurs en PVC et le mécanisme de réaction de ce dernier.

D'abord, des analyses thermogravimétriques ont été effectuées sur des pellets de bois peuplier qui contiennent 0, 1, 5, et 10 % en masse du PVC. Chaque pellet qui pèse environ 0,5 g a été chauffé de 30 °C à 800 °C aux vitesses de chauffe de 5 ,10 et 20 °C/min sous atmosphère d'azote (100 mL/min). Puis les données obtenues ont été utilisées pour déterminer les paramètres cinétiques en combinant la méthode Fraser-Suzuki pour la déconvolution des pics, la méthode « model-free » et les procédures de « master plot ». Les résultats de notre modèle sont en accord avec les données expérimentales avec une erreur de moins de 4,5 %.

Les résultats du modèle montrent qu'en présence d'une teneur faible en PVC de 1 % massique, les énergies d'activation des pseudo-composées de PW - hémicellulose et cellulose - diminuent respectivement de 136,3 à 101,6 kJ/mol et de 216,7 à 108,2 kJ/mol. Par ailleurs, l'augmentation de la teneur du PVC par un facteur de 5 et 10, diminue l'énergie d'activation de hémicellulose respectivement par 2,8 et 8,3 kJ/mol et celui de cellulose par 3,6 et 9,5 kJ/mol. Ces baisses en énergies d'activation sont grâce à l'hydrolyse acide des fibres cellulosiques par HCl, qui est formé lors de l'étape de déshydrochlorination de PVC lors de la pyrolyse.

Le mécanisme réactionnel ou l'étape limitante de la réaction entre PVC et PW a été identifié comme le mécanisme de Nucléation et de Croissance qui suit le modèle Avrami-Erofeev avec n=2 (A2). Ce modèle cinétique a été lié à la formation et croissance des cristaux de chlorure métallique par des réactions entre HCl et des minéraux dans PW.

Nos résultats sont significatifs parce que le petit nombre des modèles cinétiques actuellement dans la littérature se basse sur l'hypothèse que la co-pyrolyse de la biomasse et PVC se passe dans une seule étape ou que le mécanisme réactionnel est du premier ordre. Plusieurs auteurs ont démontrés que ces hypothèses donnent des paramètres cinétiques inexacts. Par conséquent, notre travail représente une amélioration des modèles cinétiques actuels de la co-pyrolyse de la biomasse et de PVC.

Un des principaux avantages du modèle développé dans ce travail est qu'il est facile à intégrer dans un modèle à l'échelle du réacteur d'un gazéifieur.

Modélisation de la pyro-gazéification de déchet de bois dans un réacteur downdraft

Dans ce travail, un modèle de calcul dynamique de fluides (CFD) monodimensionnel a été développé afin de simuler la pyro-gazéification de déchet de bois contaminé avec du chlore (PVC) dans un gazéifieur downdraft en régime permanant. On a utilisé OpenFOAM, un logiciel open source, pour simuler ce modèle.

Ce modèle se compose des sous-modèles de séchage, pyrolyse, oxydation et gazéification du char comme montré par la Figure C.5. Les équations mathématiques qu'on a employées incluent les équations cinétiques de réactions, le transfert de masse et de chaleur, et les bilans de masse, d'énergie et de quantité de mouvement.

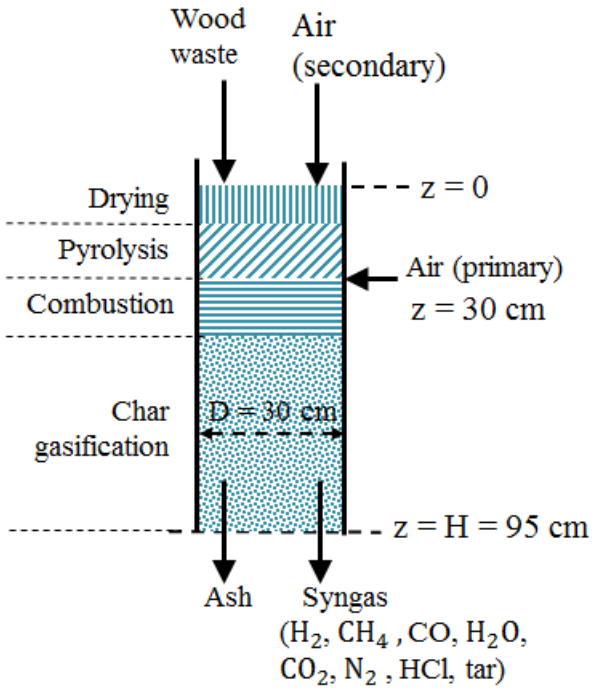

FIGURE C.5: Représentation du modèle de la gazéification du déchet de bois dans un réacteur downdraft.

La zone du réacteur où se passent les réactions de gazéification de char a été modélisée en première, et les résultats de ce modèle ont été en bon accord avec les données expérimentales dans la littérature. De plus, une analyse de sensibilité a été faite pour étudier l'influence de la porosité du lit, la température d'entrée du réacteur et la composition du gaz à la sortie du réacteur sur les résultats du modèle. Cette étude a montré que la porosité du lit n'a pas d'effet significatif sur le comportement du lit, ce qui valide l'hypothèse que ce paramètre est constant. Par contre, les concentrations en oxygène et en vapeur d'eau dans le gaz d'entrée du réacteur ont eu l'impact le plus important sur le ratio H_2/CO du syngaz. Par ailleurs, une analyse de la charge de chaleur a été effectuée en faisant un bilan énergétique sur le gazéifieur. Ceci a révélé que le gazéifieur downdraft est capable de fonctionner

sous conditions autothermiques quand la température du gazéifieur est fixée à 760 °C.

Dans la deuxième partie du travail de modélisation, on a construit des sous-modèles du séchage, de la pyrolyse et de la combustion afin de pouvoir simuler l'ensemble du procédé de la pyro-gazéification de déchet de bois. Pour le sous-modèle de pyrolyse, on a utilisé les paramètres cinétiques qu'on a déterminés auparavant dans le cadre de ce travail. De plus, la réaction d'oxydation de goudrons qui fait partie du sous-modèle de la combustion a été une source majeure d'instabilité lors de l'exécution de la simulation du modèle. La raison est peut-être une combinaison de la forte exothermicité réactionnelle et la teneur élevée en goudrons dans le gazéifieur. Une solution a été trouvée en augmentant le coefficient stœchiométrique de l'oxygène de la réaction d'oxydation de goudrons.

Le modèle complète de la pyro-gazéification a été validé avec les données obtenues à partir des essais dans un gazéifieur pilote de type downdraft avec le déchet de bois B contenant 1 % en masse de PVC (0,57 % en masse de Cl). Les résultats du modèle sont en accord avec les données expérimentales obtenues en sortie du réacteur (température, conversion de déchet, et composition du HCl et goudrons dans le syngaz) ainsi que les profils de la température et la concentration du HCl le long du réacteur. Ce travail peut être complété par la prédiction de la composition des gaz permanents du syngaz.

Purification du syngaz: Enlèvement de HCl en utilisant des adsorbants inorganiques

Dans ce travail, la performance de quatre adsorbants solides a été étudiée pour l'élimination de HCl. Parmi eux, les deux solides, CCW-S et CCW-D, sont des déchets solides industriels qui contiennent essentiellement du carbonate de calcium, alors que Bicar (bicarbonate de sodium) et Lime (chaux éteinte) sont des adsorbants commerciaux. Plusieurs analyses physico-chimiques ont été effectuées pour caractériser ces adsorbants avant et après les tests, telles que ICP, FTIR, DRX et ATG. Les résultats ont révélé que CCW-S et CCW-D sont composé en grande partie de $CaCO_3$, que Bicar est purement de $NaHCO_3$ et que Lime contient à la fois du $Ca(OH)_2$ et un petite quantité de $CaCO_3$. Les impuretés telles que Al, Fe et Mg ont été détectées dans CCW-S, CCW-D et Lime.

L'élimination de HCl a été effectuée dans un réacteur à lit fixe à l'échelle laboratoire comme montré dans la Figure C.6. Un flux descendant du gaz contenant du HCl a été introduit du haut du réacteur et le gaz en sortant du lit a été analysé en continu pour déterminer la quantité du HCl non-adsorbé. Pour toutes les expériences, le temps de passage du gaz a été fixé à 0,71 s.

La première campagne de test a été faite avec un mélange de 500 ppm HCl dans l'azote (HCl/N_2) aux conditions ambiantes. Les résultats ont montré que parmi les quatre adsorbants, Bicar est le plus performant. Le temps de percée moyenne (h)

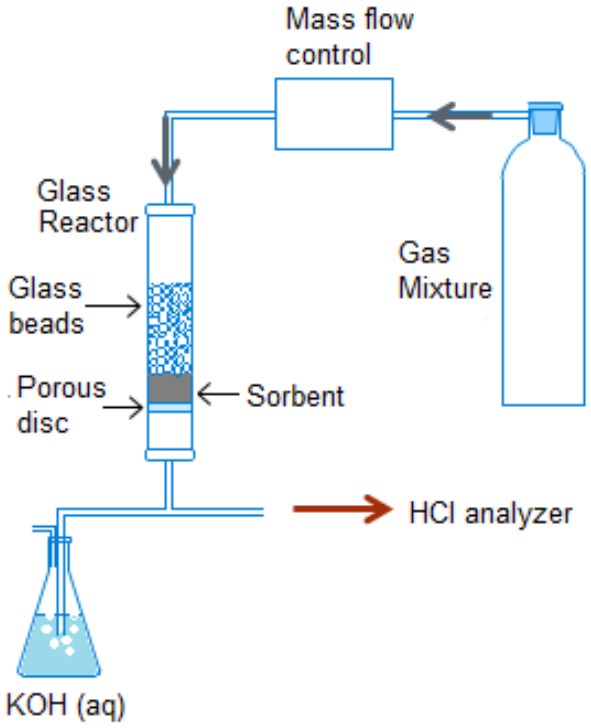

FIGURE C.6: Installation pour les expériences d'adsorption à sec du HCl.

et la capacité d'adsorption (% en masse) sont dans l'ordre suivant : Bicar (66 h ; 26,8 %) > Lime (12,4 h ; 16 %) > CCW-S (7,8 h ; 3,9 %) > CCW-D (3,6 h ; 1,3 %). Par ailleurs, les images TEM-EDX des particules de CCW-S et Bicar ont montré que les impuretés Al, Fe, et Mg, participent à la capture de HCl. De plus, les analyses DRX et MEBE ont montrés qu'il y a une formation des nouveaux cristaux sur la surface des particules Bicar et Lime, bien que pour les particules CCW-S et CCW-D, aucun cristaux aient été observés.

Pour la deuxième campagne de tests, la performance de CCW-S et Bicar a été étudiée sous une atmosphère de 200 ppm HCl/Syngaz synthétique sous conditions atmosphériques. Le temps de percée et la capacité d'adsorption de HCl sont respectivement 48,2 h et 6,7 % pour Bicar, et 2,7 h et 0,5 % pour CCW-S. Une diminution significative de la performance des adsorbants en présence du syngaz a eu lieu. Cela suggère l'effet compétitif des composés du syngaz sur la fixation de HCl par les adsorbants utilisés. D'autres études sont nécessaires pour mieux comprendre les résultats obtenus.

Conclusion

Ce travail de thèse est consacré à atteindre les trois objectifs : 1) Etudes expérimentales sur la pyro-gazéification de déchet de bois contenant une faible quantité de plastiques. 2) Développement d'un modèle CFD sur la pyro-gazéification de déchet

de bois. 3) Etudes expérimentales sur le traitement du HCl dans le syngaz. Les travaux effectués au cours de cette thèses ont montré que :

- Le teneur en plastiques - HDPE, PS et PVC - dans un mélange du bois ont des effets significatifs sur le rendement en produits, la composition du syngaz et la qualité du syngaz (valeur calorifique et teneur en HCl).

- Il y a des interactions significatives entre le bois et le PVC lors du processus de pyro-gazéification. En particulier, la présence du PVC augmente la concentration du HCl dans le syngaz, le rendement en char et la teneur en furanes et HAPs dans les goudrons.

- Le HCl produit lors de la pyrolyse du PVC augmente la vitesse de décomposition des fibres cellulosiques du bois. Ceci est démontré par la diminution significative de l'énergie d'activation de la pyrolyse du hémicellulose et cellulose dans le bois.

- L'interaction entre les éléments minéraux dans le bois et le HCl provenant de la pyrolyse du PVC est l'étape limitante dans le processus de co-pyrolyse du bois et du PVC.

- Le modèle CFD sur la pyro-gazéification du déchet de bois contenant une faible teneur en PVC donne des résultats globalement satisfaisant en comparant avec les données expérimentales. Ce travail peut être complété par la prédiction de la composition des gaz permanents du syngaz.

- Selon les résultats du modèle de la gazéification du char, les concentrations d'oxygène et de vapeur d'eau dans le gaz à l'entrée de la zone de gazéification du char jouent le rôle le plus significatif sur le ratio H2/CO dans le syngaz.

- Les résidus solides industriels issus de la production de bicarbonate et carbonate de sodium ont un potentiel intéressant par rapport aux adsorbants commerciaux pour le traitement du HCl dans le syngaz.

Bibliography

[1] World Bank. What a waste : a global review of solid waste management. Technical Report 68135, The World Bank, March 2012.

[2] Europäische Kommission, editor. *Being wise with waste: the EU's approach to waste management*. Publ. Off. of the European Union, Luxembourg, 2010. OCLC: 696552194.

[3] Harry Knoef. Handbook biomass gasification, 2012.

[4] IEO. International Energy Oulook: 2013, 2013.

[5] Umberto Arena. Gasification: An alternative solution for waste treatment with energy recovery. *Waste Management*, 31(3):405–406, March 2011.

[6] JRC-IPTS. Study on the selection of waste streams for end-of-waste assessment. *JRC Scientific and Technical Reports, EUR*, 24362, 2010.

[7] EN 14961-1. Solid biofuels - Fuel specifications and classes - Part 1: general requirements, 2010.

[8] R.C. Bailie and J.W. Everett. Solid Waste. 1999.

[9] H. Liu, M. Saffaripour, P. Mellin, C.-E. Grip, W. Yang, and W. Blasiak. A thermodynamic study of hot syngas impurities in steel reheating furnaces – Corrosion and interaction with oxide scales. *Energy*, 77:352–361, December 2014.

[10] Patrick J. Woolcock and Robert C. Brown. A review of cleaning technologies for biomass-derived syngas. *Biomass and Bioenergy*, 52:54–84, May 2013.

[11] Ke Liu, Chunshan Song, and Velu Subramani. *Hydrogen and syngas production and purification technologies*. 2010.

[12] Jeom-In Baek, Tae Hyoung Eom, Joong Beom Lee, Seong Jegarl, Chong Kul Ryu, Young Cheol Park, and Sung-Ho Jo. Cleaning of gaseous hydrogen chloride in a syngas by spray-dried potassium-based solid sorbents. *Korean Journal of Chemical Engineering*, 32(5):845–851, May 2015.

[13] Tomohito Kameda, Naoya Uchiyama, Kye-Sung Park, Guido Grause, and Toshiaki Yoshioka. Removal of hydrogen chloride from gaseous streams using magnesium–aluminum oxide. *Chemosphere*, 73(5):844–847, October 2008.

[14] P. Mondal, G.S. Dang, and M.O. Garg. Syngas production through gasification and cleanup for downstream applications — Recent developments. *Fuel Processing Technology*, 92(8):1395–1410, August 2011.

[15] Sunil D. Sharma, Keith McLennan, Michael Dolan, Ty Nguyen, and Don Chase. Design and performance evaluation of dry cleaning process for syngas. *Fuel*, 108:42–53, June 2013.

[16] Michael Stemmler and Michael Müller. Chemical hot gas cleaning concept for the "CHRISGAS process. *Biomass and Bioenergy*, 35:S105–S115, October 2011.

[17] Filomena Pinto, Miguel Miranda, and Paula Costa. Production of liquid hydrocarbons from rice crop wastes mixtures by co-pyrolysis and co-hydropyrolysis. *Fuel*, 174:153–163, June 2016.

[18] Faisal Abnisa and Wan Mohd Ashri Wan Daud. A review on co-pyrolysis of biomass: An optional technique to obtain a high-grade pyrolysis oil. *Energy Conversion and Management*, 87:71–85, November 2014.

[19] T. Cornelissen, M. Jans, J. Yperman, G. Reggers, S. Schreurs, and R. Carleer. Flash co-pyrolysis of biomass with polyhydroxybutyrate: Part 1. Influence on bio-oil yield, water content, heating value and the production of chemicals. *Fuel*, 87(12):2523–2532, September 2008.

[20] Tigabwa Y. Ahmed, Murni M. Ahmad, Suzana Yusup, Abrar Inayat, and Zakir Khan. Mathematical and computational approaches for design of biomass gasification for hydrogen production: A review. *Renewable and Sustainable Energy Reviews*, 16(4):2304–2315, 2012.

[21] Marcio L. de Souza-Santos. *Solid fuels combustion and gasification: modeling, simulation, and equipment operation.* Number 180 in Mechanical engineering. Marcel Dekker, New York, 2004.

[22] Paul T. Williams. *Waste treatment and disposal.* 2 edition, 2005.

[23] European Commission. Waste Generated and Treated in Europe, 2003.

[24] L. Evans, S. Okamura, J. Poll, and N. Barker. Evaluation of Opportunities for Converting Indigenous UK wastes to Fuels and Energy. Technical Report AEA/ED45551/Issue 1, April 2009.

[25] Stephen Burnley, Rhiannon Phillips, Terry Coleman, and Terence Rampling. Energy implications of the thermal recovery of biodegradable municipal waste materials in the United Kingdom. *Waste Management*, 31(9–10):1949 – 1959, 2011.

[26] S. Consonni, M. Giugliano, and M. Grosso. Alternative strategies for energy recovery from municipal solid waste. Part A : Mass and energy balances. *Waste Management*, 25(2):123–135, 2005.

[27] EN 15359. Solid recovered fuels - Specifications and classes, 2011.

[28] S. Mousseau. State-of-the-art of the European regulation on wood wastes and wood ashes valorization. Synthesis. Technical report, ADEME, 2007.

[29] R Frost. Incineration of sewage sludge, University of Leeds Short Course 'Incineration and Energy from Waste'., 1991.

[30] European Commission (DG Environment). Plastic waste in the environment-Final Report, 2011.

[31] PlasticsEurope. Plastics-the facts 2012_analysis of european plastics production, demand and waste for 2011.pdf, 2012.

[32] Maciej Sienkiewicz, Justyna Kucinska-Lipka, Helena Janik, and Adolf Balas. Progress in used tyres management in the European Union: A review. *Waste Management*, 32(10):1742–1751, October 2012.

[33] JRC-IPTS. End-of-waste criteria for waste plastic for conversion; Technical proposals, 2013.

[34] ERFO. Classification of Solid Recovered Fuels, 2005.

[35] Jaya Shankar Tumuluru, Shahab Sokhansanj, Christopher T. Wright, Richard D. Boardman, and Neal A. Yancey. A review on biomass classification and composition, co-firing issues and pretreatment methods. In *Proceedings of the 2011 ASABE annual international meeting. Louisville, Kentucky, USA*, pages 7–10, 2011.

[36] Prabir Basu. *Biomass gasification and pyrolysis: practical design and theory*. Academic Press, Burlington, MA, 2010.

[37] A. V. Bridgwater. Renewable fuels and chemicals by thermal processing of biomass. *Chemical Engineering Journal*, 91(2):87–102, 2003.

[38] Michael Jerry Antal and Morten Grønli. The Art, Science, and Technology of Charcoal Production. *Industrial & Engineering Chemistry Research*, 42(8):1619–1640, April 2003.

[39] Cornelia Vasile and M. A. Brebu. Thermal valorisation of biomass and of synthetic polymer waste. Upgrading of pyrolysis oils. *Cellulose chemistry and technology*, 40(7):489, 2006.

[40] Carole Couhert, Jean-Michel Commandre, and Sylvain Salvador. Is it possible to predict gas yields of any biomass after rapid pyrolysis at high temperature from its composition in cellulose, hemicellulose and lignin? *Fuel*, 88(3):408–417, March 2009.

[41] Colomba Di Blasi, Carmen Branca, Antonio Santoro, and Elier Gonzalez Hernandez. Pyrolytic behavior and products of some wood varieties. *Combustion and Flame*, 124(1–2):165–177, January 2001.

[42] G. Varhegyi, Mj Antal, T. Szekely, and P. Szabo. Kinetics of the Thermal-Decomposition of Cellulose, Hemicellulose, and Sugar-Cane Bagasse. *Energy & Fuels*, 3(3):329–335, June 1989.

[43] Umberto Arena. Process and technological aspects of municipal solid waste gasification. A review. *Waste Management*, 32(4):625–639, April 2012.

[44] P.L. Walker, F. Rusinko, and L.G. Austin. Gas reactions of carbon. *Advances in Catalysis*, 11:133–221, 1959.

[45] Colomba Di Blasi. Combustion and gasification rates of lignocellulosic chars. *Progress in Energy and Combustion Science*, 35(2):121–140, April 2009.

[46] F Mermoud, S Salvador, L Vandesteene, and F Golfier. Influence of the pyrolysis heating rate on the steam gasification rate of large wood char particles. *Fuel*, 85(10-11):1473–1482, July 2006.

[47] Capucine Dupont, Timothée Nocquet, José Augusto Da Costa Jr., and Christèle Verne-Tournon. Kinetic modelling of steam gasification of various woody biomass chars: Influence of inorganic elements. *Bioresource Technology*, 102(20):9743–9748, October 2011.

[48] I.I. Ahmed and A.K. Gupta. Kinetics of woodchips char gasification with steam and carbon dioxide. *Applied Energy*, 88(5):1613–1619, 2011.

[49] G. Teixeira, L. Van de steene, A. Ponthieux, and S. Salvador. Prediction of the gasification kinetics of a single wood char particle from a limited set of parameters. *Fuel*, 123:194–204, 2014.

[50] Colomba Di Blasi. Dynamic behaviour of stratified downdraft gasifiers. *Chemical Engineering Science*, 55(15):2931–2944, 2000.

[51] Lopamudra Devi, Krzysztof J. Ptasinski, and Frans J.J.G. Janssen. A review of the primary measured for tar elimination in biomass gasification processes. *Biomass and Bioenergy*, 24:125–140, 2003.

[52] V. Belgiorno, G. De Feo, C. Della Rocca, and R. M. A. Napoli. Energy from gasification of solid wastes. *Waste management*, 23(1):1–15, 2003.

[53] Quaak Knoef, P and H Stassen. Energy from biomass. *World Bank technical paper*, (422), 1999.

[54] Richard L. Fosgitt. Gasification using rotary kiln technology. 2010.

[55] Jeung Woo Lee, Tae U Yu, Jae Wook Lee, Ji Hong Moon, Hyo Jae Jeong, Sang Shin Park, Won Yang, and Uen Do Lee. Gasification of Mixed Plastic Wastes in a Moving-Grate Gasifier and Application of the Producer Gas to a Power Generation Engine. *Energy Fuels*, 27(4):2092–2098, 2013.

[56] Fédéric Fabry, Christophe Rehmet, Vandad Rohani, and Laurent Fulcheri. Waste gasification by thermal plasma: a review. *Waste and Biomass Valorization*, (3):421–439, September 2013.

[57] Brickner Gershman. Gasification of Non-Recycled Plastics From Municipal Solid Waste In the United States. 2013.

[58] Riedhammer. Riedhammer rotary kiln. 2014.

[59] Wellons FEI Corp. Reciprocating grate, 2016.

[60] Umberto Arena. Process and technological aspects of municipal solid waste gasification. A review. *Waste Management*, 32(4):625 – 639, 2012.

[61] Brickner Gershman. Gasification of Non-Recycled Plastics From Municipal Solid Waste In the United States. 2013.

[62] Ragnar Warnecke. Gasification of biomass: comparison of fixed bed and fluidised bed gasifier. *Biomass and Bioenergy*, (18):489–497, 2000.

[63] M Mahishi and D Goswami. Thermodynamic optimization of biomass gasifier for hydrogen production. *International Journal of Hydrogen Energy*, 32(16):3831–3840, November 2007.

[64] K. Froment, F. Defoort, C. Bertrand, J.M. Seiler, J. Berjonneau, and J. Poirier. Thermodynamic equilibrium calculations of the volatilization and condensation of inorganics during wood gasification. *Fuel*, 107:269–281, May 2013.

[65] A. Deydier, F. Marias, P. Bernada, F. Couture, and U. Michon. Equilibrium model for a travelling bed gasifier. *Biomass and Bioenergy*, 35(1):133–145, January 2011.

[66] S. Jarungthammachote and A. Dutta. Equilibrium modeling of gasification: Gibbs free energy minimization approach and its application to spouted bed and spout-fluid bed gasifiers. *Energy Conversion and Management*, 49(6):1345–1356, June 2008.

[67] Avdhesh Kr. Sharma. Equilibrium modeling of global reduction reactions for a downdraft (biomass) gasifier. *Energy Conversion and Management*, 49(4):832–842, April 2008.

[68] M. Baratieri, P. Baggio, L. Fiori, and M. Grigiante. Biomass as an energy source: Thermodynamic constraints on the performance of the conversion process. *Bioresource Technology*, 99(15):7063–7073, October 2008.

[69] Carlos R. Altafini, Paulo R. Wander, and Ronaldo M. Barreto. Prediction of the working parameters of a wood waste gasifier through an equilibrium model. *Energy Conversion and Management*, 44(17):2763–2777, October 2003.

[70] Andrés Melgar, Juan F. Pérez, Hannes Laget, and Alfonso Horillo. Thermochemical equilibrium modelling of a gasifying process. *Energy Conversion and Management*, 48(1):59–67, January 2007.

[71] Qiuhui Yan, Liejin Guo, and Youjun Lu. Thermodynamic analysis of hydrogen production from biomass gasification in supercritical water. *Energy Conversion and Management*, 47(11-12):1515–1528, July 2006.

[72] Youjun Lu, Liejin Guo, Ximin Zhang, and Qiuhui Yan. Thermodynamic modeling and analysis of biomass gasification for hydrogen production in supercritical water. *Chemical Engineering Journal*, 131(1-3):233–244, July 2007.

[73] M. Ruggiero and G. Manfrida. An equilibrium model for biomass gasification processes. *Renewable Energy*, 16(1-4):1106–1109, January 1999.

[74] X.T. Li, J.R. Grace, C.J. Lim, A.P. Watkinson, H.P. Chen, and J.R. Kim. Biomass gasification in a circulating fluidized bed. *Biomass and Bioenergy*, 26(2):171–193, February 2004.

[75] M.K. Karmakar and A.B. Datta. Generation of hydrogen rich gas through fluidized bed gasification of biomass. *Bioresource Technology*, 102(2):1907–1913, January 2011.

[76] J.K. Ratnadhariya and S.A. Channiwala. Three zone equilibrium and kinetic free modeling of biomass gasifier – a novel approach. *Renewable Energy*, 34(4):1050–1058, April 2009.

[77] Günther Schuster, Gerhard Löffler, Klaus Weigl, and Hermann Hofbauer. Biomass steam gasification–an extensive parametric modeling study. *Bioresource technology*, 77(1):71–79, 2001.

[78] M Prins, K Ptasinski, and F Janssen. From coal to biomass gasification: Comparison of thermodynamic efficiency. *Energy*, 32(7):1248–1259, July 2007.

[79] Maria Puig-Arnavat, Joan Carles Bruno, and Alberto Coronas. Review and analysis of biomass gasification models. *Renewable and Sustainable Energy Reviews*, 14(9):2841–2851, December 2010.

[80] Agus Haryanto, Sandun D. Fernando, Lester O. Pordesimo, and Sushil Adhikari. Upgrading of syngas derived from biomass gasification: A thermodynamic analysis. *Biomass and Bioenergy*, 33(5):882–889, May 2009.

[81] Gabriel Teixeira. *Gazéification de charbon de granules de bois: comportement thermochimique et mécanique d'un lit fixe continu [dissertation].* dissertation, Université de Toulouse, 2012.

[82] C Diblasi. Modeling chemical and physical processes of wood and biomass pyrolysis. *Progress in Energy and Combustion Science*, 34(1):47–90, February 2008.

[83] S. Sinha, A. Jhalani, M. R. Ravi, and Anjan Ray. Modelling of pyrolysis in wood: A review. *SESI Journal*, 10(1):41–62, 2000.

[84] Hsisheng Teng and Yun-Chou Wei. Thermogravimetric studies on the kinetics of rice hull pyrolysis and the influence of water treatment. *Industrial & Engineering Chemistry Research*, 37(10):3806–3811, 1998.

[85] Andrés Anca-Couce, Anka Berger, and Nico Zobel. How to determine consistent biomass pyrolysis kinetics in a parallel reaction scheme. *Fuel*, 123:230–240, 2014.

[86] C. A. Koufopanos, A. Lucchesi, and G. Maschio. Kinetic modelling of the pyrolysis of biomass and biomass components. *The Canadian Journal of Chemical Engineering*, 67(1):75–84, 1989.

[87] Morten Gunnar Grønli, Gábor Várhegyi, and Colomba Di Blasi. Thermogravimetric Analysis and Devolatilization Kinetics of Wood. *Industrial & Engineering Chemistry Research*, 41(17):4201–4208, August 2002.

[88] Carmen Branca, Alessandro Albano, and Colomba Di Blasi. Critical evaluation of global mechanisms of wood devolatilization. *Thermochimica Acta*, 429(2):133–141, 2005.

[89] Pious O. Okekunle, Teeranai Pattanotai, Hirotatsu Watanabe, and Ken Okazaki. Numerical and experimental investigation of intra-particle heat transfer and tar decomposition during pyrolysis of wood biomass. *Journal of Thermal Science and Technology*, 6(3):360–375, 2011.

[90] Eliseo Ranzi, Alberto Cuoci, Tiziano Faravelli, Alessio Frassoldati, Gabriele Migliavacca, Sauro Pierucci, and Samuele Sommariva. Chemical Kinetics of Biomass Pyrolysis. *Energy & Fuels*, 22(6):4292–4300, November 2008.

[91] S.S. Stringel. *High temperature gasification of millimetric wood particles between 800°C and 1400°C*. PhD thesis, Institut National Polytechnique de Toulouse, 2011.

[92] E. CETIN, B. MOGHTADERI, R. GUPTA, and T. F. WALL. BIOMASS GASIFICATION KINETICS: INFLUENCES OF PRESSURE AND CHAR STRUCTURE. *Combustion Science and Technology*, 177(4):765–791, 2005.

[93] Dong Kyun Seo, Sun Ki Lee, Min Woong Kang, Jungho Hwang, and Tae-U. Yu. Gasification reactivity of biomass chars with CO2. *Biomass and Bioenergy*, 34(12):1946–1953, December 2010.

[94] Keigo Matsumoto, Keiji Takeno, Toshimitsu Ichinose, Tomoko Ogi, and Masakazu Nakanishi. Gasification reaction kinetics on biomass char obtained as a by-product of gasification in an entrained-flow gasifier with steam and oxygen at 900–1000°C. *Fuel*, 88(3):519–527, March 2009.

[95] J. Fermoso, C. Stevanov, B. Moghtaderi, B. Arias, C. Pevida, M.G. Plaza, F. Rubiera, and J.J. Pis. High-pressure gasification reactivity of biomass chars produced at different temperatures. *Journal of Analytical and Applied Pyrolysis*, 85(1-2):287–293, May 2009.

[96] Satish Manocha, Vanraj B. Chauhan, and L. M. Manocha. Porosity development on activation of char from dry and wet babbool wood. *Carbon letters*, 3(3):133–141, 2002.

[97] R. P. W. J. Struis, C. von Scala, S. Stucki, and R. Prins. Gasification reactivity of charcoal with CO2. Part I: Conversion and structural phenomena. *Chemical Engineering Science*, 57(17):3581 – 3592, 2002.

[98] G. Teixeira, L. Van de steene, A. Ponthieux, and S. Salvador. Prediction of the gasification kinetics of a single wood char particle from a limited set of parameters. *Fuel*, 123:194–204, May 2014.

[99] C. Guizani, F. J. Escudero Sanz, and S. Salvador. The gasification reactivity of high-heating-rate chars in single and mixed atmospheres of H2o and CO2. *Fuel*, 108:812–823, 2013.

[100] L. Van de steene, J. P. Tagutchou, F. J. Escudero Sanz, and S. Salvador. Gasification of woodchip particles: Experimental and numerical study of char–H2o, char–CO2, and char–O2 reactions. *Chemical Engineering Science*, 66(20):4499–4509, October 2011.

[101] Yiqun Wang and Lifeng Yan. CFD Studies on Biomass Thermochemical Conversion. *International Journal of Molecular Sciences*, 9(6):1108–1130, June 2008.

[102] Behdad Moghtaderi. The state-of-the-art in pyrolysis modelling of lignocellulosic solid fuels. *Fire and Materials*, 30(1):1–34, January 2006.

[103] Johann C. Wurzenberger, Susanne Wallner, Harald Raupenstrauch, and Johannes G. Khinast. Thermal conversion of biomass: Comprehensive reactor and particle modeling. *AIChE Journal*, 48(10):2398–2411, 2002.

[104] D. L. Giltrap, R. McKibbin, and G. R. G. Barnes. A steady state model of gas-char reactions in a downdraft biomass gasifier. *Solar Energy*, 74(1):85–91, January 2003.

[105] B.V. Babu and A.S. Chaurasia. Pyrolysis of biomass: improved models for simultaneous kinetics and transport of heat, mass and momentum. *Energy Conversion and Management*, 45(9-10):1297–1327, June 2004.

[106] Soteris A. Kalogirou. Artificial neural networks in renewable energy systems applications: a review. *Renewable and sustainable energy reviews*, 5(4):373–401, 2001.

[107] Daya Shankar Pandey, Saptarshi Das, Indranil Pan, James J. Leahy, and Witold Kwapinski. Artificial neural network based modelling approach for municipal solid waste gasification in a fluidized bed reactor. *Waste Management*, August 2016.

[108] Gang Xiao, Ming-jiang Ni, Yong Chi, Bao-sheng Jin, Rui Xiao, Zhao-ping Zhong, and Ya-ji Huang. Gasification characteristics of MSW and an ANN prediction model. *Waste Management*, 29(1):240–244, January 2009.

[109] Bing Guo, Dingkai Li, Congming Cheng, Zi-an Lü, and Youting Shen. Simulation of biomass gasification with a hybrid neural network model. *Bioresource Technology*, 76(2):77–83, January 2001.

[110] Miloslav Hajek and M. Robin Judd. Use of neural networks in modelling the interactions between gas analysers at coal gasifiers. *Fuel*, 74(9):1347–1351, 1995.

[111] Sergey Vyazovkin, Alan K. Burnham, José M. Criado, Luis A. Pérez-Maqueda, Crisan Popescu, and Nicolas Sbirrazzuoli. ICTAC Kinetics Committee recommendations for performing kinetic computations on thermal analysis data. *Thermochimica Acta*, 520(1-2):1–19, June 2011.

[112] C. Guizani, F. J. Escudero Sanz, and S. Salvador. Influence of temperature and particle size on the single and mixed atmosphere gasification of biomass char with H2o and CO2. *Fuel Processing Technology*, 134:175–188, 2015.

[113] S. Septien, F. J. Escudero Sanz, S. Salvador, and S. Valin. Steam gasification of char from wood chips fast pyrolysis: Development of a semi-empirical model for a fluidized bed reactor application. *Biomass and Bioenergy*, 77:64–74, 2015.

[114] Pedro E. Sánchez-Jiménez, Luis A. Pérez-Maqueda, Antonio Perejón, and José M. Criado. Generalized master plots as a straightforward approach for determining the kinetic model: The case of cellulose pyrolysis. *Thermochimica Acta*, 552:54–59, January 2013.

[115] Michael E. Brown. *Handbook of thermal analysis and calorimetry: Principles and Practice*, volume 1. Elsevier, 1998.

[116] Katarzyna Slopiecka, Pietro Bartocci, and Francesco Fantozzi. Thermogravimetric analysis and kinetic study of poplar wood pyrolysis. *Applied Energy*, 97:491–497, September 2012.

[117] Andrés Anca-Couce. Reaction mechanisms and multi-scale modelling of lignocellulosic biomass pyrolysis. *Progress in Energy and Combustion Science*, 53:41–79, March 2016.

[118] Junmeng Cai, Weixuan Wu, and Ronghou Liu. An overview of distributed activation energy model and its application in the pyrolysis of lignocellulosic biomass. *Renewable and Sustainable Energy Reviews*, 36:236–246, August 2014.

[119] Xun Wang, Mian Hu, Wanyong Hu, Zhihua Chen, Shiming Liu, Zhiquan Hu, and Bo Xiao. Thermogravimetric kinetic study of agricultural residue biomass pyrolysis based on combined kinetics. *Bioresource Technology*, 219:510–520, November 2016.

[120] Mian Hu, Zhihua Chen, Shengkai Wang, Dabin Guo, Caifeng Ma, Yan Zhou, Jian Chen, Mahmood Laghari, Saima Fazal, Bo Xiao, Beiping Zhang, and Shu Ma. Thermogravimetric kinetics of lignocellulosic biomass slow pyrolysis using distributed activation energy model, Fraser–Suzuki deconvolution, and iso-conversional method. *Energy Conversion and Management*, 118:1–11, June 2016.

[121] Panusit Sungsuk, Sasiporn Chayaporn, Sasithorn Sunphorka, Prapan Kuchonthara, Pornpote Piumsomboon, and Benjapon Chalermsinsuwan. Prediction of pyrolysis kinetic parameters from biomass constituents based on simplex-lattice mixture design. *Chinese Journal of Chemical Engineering*, 24(4):535–542, April 2016.

[122] Khanh-Quang Tran, Quang-Vu Bach, Thuat T. Trinh, and Gulaim Seisenbaeva. Non-isothermal pyrolysis of torrefied stump – A comparative kinetic evaluation. *Applied Energy*, 136:759–766, December 2014.

[123] Song Hu, Andreas Jess, and Minhou Xu. Kinetic study of Chinese biomass slow pyrolysis: Comparison of different kinetic models. *Fuel*, 86(17-18):2778–2788, December 2007.

[124] Pedro E. Sánchez-Jiménez, Luis A. Pérez-Maqueda, Antonio Perejón, and José M. Criado. Generalized Kinetic Master Plots for the Thermal Degradation of Polymers Following a Random Scission Mechanism. *The Journal of Physical Chemistry A*, 114(30):7868–7876, August 2010.

[125] P. Rajeshwari and T. K. Dey. Advanced isoconversional and master plot analyses on non-isothermal degradation kinetics of AlN (nano)-reinforced HDPE composites. *Journal of Thermal Analysis and Calorimetry*, 125(1):369–386, July 2016.

[126] Zhihua Chen, Mian Hu, Xiaolei Zhu, Dabin Guo, Shiming Liu, Zhiquan Hu, Bo Xiao, Jingbo Wang, and Mahmood Laghari. Characteristics and kinetic study on pyrolysis of five lignocellulosic biomass via thermogravimetric analysis. *Bioresource Technology*, 192:441 – 450, 2015.

[127] Salvador Naya, Ricardo Cao, Ignacio López de Ullibarri, Ramón Artiaga, Fernando Barbadillo, and Ana García. Logistic mixture model versus Arrhenius for kinetic study of material degradation by dynamic thermogravimetric analysis. *Journal of Chemometrics*, 20(3-4):158–163, March 2006.

[128] J. M. Cai, S. Y. Chen, and R. H. Liu. Weibull mixture model for isoconversional kinetic analysis of biomass oxidative pyrolysis. *Journal of the Energy Institute*, 82(4):238–241, 2009.

[129] Paolo De Filippis, Benedetta de Caprariis, Marco Scarsella, and Nicola Verdone. Double Distribution Activation Energy Model as Suitable Tool in Explaining Biomass and Coal Pyrolysis Behavior. *Energies*, 8(3):1730–1744, March 2015.

[130] Zhicai Cheng, Weixuan Wu, Peng Ji, Xiaotong Zhou, Ronghou Liu, and Junmeng Cai. Applicability of Fraser–Suzuki function in kinetic analysis of DAEM processes and lignocellulosic biomass pyrolysis processes. *Journal of Thermal Analysis and Calorimetry*, 119(2):1429–1438, February 2015.

[131] Antonio Perejón, Pedro E. Sánchez-Jiménez, José M. Criado, and Luis A. Pérez-Maqueda. Kinetic Analysis of Complex Solid-State Reactions. A New Deconvolution Procedure. *The Journal of Physical Chemistry B*, 115(8):1780–1791, March 2011.

[132] Stefano Consonni and Federico Viganò. Waste gasification vs. conventional Waste-To-Energy: A comparative evaluation of two commercial technologies. *Waste Management*, 32(4):653–666, 2012.

[133] H. Boerrigter and R. Rauch. Syngas production and utilisation. In H.A.M Knoef, editor, *Handbook Biomass Gasification*. Biomass Technology Group (BTG), 2005.

[134] Thomas A. Milne, N. Abatzoglou, and Robert J. Evans. Biomass gasifier" tars": their nature, formation, and conversion. 1998.

[135] Patrick J. Woolcock and Robert C. Brown. A review of cleaning technologies for biomass-derived syngas. *Biomass and Bioenergy*, 52:54–84, May 2013.

[136] A. A. Khan, W. de Jong, P. J. Jansens, and H. Spliethoff. Biomass combustion in fluidized bed boilers: Potential problems and remedies. *Fuel Processing Technology*, 90(1):21–50, January 2009.

[137] Matthew M. Yung, Whitney S. Jablonski, and Kimberly A. Magrini-Bair. Review of Catalytic Conditioning of Biomass-Derived Syngas. *Energy & Fuels*, 23(4):1874–1887, April 2009.

[138] Mohammad Asadullah. Biomass gasification gas cleaning for downstream applications: A comparative critical review. *Renewable and Sustainable Energy Reviews*, 40:118–132, December 2014.

[139] Poulomi Sannigrahi and Arthur J. Ragauskas. Poplar as a feedstock for biofuels : a review of compositional characteristics. *Biofuels, Bioprod. Bioref.*, 4:209–226, 2010.

[140] H. P. Wenning. The VEBA OEL technologie pyrolysis process. *Journal of analytical and applied pyrolysis*, 25:301–310, 1993.

[141] EN 15415-2. Solid recovered fuels - Determination of particle size distribution - Part 2: Maximum projected length method (manual) for large dimension particles, 2012.

[142] EN 15415-1. Solid recovered fuels - Determination of particle size distribution - Part 1: Screen method for small dimension particles, 2011.

[143] EN 15443. Solid recovered fuels - Methods for the preparation of the laboratory sample, 2011.

[144] Pratik N. Sheth and B.V. Babu. Experimental studies on producer gas generation from wood waste in a downdraft biomass gasifier. *Bioresource Technology*, 100(12):3127–3133, June 2009.

[145] EN 15414-3. Solid recovered fuels - Determination of moisture content using the oven dry method., 2011.

[146] Myer Kutz, editor. *Applied plastics engineering handbook: Processing and materials*. Elsevier, 2011.

[147] EN 15402. Solid recovered fuels - Determination of the content of volatile matter, 2011.

[148] I Obernberger, T Brunner, and G Barnthaler. Chemical properties of solid biofuels—significance and impact. *Biomass and Bioenergy*, 30(11):973–982, November 2006.

[149] EN 15403. Solid recovered fuels - Determination of ash content, 2011.

[150] EN 15410. Solid recovered fuels - Methods for the determination of the content of major elements (Al, Ca, Fe, K, Mg, Na, P, Si, Ti), 2011.

[151] EN 15411. Solid recovered fuels - Methods for the determination of the content of trace elements (As, Ba, Be, Cd, Co, Cr, Cu, Hg, Mo, Mn, Ni, Pb, Sb, Se, Tl, V and Zn), 2012.

[152] EN 15407. Solid recovered fuels - Methods for the determination of carbon (C), hydrogen (H) and nitrogen (N) content, 2011.

[153] EN 15400. Solid recovered fuels - Determination of calorific value, 2011.

[154] P.K. Dadzie, M. Amoah, K. Frimpong-Mensah, and F. Oheneba-Kwarteng. Some physical, mechanical and anatomical characteristics of stewood and branchwood of two hardwood species used for structural applications. *Materials and structures*, 49(12):4947 – 4958, 2016.

[155] James E. Mark. *Polymer data handbook*. Oxford university press, 2 edition, 2009.

[156] World Nuclear Association. Heating values of various fuels, 2016.

[157] Emil Vainio, Hanna Kinnunen, Tor Laurén, Anders Brink, Patrik Yrjas, Nikolai DeMartini, and Mikko Hupa. Low-temperature corrosion in co-combustion of biomass and solid recovered fuels. *Fuel*, 184:957–965, November 2016.

[158] Akio Yasuhara, Takeo Katami, and Takayuki Shibamoto. Formation of PCDDs, PCDFs, and Coplanar PCBs from Incineration of Various Woods in the Presence of Chlorides. *Environmental Science & Technology*, 37(8):1563–1567, April 2003.

[159] Rolf-Dieter Peek. EU directives and national regulations for the recycling and disposal of waste wood. In *Proceedings, Environmental Impacts of Preservative-treated Wood Conference*, pages 210–226. Citeseer, 2006.

[160] Demirbas, A. Fuel and Combustion Properties of Bio-wastes. *Energy Sources*, 27(5):451–462, 2005.

[161] J. Werther, M. Saenger, E.-U Hartge, T. Ogada, and Z. Siagi. Combustion of agricultural residues. *Progress in Energy and Combustion Science*, 26:1–27, 2000.

[162] B. M Jenkins, L. L Baxter, T. R Miles Jr., and T. R Miles. Combustion properties of biomass. *Fuel Processing Technology*, 54(1–3):17–46, March 1998.

[163] Mass Quincy. Thermal decomposition of polymers. In *SFPE handbook of fire protection engineering*. Springer New York, 2 edition, 1995.

[164] Elizabeth A. Williams and P.T. Williams. The pyrolysis of individual plastics and a plastic mixture in a fixed bed reactor. *Chemical Technology and Biotechnology*, 1997.

[165] T. Cornelissen, J. Yperman, G. Reggers, S. Schreurs, and R. Carleer. Flash co-pyrolysis of biomass with polylactic acid. Part 1: Influence on bio-oil yield and heating value. *Fuel*, 87(7):1031–1041, June 2008.

[166] Wu-Jun Liu, Ke Tian, Hong Jiang, Xue-Song Zhang, and Guang-Xi Yang. Preparation of liquid chemical feedstocks by co-pyrolysis of electronic waste and biomass without formation of polybrominated dibenzo-p-dioxins. *Bioresource Technology*, 128:1–7, January 2013.

[167] Ille Johannes, Laine Tiikma, and Hans Luik. Synergy in co-pyrolysis of oil shale and pine sawdust in autoclaves. *Journal of Analytical and Applied Pyrolysis*, 104:341–352, November 2013.

[168] E. M. Grieco and G. Baldi. Pyrolysis of polyethylene mixed with paper and wood: Interaction effects on tar, char and gas yields. *Waste Management*, 32(5):833–839, 2012.

[169] Jingxuan Yang, Jenny Rizkiana, Wahyu Bambang Widayatno, Surachai Karnjanakom, Malinee Kaewpanha, Xiaogang Hao, Abuliti Abudula, and Guoqing Guan. Fast co-pyrolysis of low density polyethylene and biomass residue for oil production. *Energy Conversion and Management*, 120:422–429, July 2016.

[170] Sasa Papuga, Petar Gvero, and Ljiljana Vukic. Temperature and time influence on the waste plastics pyrolysis in the fixed bed reactor. *Thermal Science*, 20(2):731–741, 2016.

[171] Jian-Ping Sun, Shu-Juan Sui, Zhi-Jun Zhang, Shun Tan, and Qing-Wen Wang. Study on the pyrolytic behavior of wood-plastic composites using Py-GC/MS. *BioResources*, 8:6196–210, 2013.

[172] Filipe Paradela, Filomena Pinto, Ibrahim Gulyurtlu, Isabel Cabrita, and Nuno Lapa. Study of the co-pyrolysis of biomass and plastic wastes. *Clean Technologies and Environmental Policy*, 11(1):115–122, February 2009.

[173] V. I. Sharypov, N. Marin, N. G. Beregovtsova, S. V. Baryshnikov, B. N. Kuznetsov, V. L. Cebolla, and J. V. Weber. Co-pyrolysis of wood biomass and synthetic polymer mixtures. Part I: influence of experimental conditions on the evolution of solids, liquids and gases. *Journal of Analytical and Applied Pyrolysis*, 64(1):15–28, 2002.

[174] Adetoyese Olajire Oyedun, Choun Zhi Tee, Svenja Hanson, and Chi Wai Hui. Thermogravimetric analysis of the pyrolysis characteristics and kinetics of plastics and biomass blends. *Fuel Processing Technology*, 128:471–481, 2014.

[175] Eylem Önal, Başak Burcu Uzun, and Ayşe Eren Pütün. Bio-oil production via co-pyrolysis of almond shell as biomass and high density polyethylene. *Energy Conversion and Management*, 78:704–710, February 2014.

[176] Atila Caglar and Bahattin Aydinli. Isothermal co-pyrolysis of hazelnut shell and ultra-high molecular weight polyethylene: The effect of temperature and composition on the amount of pyrolysis products. *Journal of Analytical and Applied Pyrolysis*, 86(2):304–309, November 2009.

[177] Dong Kyoo Park, Sang Done Kim, See Hoon Lee, and Jae Goo Lee. Co-pyrolysis characteristics of sawdust and coal blend in TGA and a fixed bed reactor. *Bioresource Technology*, 101(15):6151 – 6156, 2010.

[178] M. Bernardo, N. Lapa, M. Gonçalves, B. Mendes, F. Pinto, I. Fonseca, and H. Lopes. Physico-chemical properties of chars obtained in the co-pyrolysis of waste mixtures. *Journal of Hazardous Materials*, 219-220:196–202, June 2012.

[179] Özge Çepelioğullar and Ayşe E. Pütün. Products characterization study of a slow pyrolysis of biomass-plastic mixtures in a fixed-bed reactor. *Journal of Analytical and Applied Pyrolysis*, 110:363–374, November 2014.

[180] Yoshiaki Matsuzawa, Muneo Ayabe, and Junya Nishino. Acceleration of cellulose co-pyrolysis with polymer. *Polymer degradation and stability*, 71(3):435–444, 2001.

[181] Yoshiaki Matsuzawa, Muneo Ayabe, Junya Nishino, Nobuhiko Kubota, and Mikio Motegi. Evaluation of char fuel ratio in municipal pyrolysis waste. *Fuel*, 83(11-12):1675–1687, August 2004.

[182] John Scheirs and Walter Kaminsky. *Feedstock recycling and pyrolysis of waste plastics - Converting waste plastics into diesel and other fuels*. John Wiley & Sons, 2006.

[183] Paul T. Williams and Elizabeth A. Williams. Interaction of Plastics in Mixed-Plastics Pyrolysis. *Energy & Fuels*, 13(1):188–196, January 1999.

[184] Faisal Abnisa, W.M.A. Wan Daud, and J.N. Sahu. Pyrolysis of mixtures of palm shell and polystyrene: An optional method to produce a high-grade of pyrolysis oil. *Environmental Progress & Sustainable Energy*, 33(3):1026–1033, October 2014.

[185] Sijiang Xiong, Jiankun Zhuo, Hui Zhou, Renzhong Pang, and Qiang Yao. Study on the co-pyrolysis of high density polyethylene and potato blends using thermogravimetric analyzer and tubular furnace. *Journal of Analytical and Applied Pyrolysis*, 112:66–73, March 2015.

[186] Faisal Abnisa, W.M.A. Wan Daud, Sujahta Ramalingam, Muhamad Naqiuddin Bin M. Azemi, and J.N. Sahu. Co-pyrolysis of palm shell and polystyrene waste mixtures to synthesis liquid fuel. *Fuel*, 108:311–318, June 2013.

[187] Mihai Brebu, Suat Ucar, Cornelia Vasile, and Jale Yanik. Co-pyrolysis of pine cone with synthetic polymers. *Fuel*, 89(8):1911–1918, August 2010.

[188] Hui Zhou, Chunfei Wu, Jude A. Onwudili, Aihong Meng, Yanguo Zhang, and Paul T. Williams. Effect of interactions of PVC and biomass components on the formation of polycyclic aromatic hydrocarbons (PAH) during fast co-pyrolysis. *RSC Adv.*, 5(15):11371–11377, 2015.

[189] Jon Alvarez, Shogo Kumagai, Chunfei Wu, Toshiaki Yoshioka, Javier Bilbao, Martin Olazar, and Paul T. Williams. Hydrogen production from biomass and plastic mixtures by pyrolysis-gasification. *International Journal of Hydrogen Energy*, 39(21):10883–10891, 2014.

[190] A. Marongiu, T. Faravelli, G. Bozzano, M. Dente, and E. Ranzi. Thermal degradation of poly(vinyl chloride). *Journal of Analytical and Applied Pyrolysis*, 70(2):519–553, December 2003.

[191] Özge Çepelioğullar and Ayşe E. Pütün. A pyrolysis study for the thermal and kinetic characteristics of an agricultural waste with two different plastic wastes. *Waste Management and Research*, 32:971–979, 2014.

[192] Hui Zhou, YanQiu Long, AiHong Meng, QingHai Li, and YanGuo Zhang. Interactions of three municipal solid waste components during co-pyrolysis. *Journal of Analytical and Applied Pyrolysis*, 111:265–271, January 2015.

[193] H Kuramochi, D Nakajima, S Goto, K Sugita, W Wu, and K Kawamoto. HCl emission during co-pyrolysis of demolition wood with a small amount of PVC film and the effect of wood constituents on HCl emission reduction. *Fuel*, 87(13-14):3155–3157, October 2008.

[194] Jie Yu, Lushi Sun, Chuan Ma, Yu Qiao, and Hong Yao. Thermal degradation of PVC: A review. *Waste Management*, 2015.

[195] Hui Zhou, YanQiu Long, AiHong Meng, QingHai Li, and YanGuo Zhang. Thermogravimetric characteristics of typical municipal solid waste fractions during co-pyrolysis. *Waste Management*, 38:194 – 200, 2015.

[196] Marwa Said, Laurent Cassayre, Jean-Louis Dirion, Ange Nzihou, and Xavier Joulia. Behavior of heavy metals during gasification of phytoextraction plants: thermochemical modelling. In *Computer aided chemical engineering*, volume 37, pages 341–346, 2015.

[197] CEN BT/TF 143. Sampling and analysis of tar and particles in biomass producer gases - Technical Report, July 2005.

[198] Bin Han, Yu Chen, Yulong Wu, Derun Hua, Zhen Chen, Wei Feng, Mingde Yang, and Quanhua Xie. Co-pyrolysis behaviors and kinetics of plastics–biomass blends through thermogravimetric analysis. *Journal of Thermal Analysis and Calorimetry*, 115(1):227–235, January 2014.

[199] Özge Çepelioğullar and Ayşe E. Pütün. Thermal and kinetic behaviors of biomass and plastic wastes in co-pyrolysis. *Energy Conversion and Management*, 75:263–270, November 2013.

[200] A. Aboulkas and K. El Harfi. Co-pyrolysis of olive residue with poly (vinyl chloride) using thermogravimetric analysis. *Journal of thermal analysis and calorimetry*, 95(3):1007–1013, 2009.

[201] Xiao-yan Bai, Qing-wen Wang, Shu-juan Sui, and Chun-sheng Zhang. The effects of wood-flour on combustion and thermal degradation behaviors of PVC in wood-flour/poly(vinyl chloride) composites. *Journal of Analytical and Applied Pyrolysis*, 91(1):34–39, 2011.

[202] L. Sorum, M.G. Gronli, and J.E Hustad. Pyrolysis characteristics and kinetics of municipal solid wastes. *Fuel*, 80, 2000. OCLC: 69098003.

[203] Alan K. Burnham, Xiaowei Zhou, and Linda J. Broadbelt. Critical Review of the Global Chemical Kinetics of Cellulose Thermal Decomposition. *Energy & Fuels*, 29(5):2906–2918, May 2015.

[204] Sibel Irmak, Mehtap Kurtuluş, Arif Hasanoğlu (Hesenov), and Oktay Erbatur. Gasification efficiencies of cellulose, hemicellulose and lignin fractions of biomass in aqueous media by using Pt on activated carbon catalyst. *Biomass and Bioenergy*, 49:102–108, February 2013.

[205] Panusit Sungsuk, Sasiporn Chayaporn, Sasithorn Sunphorka, Prapan Kuchonthara, Pornpote Piumsomboon, and Benjapon Chalermsinsuwan. Prediction of pyrolysis kinetic parameters from biomass constituents based on simplex-lattice mixture design. *Chinese Journal of Chemical Engineering*, 24(4):535–542, April 2016.

[206] Junbo Zhou, Ben Gui, Yu Qiao, Jian Zhang, Wenxia Wang, Hong Yao, Yun Yu, and Minghou Xu. Understanding the pyrolysis mechanism of polyvinylchloride (PVC) by characterizing the chars produced in a wire-mesh reactor. *Fuel*, 166:526–532, February 2016.

[207] M. Mehl, A. Marongiu, T. Faravelli, G. Bozzano, M. Dente, and E. Ranzi. A kinetic modeling study of the thermal degradation of halogenated polymers. *Journal of Analytical and Applied Pyrolysis*, 72(2):253–272, November 2004.

[208] A. Aboulkas, K. El harfi, A. El bouadili, M. Nadifiyine, M. Benchanaa, and A. Mokhlisse. Pyrolysis kinetics of olive residue/plastic mixtures by non-isothermal thermogravimetry. *Fuel Processing Technology*, 90(5):722–728, May 2009.

[209] Davis, Philip J and Philip Rabinowitz. *Methods of numerical integration*. Courier Corporation, 2007.

[210] T. Hatakeyama and F.X. Quinn. *Thermal analysis: Fundamentals and applications to polyer science*. John Wiley & Sons, 2 edition, 1999.

[211] Pedro E. Sánchez-Jiménez, Antonio Perejón, José M. Criado, María J. Diánez, and Luis A. Pérez-Maqueda. Kinetic model for thermal dehydrochlorination of poly(vinyl chloride). *Polymer*, 51(17):3998–4007, August 2010.

[212] Rosa Miranda, Jin Yang, Christian Roy, and Cornelia Vasile. Vacuum pyrolysis of PVC I. Kinetic study. *Polymer degradation and stability*, 64(1):127–144, 1999.

[213] Abhishek Bhargava, Patrick van Hees, and Berit Andersson. Pyrolysis modeling of PVC and PMMA using a distributed reactivity model. *Polymer Degradation and Stability*, 129:199–211, July 2016.

[214] Rosa Miranda, Jin Yang, Christian Roy, and Cornelia Vasile. Vacuum pyrolysis of commingled plastics containing PVC I. Kinetic study. *Polymer Degradation and stability*, 72(3):469–491, 2001.

[215] Vikram Seshadri and Phillip R. Westmoreland. Role of pericyclic reactions in the pyrolysis of cellulose and hemicellulose. In *Role of pericyclic reactions in the pyrolysis of cellulose and hemicellulose*, volume Paper ENFL-133, San Francisco, CA, 2014.

[216] Vikram Seshadri and Phillip R. Westmoreland. Concerted Reactions and Mechanism of Glucose Pyrolysis and Implications for Cellulose Kinetics. *The Journal of Physical Chemistry A*, 116(49):11997–12013, December 2012.

[217] Joan J. Manyà, Enrique Velo, and Luis Puigjaner. Kinetics of Biomass Pyrolysis: a Reformulated Three-Parallel-Reactions Model. *Industrial & Engineering Chemistry Research*, 42(3):434–441, February 2003.

[218] Claudia J. Gómez, Joan J. Manyà, Enrique Velo, and Luis Puigjaner. Further Applications of a Revisited Summative Model for Kinetics of Biomass Pyrolysis. *Industrial & Engineering Chemistry Research*, 43(4):901–906, February 2004.

[219] S. Volker and Th. Rieckmann. The potential of multivariate regression in determining formal kinetics of biomass pyrolysis. In *Progress in thermochemical biomass conversion*. A.v. bridgwater edition, 2008.

[220] Carmen Branca, Alessandro Albano, and Colomba Di Blasi. Critical evaluation of global mechanisms of wood devolatilization. *Thermochimica Acta*, 429(2):133–141, May 2005.

[221] J.A Caballero, J.A Conesa, R. Front, and A. Marcilla. Pyrolysis kinetics of almond shells and olive stones considering their organic fractions. *Journal of Analytical and Applied Pyrolysis*, 42(2):159–75, 1997.

[222] Agustín García Barneto, José Ariza Carmona, José E. Martín Alfonso, and Rafael Sánchez Serrano. Simulation of the thermogravimetry analysis of three non-wood pulps. *Bioresource Technology*, 101(9):3220–3229, May 2010.

[223] G. Varhegyi, M.J. Antal, E. Jakab, and P. Szabo. Kinetic modeling of biomass pyrolysis. *Journal of Analytical and Applied Pyrolysis*, 42:73–87, 1997.

[224] Erika Mészáros, Gábor Várhegyi, Emma Jakab, and Béla Marosvölgyi. Thermogravimetric and reaction kinetic analysis of biomass samples from an energy plantation. *Energy & Fuels*, 18(2):497–507, 2004.

[225] J. J. M. Orfao, F. J. A. Antunes, and J. Lz Figueiredo. Pyrolysis kinetics of lignocellulosic materials—three independent reactions model. *Fuel*, 78(3):349–358, 1999.

[226] Ronny Bar-Gadda. The kinetics of xylan pyrolysis. *Thermochimica Acta*, 42(2):153–163, 1980.

[227] Zhengqi Li, Wei Zhao, Baihong Meng, Chunlong Liu, Qunyi Zhu, and Guangbo Zhao. Kinetic study of corn straw pyrolysis: Comparison of two different three-pseudocomponent models. *Bioresource Technology*, 99(16):7616–7622, November 2008.

[228] J.E.J Staggs. Modelling random scission of linear polymers. *Polymer Degradation and Stability*, 76:37–44, 2002.

[229] Lina N. Samuelsson, Rosana Moriana, Matthaus U. Babler, Monica Ek, and Klas Engvall. Model-free rate expression for thermal decomposition processes: The case of microcrystalline cellulose pyrolysis. *Fuel*, 143:438–447, March 2015.

[230] T.J.W. De Bruijn, W.A. De Jong, and P.J. Van Den Berg. Kinetic parameters in Avrami-Erofeev type reactions from isothermal and non-isothermal experiments. *Thermochimica Acta*, 1981.

[231] W. Duo, J. Ps K. Sevill, N. F. Kirkby, and R_ Clift. Formation of product layers in solid-gas reactions for removal of acid gases. *Chemical Engineering Science*, 49(24):4429–4442, 1994.

[232] Augustina Ephraim, Victor Pozzobon, Olivier Louisnard, Doan Pham Minh, Ange Nzihou, and Patrick Sharrock. Simulation of biomass char gasification in a downdraft reactor for syngas production. *AIChE Journal*, 62(4):1079–1091, April 2016.

[233] Pierre Lamarche, Mohand Tazerout, Franck Gelix, Stefanie Köhler, Karim Mati, and Frédéric Paviet. Modelling of an indirectly heated fixed bed pyrolysis reactor of wood: Transition from batch to continuous staged gasification. *Fuel*, 106:118–128, 2013.

[234] Rãzvan Vı̂jeu, Luc Gerun, Mohand Tazerout, Cathy Castelain, and Jérôme Bellettre. Dimensional modelling of wood pyrolysis using a nodal approach. *Fuel*, 87(15–16):3292–3303, November 2008.

[235] S.A. Ergun and A.A. Orning. Fluid flow through randomly packed columns and fluidized beds. *Industrial & Engineering Chemistry*, 41(6):1179–1184, 1949.

[236] J. Comiti and M. Renaud. A new model for determining mean structure parameters of fixed beds from pressure drop measurements: application to beds packed with parallelepipedal particles. *Chemical Engineering Science*, 44(7):1539–1545, 1989.

[237] Gabriel Teixeira, Laurent Van de Steene, Sylvain Salvador, Franck Gelix, Jean-Louis Dirion, and Frédéric Paviet. Gasification of continuous wood char bed: modelling and experimental approach. *Chemical Engineering Transactions*, 37:247–252, 2014.

[238] G. Teixeira, L. Van de Steene, E. Martin, F. Gelix, and S. Salvador. Gasification of char from wood pellets and from wood chips: Textural properties and thermochemical conversion along a continuous fixed bed. *Fuel*, 102:514–524, 2012.

[239] J.M. Moe. Design of water-gas shift reactors. *Chemical Engineering Progress*, 58(3), 1962.

[240] Donald A. Nield and Adrian Bejan. Heat Transfer Through a Porous Medium. In *Convection in Porous Media*, pages 31–46. Springer New York, New York, NY, 2013.

[241] Chase, M.W., Jr. NIST-JANAF Themochemical Tables, Fourth Edition. *Journal of Physical and Chemical Reference Data, Monograph 9*, pages 1–1951, 1998.

[242] L. Van de steene, J. P. Tagutchou, F. Mermoud, E. Martin, and S. Salvador. A new experimental Continuous Fixed Bed Reactor to characterise wood char gasification. *Fuel*, 89(11):3320–3329, November 2010.

[243] G. Teixeira, L. Van de Steene, E. Martin, F. Gelix, and S. Salvador. Gasification of char from wood pellets and from wood chips: Textural properties and thermochemical conversion along a continuous fixed bed. *Fuel*, 102:514–524, 2012.

[244] Chao Yang, Lishan Jia, Shuai Su, Zhongbiao Tian, Qianqian Song, Weiping Fang, Changping Chen, and Guangfa Liu. Utilization of CO2 and biomass char derived from pyrolysis of Dunaliella salina: The effects of steam and catalyst on CO and H2 gas production. *Bioresource Technology*, 110:676–681, 2012.

[245] Yao Bin Yang, ChangKook Ryu, Vida N. Sharifi, and Jim Swithenbank. Effect of Model and Operating Parameters on Air Gasification of Char. *Energy Fuels*, 20(4):1698–1708, 2006.

[246] Feng Yan, Si-yi Luo, Zhi-quan Hu, Bo Xiao, and Gong Cheng. Hydrogen-rich gas production by steam gasification of char from biomass fast pyrolysis in a fixed-bed reactor: Influence of temperature and steam on hydrogen yield and syngas composition. *Bioresource Technology*, 101(14):5633–5637, 2010.

[247] Heidi C. Butterman and Marco J. Castaldi. CO2 as a Carbon Neutral Fuel Source via Enhanced Biomass Gasification. *Environmental Science & Technology*, 43(23):9030–9037, December 2009.

[248] Kenneth M. Bryden, Kenneth W. Ragland, and Christopher J. Rutland. Modeling thermally thick pyrolysis of wood. *Biomass and Bioenergy*, 22(1):41–53, 2002.

[249] A. G. LIDEN, F. BERRUTI, and D. S. SCOTT. A kinetic model for the production of liquids from the flash pyrolysis of biomass. *Chemical Engineering Communications*, 65(1):207–221, 1988.

[250] Takashi Kashiwagi and Hidesaburo Nambu. Global kinetic constants for thermal oxidative degradation of a cellulosic paper. *Combustion and Flame*, 88(3-4):345–368, 1992.

[251] Kenneth M. Bryden and Kenneth W. Ragland. Numerical modeling of a deep, fixed bed combustor. *Energy & Fuels*, 10(2):269–275, 1996.

[252] Michael L. Boroson, Jack B. Howard, John P. Longwell, and William A. Peters. Product yields and kinetics from the vapor phase cracking of wood pyrolysis tars. *AIChE Journal*, 35(1):120–128, 1989.

[253] Elias Daouk. *Etudes expérimentale et numérique de la pyrolyse oxydante de la biomasse en lit fixe*. PhD thesis, École des Mines de Nantes, 2015.

[254] Nourredine Abdoulmoumine, Sushil Adhikari, Avanti Kulkarni, and Shyamsundar Chattanathan. A review on biomass gasification syngas cleanup. *Applied Energy*, 155:294–307, October 2015.

[255] Mohammad Asadullah. Biomass gasification gas cleaning for downstream applications: A comparative critical review. *Renewable and Sustainable Energy Reviews*, 40:118–132, December 2014.

[256] Sunil D. Sharma, M. Dolan, A.Y. Ilyushechkin, K.G. McLennan, T. Nguyen, and D. Chase. Recent developments in dry hot syngas cleaning processes. *Fuel*, 89(4):817–826, April 2010.

[257] B. S. Turk, T. Merkel, A. Lopez-Ortiz, R. P. Gupta, J. W. Portzer, G. N. Krishnan, B. D. Freeman, and G. K. Fleming. Novel technologies for gaseous contaminants control. *Contract DE-AC26-99FT40675 for US DOE by Research Triangle Institute, Research Triangle Park, North Carolina, September*, 2001.

[258] N. Verdone and P. De Filippis. Reaction kinetics of hydrogen chloride with sodium carbonate. *Chemical Engineering Science*, 61(22):7487–7496, November 2006.

[259] Nicola Verdone and Paolo De Filippis. Thermodynamic behaviour of sodium and calcium based sorbents in the emission control of waste incinerators. *Chemosphere*, 54(7):975–985, February 2004.

[260] Miloslav Hartman, Karel Svoboda, Michael Pohořelý, Michal Šyc, Siarhei Skoblia, and Po-Chuang Chen. Reaction of Hydrogen Chloride Gas with Sodium Carbonate and Its Deep Removal in a Fixed-Bed Reactor. *Industrial & Engineering Chemistry Research*, 53(49):19145–19158, December 2014.

[261] K.T. Fellows and M.J. Pilat. HCl sorption by dry NaHCO3 for incinerator emissions control. *Journal of Air and Waste Management Association*, 40(6), 1990.

[262] G. N. Krishnan, B.J. Wood, and G.T. Tong. Removal of hydrogen chloride from high temperature coal gases. *Jouranl of American Chemical Society*, 33(1), 1988.

[263] Binlin Dou, Weiguo Pan, Jianxing Ren, Bingbing Chen, Jungho Hwang, and Tae-U Yu. Single and Combined Removal of HCl and Alkali Metal Vapor from High-temperature Gas by Solid Sorbents. *Energy & Fuels*, 21(2):1019–1023, March 2007.

[264] Binlin Dou, Jinsheng Gao, Seung Wook Baek, and Xingzhong Sha. High-Temperature HCl Removal with Sorbents in a Fixed-Bed Reactor. *Energy & Fuels*, 17(4):874–878, July 2003.

[265] Binlin Dou, Bingbing Chen, Jinsheng Gao, and Xingzhong Sha. HCl Removal and Chlorine Distribution in the Mass Transfer Zone of a Fixed-Bed Reactor at High Temperature. *Energy & Fuels*, 20(3):959–963, May 2006.

[266] Chien-Song Chyang, Yun-Long Han, and Zi-Chao Zhong. Study of HCl Absorption by CaO at High Temperature. *Energy & Fuels*, 23(8):3948–3953, August 2009.

[267] W. Wang, Y. Zhicheng, and I. Bjerle. The kinetics of the reaction of hydrogen chloride with fresh and spent Ca-based desulfurization sorbents. *Fuel*, 75(2):207–212, 1996.

[268] M. Daoudi and J. K. Walters. The reaction of HCl gas with calcined commercial limestone particles: the effect of particle size. *The Chemical Engineering Journal*, 47(1):11–16, 1991.

[269] Zhenchao Sun, Fu-Chen Yu, Fanxing Li, Songgeng Li, and Liang-Shih Fan. Experimental Study of HCl Capture Using CaO Sorbents: Activation, Deactivation, Reactivation, and Ionic Transfer Mechanism. *Industrial & Engineering Chemistry Research*, 50(10):6034–6043, May 2011.

[270] Junjun Tan, Guohua Yang, Jingqiao Mao, and Huichao Dai. Laboratory study on high-temperature adsorption of HCl by dry-injection of Ca(OH)2 in a dual-layer granular bed filter. *Frontiers of Environmental Science & Engineering*, 8(6):863–870, 2014.

[271] G. Mura and A. Lallai. Reaction kinetics of gas hydrogen chloride and limestone. *Chemical engineering science*, 49(24):4491–4500, 1994.

[272] Jun Cao, Wenqi Zhong, Baosheng Jin, Zhifei Wang, and Kai Wang. Treatment of Hydrochloric Acid in Flue Gas from Municipal Solid Waste Incineration with Ca–Mg–Al Mixed Oxides at Medium–High Temperatures. *Energy & Fuels*, 28(6):4112–4117, June 2014.

[273] Thallada Bhaskar, Toshiki Matsui, Koji Nitta, Md. Azhar Uddin, Akinori Muto, and Yusaku Sakata. Laboratory Evaluation of Calcium-, Iron-, and Potassium-Based Carbon Composite Sorbents for Capture of Hydrogen Chloride Gas. *Energy & Fuels*, 16(6):1533–1539, November 2002.

[274] Yasuo Ohtsuka, Naoto Tsubouchi, Takemitsu Kikuchi, and Hiroyuki Hashimoto. Recent progress in Japan on hot gas cleanup of hydrogen chloride, hydrogen sulfide and ammonia in coal-derived fuel gas. *Powder Technology*, 190(3):340–347, March 2009.

[275] Miguel Galván-Ruiz, Juan Hernández, Leticia Baños, Joaquín Noriega-Montes, and Mario E. Rodríguez-García. Characterization of Calcium Carbonate, Calcium Oxide, and Calcium Hydroxide as Starting Point to the Improvement of Lime for Their Use in Construction. *Materials in Civil Enginering*, 21(11), 2009.

[276] Cem E. Celik, Mark William Ackley, and James Smolarek. Modular compact adsorption bed, July 2011.

[277] P.V. Aravind and Wiebren de Jong. Evaluation of high temperature gas cleaning options for biomass gasification product gas for Solid Oxide Fuel Cells. *Progress in Energy and Combustion Science*, 38(6):737–764, December 2012.

[278] Tomohito Kameda, Naoya Uchiyama, and Toshiaki Yoshioka. Treatment of gaseous hydrogen chloride using MgAl layered double hydroxide intercalated with carbonate ion. *Chemosphere*, 81(5):658–662, October 2010.

[279] Tomohito Kameda, Naoya Uchiyama, and Toshiaki Yoshioka. Removal of HCl, SO2, and NO by treatment of acid gas with Mg–Al oxide slurry. *Chemosphere*, 82(4):587–591, January 2011.

[280] M. Blachman. Process for removing HCI from fluids with novel adsorbent, March 2001.

[281] J Partanen, P Backman, R Backman, and M Hupa. Absorption of HCl by limestone in hot flue gases. Part II: importance of calcium hydroxychloride. *Fuel*, March 2005.

[282] William Tongamp, Qiwu Zhang, Miyagi Shoko, and Fumio Saito. Generation of hydrogen from polyvinyl chloride by milling and heating with CaO and Ni(OH)2. *Journal of Hazardous Materials*, 167(1-3):1002–1006, August 2009.

[283] W. Duo and N.F. Kirkby. Kinetics of HCl reactions with calcium and sodium sorbents for IGCC fuel gas cleaning. *Chemical Engineering Science*, 51(11):2541–2546, 1996.

[284] J Partanen, P Backman, R Backman, and M Hupa. Absorption of HCl by limestone in hot flue gases. Part I: the effects of temperature, gas atmosphere and absorbent quality. *Fuel*, March 2005.

[285] Hans T. Karlsson, Jonas Klingspor, and Ingemar Bjerle. Adsorption of Hydrochloric Acid on Solid Slaked Lime for Flue Gas Clean Up. *Journal of the Air Pollution Control Association*, 31(11):1177–1180, November 1981.

[286] I.I. Ahmed, N. Nipattummakul, and A.K. Gupta. Characteristics of syngas from co-gasification of polyethylene and woodchips. *Applied Energy*, 88(1):165–174, January 2011.

[287] F. Pinto, C. Franco, R. N. André, M. Miranda, I. Gulyurtlu, and I. Cabrita. Co-gasification study of biomass mixed with plastic wastes. *Fuel*, 81(3):291–297, 2002.

[288] Bernard Le Neindre. Mesure de la conductivité thermique des liquides et des gaz. *Techniques de l'ingénieur*, R2920:15–22, 1996.

[289] Murlidhar Gupta, Jin Yang, and Christian Roy. Specific heat and thermal conductivity of softwood bark and softwood char particles. *Fuel*, 82(8):919–927, 2003.

List of Figures

List of Tables

Valorization of wood and plastic waste by pyro-gasification and syngas cleaning

Abstract: Wood and plastic waste are interesting feedstock for the production of syngas via pyro-gasification, mainly due to their abundant supply and good fuel properties. However, syngas derived from waste may contain significant amounts of hydrogen chloride (HCl), which is corrosive and toxic and must therefore be removed.

In this work, co-pyrolysis experiments were first conducted in order to study the influence of mixing different plastics with wood samples on the pyrolysis products. It was found that HDPE and PS significantly increase the heating value and HCl content of the gas product respectively, while PVC increases the yield of char and HCl. Next, pilot-scale experiments were performed, which revealed that adding 1 wt% PVC to wood waste raises the content of tar and HCl in syngas by factors of 2 and 5,5 respectively, and also elevates the chlorine concentration in the char residue 16 time over the value obtained in the absence of PVC.

In parallel, a CFD model was developed to simulate the pyro-gasification of wood waste by coupling fluid flow, heat and mass transfer, and chemical reactions. This model consists of drying, pyrolysis, oxidation and char gasification sub-models. The simulation results were in good agreement with experimental data obtained from the pilot-scale experiments. Furthermore, sensibility analyses on the char gasification sub-model were performed.

Finally, an experimental study was conducted on the removal of HCl from syngas. The study focused on valorizing two industrial solid wastes generated from the process of sodium carbonate and sodium bicarbonate manufacture. Their HCl adsorption performance were compared to those of the commercial sorbents, $NaHCO_3$ et $Ca(OH)_2$. Moreover, the effect of gas matrix on their performance was studied. The industrial wastes showed potential for treating acid gas as compared to the commercial sorbents used. This opens up new approaches to the purification of syngas generated by the pyro-gasification of wood and plastic waste.

Keywords: Waste, Pyrolysis, Gasification, Modelling, Hydrogen chloride, Syngas cleaning.

Valorisation de déchets de bois et matières plastiques par pyrogazéification et épuration des gaz

Résumé : Les déchets de bois et de plastiques sont des ressources prometteuses pour la production du gaz de synthèse (syngaz) par la pyro-gazéification grâce à leurs disponibilités et leurs caractéristiques énergétiques. Cependant, le syngaz issu de ces déchets peut contenir des teneurs élevées en chlorure d'hydrogène (HCl) qui est corrosif et toxique et qui doit donc être éliminé.

Premièrement, les expériences de pyrolyse des mélanges de bois de peuplier et de plastiques ont mis en évidence l'influence des plastiques sur les produits obtenus. En effet, le HDPE et PS augmente respectivement le pouvoir calorifique du syngaz et le rendement en huiles, tandis que le PVC augmente le rendement en char et le HCl dans le syngaz. Ensuite, les expériences de pyro-gazéification à l'échelle pilote ont montré que l'ajout de 1 % en masse de PVC dans un déchet de bois augmente la teneur en goudrons et HCl dans le syngaz par un facteur respectivement de 2 et 5,5, tandis que la concentration de chlore dans le char résiduel est 16 fois plus élevée.

En parallèle, un model CFD a été développé pour simuler la pyro-gazéification du déchet de bois en couplant les phénomènes d'écoulement de fluides, transfert de masse et de chaleur, et les réactions chimiques. Ce modèle se compose des sous-modèles de séchage, pyrolyse, oxydation et gazéification du char. Les résultats de simulation sont en bon accord avec les données expérimentales obtenues par des expériences dans un gazéifieur à l'échelle pilote. En outre, les analyses de sensibilités du sous-modèle de la gazéification de char ont été réalisées.

Finalement, une étude expérimentale a été conduite sur le traitement de HCl dans le syngaz. L'étude se concentre sur la valorisation de deux résidus solides industriels issus de la production de bicarbonate et carbonate de sodium. Leurs réactivités sont comparés avec celles de deux adsorbants commerciaux, $NaHCO_3$ et $Ca(OH)_2$. L'effet de la matrice gazeuse sur la performance des adsorbants est également examiné. Les résidus industriels ont un potentiel intéressant par rapport aux adsorbants commerciaux. Les résultats obtenus montrent des nouvelles approches pour la purification du syngaz généré par la gazéification des déchets de bois et de plastiques.

Mots-clés : Déchet, Pyrolyse, Gazéification, Modélisation, Chlorure d'hydrogène, Purification du syngaz.